Root Causes of Cycle-to-Cycle Combustion Variations in Spark Ignited Engines

by

Philipp Schiffmann

A dissertation submitted in partial fulfillment
of the requirements for the degree of
Doctor of Philosophy
(Mechanical Engineering)
in the University of Michigan
2016

Doctoral Committee:

Professor Volker Sick, Chair
Professor Andre L. Boehman
SeungHwan Keum, General Motors Co.
Cecile Pera, Infineum Ltd.
Professor Venkat Raman, Cognate
Research Scientist David L. Reuss

DEDICATION

I dedicate this work my family and friends.

ACKNOWLEDGEMENTS

Acknowledgments

I wish to thank the University of Michigan General Motors Collaborative Research Laboratory and the PRISME Laboratory for financial support. Further, I would like to thank all members at General Motors R&D, University of Wisconsin and Pennsylvania State University of the large eddy simulation working group for insightful discussions and advice, especially Todd Fansler, Tang-Wei Kuo, SeungHwan Keum, Xiaofeng Yang and Kevin Peterson. The author also would like to thank Gerald Silvas (GM R&D), Rick Davis and Norm Maasshoff (both GM Powertrain) on their support and advice on engine hardware and pressure diagnostics.

The author also wishes to thank Charles Endouard, Pierre Brequigny, Bruno Moreau and Florian Lespinasse for their assistance with the combustion vessel setup.

The discussions about statistical analysis with CSCAR (consulting for statistics, computing and analytics research) advisors Alex Cao and Kirby Shedden were much appreciated.

Finally, the author likes to thank all past and current “Sicklab” members for fruitful discussions and making research and lab work more productive and fun.

TABLE OF CONTENTS

LIST OF TABLES

LIST OF FIGURES

LIST OF APPENDICES

LIST OF ABBREVIATIONS

Abbreviation	Explanation	Abbreviation	Explanation
A	area	EGR	exhaust gas recirculation
ATDCE	after top dead center exhaust	EMF	electromagnetic field
Avg	average	EPL	exhaust valve peak lift
b	burned	EVC	exhaust valve closing
BDC	bottom dead center	EVO	exhaust valve opening
BDCE	bottom dead center exhaust	f	focal length
BDCI	bottom dead center intake	F/A	fuel to air ratio
BSFC	break specific fuel consumption	FOV	field of view
C	circumference	GM	general motors
CA	crank angle (of crank shaft)	h	enthalpy
CA10	crank angle at which 10% mass fraction burnt	HC	hydro carbon
CA50	crank angle at which 50% mass fraction burnt	HRR	heat release rate
CA90	crank angle at which 90% mass fraction burnt	HSC	high-speed controller
CAD	crank angle degree	i	current
cc	cubic centimeter	ICA	independent component analysis
CCD	charge-coupled device	ICE	internal combustion engine
CCV	cycle-to-cycle variation	IMAP	intake manifold absolute pressure
CFD	computational fluid dynamics	IMEP	indicated mean effective pressure
CMOS	complimentary metal-oxide-semiconductor	IPL	intake valve peak lift
COV	coefficient of variance	IVC	intake valve closing
cp	specific heat at constant pressure	IVO	intake valve opening
CR	compression ratio	J	joules
CSCAR	consulting for statistics, computing and analytics research	Ka	Karlovitz number ratio of chemical and smallest turbulent time scales
cv	specific heat at constant volume	L	integral length scale; Markstein length; as sub-script: laminar
DAQ	data acquisition system	LDV	laser Doppler velocimetry
DI	direct injection	LES	large eddy simulation
DNS	direct numerical simulation	m	mass
E	energy; component of 2D strain tensor	Ma	Markstein number

Abbreviation	Explanation	Abbreviation	Explanation
MBT	mean best torque timing	RPM	revolutions per minute
MFB	mass fraction burned	s	flame speed
MPS	mean piston speed	SA	spark angle
n	polytropic compression/expansion coefficient; number	SACI	spark-assisted homogeneous charge compression ignition
Nd:YAG	Neodyium-doped yttrium aluminum garnet	SI	spark ignited; structure index
Nd:YLF	Neodyium-doped yttrium lithium fluoride	SOI	start of ignition
OH*	electronically excited hydroxyl molecule, molecule that can be used as flame front tracer	SPIV	stereo particle image velocimetry
p	pressure	StDev	standard deviation
P	perimeter	T	temperature
Pa	Pascal	T	as sub-script: turbulent
PCESC	personal computer engine system controller	t	time
PFI	port fuel injection	TCC	transparent combustion chamber
PIV	particle image velocimetry	TDC	top dead center
PLIF	planar laser induced fluorescence	TDCC	top dead center compression
PLIF	planer laser induced fluorescence	TEM	transverse electromagnetic mode
POD	proper orthogonal decomposition	TKE	turbulent kinetic energy
ppc	pulse per cycle	u	voltage
ppr	pulse per revolution	u	unburned
PTU	programmable timing unit	u'	turbulence intensity
r	radius	UV	ultra violet light
R	correlation coefficient; resistance; spatial or temporal correlation function; universal gas constant (R=8.3166 J/molK)	V	volume
R^2	coefficient of determination	W	wrinkling factor
RBG	residual burned gas	WOT	wide open throttle
Re	Reynolds number	x	mass fraction; coordinate direction
RMS	root mean square velocity	y	volume fraction; coordinate direction

Abbreviation	Explanation	Abbreviation	Explanation
z	coordinate direction, as defined by x and y in a right handed coordinate system	Ze	Zel’dovich number

LIST OF SYMBOLS

Symbol	Explanation	Symbol	Explanation
ϕ	fuel-air equivalence ratio	λ	Taylor micro scale; air-fuel equivalence ratio; wavelength in electromagnetic spectrum
α	thermal conductivity; proportional	μ	micro
γ	ratio of specific heats	ν	kinematic viscosity
δ	flame thickness	ρ	density
η	Kolmogorov scale	τ	characteristic time
κ	stretch rate	Ω	Ohm

ABSTRACT

Stricter governmental emission regulations, climate change concerns, and consumer demands for high fuel efficiency push the development of advanced cleaner and more efficient combustion strategies. Many strategies that rely on spark ignition are limited in their peak efficiencies by excessive cycle-to-cycle combustion variations (CCV). In this study, various laser-based and passive optical techniques are used to measure flow fields, spark discharge and other factors that impact early flame growth from which CCV originate.

Bulk flow motion, as one contributing factor to CCV, is characterized in an optical engine under motored and fired conditions. In the fired cases, the flow velocities are higher during the gas exchange period but lower at the time of ignition, due to higher charge viscosities, caused by higher gas temperatures. Ten different fuel-air mixtures are strategically chosen to isolate the effects of laminar flame speed, thermo-diffusive mixture properties and change of stoichiometrically deficient species on the mechanisms that are responsible for cycle-to-cycle variability.

Single value decomposition methods are found to be inefficient in identifying flow structures that are related to combustion variability. Physical flow parameters such as velocity magnitude and shear strength around time of ignition are identified to affect combustion variability. The relative impact of these parameters on energy output and combustion phasing are quantified for all mixtures and show some weak dependence on Markstein number and laminar flame speed.

In a more fundamental fan-stirred combustion vessel experiments, variability effects of flame-flow interactions on CCV are isolated and thermo-diffusive effects are shown to impact combustion variability. Unstable negative Markstein number mixtures tend to exhibit higher combustion variability when interacting with gradients in the flow field around the time of ignition. High shear strength at the point of ignition causes an increased flame wrinkling, increasing the surface area, leading to faster combustion. This is an important finding because the common Lewis number equals 1 assumption in CFD simulations might lead to an under-prediction of CCV in low turbulence cases for negative Markstein number mixtures.

CHAPTER 1 INTRODUCTION

Regulatory institutions worldwide require ever stricter fuel efficiency standards to limit the extent of global warming caused by greenhouse gas emissions such as CO_2 [1]. Contrary to toxic pollutants (i.e. CO, NOx, soot), CO_2 is an unavoidable end product of a fully oxidized hydrocarbon fuel combustion and can only be reduced by decreasing energy demand, changing transportation fuels or increasing combustion system efficiency. More efficient down-sized boosted lean burn engines and advanced combustion concepts like spark-assisted homogeneous charge compression ignition (SACI) are the industry's response to meet these higher efficiency needs.

While efficiency increases with higher compression ratio and higher dilution levels, the full fuel-saving potential of these concepts cannot be reached due to knock and flammability limits that are defined by rare outlier cycles that occur during advanced or retarded combustion timing. This variability in combustion phasing is mostly determined during the ignition delay period to up to 10% mass burn fraction (CA10). Quantifying the impact of flow conditions together with cycle-resolved spark-discharge characteristics on the ignition and early flame kernel stages of combustion is essential to develop the knowledge necessary to push closer to the high-efficiency limits.

Many of the factors influencing the cyclic variability have been recognized in the literature (i.e. variability in flow, inhomogeneities, spark discharge characteristics, etc.) by measuring usually one influencing factor at a time, resulting in partial explanations rather than a fundamental understanding. Recent direct numerical simulation (DNS) studies by Pera et al. [2] show that initial flame kernel size and turbulence structure (flow surrounding the spark plasma, at constant length scales and turbulence intensity) are more important than integral length scale or turbulence intensity for flame growth.

By measuring the flow structure effects in the immediate vicinity of the spark plug, with simultaneous temperature stratification measurements using planar laser-induced fluorescence (PLIF), and spark-discharge energy and duration, valuable insights into the influence of these properties on the cyclic variability of the early flame kernel can be gained. Systematic variations in equivalence ratio, dilution, and fuel will allow conclusions to be drawn about the sensitivity of the flame kernel to laminar flame speed and thermo-diffusive effects as characterized by the Markstein number. With this information and a better understanding at hand, it will be possible to make design changes to reduce cyclic variability and push closer to combustion limits, which facilitates improved engine efficiency and reduced emissions.

The optimization of combustion system is nowadays a combined approach between experiments and simulations. For gaining valuable information from the simulations, the right assumptions need to be made to capture the governing physical phenomena. The data collected in this thesis will be made available on a Deepblue data repository for researchers to use. Additionally the findings from this thesis on the importance of thermo-diffusive effects on combustion variability can help the engine CFD modeling community to decide if the error induced by Lewis number equals to 1 assumption is acceptable for the specific running condition they try to model. Capturing these phenomena is computationally expensive, but might be feasible thanks to the use of high-performance computing and parallel computing. In this respect this work provides guidance on where to best initialize CFD simulations and on how much artificially added perturbation in the flow field is realistic.

1.1 Guide to This Thesis

In this chapter fundamentals of the topic of cycle-to-cycle variations are explained. To put the topic in context, first the working principle of spark-ignited (SI) engines is explained. Then the theoretical thermodynamic process is covered to show the principlal parameters influencing combustion efficiency, before moving to real world combustion cycle and actual log(pressure)-log(volume) plots. After the general combustion behavior is explained, the variability aspect is described in detail. The variables affecting combustion are covered in chronological order from ignition, laminar early flame kernel phase, transition into the turbulent regime, and finally to flame extinction. Examples on each of these variability aspects from literature have been

included here to point out the lack of knowledge and understanding in literature on combustion variability. The objective of this work is explained at the end of Chapter 1 together with the hypotheses that are tested in this work.

Chapter 2 generally explains the tools that are used to achieve the research objectives. First the setup of the transparent combustion chamber (TCC) engine is explained and how it is instrumented to measure pressures and spark characteristics with high accuracies. The general engine and trigger control setup are explained before measurement uncertainties are analyzed. Because the engine needs to be disassembled after each run for cleaning, the test-to-test pressure and flow repeatability is quantified. After the characterization of the TCC engine the second combustion system setup used in this thesis, the University of Orléans combustion vessel, is explained. All imaging techniques used are explained in the end of Chapter 2. The general working principle, physical setup and processing techniques are covered with example images and results.

Chapter 3 is based on the author's paper [3] on bulk flow variability in the TCC engine but is expanded with the addition of fired engine operation results. The variability of the in-cylinder flow is measured in four planes throughout the entire cycle. Effects of change in engine speed and engine load for motored condition are documented, and the effects of combustion on the intake and compression stroke flow are investigated. Ensemble average flow and root mean square velocity (RMS) fields are compared, and the changes in spatial and temporal flow scales are evaluated. In the last part of Chapter 3, the influencing factors on combustion are investigated for a well burning and a very lean combustion high-variability case.

Chapter 4 shows preliminary experiments with the purpose of identifying a test matrix of different intake charge mixtures to isolate flame speed, thermo-diffusive effects, and the change of deficient species on combustion variability behavior. One case exhibiting high cycle-to-cycle variability, during which flow fields are acquired, is used as a first iteration step that identifies the experimental needs for detailed experiments covered in Chapter 5 and Chapter 6.

Chapter 5 describes the isolated study of flame-flow interactions in a fan-stirred combustion vessel. These experiments show to which flow parameters trigger ultimately cycle-to-cycle

variations. Turbulent length and time scales are calculated and consequently used to conduct the vessel experiments in the same turbulent flame regimes as in the engine. First, some specific examples of flames and flow-induced variability are shown, before using statistical methods of understanding the general variability behavior of different mixtures. It is shown that under engine-like conditions thermo-diffusive properties play an important role in cycle-to-cycle variations, due to the change in the flame's sensitivity to stretch.

Chapter 6 shows the combined results of a multi-diagnostic engine experiment that is based on the findings of the previous chapters. Spark discharge characteristics, flow field, temperature field and flame propagation, have been measured in high spatial and temporal resolution simultaneously. Significant combustion variables are first identified and then used in a multi-variant model to quantify their effect on cycle-to-cycle variations. It is shown that flow structures as identified by proper orthogonal decomposition and independent component analysis are not as relevant to the flame development as physical flow parameters such as flow velocity magnitude, direction and flow gradients parameters.

Chapter 7 summarizes the findings of the previous chapters and explains the impact the results have on engine development in the context of cycle-to-cycle variations. The future work and suggested next steps are then pointed out.

1.2 Spark Ignition Engines

Reciprocating Internal Combustion Engines (ICE) are and continue to be the main energy converters in transportation and small scale power generation sector. They extract the chemical energy from hydrocarbons via combustion and convert it to mechanical energy that can be used to drive a vehicle. Although engines have an over 125 year old history from their invention, their fundamental working principles have stayed the same and are well documented in literature [4-6]. Homogenous charge SI ICEs are the most common combustion engines, because they are relatively cheap and run reliably. ICEs usually run on the four-stroke Otto-cycle (in automotive applications, 2-strokes are rare).

In the past, the combustible air-fuel mixture was generated by carburetors, but for today's automotive application port fuel injection (PFI) and early direct injection (DI) are the standards. In the intake stroke fuel-air mixture (only air for DI) is sucked through the open intake valve by the downward motion of the piston. After bottom dead center intake (BDC), the intake valve starts closing and the mixture is compressed by an upward moving piston. 50 to 10 crank angle degrees (CAD) before top dead center compression (TDC), the mixture is ignited by a spark. The combustion releases the chemically bound energy into heat that causes the gases to expand, resulting in a pressure increase. In the compression stroke around 10 CAD after TDC, about 50% of the fuel is burned and the piston is pushed downward by the in-cylinder pressure. Before BDC, the exhaust valve opens and the burned gas is pushed out by the piston. Around TDC, the exhaust valve closes and the intake valve opens and a new cycle begins.

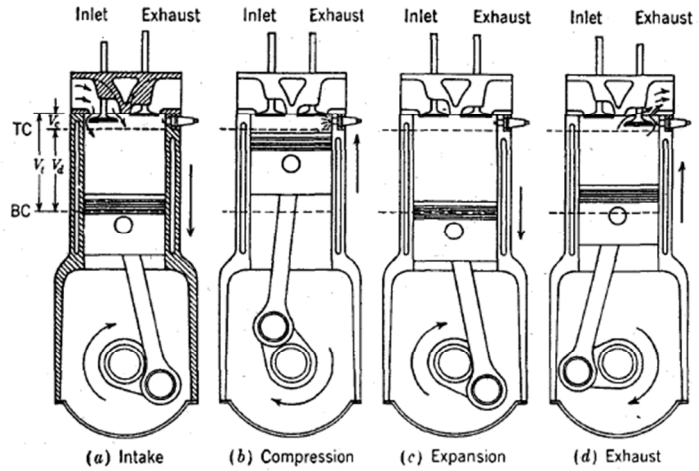

Figure 1-1Illustration 4-stroke Otto-cycle (extracted from [4])

1.2.1 Constant Volume Process

To first order combustion in SI ICE follows the constant volume process. While intake (points 6->1 of Figure 1-2) and exhaust stroke (points 5->6) are at constant pressure the scavenging loop collapsed to a line and does not contribute to the energy balance. The mixture is isentropically compressed (points 1->2) which requires work input. The actual combustion event is modeled to happen instantaneously by heat addition (points 2->3). In the following power stroke (points 3->4) the gas expands isentropically to BDC where heat is instantaneously ejected at constant volume (points 4->5).

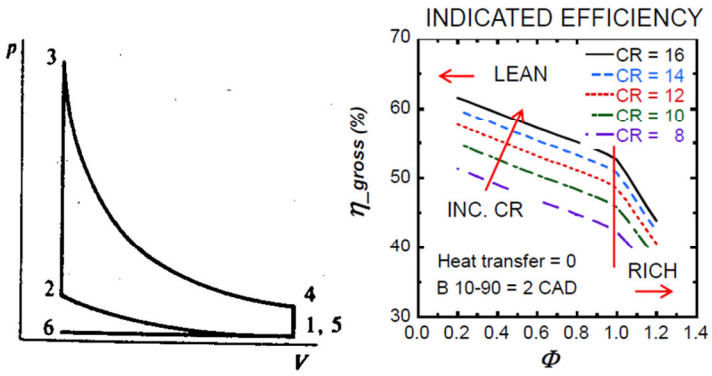

Figure 1-2 Unthrottled constant volume process (extracted from [4])

In this constant volume process the theoretical efficiency is determined by the isentropic exponent of the working fluid γ and the compression ratio CR of the engine only and can be calculated as follows $\eta_{IDEAL} = 1 - \frac{1}{CR^{(\gamma-1)}}$ where $\gamma = \frac{c_p}{c_v}$ is the ratio of specific heats of the working fluid, and $CR = \frac{V_{BDC}}{V_{TDC}}$ is the geometric compression ratio [4]. Although the constant volume process is simple, it still yields valuable insights in how to improve the theoretical efficiency of an ICE, by increasing compression ratio and increasing the ratio of specific heats of the working fluid (by adding dilution). These effects are illustrated in Figure 1-2 b).

1.2.2 Real Engine Working Cycle

In contrast to the idealized constant volume cycle, a real engine has heat losses, blow-by, pumping losses, pressure wave dynamics in the intake and exhaust systems, and operates with a non-instantaneous combustion process. The effects of these phenomena can be observed in the measured log P – log V trace illustrated in Figure 1-3.

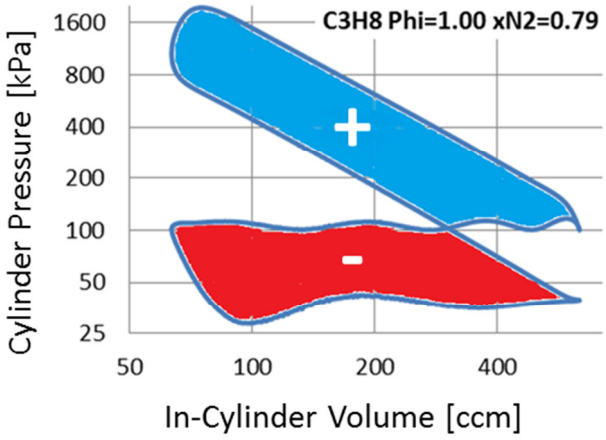

Figure 1-3 Cylinder pressure vs. in-cylinder volume plot of actual engine cycle under throttled conditions

The scavenging loop is marked in red. It is a counter-clockwise loop that requires energy to push exhaust gases out at ambient pressure and draws fresh mixture in; here at about 40 kPa. The mixture is then compressed polytropically, which reduces the slope compared to isentropic compression, due to heat losses to cylinder walls and blow-by. The mixture is ignited at around 310 to 350 after TDC exhaust (ATDCE) to account for an ignition delay of the mixture of about 15-50 CAD. This is the time the flame needs to burn 0.5%-10% of the mixture, depending on definition. The pressure rises as the charge temperature increases caused by the combustion process. The increased pressure in the cylinder pushes the piston down and the mechanical energy generated is transferred by the connecting rod on the crankshaft from where it can be extracted.

1.2.3 MBT and Limits in ICE Operation

ICEs perform over a range of engine speed and load conditions, for which at each operating point there exists a spark timing that yields the highest torque output on average. This spark timing is called maximum break torque (MBT) timing and can be determined by a spark sweep. In Figure 1-4, indicated mean effective pressure (IMEP) (proportional to engine-out torque) and coefficient of variance of IMEP (COV_{IMEP}) are plotted as a function of spark angle (SA) in the TCC-III engine at 1300RPM and 40kPa IMAP with stoichiometric premixed propane as fuel. At a SA of 342 CAD, IMEP is highest, which defines the MBT timing for this operating condition. At around the same CA, COV_{IMEP} is lowest. Earlier spark timings than MBT cause in-cylinder

pressures to be high too early and as such acting against the rotary direction of the crank shaft. Whereas later than MBT spark timing causes pressure to be build up later than ideal and the energy cannot be used efficiently.

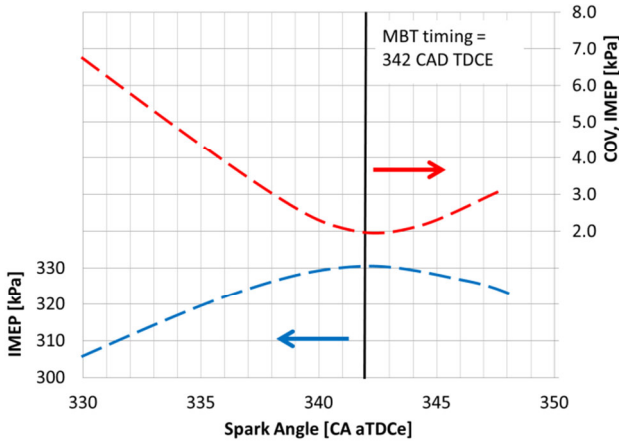

Figure 1-4 MBT timing for TCC-III engine at 1300RPM 40kPa Φ=1.0 condition

At high loads and low speeds, engines exhibit the highest tendency for engine knock. Engine knock is the spontaneous end gas auto ignition due to high pressures and temperatures. This leads to increased pressure rise rates and high cylinder peak pressures audible by a characteristic knocking sound. To avoid engine knocking the spark needs to be retarded in order to avoid damage to the engine hardware. Retarded SA from MBT leads to a lower efficiencies. Besides the SA, the maximum compression ratio (higher CR increases efficiency) and the minimum octane rating of the fuel used (higher octane rating premium fuels tend to be more expensive) are also limited by engine knock.

At idle condition, the engine needs to only produce just enough energy to drive the auxiliary loads (water and oil pump, alternator etc.) and to overcome friction losses. Here the engine speed needs to be high enough to have enough kinetic energy stored in the flywheel and other moving components to be able to compress the charge for the next combustion event, without exhibiting a rough running behavior (high deviations in engine speed).

1.2.4 Cycle-to-Cycle Variability (CCV)

Until now only average behavior of the combusiton process in an engine have been mentioned. In reality, though, every engine cycle is more or less different in their combustion behavior, as

illustrated in Figure 1-5. Although knock and idle limits are totally different phenomena, they are both limited by single cycle phenomena.

In case of knocking the limit is determined by the fastest burning cycles that show an advanced combustion phasing and produce early high pressures and temperatures which lead to the aforementioned auto ignition of the unburned mixtures. This means that automanufacturers are constrained by few faster burning cycles and have to use a lower compression ratio and run a later than ideal SA, which reduces the engine's efficiencies in these regimes.

On the other hand, the idle speed is limited by the most retarded and lowest IMEP producing cycle, that either would lead to a "rough" running engine or to a complete stop of the engine, which would have to be restarted. Therefore, in these lower than average IMEP cycles, the idle speed is higher than actually needed with the draw back of increased fuel consumption.

Besides the two limiting operation conditions this variability causes the engine to produce less than possible power. The causes of and more details on the causes of cycle-to-cycle variations can be found on page 17.

Although with pressure transducers the effects of the variabilty can be readily measured, this data only provides very limited information about causes and essentially no information about the physics behind these processes. . In order to extract such valuable information from the system, one needs to resolve complex transient physical processes that involve experimentally challenging ranges of length scales (ideally from atomic dimensions: $\sim 10^{-10}$ m to cylinder dimensions: $\sim 10^{-1}$ m) and time (from spark breakdown: $\sim 10^{-10}$ s to thermal transient times $\sim 10^{3}$ s) scales. Herein this project, in pursuit of reaching insightful physical answers to this complicated problem, sophisticated optical diagnostic methods are proposed and performed in a transparent combustion chamber (TCC) engine that allows maximum optical access to the combustion chamber.

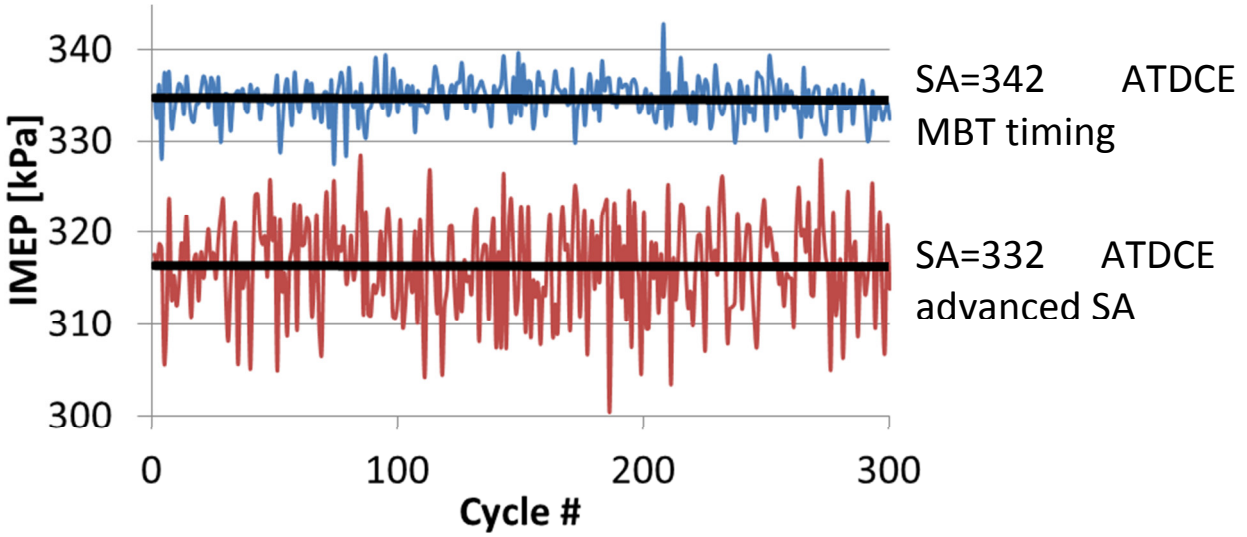

Figure 1-5 IMEP vs cycle number for MBT timing and 10 CAD advanced SA timing, black lines indicate test averages

1.3 Combustion Variability in SI Engines

In this chapter engine combustion is divided into spark and flame initiation, initial kernel development, turbulent flame propagation and flame termination, as suggested by [7]. Factors that influence cyclic-variability are shown and it is pointed out how they relate to the overall combustion success measured by IMEP. The early stages of combustion are especially susceptible to cycle-to-cycle variations of local properties close to the spark plug, affecting ignition delay and the thermodynamic state at which the successive combustion events happen. The combustion variations introduced during the early flame kernel period persist throughout laminar-to-turbulent transition, turbulent flame propagation with compression until the location of peak cylinder pressure and the late burn with a cooling expansion of the end gas.

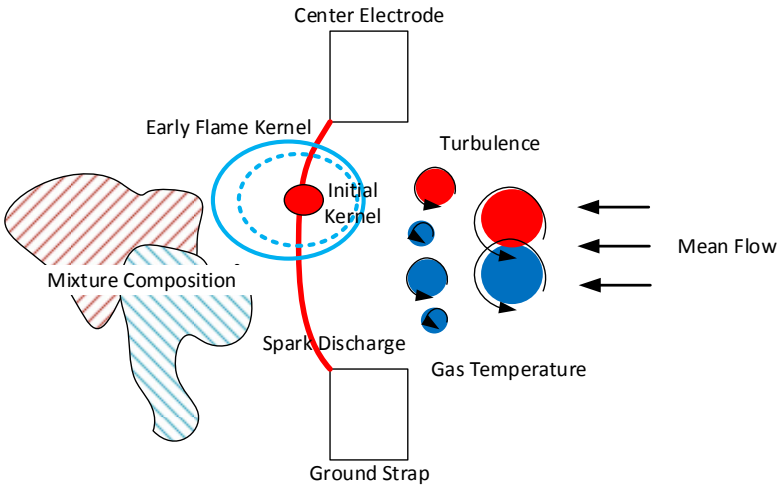

Figure 1-6 Illustration of parameters that effect cycle to cycle variability

1.3.1 Spark and Flame Initiation

In a homogenous SI engine the combustion chamber is filled with flammable fuel-air mixture at the time of ignition, which is usually around 50 to 10CAD before TDC compression, depending on the speed and load operating condition to maintain mean best torque timing and maximize the engines efficiency. Capacitive and inductive ignition systems are the most common ones used in the automotive sector. In the TCC engine an inductive ignition system is used to initiate combustion by discharging energy which is stored in a magnetic field in the spark plug gap. Of the total energy provided to spark plug gap, only about 30% (estimated from Figure 1-7, extracted from [8]) is actually used to initiate combustion whereas the rest is lost through ohm type resistance and heat losses. The entire spark event lasts up to a few milliseconds with four different phases: breakdown, arc, transition and glow discharge [9].

During the breakdown phase, a plasma channel is developed between center electrode and ground strap of the spark plug over which an initial potential difference of 10-40kV exists and currents of more than 100A for a few nanoseconds flow increasing local temperatures inside the spark channel (~40µm diameter) up to 60000K. This plasma channel provides a lower resistance conduction path for the arc phase, during which the voltage drops below 100V, current drops to 1A, and temperatures decrease to a few thousand Kelvin. The duration of this

phase is usually up to one microsecond. Following the arc, glow discharge occurs during which the bulk part of the energy is released over the period of a few milliseconds. Due to the decreasing amount of ions, resistance increases and causes a higher voltage of a few 100V, while the current continues to drop.

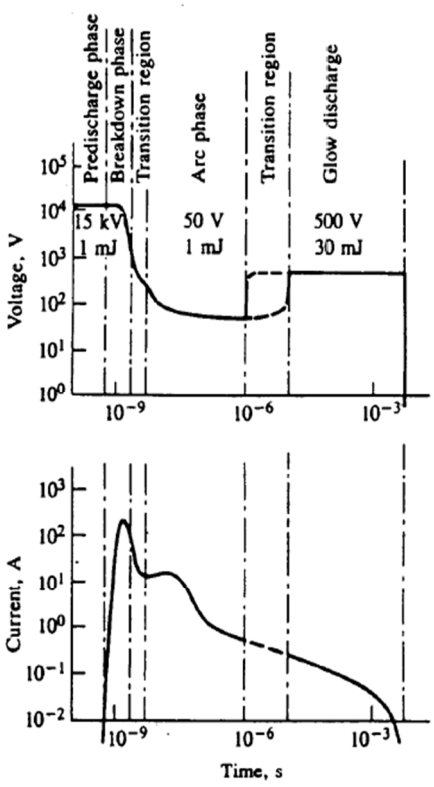

Figure 1-7 Spark voltage and current during different spark phases. Extracted from [9]

The spark location on the electrodes is determined by the strongest E-field location on the edges, and the surface properties of the electrodes. The surrounding flow field can deform the plasma channel, make it move along the electrodes and at sufficiently high velocities (≥25m/s) cause restrikes of the spark [10]. One important aspect of the ignition system is how much energy it can release during a spark event [7]. Flammability limits can be increased and the COV_{IMEP} can be decreased under lean or dilute conditions with higher spark energies [11]. Maly found that not only is the magnitude of the energy released important, but also the characteristics of the energy deposition [10]. It is shown that high power discharges over a shorter period of time is more effective than low power long discharges at a constant energy level. A flame kernel forms around the plasma channel, if conditions are suitable in the vicinity

of the spark plug. Maly describes that a minimum flame kernel radius has to be established for a successful ignition to occur. The critical radius can be calculated according to the following equation:

$$r_{min} \geq \frac{2RT_0\overline{\alpha_0}(T_F - T_0)}{p_0(xq - \overline{\Delta H_F})v_p} \qquad (1)$$

according to [10], where r_{min} is the minimum radius required for successful ignition, R is the universal gas constant (R=8.3166J/molK), T_o is the ambient temperature, $\overline{\alpha_0}$ is the average thermal conductivity of the mixture at indicated temperature, T_F is the flame temperature, p_0 is the ambient pressure, x is the mole fraction of the fuel, q is the molar heat of combustion, $\overline{\Delta H_F}$ is the average enthalpy of formation at flame temperature, and v_p is the velocity at the plasma surface [10].

Maly found that the bigger the initial ignition radius (more spark energy), the faster the initial reaction velocity will be, which would in the context of an engine relate to fast burning cycles [12]. Another finding was that lean limit, excessive flow or turbulence or heat losses can be compensated by sufficiently large ignition radii. Neither turbulence nor dilution affects initial flame kernel size [12]. Increased turbulence intensity increases flame kernel growth rate, however this effect became less important as spark power increased. As a consequence, the effect of increased spark power is less significant for higher turbulent cases [12]. The initial kernel size was not affected by the degree of heterogeneity [12]. No strong correlation between early flame kernel growth rate and size of the flame kernel was achieved until 2ms after ignition [12].

To initiate the flame, the kernel has to have a flame front formed around it and sufficient energy stored to sustain its temperature. Initially the kernel continues to receive energy from the spark until the kernel convects away or the coil is depleted.

1.3.2 Initial Kernel Development

The kernel initially has a smooth surface and its burning velocity is close to the laminar flame speed because its size is smaller than the turbulent length scales, hence it is laminar [13-15]. This phase usually lasts to 1 or 2% mass burned fraction. In this phase it also is determined if

the flame is quenched. The energy provided by the spark, combined with the energy that is already released due to combustion in the spark region, needs to be high enough to push the flame kernel over a critical radius as illustrated in Figure 1-8. Two effects play a major role at this stage. One is the high gas temperature from the spark plasma that increases flame speeds, and the other is the strain imposed on the flame surface due to the high curvature at small radii that decreases flame speeds and eventually causes extinction. Both temperature and strain rate are maximal at small radii, decreasing with increasing flame radius. While up to 1mm radius the temperature has a leading effect on increasing the flame speed, the flame speed is decreased at radii between 1-2mm, during which the flame is most prone to extinction and slow growth eventually leading to longer ignition delays. This radius is called critical flame radius. Once the flame has grown bigger, strain rates due to curvature become smaller and the flame produces sufficient heat to sustain a thermal runaway combustion. Spark and early kernel phase are better described in time space rather than in crank angle space according to [10].

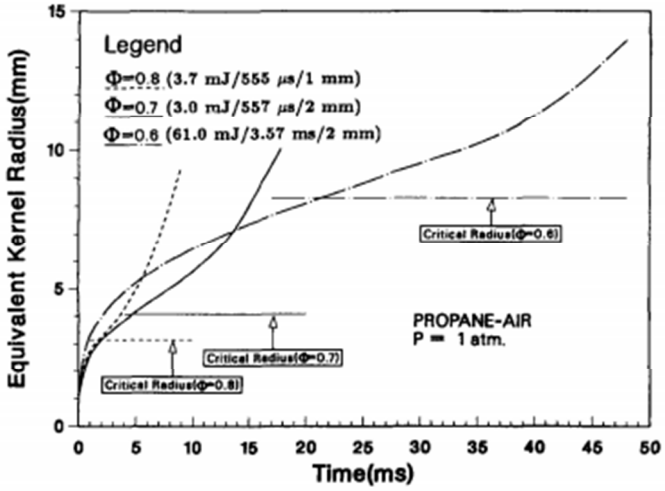

Figure 1-8 Minimum ignition energies for lean propane at ambient pressure and temperature [16]

While Maly [10] only took strain effects into account, Pischinger and Heywood [17] show that for a 1mm spark plug gap the flame kernel contact area (with spark plug) to burned gas volume ratio is highest during this period (see Figure 1-9), leading to additional heat losses to the walls.

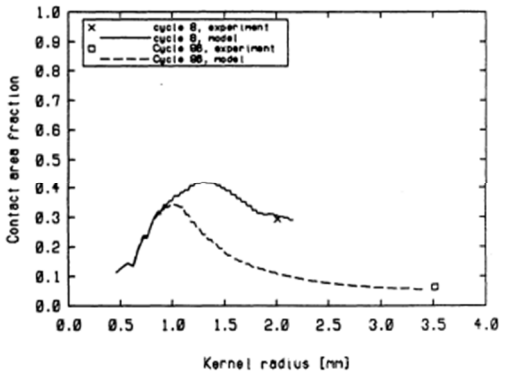

Figure 1-9 Contact area fraction of two flame kernels,[17]

Like during flame initiation, combustion is sensitive to many factors since the flame kernel is still small (d≈5mm) and encounters many fluctuations in local equivalence ratios and in the 'wetted area' of the spark plug. Equivalence ratio around one, little dilution, high temperatures and lower heat losses to the surroundings accelerate the kernel growth compared to the average timing. [18] found that cyclic variability is mostly determined during early part of ignition as shown in Figure 1-10.

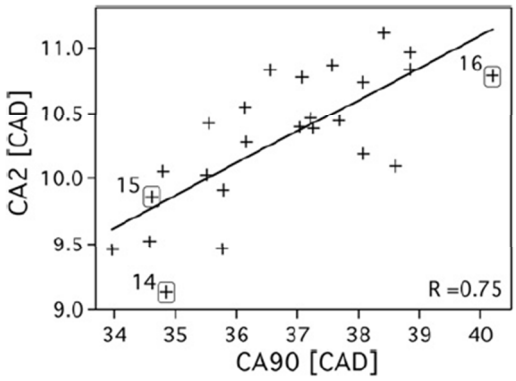

Figure 1-10 Correlation between 2% and 90% mass burned fraction [18]

Increasing the laminar flame speed, for example by higher temperatures or hydrogen addition, helps to reduce variability during the early part of combustion and with this throughout the entire combustion process [19]. The most important parameters controlling initial growth are the local laminar flame speed at the spark plug and the size of first eddy burned τ_b [19, 20].

$$\Delta\tau_b = \left(\frac{1}{S_L}\Delta\lambda_{micrsc}\right) - \left(\frac{\lambda_{micrsc}}{(S_L)^2}\Delta S_L\right)$$

Variability due to microscale — Variability due to laminar flame speed

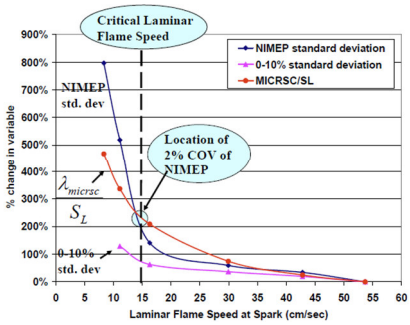

Figure 1-11 Variability of the first eddy burn time is determined by variability in Taylor microscale and in flame speed, causing steep increase in IMEP after minimum flame speed [19]

Especially in the early phase, combustion is very susceptible to local equivalence ratio, local level of dilution, bulk flow that convects the plasma and the kernel, turbulence intensity, cycle-to-cycle differences in spark characteristics, and the contact area of the kernel with the spark plug. All these factors play a role in how fast (or if at all) the initial kernel grows and at what size it transitions to a turbulent flame.

1.3.3 Turbulent Flame Propagation

Flow-flame interactions and instabilities in the flame fronts themselves cause wrinkling of the kernel surface once it has reached a size at the order of the turbulent length scales. This turbulent flame is established after 2-10% mass fraction burned (MFB). Bulk flow (tumble, swirl, squish) and turbulent eddies distort the flame and increase surface area of the flame front and with that enhance burning rate [7].

During this phase, local heterogeneities do not play an important role anymore, because the overall effects are obtained from averaging over many local events [7]. Heterogeneity causes wrinkling and distortion of flame surface because the flame is accelerated in some place more than others [12]. In general, this combustion stage is less contributing to the cyclic variability than the initial kernel stage. The phasing difference determined by the previous stages usually plays the biggest role, saying that kernels that had a fast growth continue to burn fast, while slow burning cycles continue to burn slow.

Contributing to CCV during the turbulent flame propagation phase are global parameters like equivalence ratio, mixture dilution, volumetric efficiency, turbulence intensity, and combustion phasing determined by early flame kernel phase.

1.3.4 Flame Termination

After about 90% of the fuel mass is burned, the last combustion phase, the flame termination begins. This phase is less important for the overall power output of the engine or fuel efficiency but plays a role especially in unburned hydrocarbon emissions. The minimal quenching distance to metal, the wall temperature, as well as crevice volumes and design mostly determine these emissions.

1.4 Causes of CCV

In this chapter, sources of cyclic variability in combustion in SI engines are explained. How big the impact of each contributing factor is depends on the specific engine design, fuel, its operating point etc. One can differentiate between effects that actually cause combustion to be different from cycle-to-cycle and parameters that influence the level of variability.

1.4.1 Fluid Mechanics

Variations of mixture motion in cylinder at time of spark [4, 21-23] are one factor in cyclic combustion variability. For example, Johansson et al. [24] found that flow variations cause the flame kernel to be convected towards or away from the ground strap which causes the flame kernel to lose more or less heat, respectively, due to the amount of contact area with the ground strap. Consequently, gas temperatures vary, which causes changes in burn rate. Later in the combustion process, convection changes flame location and flame-wall interactions. Variability in the flame center location will be highest in the early combustion process, when the flame is small. Variability in the flame/wall interactions continues to be important as the flame is more developed [19].

Besides this convection effect, [19, 24] found that increased turbulence levels favor heat release independent of equivalence ratio up to a certain level after which too much heat is lost or excessive levels of strain are exerted on the flame, so that the flame quenches locally. Figure

1-12 shows combustion advances by 4-6 CAD by increasing the turbulence level from 0.5 to 2.5 m/s independent of equivalence ratio.

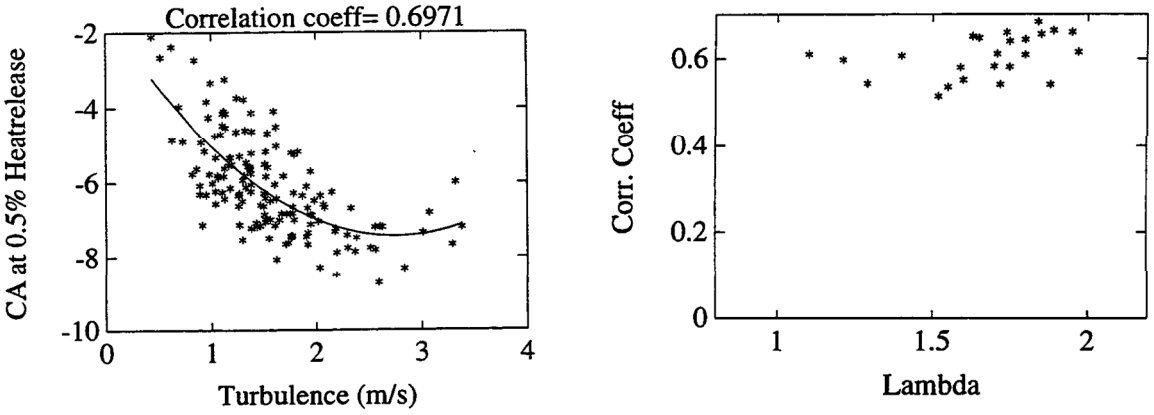

Figure 1-12 Influence of turbulence level on combustion phasing [24]

Not only the magnitude of turbulence intensity matters but also the length scales of the structures that interact with the flame [19, 24]. Turbulent eddies of 1mm diameter are the most effective in increasing surface area and with that increases the turbulent flame speed, as shown in Figure 1-13 [24].

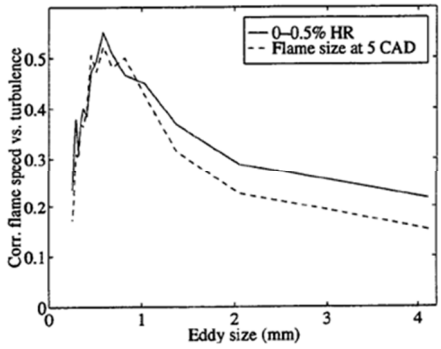

Figure 1-13 Correlation between eddy size and the correlation coefficient between turbulence intensity and flame speed

Vermorel et al. [25] found that in their multi-cycle engine Large Eddy Simulation (LES) results are sensitive to cyclic variations of the bulk tumble motion and the level of turbulence intensity during ignition. They show that high levels of turbulent kinetic energy (TKE) at the spark plug decreases ignition delay (Figure 1-14 a)) and a strong tumble motion decreases burn time (Figure 1-14b)) in the modeled engine.

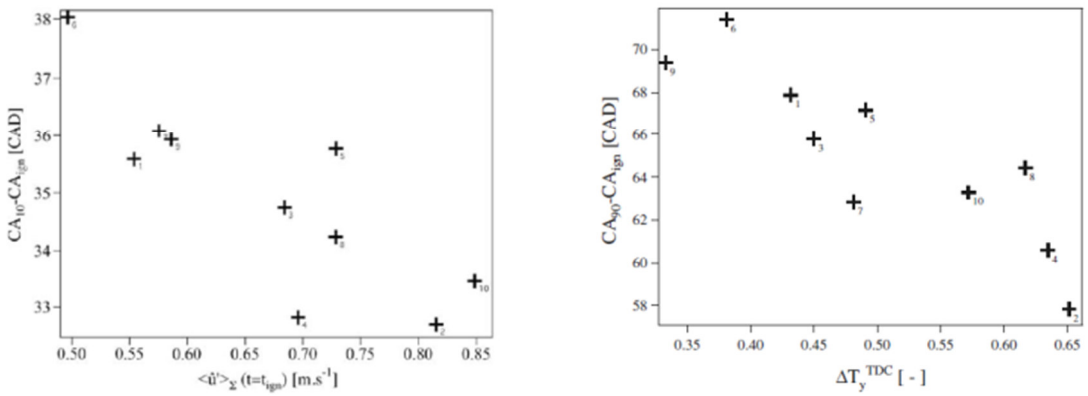

Figure 1-14 a) Ignition delay is decreasing when turbulence intensity at the spark plug at time of ignition is increased (left); b) 90% mass fraction burned duration decreases with higher tumble ratio (right) [25]

Enaux et al. [18] discovered using LES that the flow in the vicinity of the spark plug has a major impact on combustion depending on whether it convects the flame kernel away from the head, which decreases heat losses and accelerates flame propagation, or into the spark crevice volume, which leads to an increased heat transfer, partial quenching and retarded combustion, as illustrated in Figure 1-15.

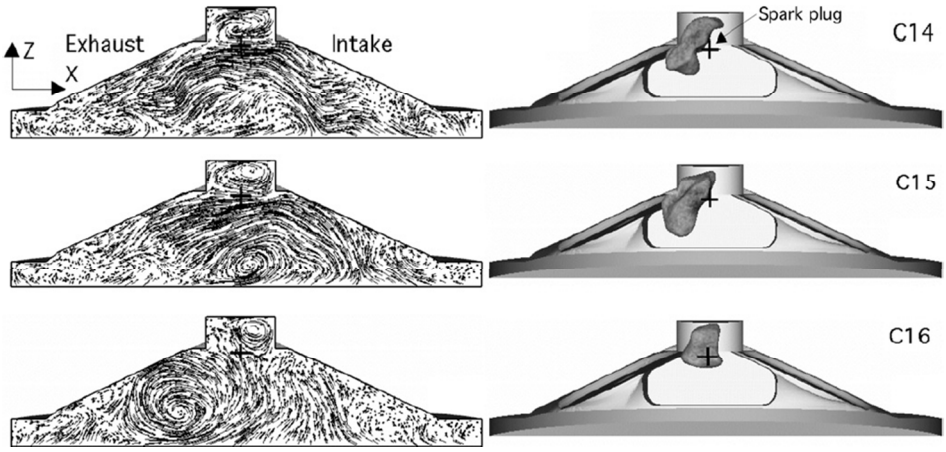

Figure 1-15 Flow fields (left) and flame surface (right) for three consecutive cycles Left: velocity field at start of ignition in a cut plane through spark plug. Right: iso-surface of progress variable 5CAD after ignition [18]

Enaux et al. [18] show that the average turbulence intensity over the flame surface is lower in the cycle during which the flame kernel was pushed in the spark plug gap. The slow flame growth is induced by the low turbulence intensities and increased heat losses to the walls.

In order to isolate the effects of different global parameters like size of integral length scale and turbulence intensity from the individual flow pattern and wall cooling effects on flame kernel development, Pera et al. [2] used a 2D DNS approach, accessing the relative impact of each turbulence parameter on isooctane flame kernels.

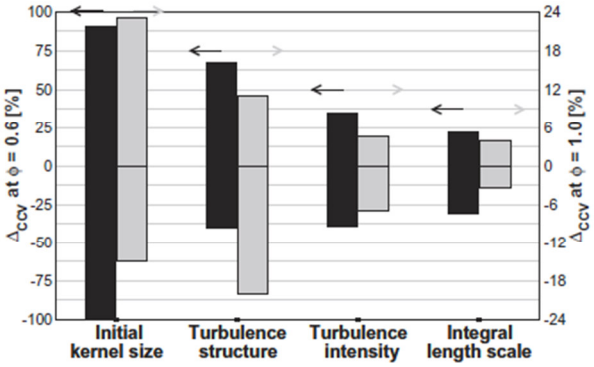

Figure 1-16 Relative impact on CCV under lean and stoichiometric conditions of initial kernel size, turbulence structure and intensity, and integral length scale [2]

Figure 1-17 illustrates the effects of the variation in flame kernel growth for 8 different turbulent flow structures (at same turbulence intensity) and different turbulence intensities (Avg+/-StdDev=7%of Avg) at fixed turbulence fields. It shows that structure has a bigger influence than intensity, and effects that are relatively weak at stoichiometry get amplified for lean mixtures, because of lower laminar flame speeds.

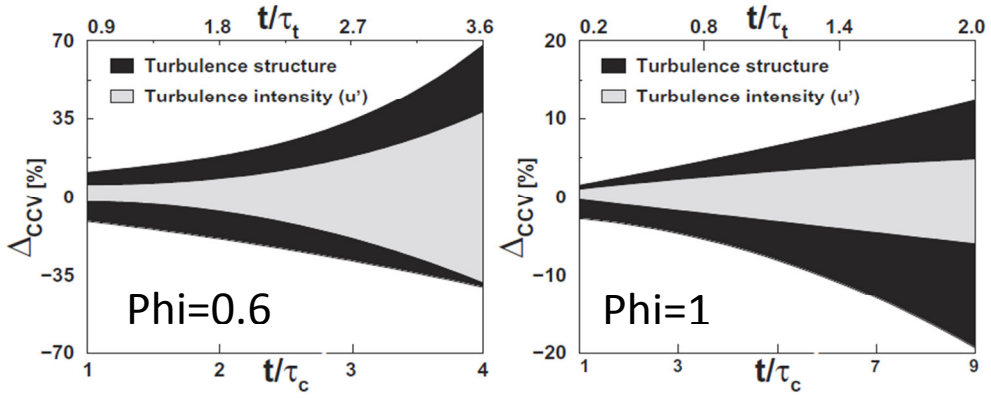

Figure 1-17 Influence of turbulence structure and turbulence intensity on CCV for different equivalence ratios [2]. t being simulation time normalized by the turbulent time scale τ_t or the characteristic chemical time scale τ_c

Further it was observed that turbulence distorts the flame kernel and the initial circular shape was lost very quickly (0.5 of chemical timescale≈50µs). Significantly larger Karlovitz numbers (non-dimensional number characterizing stretch rate) for the lean mixture led to local flame quenching and the creation of multiple unconnected sub-kernels as illustrated Figure 1-18 [2].

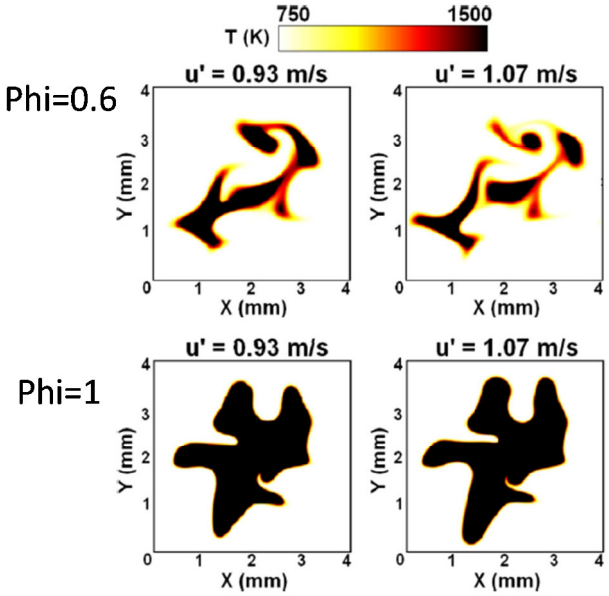

Figure 1-18 Influence of turbulence intensity (u') on flame kernel growth for different equivalence ratios [2]

The results in [2] show that the random nature of the turbulent flow structure must be taken into account, as well as the global turbulence intensity and length scales. The structure to the flame kernel given is preserved when it grows [26]; the flame shape is self-similar.

Depending on the characteristic size of the first eddy that interacts with the flame kernel the flame transitions from laminar to turbulent [27]. Once the flame transitioned to a turbulent flame, the flame structure effect on the global growth is low since it is averaged over the entire flame surface, but variability in the turbulence intensity plays a role throughout the entire combustion process [19]. Burning rates increase with higher turbulence intensity [28] by increasing the flame surface area. A common scaling equation is $\frac{A_T}{A_L} = \frac{s_T}{s_L}$ where $s_T \sim$ u'. Hill [29] shows that the Taylor microscale decreases with higher turbulence intensity, which also reduces the length scale of the first eddy interacting with the flame kernel, eventually causing an earlier transition to a turbulent flame, hence reducing CCV. Now the relative position of the

flame to the combustion chamber, which is determined by the spark plug location and by the convection from the flow, also matters since this determines where the flame touches the walls and quenches [27]. This determines the later part of the heat release curve during the cycle.

1.4.2 Variations in Cylinder Charge, Mixing and Mixture Composition

Besides the variability in the flow, the amounts of fuel, air, residuals and recirculated exhaust gas (EGR) can also change from cycle to cycle [4], which, of course change the amount of trapped mass, thermodynamic state of the mixture and mixture, composition. This affects equivalence ratio and amount of dilution, and in consequence laminar flame speed. Additionally, variations in mixing of fresh charge and residual gases, especially in the vicinity of the spark plug can change [4].

Aleiferis [30] observed that the in-cylinder equivalence ratio of the reacting mixture exhibited large variations on a cycle-by-cycle basis and consistently produced negative correlation coefficients with the CAD at 0.5% heat released, especially for lean stratified operating conditions. In agreement with this Johansson [24] found that there is a strong correlation between the F/A in the vicinity (5mm) of the spark plug and ignition delay. Figure 1-19 shows that when the mixture is locally lean at the spark plug the ignition delay is increased. This correlation became weak for homogeneous conditions.

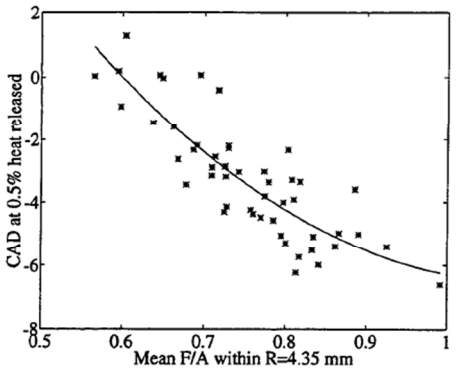

Figure 1-19 CA05 as a function of local equivalence ratio for non-homogeneous mixture

In a second experiment Johansson [24] looked at the fluctuations of water level from residual trapped gas in vicinity of spark plug and how it influences the CCV of ignition delay. In Figure 1-20 is shown that a higher concentration of residual gas in the vicinity of the spark plug

increases the ignition delay. Agreeing with this Bates [26] discovered that partial burns in a previous cycle can cause stronger burns in the following cycle, due to increased amounts of unburned fuel in the residual trapped mass.

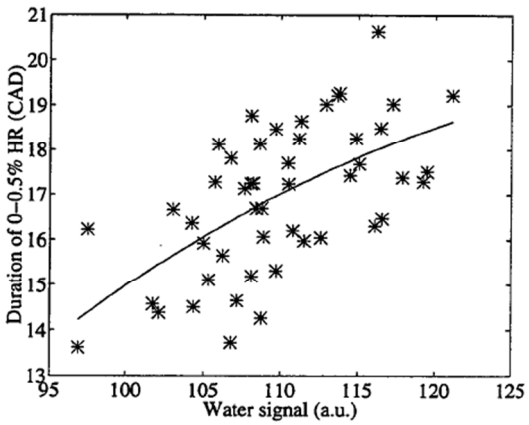

Figure 1-20 Ignition delay as a function of local residual gas concentration

In contrary to the previous sources Vermorel [25] observed that variations in the overall or local mixture were not found of sufficient importance to induce significant modifications in the combustion process. But in contrary to previous stratified studies, Vermorel used propane in an LES simulation, indicating that the mixture is well mixed by the time of ignition without significant temperature stratification effects.

Pera et al. [31] observed that the flame shape is influenced by local mixture conditions, in a way that at regions with mixtures in which laminar flame speeds (either by higher temperature, less diluent, or more favorable equivalence ratio) are higher the flame accelerates, whereas it decelerate in other areas compared to the mean velocity (see Figure 1-21). This causes wrinkling of the flame, leading to an area increase and a global increase in heat release which persists as the flame grows due to its self-similarity.

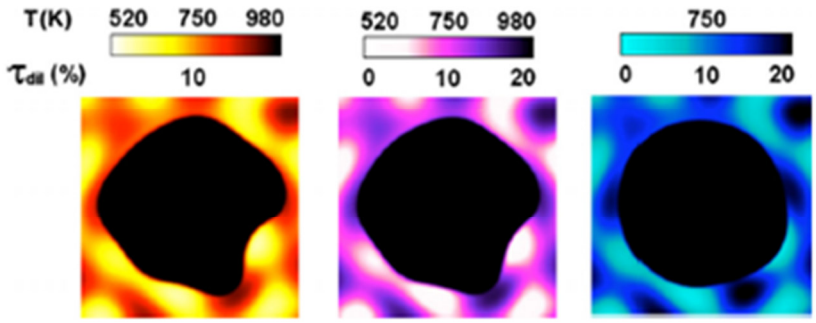

Figure 1-21 Heterogeneity effects of temperature (left), temperature + dilution (middle), dilution (right). Extracted from [31].

The average level of heterogeneity determines the level of CCV [12] due to local variation in flame speed at the ignition source [11].

1.4.3 Variations in Spark

A third component that influences CCV besides flow field and charge variations is different spark discharge characteristics and spark energy in each cycle [2, 7, 25, 32, 33]. Maly [10] explains that the bigger the initial ignition radius the faster the reaction velocity. The initial radius is bigger with higher the power input. This means that cycles in which the spark discharge had higher power at the beginning, show usually faster initial flame growth and with advanced timing. In agreement with this, Bates et al. [26] found that very early (at negligible MBF) large flame kernels correlate to faster burn rates through early stages of combustion using premixed propane mixture at ϕ=0.75. Although using the same fuel Keck et al. [20] found no influence of spark energy on the combustion at phi=0.87. For the work planned, Hill [29] recommends that an observation of the spark and early flame kernel stage needs a spatial resolution of at least 0.1mm.

1.4.4 Variations in Thermodynamic State

Johansson et al. [24] found that global pressure and temperature vary little from cycle-to-cycle and no effect on CCV could be found. Whereas Pera et al. [31] showed that locally occurring temperature heterogeneity is dominant over the dilution effect. Consequently, for representative conditions of low-load engine operation, the residual burned gas (RBG) heterogeneity effect is primarily caused by temperature influences.

1.4.5 Factors that Change CCV Levels

Certain operating conditions show higher levels of cycle-to-cycle variations than others. [4, 7, 24] listed some of these "rough" operating points: Low loads or speeds, leaner and more dilute combustion increase CCV and bad ignition timing, which can lead to partial burns and misfires[7]. This causes losses in efficiency, high HC emissions, torque variations, roughness and loss in power[4]. Also different spark plugs and their location and ignition systems can have an effect on CCV, as do intake geometries. Another important parameter is the specific fuel, in particular its laminar burning velocity, which is important especially during the initial kernel stage. It was shown that high burning rates reduce CCV [7].

Heywood shows that the lean limit is determined by the unacceptable limit of high COV [19]. As the mixture for a given fuel becomes more lean or dilute the CA10 duration becomes longer and its variability higher. This can be explained with the inverse dependence of the first eddy burn time with laminar flame speed. In their engine, Ayla and Heywood found a critical laminar flame speed of ~15 cm/sec for the given RPM and engine [19].

1.5 Flame Speed and Mixture Effects

1.5.1 Laminar Flame Regime

A flame is perceived as a 1-D propagating (deflagration) wave typically divided into three regions. The preheat zone is most simply modeled as a convective balance between the convection of the unburned fuel-air mixture ahead of the flame and the diffusion of heat from the reaction zone. The reactants experience a temperature increase due to heat conducted from the reaction zone. There the fuel is also already converted to some intermediate species but no significant heat is produced in exothermic reactions. The reaction zone is where a bulk part of the chain-branching radical formation and heat release take place. In the post-reaction zone some remaining intermediate species are oxidized and the mixture converges to its equilibrium composition, and only a small amount of heat is released. This process is illustrated in Figure 1-22 by N. Peters.

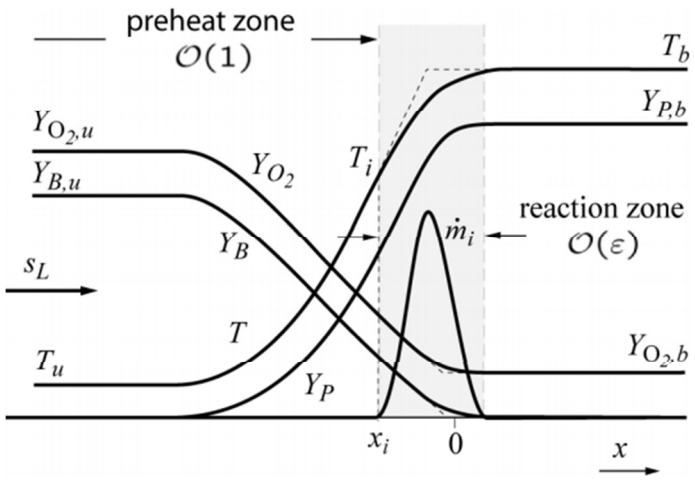

Figure 1-22 Laminar flame topology, by Norbert Peters

With chemical kinetics software packages (i.e. CHEMKIN) the combustion process can be simulated in detail. Figure 1-23 shows some results of the species conversion. In the left figure, the major reactant and product species, as well as CO as the major intermediate species. Also note that most of the water is formed in the reaction zone, which is the largest source of enthalpy. On the right some key intermediates are shown to be hydrogen, ethane, formaldehyde, hydroxyl radical and atomic oxygen. The speed with which the flame front propagates through the unburned gas is called the laminar flame speed.

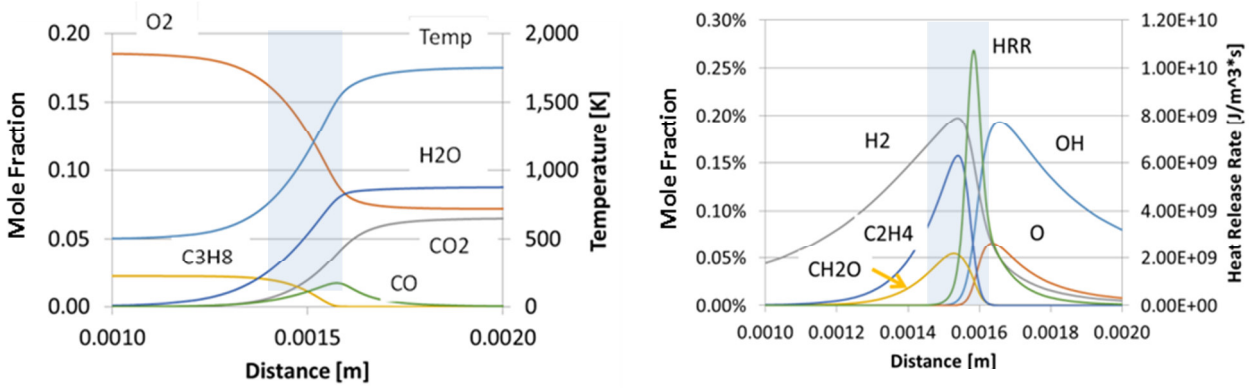

Figure 1-23 Major species and temperature of stoichiometric propane combustion in air with 81% N_2 by volume at an initial pressure of 5bar, reaction zone indicated with grey shaded area.

1.5.2 1-D Laminar Flame Speed

The laminar flame speed describes the propagation speed of a 1-D unstretched flame through homogeneously premixed unburned gas. It is specific for each fuel-oxidizer composition and depends on temperature and pressure. For hydrocarbon fuels, it usually peaks around Φ=1-1.1. Where Φ, the equivalence ratio, is defined as:

$$\Phi = \frac{1}{\lambda} = \frac{\left({}^{Fuel}/_{Air}\right)_{Actual}}{\left({}^{Fuel}/_{Air}\right)_{Stoichiometric}} \qquad (2)$$

At Φ=1, i.e. stoichiometric mixture, all oxidizer and fuel are fully converted to complete combustion products. The laminar flame speed decreases from this maximum non-linearly in the richer and leaner mixtures to the flammability limits at which the flame extinguishes. Higher pressures compress the flame fronts and reduce the laminar flame speed. Increased temperatures elevate the sensible energy of the unburned gas, resulting in a decreased energy needed to start chemical reactions, leading to higher laminar flame speeds.

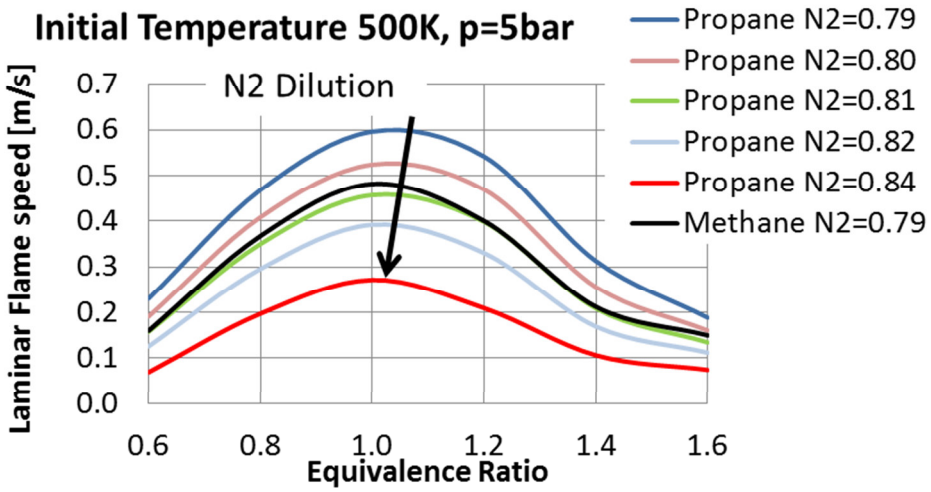

Figure 1-24 Laminar flame speed variation as a function of dilution from ChemKin PRO calculation.

The inert component, nitrogen does not contribute to any exothermic reaction, but needs to be heated up, which reduces the flame speed. Figure 1-24 shows laminar flame speeds at pressures and temperatures that are similar to the conditions in an SI engine at low load at the point of ignition. The flame speed results are correct only for un-stretched laminar flames. In engines, flame stretch occurs, requiring these numbers to be corrected.

1.5.3 Thermo-Diffusive Behavior of 3-D Flames

In the laminar case the flame is thought of as a 1-D deflagration wave, in real-world combustion applications such as IC engines also the thermo-diffusive behavior of the mixture is important to understand the flame propagation. Three laws describe the spatial gradient based transport mechanisms[34]: Fick's law of mass transport, Newton's law of momentum transport, and Fourier's law of energy transport. From the ratio coefficients of the three laws (mass diffusivity D, momentum diffusivity ν, and thermal diffusivity α) the dimensionless Schmidt, Prandtl, and Lewis numbers can be formed [34]. In this work the Lewis number $\left(Le \stackrel{\text{def}}{=} \frac{\alpha}{D}\right)$ is especially of concern, describing the ratio rate of energy transport to the rate of mass transport. The Lewis number of the deficient species (under lean condition the deficient species is the fuel, under rich conditions the deficient species is oxygen) can be used to describe the flames response to stretch [35]. The active reactant mass diffusivities rank as follows $D_{CH4} > D_{O2} > D_{C3H8}$, such that lean methane and rich propane have a Lewis number smaller than one, and rich methane and lean propane greater than unity. Before explaining the details of the thermo-diffusive behavior the sign of flame stretch needs to be defined, as various textbooks differ from each other. This thesis follows the convention of Kuo [34] in which the flame is under tension in case of positive stretch (Figure 1-25).

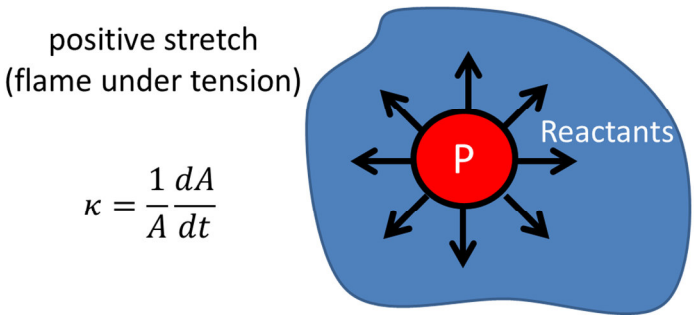

Figure 1-25 Flames under tension are defined here under positive stretch

Figure 1-26 illustrates the stable and unstable flame behavior on the example of propane. Propane has a lower mass diffusivity than oxygen. In case of a fuel rich reactant mixture, the higher oxygen diffusivity compared to propane leads to an increase in oxygen concentration at the flame front. In a rich environment this leads to a local increase in laminar flame speed

compared to the unstretched case (change of flame speed illustrated by yellow areas in Figure 1-26). In negatively stretched areas oxygen diffuses also faster than propane, but due to the convex curvature the oxygen also diffuses to the flanks, reducing the oxygen concentration in these nadirs. This results in a further decrease in flame speed in these nadirs. The tendency to enhance flame growth in positively stretched areas, and slow down negatively stretched areas, which increases the wrinkling of the flame, is labeled unstable flame behavior. Here, the case of a stable flame (Figure 1-26 bottom) is explained on the example of lean propane. In the fuel lean reactant mixture, oxygen diffuses faster to the flame front than propane, causing a further increased local oxygen concentration on the positively stretched flame areas. This results in a decrease in flame speed compared to the unperturbed flame. In the negatively stretched area, oxygen diffuses besides to the bottom of the nadir also to the flanks, decreasing the local oxygen concentration. This increases the local flame speed and smoothens out the flame front. This smoothing property is labeled as stable flame. As opposed to propane, methane has a higher mass diffusivity than oxygen, which results in a stable rich flame, and an unstable lean flame.

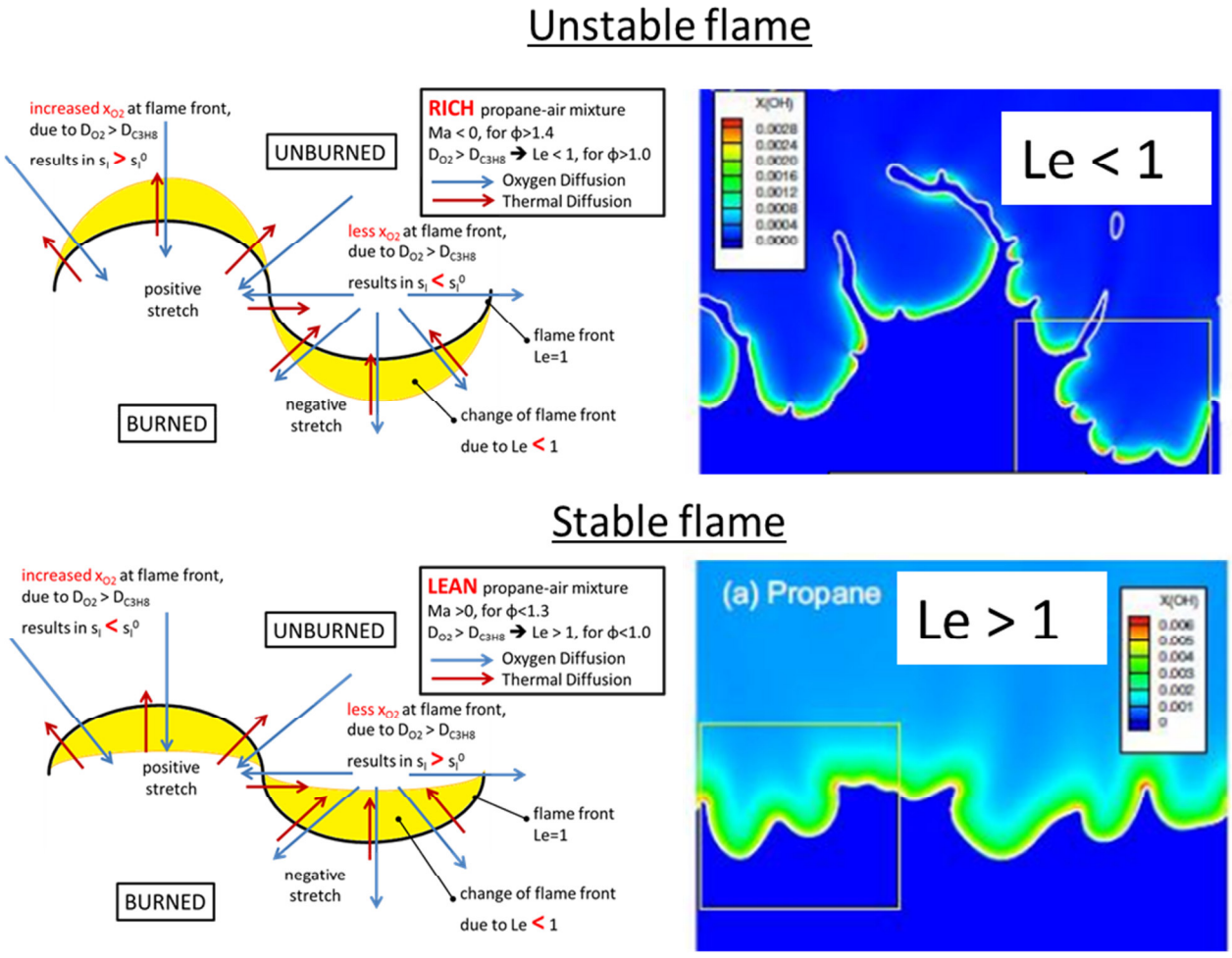

Figure 1-26 Left: Schematic of thermo-diffusive effects (created by the author). Right: Simulation results of OH concentration for illustration of unstable (lean Hydrogen) and stable (lean propane) flame shapes (extracted from [36])

The Lewis number can be calculated from fundamental molecular properties, but is ill defined at stoichiometry, because there is no deficient species. Bechtold and Matalon developed for a more consistent Lewis number definition, the effective Lewis number [37] , which is calculated as:

$$Le_{eff} = 1 + \frac{(Le_E - 1) + (Le_D - 1)A}{1 + A}, \text{ with } A = 1 + \beta(\phi - 1) \quad \text{(3a) and (3b)}$$

Matalon and Bechtold use essentially this set of equations to weigh the deficient species (subscript D) against the excess species (subscript E) with A being the weighting factor of the deficient species. β is the Zel'dovich number and is calculated from the total activation energy

E, the difference of adiabatic and unburned temperatures, T_a and T_u respectively, and the gas constant R^0.

$$\beta = \frac{E(T_a - T_u)}{R^0 T_a^2} \quad (4)$$

Although this definition of the effective Lewis number removes the ambiguity and discontinuity at stoichiometry, Bradley et al. have reported to better explain experimental observations using the Markstein number should be used [38]. The author of this work has made similar experiences as shown in Figure 1-27 in explaining the flames' sensitivity of flame growth to shear strength. Both, Lewis number and Markstein number show the same trends, but the Markstein number also describes the offset between both fuels and reduces the spread in the data.

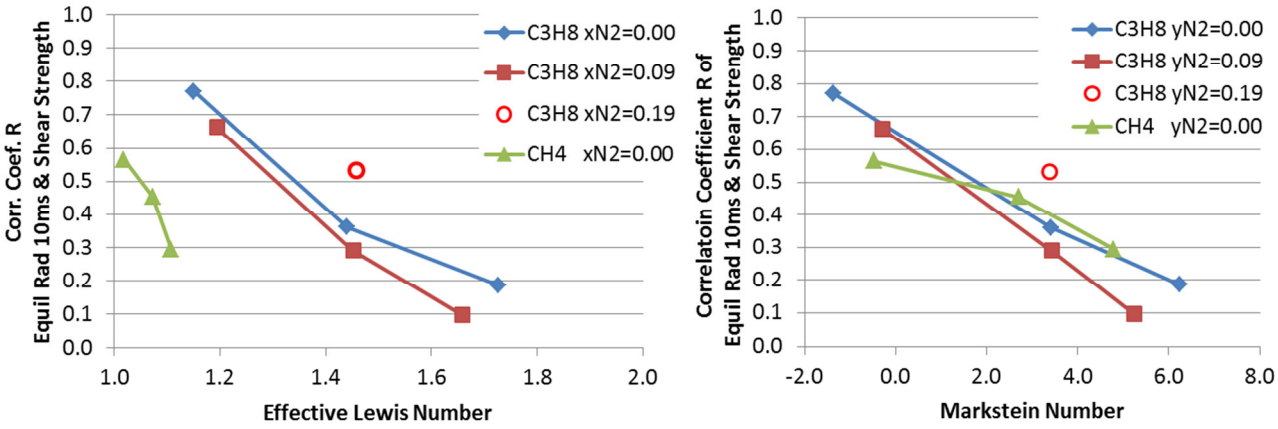

Figure 1-27 Flame sensitivity to shear strength as function of effective Lewis number and Markstein number. Symbols indicate data points taken in combustion vessel experiment as described in Chapter 5. Here the correlation coefficient R is used as it also contains information of sign (not be confused with the coefficient of determination R^2).

The success of the Markstein number leads to several questions. What is it and how is it defined? How is it different from the Lewis number? How is it determined?

The Markstein number describes the change of laminar flame speed with stretch, compared to the laminar unstretched flame speed, as for example determined in a 1-D CHEMKIN simulation. Kuo equates the ratio of unstretched to stretched laminar flame speed to 1 plus the Markstein number Ma times the non-dimensional stretch as given by the Karlovitz number Ka [34].

$$\frac{S_L^0}{S_L} = 1 + Ma\ Ka \qquad (5)$$

The Markstein number strictly quantifies the change of flame speed with stretch, whereas the Lewis number describes the ratio of energy transport to the rate of mass transport of the deficient species. Both numbers can be used characterize a flame as stable or unstable. Figure 1-28 illustrates the different Lewis number and Markstein number behavior of methane and propane. The effective Lewis number correlations are calculated from CHEMKIN transport mechanism and the procedure developed by Bechtold and Matalon [37]. The linear correlations of Driscoll are used for the Markstein number calculation [39]. Generally Lewis numbers below unity are considered unstable, whereas Lewis numbers greater than one are stable [35]. This stable/unstable threshold is at zero for Markstein numbers, such that positive Markstein numbers designate stable flames and negative Ma, unstable flames.

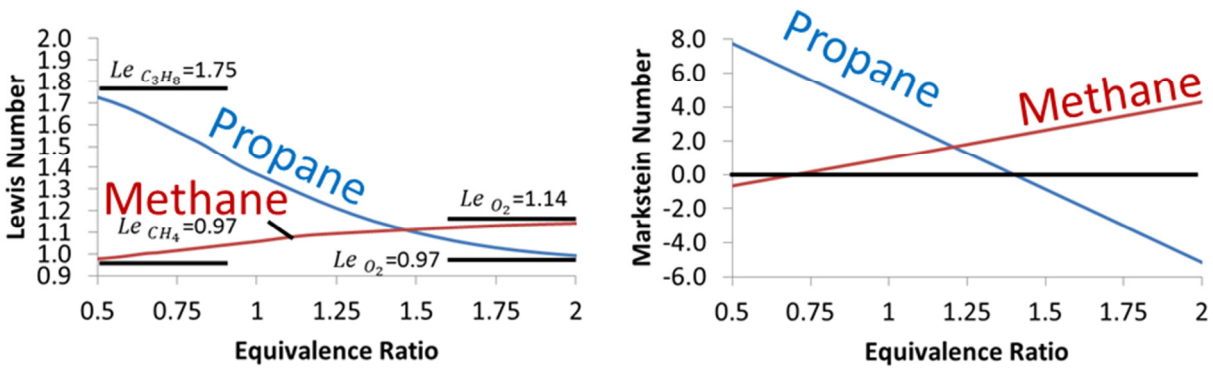

Figure 1-28 Lewis number and Markstein number correlations for propane and methane.

While the Lewis number can be calculated from fundamental conductivity and molecular transport phenomena, the Markstein number in contrast is usually an empirically determined quantity. Markstein numbers can be determined from laminar outwardly propagating flames in quiescent combustion vessels. Here the flame is typically assumed to be perfectly spherical, such that the geometric stretch rate [34] can be determined by the flame radius r and the displacement velocity

$$\kappa = \frac{2}{r}\frac{dr}{dt} \qquad (6)$$

From this the Markstein length L can be calculated as the stretched laminar flame speed s_L is determined from the images and the unstretched laminar flame speed for a given condition is known.

$$S_L = S_L^0 - L\,\kappa \qquad (7)$$

The Markstein number is a mixture property [35] and is the ratio of Markstein length and laminar flame thickness δ_L .

$$Ma \overset{\text{def}}{=} \frac{L}{\delta_L} \qquad (8)$$

The derivation of the Markstein number is here explained based on the procedure and figures used by Tseng et al. [40]. They measured the flame growth of various hydrocarbons in a constant volume vessel using shadowgraphy. The mixtures are ignited with minimum ignition energy to avoid extra energy addition during the early Kernel growth. Figure 2-29 shows the mean radius derived from the images as a function of time for propane flames at various equivalence ratios. The expansion corrected laminar flame speed is derived from the change of radius over time and is plotted over the mean radius. Here, the difference in unstable and stable behavior is already much clearer. At high geometric stretch conditions (small radius) unstable flames show higher velocities compared to low stretch (r = 30mm). For stable conditions the flame speed at low radii is lower than in the unstretched case.

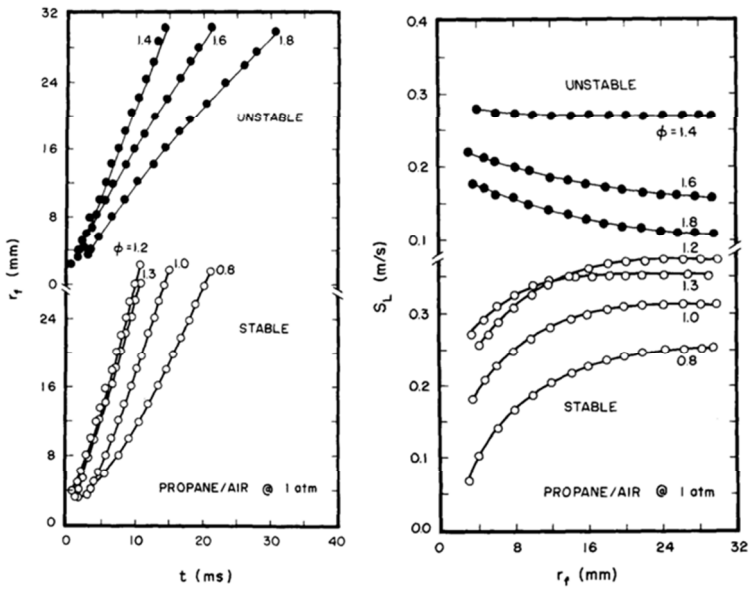

Figure 1-29 Mean radius development over time for various propane mixtures (left); Flame speed as function of radius (right) (figures extracted from [40]).

From the expansion velocity and radius the stretch rate κ can be calculated, which is then used to compute the non-dimensional stretch, as given by the Karlovitz number

$$Ka = \kappa \frac{\delta_D}{s_L} \quad (9)$$

The laminar flame thickness $\delta_D$is in Tseng's work derived from the ratio of binary diffusivity of the fuel and the laminar flame speed s_L. The results for change in laminar flame speed with stretch are summarized in Figure 1-30 for methane and propane. At large radii, which equals to Ka≈0, the flames experience no stretch, such that the ratio of unstretched laminar flame speed to stretched laminar flame speed equals 1 independent of the mixture. This ratio changes linearly for different fuels at different equivalence ratio's with increasing stretch (increasing Ka). The slope of these linear correlations is the Markstein number.

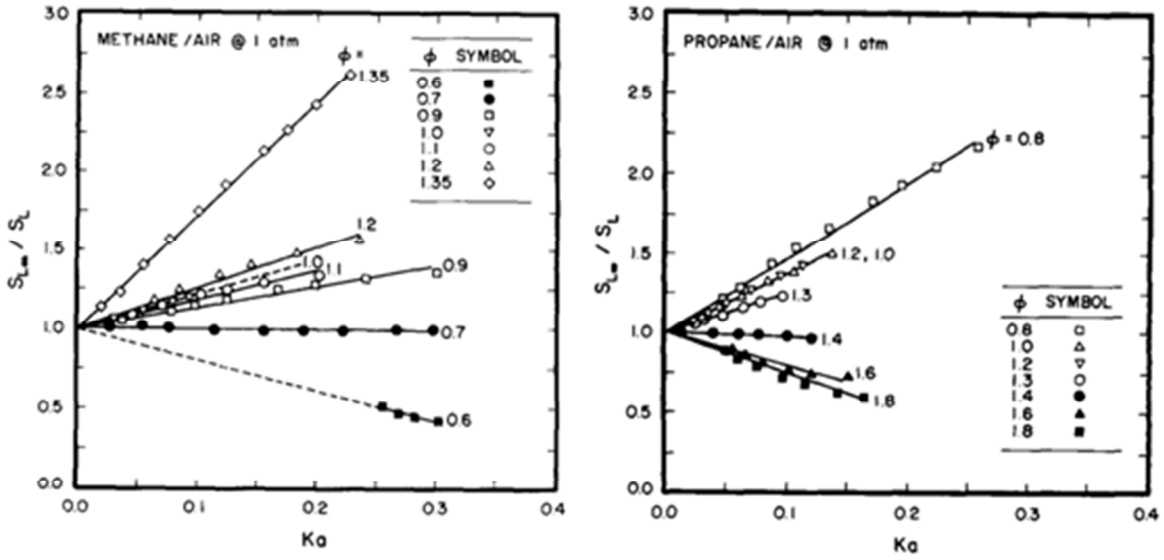

Figure 1-30 Change of flame speed with non-dimensionalized stretch as given by the Karlovitz number for methane and propane (figures extracted from [40]).

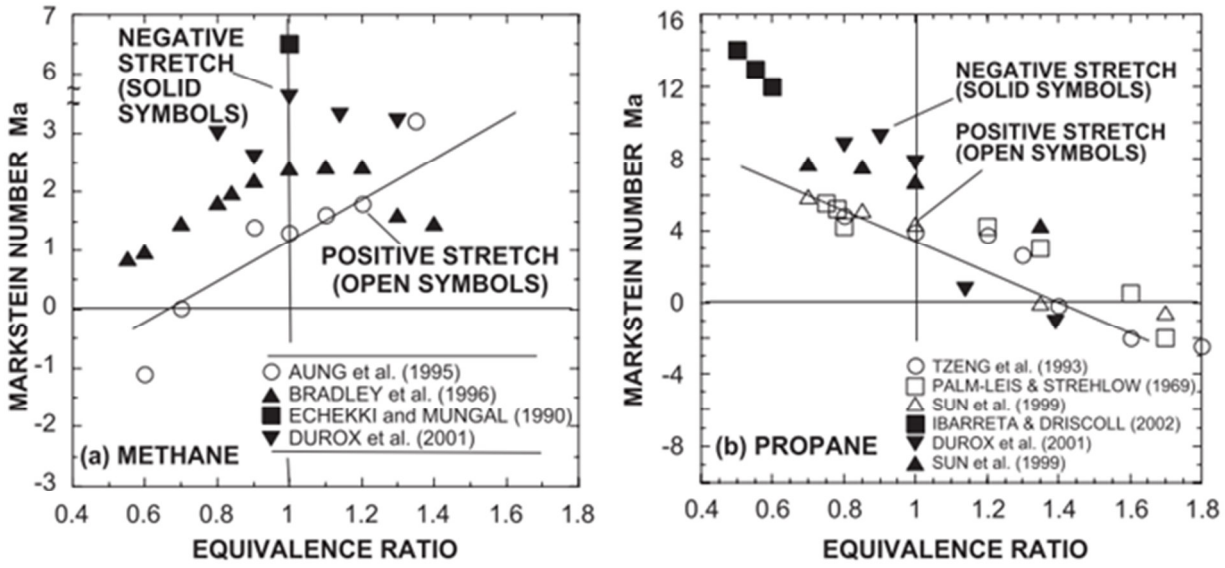

Figure 1-31 Markstein number correlation for methane and propane (figure from [39]).

In his 2008 review paper on premixed combustion [39] Driscoll combines Markstein number results derived from various experiments [40-48] proposes the following correlations for propane and methane Markstein numbers:

$$Ma_{C3H8} = -8.6(\Phi - 1.4) \quad (10)$$

$$Ma_{CH4} = 3.3(\Phi - 0.7) \quad (11)$$

These correlations are used in this work to calculate the Markstein numbers for different fuel-air mixtures. As can be seen in Figure 1-31 there is significant spread in the experimental data published, such that these correlations should be considered as giving a trend of flame behavior rather than an absolutely precise number.

1.5.4 Turbulent Flames

Most practical combustion applications rely on turbulent flames to convert the chemically bound energy in fuels into heat. Turbulent flames are very effective in this conversion process because of their high surface area density, due to their wrinkled surface area. The power that can be converted is calculated by the product of the reactant density, the turbulent flame speed, the laminar flame area and the lower heating value.

$$P = \varrho_R S_T A_L * LHV \quad (12)$$

The turbulent flame speed scales linearly with the turbulent flame area [39]

$$\frac{S_T}{S_L^0} = \frac{A_T}{A_L} I^0 \quad (13)$$

with I^0 being the stretch factor. These wrinkles increase the flame surface area which increases the mixture consumption rate of the flame. Wu et. al. showed that even in high Reynolds number hydrogen flames these thermal diffusive effects play a role. The two hydrogen mixtures in Figure 1-32 have nominally the same laminar flame speed, but due two different Markstein numbers (low Ma≈0.5 for lean, high Ma≈5.0 for rich) the turbulent flame speed is different for the two cases.

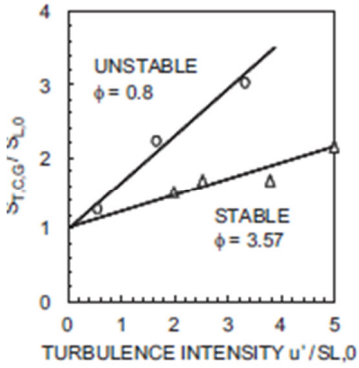

Figure 1-32 Markstein number effect on turbulent flame speed, for two hydrogen flames at same laminar flame speeds but different Markstein Numbers, figure extracted from [49]

1.6 Measures to Quantify CCV

There are many ways to quantify the stability of combustion in an engine. Traditionally pressure based metrics allow a good quantification of variation in combustion phasing and heat released, and are easy to implement and post-process. Flame front related parameters are rather difficult to determine in metal engines, require more involved post-processing and are usually limited by their field of view.

1.6.1 Pressure and Burn Rate Related Parameters

Cylinder peak pressure ($P_{cyl,max}$), location of cylinder peak pressure (LPP), maximum pressure rise rate($\dot{P}_{cyl,max}$) and indicated mean effective pressure ($IMEP$) allow valuable insight into

CCV[4, 50]. Usually calculated from pressure data, the maximum rate of heat release (HRR_{max}), maximum mass burning rate, flame development angle, rapid burning angle, crank angle at which a certain mass fraction of the fuel burned (crank angle at which 10% of the fuel burned = CA10, CA50, CA90), ignition delay, combustion duration can be determined [4, 7, 50].

These parameters are relatively easy to measure and compute but are not informative in the sense that they give no physical insight into why CCV occur. Also the pressure information is sensitive enough to capture well the early part of ignition due to the low pressure increase of the early kernel on top of the high pressure values at the end of compression stroke.

1.6.2 Flame Front Related Parameters

Using imaging techniques, the flame radius, flame front area, enflamed or burned volume at a given CA or the flame arrival time at a given location change from cycle-to-cycle, displacement of the flame kernel from spark plug gap can be determined [4, 7, 50].

These optical techniques are able to detect minor changes in flame kernel development, such as flame kernel convection velocity and direction, rate and extent of flame front wrinkling, and rate of flame kernel growth, and provide valuable information about CCV contributions, but are complicated and expensive, have limited spatial and temporal resolution and eventually need specially designed optical engines.

1.7 Summary of the Literature Review

Cyclic variability is mostly determined during the spark and early kernel phase (MFB<2%) during which combustion is influenced by (i) the spark discharge characteristics, (ii) mixture homogeneity and (iii) the flow in the vicinity of the spark plug. Depending on the engine design and operating condition, the relative contribution to the total variability of each factor varies. All these phenomena are strongly coupled, dependent of the engine geometry or engine operation, and thus difficult to predict at the stage of the engine design [25].

In general fluid flow is the most influential under homogenous stable running conditions. When operating lean or dilute, spark discharge seems to become increasingly important, while at

heterogeneous conditions the local laminar flame speed effect in the vicinity of the spark plug will dominate. A normal spark ignition engine will operate at part load, with the fuel semi-premixed. This means that the relative importance of the three parameters generally is unknown, and will change even with a slight variation in engine operating conditions [24].

Many of the parameters have been studied independently but there is a lack of simultaneous measurements [24] of all factors influencing the early flame in a well-crafted experiment that allows for some of the influencing factors to be assumed small.

1.8 Research Objective

Developing internal combustion engines is still driven by experience and assumptions rather than a fundamentally understood science. Over the past century great improvements in terms of emissions, performance, and efficiency have been made. In this process, CFD played an important role in gaining insights and accelerating the engine design process. Using Reynolds Averaged Navier Stokes (RANS) type codes, the average in-cylinder flows and average combustion behavior can be computed with good accuracy. These calculations have the drawback of not being able to get an insight in cycle-to-cycle variations. Large eddy simulations (LES) could resolve this issue but are computationally more expensive, not as well refined yet and with today's computers no design optimization is possible due to excessive computational expense.

This lack of understanding of the cyclic variability leads to the issue that ICE combustion science fails to progress. For an individual cycle, the average flow and combustion characteristic is meaningless, because flow flame interactions are different every cycle due to differences in the turbulence fields, local mixture and temperature inhomogeneity, and spark discharge characteristics. A result follows that even under steady state conditions, the engine's cylinder peak pressure, ignition delay, and indicated mean effective pressure are changing from cycle to cycle, causing drawbacks in brake specific fuel consumption (BSFC), decrease in power, and the increase of pollutant emission.

At every operating point, the optimal spark timing is set for an average cycle[4]. Faster-than-average-cycles have effectively over advanced combustion and slower-than-average cycles have effectively spark retarded combustion. Both lead to losses in power and thermodynamic efficiency[7] due to unnecessarily high pressures before top dead center that effectively act as a brake in the former case, or the piston is already on a downward movement and less work than possible is converted to mechanical energy in the latter case. Besides these draw backs the extremes of CCV limit the engines operation[4, 7].

Under high load and low speed operation, spark ignited engines can tend to knock at the MBT timing. These high pressure rise rates and high peak pressures caused by spontaneous end-gas autoignition (makes a knocking sound, hence the name) can cause damage to the engine hardware. For this reason the spark timing needs to be retarded to a CA at which the knock tendency is reduced. This is determined by the fastest burning cycles with over advanced spark, since those are most likely to knock which reduces efficiency as stated above. Further, the design process also determines the engine's octane requirement, and with that the fuel price the customer has to pay (higher octane fuels have lower knock tendency) and limits the engines compression ratio. Higher compression ratios have better thermodynamic efficiencies but also a higher knock tendency. If CCV could be eliminated engine break power could be increased by 10% [51].

On the other hand, the slowest cycles burn incompletely until exhaust valve opening (EVO) leading to high hydrocarbon emissions (HC). These cycles with retarded timing also limit the maximum dilution (air and/or EGR) levels. Both gases reduce the peak combustion temperature and with that heat losses. Excess air in particular has a higher ratio of specific heat than reaction products which increases the thermal efficiency of the engine. These slow burning cycles also limit the minimum idle speed. By having a low IMEP output in these cycles, the engine speed drops, which leaves the impression of a poorly running engine or in worst case even stalls the engine. If the CCV_{IMEP} can be reduced, the idle speed could be dropped further, which decreases fuel consumption.

Modern engine development is done with both experiments and simulations. The findings form this work are able to help the CFD modeling in two ways, besides providing validation data. Firstly the insights gained give guidance if the Lewis number equals 1 assumption is appropriate and might be used to gauge the error introduced by doing so. Secondly it provides insights on how similar motored and fired flows are and which motored flow fields should be used to initialize fired CFD simulation runs, to save time and money, and minimizing the introduced error.

The combined information from CFD and experiments leads to a better understanding of CCV would allow engine designers to take measures that reduce cycle variability, allowing to push closer to more efficient combustion at the limit of stability, while/thereby reducing engine-out emissions and improving engine efficiency.

As such, following questions are answered:

- How do the in-cylinder flow field average and flow variations change from motored to fired conditions?
- What is the impact of the charge mixtures thermo-diffusive properties on cycle-to-cycle variations?
- Which quantities in the flow impact on cycle-to-cycle variations? And are decomposition methods like proper orthogonal decomposition (POD) and independent component analysis (ICA) suitable to isolate these quantities?

CHAPTER 2 EXPERIMENTAL APPROACH

2.1 The Transparent Combustion Chamber (TCC) Engine

The TCC engine (Figure 2-1) was originally designed and built at General Motors R&D in the late 1980s for the purpose of investigating combustion using optical diagnostics. After successful use in measuring flow fields and variability in the flow, GM's interests changed and the engine was torn down. Resurrected in 2008 at the University of Michigan, prior to this work the focus laid on cycle-to-cycle flow variability under motored operation. For this work the engine has been upgraded for fired operation.

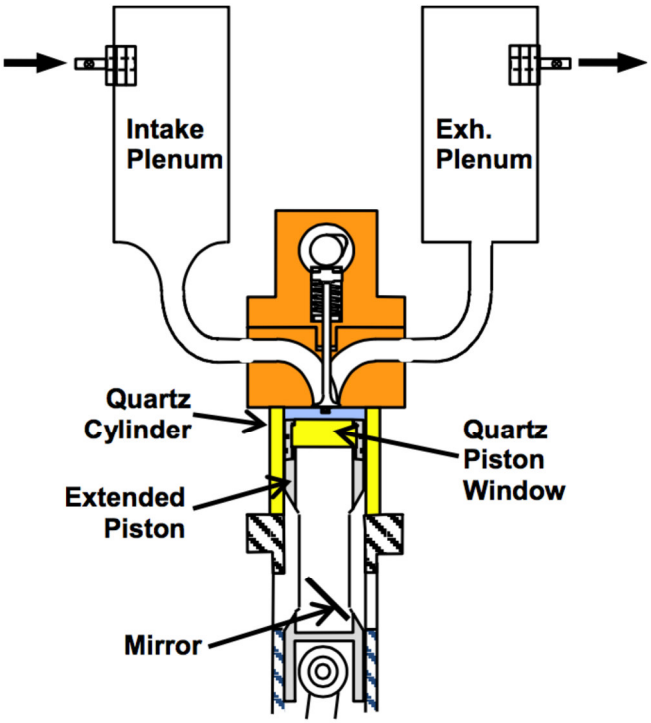

Figure 2-1 Schematic of TCC engine modified from [52]

During the design process, the most important requirements were a maximum of optical access which it has in its current configuration using a full quartz liner and an optical piston with a 70mm diameter quartz window. It has an easy to grid geometry to reduce the computation time in models that would be validated using the experimental data. For these reasons, a disc

shaped combustion chamber (flat head and flat piston) with two intake valves was chosen. The valve curtain area to piston diameter is smaller than in a production engine, which produces higher intake jet velocities and reducing the charge efficiency of the engine already at much lower engine speeds. The engine has a bore x stroke = 92 x 86mm and a geometric compression ratio of 10:1. Large intake and exhaust plenums, which smooth out pressure fluctuations, are connected to the cylinder head with short runners.

Bore, cm	9.20	Conrod length, cm	23.10
Stroke, cm	8.60	Piston-pin offset, cm	0.00
Clearance @ TDC	0.95	EVC, aTDCexh	12.80
Comb Chamber, cc	63.15	IPL, aTDCexh	114.80
Top Land Crevice, cc	0.37	IVC, aTDCexh	240.8
SpkPlug crevice, cc	0.02	EVO, aTDCexh	484.8
TDC Vol., cc	63.54	EPL, aTDCexh	606.8
Swept Vol, cc	571.7	IVO, aTDCexh	712.8
Geometric CR	10.00	Delco Spk Plg	R44LTS
Effective (IVC) CR	8.00	Valve seat angles, deg	30/45/60/75
		Steady-Flow Swirl Ratio	0.4

Table 2-1 TCC engine geometry and valve timings [3]

2.1.1 Pressure Analysis and Run Procedures

The intake and exhaust systems were instrumented with high-frequency piezo-resistive absolute-pressure transducers (Kistler 4007B in the intake and Kistler 4049A in the exhaust (water cooled)) to record the intra-cycle pressure every 0.5 CAD and to determine CCV in the intake and exhaust systems. The intake plenum and runner, exhaust runner, and cooling water were electrically heated to the 45°C intake-air operating point to minimize temperature gradients in the air flow. The engine was warmed up and transducer zero-drift adjusted to barometric standards prior to each test. The uncertainty of the transducers is estimated to be 0.1 – 0.2% of full scale output = ±0.5 – 1kPa for the 500kPa transducers in use. A closed intake system (not open to atmospheric pressure) was used with the air flow metered using critical flow nozzles and monitored with a redundant laminar-flow meter upstream of the nozzles. Estimated precision and accuracy are 0.1% and 0.5% of the measured value respectively. A

back-pressure valve just downstream of the flame arrester was used to maintain the exhaust plenum operation set point at 101.5 kPa average pressure.

Operating procedures were instituted to assure engine operation repeatability, including charting of the run-time control parameters. The engine was motored for 15-20 minutes to achieve conditions that were nearly in steady-state, and repeatable. The temperature of the quartz cylinder outside-surface at mid-stroke was brought to 40±4 °C, depending on operating condition. At run time, the engine speed, delivered air mass flow, and the average intake and exhaust pressures were controlled. The average port pressures, peak cylinder pressure and IMEP were monitored to ensure the engine trapped mass was repeatable.

2.1.2 Spark Energy Measurements

When performing spark ignited combustion studies, it is important to monitor the spark event because of its importance to the success of the combustion during that cycle. In order to measure spark energy a system consisting of a voltage probe (Tektronix P6015A with an attenuation of 1000x) was used to measure the potential difference between spark plug terminal and ground (Figure 2-2). A Tektronix CP312 current probe measures the current on the ground wire that connects cylinder head with ignition coil. This ground wire is looped four times through the probe to increase the measured signal. Together with the sensitivity setting on the amplifier (amplifier sensitivity is 1V/A) a system sensitivity factor of 4V/A is achieved. A NI PCI 5105 data acquisition card is used to record voltage, current and camera f-sync signal at 1MHz. The spark signal from the engine controller is used to trigger the data acquisition.

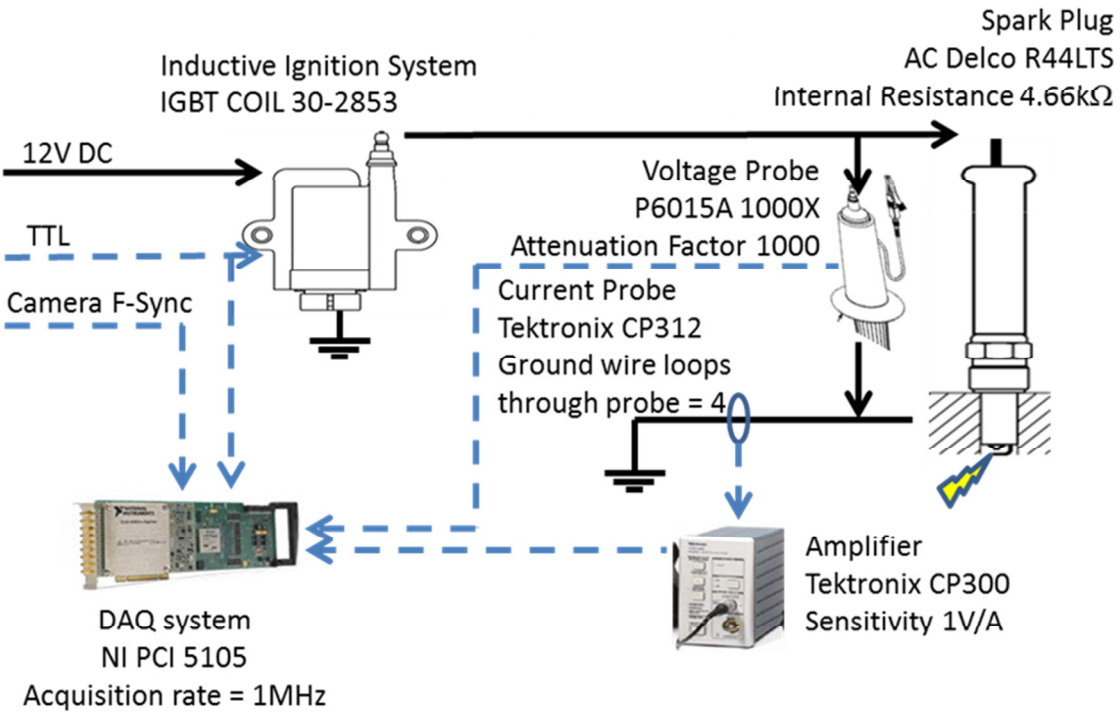

Figure 2-2 Ignition system setup schematic

The energy measured at the spark plug connector is calculated by:

$$E_{meas} = \int_{t=t_{start\ of\ spark}}^{t=t_{end\ of\ spark}} i_{meas} * u_{meas}\, dt \quad (14)$$

where i_{meas} is the measured current and u_{meas} is the measured voltage. The energy provided to the gap is lower than the measured energy because of the ohm type resistance in the spark plug. Resistance in the spark plug wire and spark plug are needed to limit the peak currents and reduce the EMF noise on the acquisition systems. To account for the difference the actual voltage drop over the gap is calculated using:

$$u_{gap} = u_{meas} - u_{spark\ plug} \quad (15)$$

$$u_{gap} = u_{meas} - i_{meas} * R_{spark\ plug} \quad (16)$$

Using the gap voltage the energy in the gap equals to:

$$E_{gap} = \int_{t=t_{start\ of\ spark}}^{t=t_{end\ of\ spark}} i_{meas} * u_{gap}\, dt \quad (17)$$

Start and end of spark are determined using the current signal. When the current rises over a threshold of (0.5mA) over noise level the start of spark timing is defined. Here the exact

threshold level is not critical, because of the steep current slope. The first data point that drops back to a current value of zero determines the end of the spark event. In the current TCC III configuration no restrikes have been observed which would complicate the definition of the end of spark time.

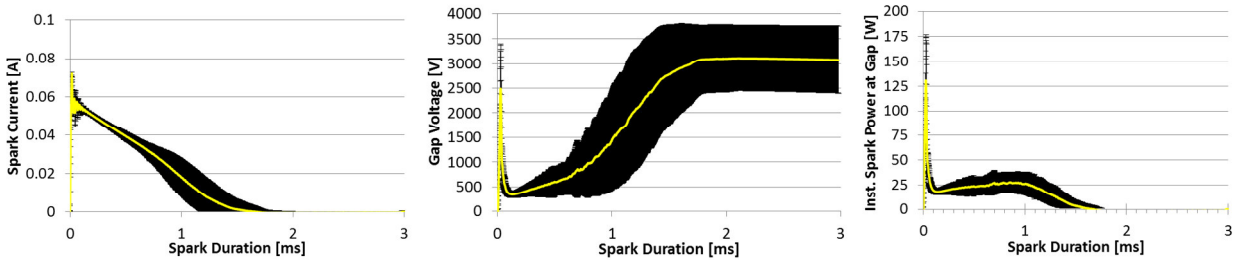

Figure 2-3 Spark current, voltage and power profiles. Yellow line shows the ensemble average trace for 3ms dwell time. Black envelope is +/- 1 StDev

In all tests the electrical energy deposited in the spark plug gap is on average 26.9mJ with a standard deviation of 3.6mJ. The average spark duration is about 1.3+/-0.3ms. The energy transfer efficiency from the spark to the gas depends on the ambient pressure and crossflow velocity and is for the tested conditions about 40% (interpolated from [8]) but is not included into the gap energy calculation. The spark plug gap is 1.2mm in distance and the internal resistance was measured to 5.57kOhm. The relatively large diameter of 2.35mm of the center electrode and width of the ground strap =2.8mm limit the optical access and provide a big surface area to which the flame kernel loses heat.

2.2 Measurement and Trigger Setup

The measurement setup consists of a complex system of control and acquisition systems. On the engine's crankshaft a 0.5CAD resolution angle encoder is mounted that provides a half CAD increment and a once per revolution signal to the PCESC (Personal Computer Engine System Controller). The once per cycle signal is measured on a balance shaft that runs at camshaft speed. These signals are offset-corrected in the PCESC to the match the actual engine CA space. These timing offsets were verified with a long distance microscope and strobe light setup, which also was used to measure intake and exhaust valve lift profiles in the running engine.

The crankshaft is connected to a hydraulic dynamometer unit with which the engine speed is controlled. It has its own set of sensors to measure engine speed and torque output, which are used as input parameters for the PID dyno controller and are not recorded.

From the PCESC CA increment and one pulse per cycle (1PPC) signals are sent to the CA based analogue signal acquisition and real time combustion analysis system Phoenix AM (R&D technologies). It logs all five pressure transducer signals, performs a real time combustion analyses, and records further signals like laser power monitor traces and heat flux probe data every half CAD. Also the camera timing signals from the imaging systems are recorded, to allow a synchronisation in the data post-processing.

A National Instruments low speed acquisition system displays and logs all signals with long time constants at a rate of approximately 1/s. It records fuel, air, seed air, dilution, and tracer mass flows, temperatures, ambient and oil pressure. It is manually triggered and as such user synchronized with the other acquisition systems.

Spark current and voltage are measured with a NI scope card at a rate of 1MHz for 3ms. The recording is triggered by the ignition pulse sent by the PCESC. Here also the imaging clock of the high-speed optical recording system was recorded for synchronization in the post-processing.

Two independent timing systems for cameras and lasers were used. A low speed programmable timing unit (PTU) for the Toluene PLIF imaging and a high-speed controller (HSC) for PIV and OH* imaging. Both timing units receive a 1/10CAD increment signal and a 1PPC pulse for synchronization. The low speed PLIF imaging system records two images per cycle. These two images are intended for temperature measurement at the desired CA, and +360CAD later to record an intensity background image.

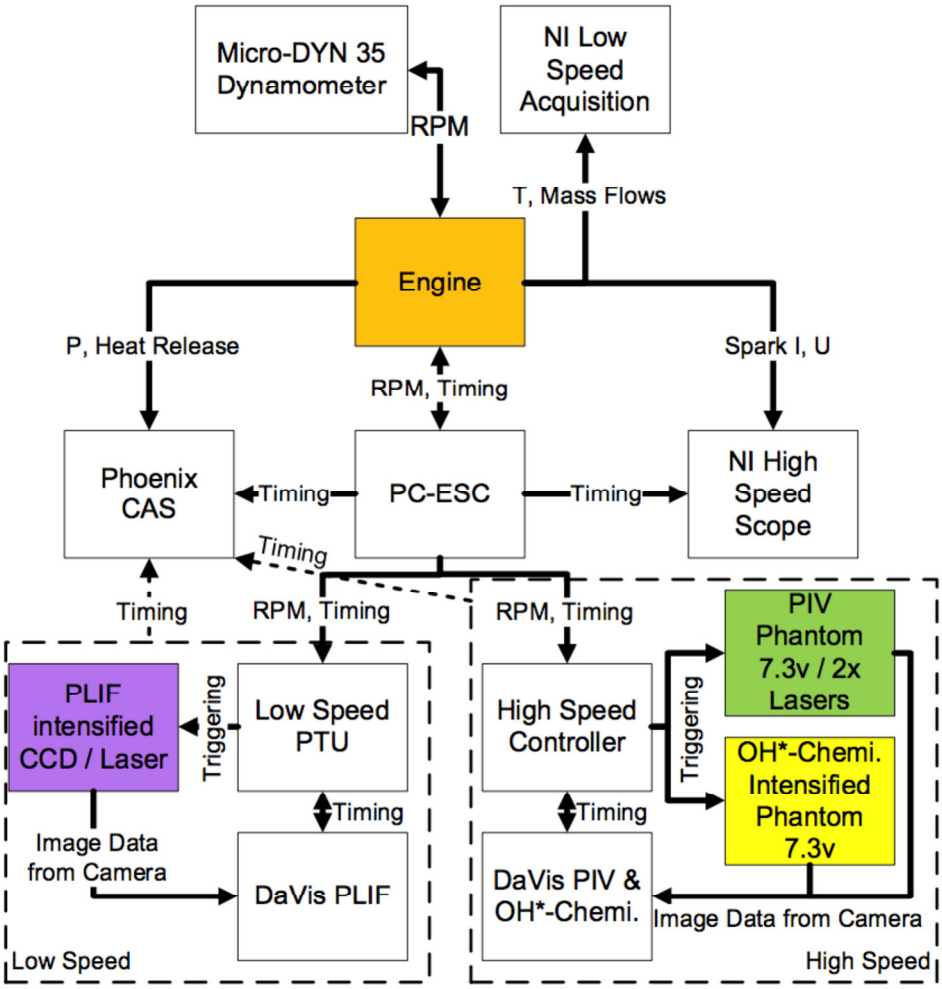

Figure 2-4 Engine control and data acquisition systems. Figure extracted from [53]

2.3 Fired Test Procedure

In an optical engine it is not possible to fire for a sufficiently long time to establish a full steady state condition, because the quartz windows and cylinder wall become dirty, which reduces image quality. Data acquisition during a transient process makes it difficult to identify clear sources of variability, because too many parameters are changing with time. A good trade-off has to be found that enables to acquire repeatable quality data during a quasi-steady state condition.

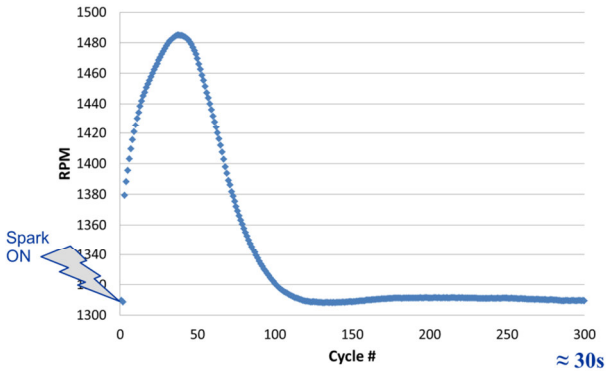

Figure 2-5 Initial engine speed transient after ignition system is turned on

Data was recorded 30s after the first fired cycle (see Figure 2-5). This time seemed to be sufficient for the engine system to recover from a 200RPM engine speed transient. After the engine speed recovered, the combustion phasing keeps advancing as the wall temperatures heat up and the plenum pressures need more time to stabilize. This long transient period is partially caused by the poor performance of the dyno controller that is not adequate to handle rapid torque changes. IMEP, cylinder peak pressure and 10, 50 and 90% mass fraction burned curves do not become steady until after about 400 cycles after enabling the ignition system. Figure 2-6 gives an overview how these parameters are developing after the initial speed transient. Although data acquisition has to start before a complete steady state is achieved, the transients and tests were shown to be repeatable. Although the rich methane case shows the highest deviation from 1300RPM set point parameter, the 30RPM excursions are repeatable from test-to-test. A detailed description of pressure repeatability can be found on page 51 ff.).

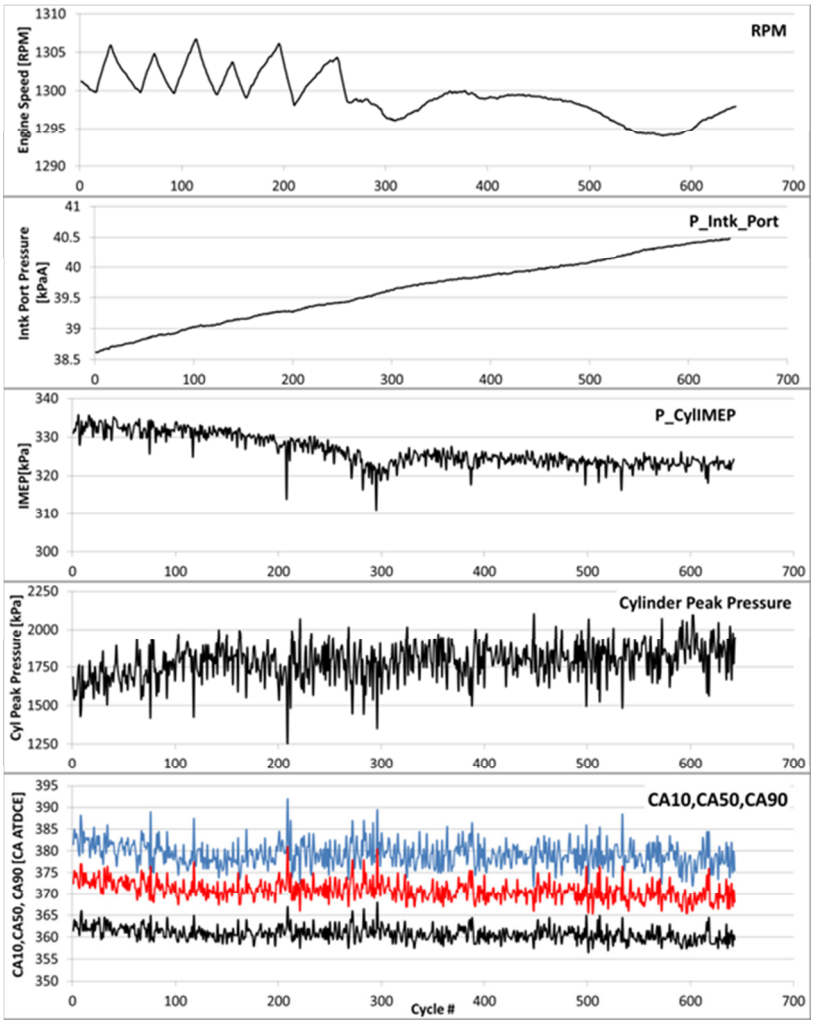

Figure 2-6 Engine parameters as function of cycle number, to judge when quasi-steady state is reached (S_2014_05_13_01)

To make valid comparisons between IMEP, ignition delay and flow field features also the steady state of the mean flow field needs to be verified. Figure 2-7 shows subsample ensemble averages of flow in the z=-5mm swirl plane. Flow at 260 and 300CAD ATDCE seems to be steady from cycle 128 onwards. Because of the small sample size of about 64cycles, statistically no perfect match can be expected. The differences between subsamples become much bigger at the start of ignition. The flow at the spark plug is initially moving predominately from left to right eventually moving the initial spark kernel away from the ground strap. This flow direction changes by the formation of a vortex that pushes the flame kernel on average towards the ground strap, leading to increased heat losses during the early kernel phase.

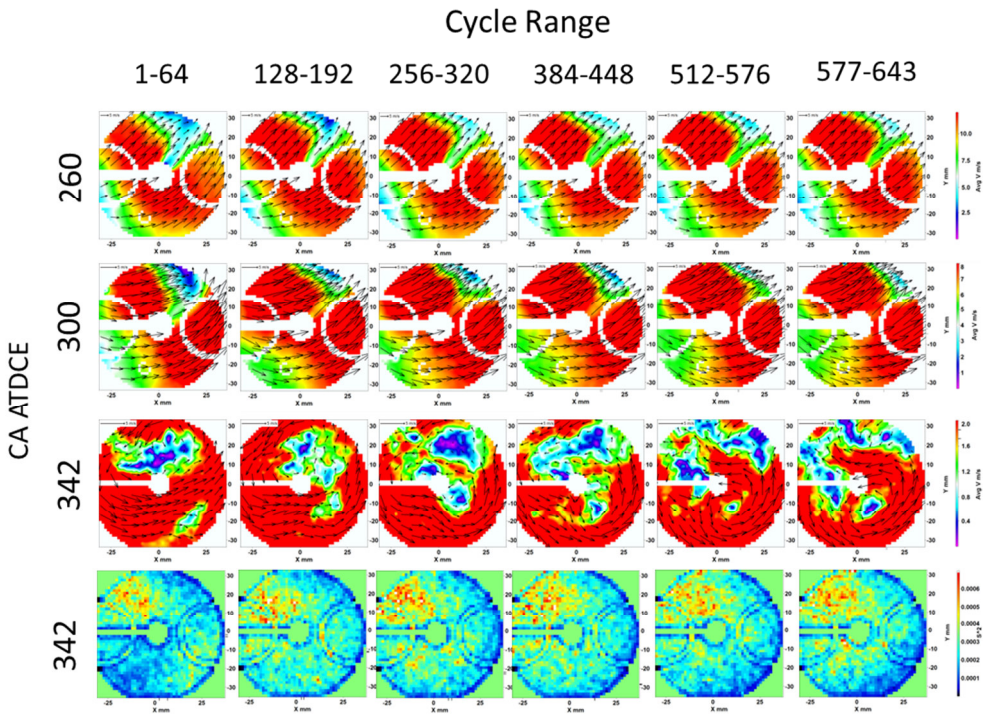

Figure 2-7 Evolution of fired ensemble average flow field in z=-5mm plane (top three rows), and shear strength (bottom row) in stoichiometric stable test case (S_2014_05_13_01)

Ensemble average shear strength at point of ignition achieves a steady state faster than the subsample mean flow fields. Like the flow fields at 260 and 300CAD, the mean shear strength steadies out after about 100 cycles after start of recording. In "LaVision, DaVis" shear strength is calculated from the eigenvalues of the 2D strain tensor matrix $\begin{pmatrix} E_{xx} & E_{xy} \\ E_{yx} & E_{yy} \end{pmatrix}$. It is calculated to

$$Shear\ Strength = \max\left(0, E_{xy} \cdot E_{yx} - \frac{E_{xx} \cdot E_{yy}}{2} + \frac{E_{xx}^2 + E_{yy}^2}{4}\right) \quad (18)$$

the other components are set to zero to display shear only [LaVision, Davis 8.2 Manual]. The strain tensor $E_{ij} = {}^{\partial V_i}/_{\partial j}$ is the spatial derivative of the velocity components in x and z direction. To ensure that in a high COV_{IMEP} lean propane Φ=0.61 test case (S_2014_05_09_02) also achieves steady state its flow field convergence is confirmed (Figure 2-8). In this test spark is advanced from 342 to 318CA ATDCE to match CA50 with the stoichiometric case. Another

important flow parameter that correlated with CA10 is von Mises strain. It is calculated in DaVis as follows:

$$\text{von Mises Strain} = \frac{2}{3}\sqrt{E_{xx}^2 + E_{yy}^2 + E_{zz}^2 - E_{xx}\cdot E_{yy} - E_{xx}\cdot E_{zz} - E_{yy}\cdot E_{zz} + 3 * E_{xy}^2} \quad (19)$$

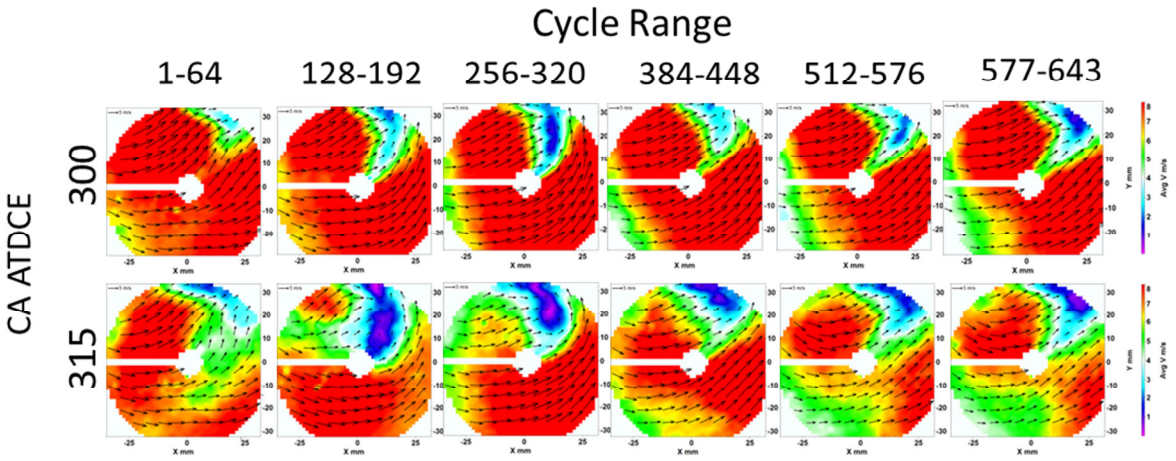

Figure 2-8 Evolution of ensemble average flow fields in z=-5mm plane for lean high COV case (S_2014_05_09_02)

2.4 Test-to-Test Repeatability

Test-to-test repeatability is important to show that the results shown are reproducible. Ensemble pressure traces are shown here in kPa absolute (kPaA), whereas differences between the individual-test average (over hundreds of cycles) and the average of all tests (Discrepancy in %) are quantified. Here (Figure 2-9 and appendix 0) the discrepancy is plotted since the differences are too small to discriminate on a full-scale plot of the absolute values. The test-to-test deviation in the plenum and ports for motored cases is below 1%. In-cylinder pressures are similar through much of the cycle but deviate up to 2% though during the valve overlap and early part of the intake stroke (-45 to 90CAD ATDCE) for wide open throttle (WOT) motored tests.

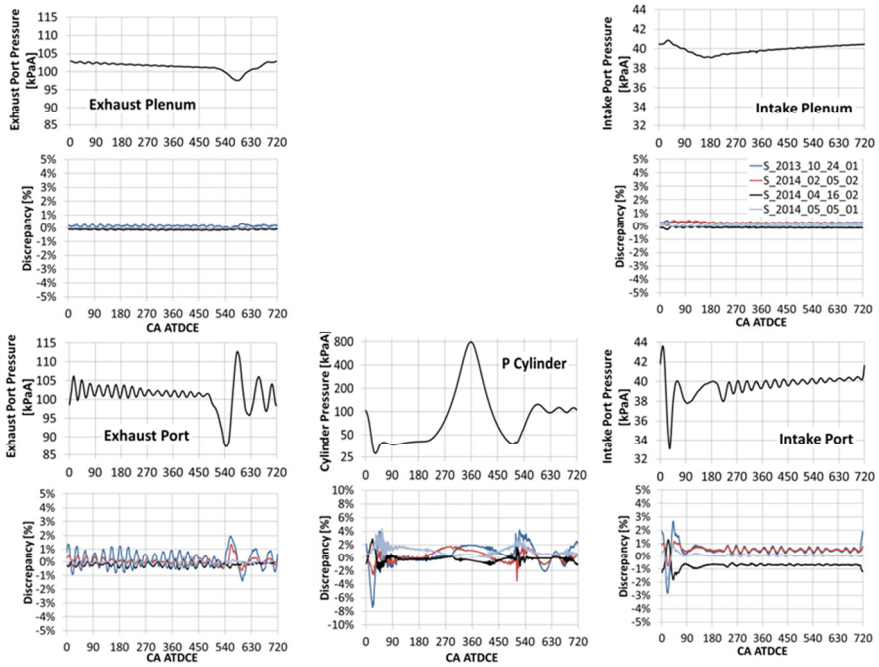

Figure 2-9 Pressure traces and test-to-test pressure discrepancy 1300RPM 40kPa motored condition

Compared to the motored tests, variation is higher for fired operation (Figure 2-10). The increase in cycle-to-cycle variability can be explained that the fired test could not be performed at steady state due to the engine walls getting dirty relatively quickly during fired operation. Instead a repeatable run procedure was followed in these experiments to ensure test-to-test repeatability. In detail: The engine was first motored at steady 1300RPM , intake and exhaust plenum pressures were set to 40kPa and 101.5kPa, respectively, with fuel flow adjusted to have an equivalence ratio of 1.0, then the ignition is switched on, after 30s the engine was believed to run at a stable engine speed and the data acquisition was started.

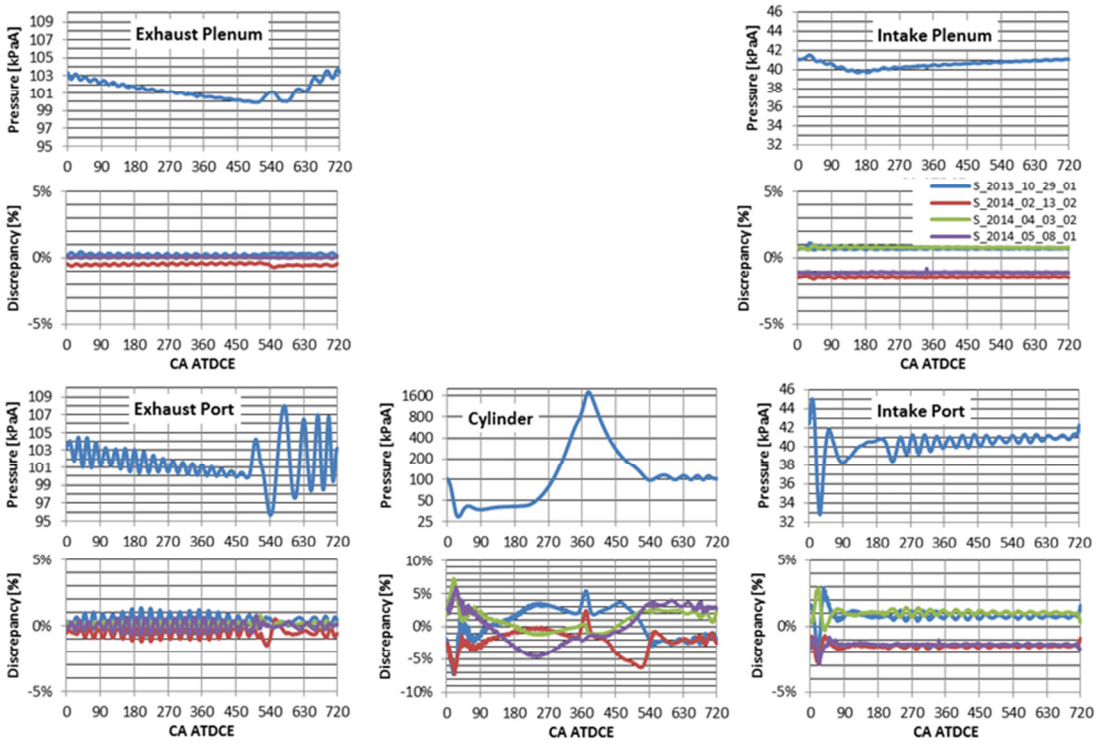

Figure 2-10 Pressure traces and test-to-test pressure discrepancy 1300RPM 40kPa fired condition

Nonetheless the way the engine recovers from the speed transient due to the rapid torque change, caused by the switch from motored to fired operation, is consistent from test-to-test. A better control over the combustion process is achieved by holding the intake mass flow constant instead of the intake plenum pressure, since the IMAP is the engine systems response to an adjusted air and fuel mass flow.

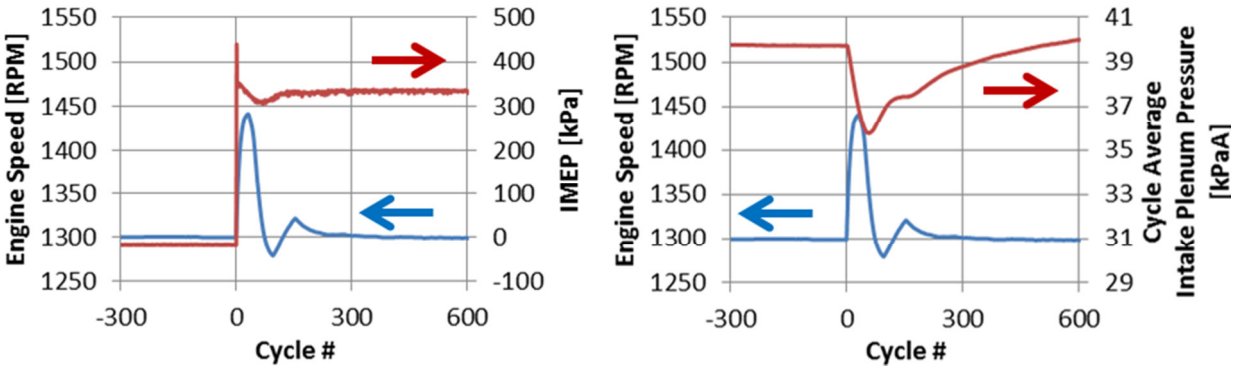

Figure 2-11 Motored to fired transient effects on engine speed and intake plenum pressures

2.5 Orléans Turbulent Combustion Vessel Setup

The 4.2L spherical constant volume combustion vessel at the University of Orléans has an internal diameter of 200mm and is used in this thesis to perform a targeted experiment to isolate flow-flame interaction effects on combustion variability. Isentropic turbulence in the center 50mm region of the vessel is created by six 40mm diameter fans [54]. 4 Quartz windows of 70mm diameter and 60mm thickness provide optical access and can resist post ignition pressures up to a maximum initial gas temperature and pressure of 473K and 10bar, respectively.

The vessel control is fully automated by a National Instrument LabView interface. Before each test, the preheated vessel is flushed with shop air and evacuated to a vacuum of 0.003bar to ensure the removal from all remaining exhaust gases. Then the fresh gas mixture is prepared by up to six different mass flow controllers according to user specifications to the desired pressure, temperature, dilution and equivalence ratio. During the charging process the fans turn at reduced speed to provide a continuous mixing. Towards the completion of the charging, the fans spin up to the set-point fan speed in order to create the desired turbulence conditions. The inlet system is protected by a high-pressure valve that seals the combustion chamber after completion of the charging process. A pair of pointed 0.5mm diameter Tungsten electrodes coupled to a Delphi pencil ignition coil ignites the mixture with an average energy of 18mJ (+-1.3mJ StDev) electrical energy provided to the electrode gap. Average spark discharge duration is 1.9ms (+-0.15ms StDev). After combustion, the fans turn off and after the temperature dropped below 523K threshold temperature the vessel is flushed again for 30s and the next cycle starts at the users command.

The combustion vessel is instrumented with several thermocouples to ensure proper boundary temperatures and one in vessel thermocouple. These temperature signals together with mass flow and a low speed pressure sensor data are saved along with mixture properties in the low speed vessel control and acquisition system and provide a one per test data point. In-vessel pressure is time resolved measured with a Kistler 7001 high-speed piezo electric pressure transducer in combination with a Kistler 5011 charge amplifier, that was offset zeroed right before each ignition event. A high amplifier gain was chosen to resolve smallest pressure

increases. The pressure data is recorded at 500kHz on a NI 6123 PCI card +/- 10V 16bit digitizer together with the voltage and current. This resulted in a 3Pa pressure, 0.3V and 0.1mA digitization step size for pressure, voltage and current measurement, respectively. The wiring and equipment of the spark energy measurement system is similar to the system at the TCC engine. The voltage was also measured with a Tektronix 6015A voltage probe with a 1000x attenuation. The ground electrode wire was lead 3x through a Pearson Model 2877 current probe with a sensitivity of 1V/A to increase its measurement sensitivity to 3V/A. In order to match impedance the current probe signal was terminated with a 50Ω resistor by the digitization system.

While current and voltage signals were processed unfiltered to determine the electrical energy provided to the gap, the pressure trace was in post-processing filtered and reduced to 10kHz to match the image acquisition rate.

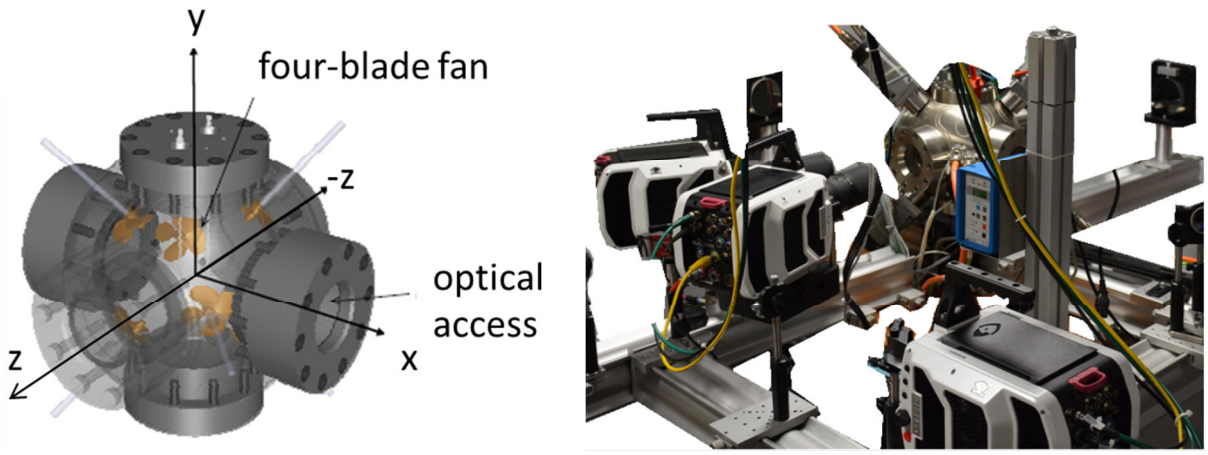

Figure 2-12 CAD rendering [55] and picture of the Orléans combustion vessel

Figure 2-12 shows a CAD rendering [55] of the combustion vessel indicating fan and electrode positions. In this worked a right handed coordinate system was used which flips the z-axis, but the origin is still in the center of the combustion vessel. On the right side a picture of the setup shows the camera setup around the vessel, which will be described in detail in chapters 2.6.5 and 2.6.10.

2.6 Background Imaging Techniques

This sub-chapter is a short introduction to all imaging techniques used in the course of this thesis.

2.6.1 Particle Image Velocimetry (PIV)

This chapter introduces the basics of the measurement system, explains the components that are needed for the test setup and ends with a detailed description of the PIV system and its performance. Most of the information for this chapter is used from Raffel, Willert and Kompenhans [56] ,and Adrian and Westerweel [57].

Particle Image Velocimetry is an optical non-intrusive velocity measuring technique. A PIV measurement is based on the evaluation of two plane images of a fluid which were taken with a small known time delay. The spatial displacement of tracer particles (in most cases, added to the fluid for the purpose of the PIV experiment) can be measured and the velocity field in the plane can be determined.

In most of the fluids that are investigated tracer particles have to be added before it enters the area of interest that the fluid motion can be observed. This process is called seeding.

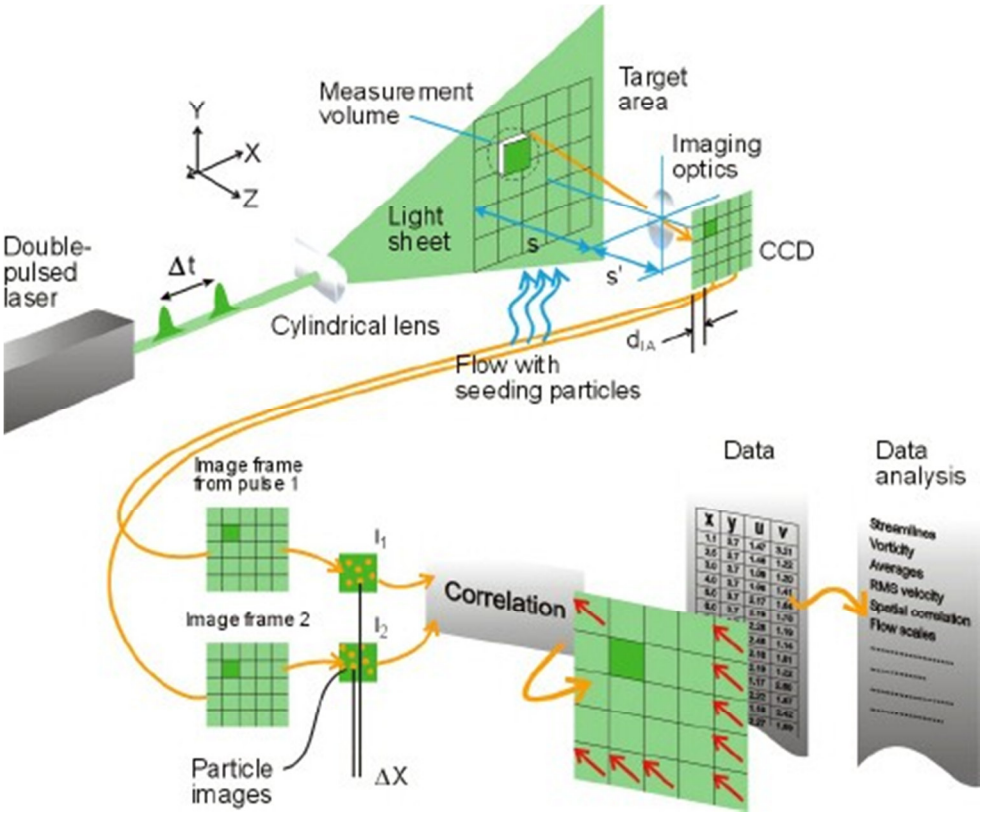

Figure 2-13 Schematic of PIV measurement and analysis [58]

Hence, the small particles (see [59]) are moving fast with the fluid and the exposure time is short (that the particles don't move more than a quarter than a length of the interrogation window. Therefore the flash to illuminate the pictures has to be intense. Today's work horse in research for illumination in PIV systems is the Nd:YLF Laser. Its beam is transformed with optics into a thin light sheet and illuminates a section of the flow.

2.6.1.1 Seeding

Seeding is the process by which the fluid is mixed with tracer particles. These particles can be, for example, smoke, liquids or powders. In these experiments silicone oil is used because it does not damage the engine.

Due to the difference in densities between the oil and the air, the oil particles have to be very small to track the flow well. This behavior can be observed in Fig. 2.1 which shows the normalized speed of tracer particles over the time response [59].

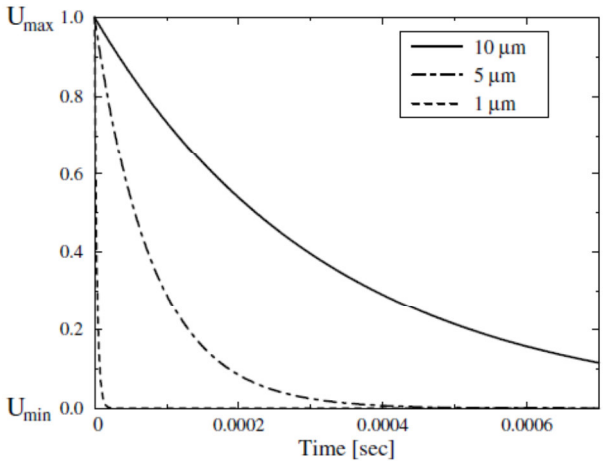

Fig. 2.1 Time response of oil particles with different diameters in a decelerating air flow [59]

One problem that arises with small particles is that they scatter less light than bigger ones. To make sure that enough light scatters on the imaging plane of the camera the laser needs to be intense enough. Not only is the size of the particles important to take good pictures with limited illumination power, the direction of the light is important as well. Fig. 2.2 shows how Mie scattering works. The particles are illuminated with a green laser ($\lambda = 532nm$). The graphs below show forward scattering should be preferred compared to the back scattering due to much higher light intensity.

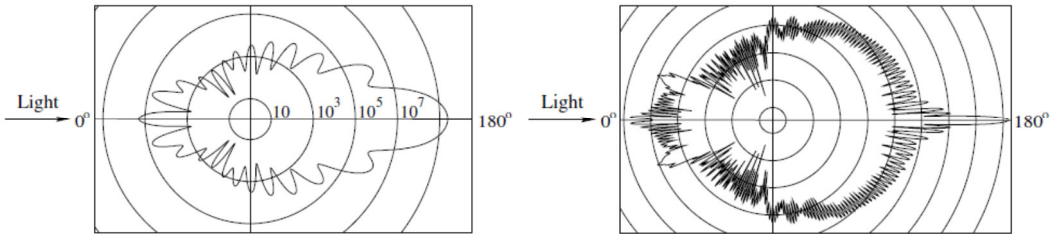

Fig. 2.2 Intensity of light scattering by oil particles in air (Left Ø=1 µm; Right Ø=10 µm) [59]

2.6.1.2 Illumination

The light source in this PIV setup is a laser. It has many advantages compared to a flash lamp:

- Emission of monochromatic light
- High energy density
- Light sheets can easily be overlapped if the beam is of decent quality
- High repetition rate

Using a Nd:YAG Laser has another advantage; it emits the light in a wave length (frequency doubled mode; $\lambda = 527nm$) in which the CCD Cameras have their biggest sensitivity. In the experiments, a Neodymium-doped Yttrium Lithium Fluoride (Nd:YLF) laser type Darwin-Duo, made by LaVision, is used in the full field of view (FOV) (light sheet width =60mm and thickness = 2mm). For the high resolution measurements in vicinity of the spark plug two Quantronix Hawk Nd:YAG $\lambda = 532nm$ modified to run in TEM_{00} mode were used to illuminate a 20x1mm light sheet with a shot energy of 1mJ each.

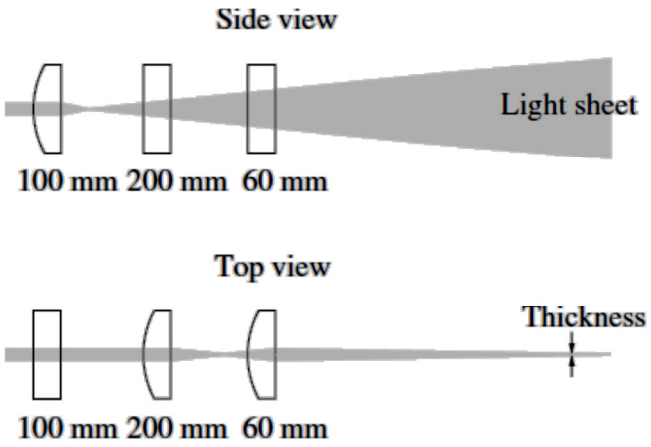

Fig. 2.3 Light sheet optics using three cylindrical lenses [56]

The light sheet optics transforms the laser beam into a thin laser sheet that illuminates a plane in the area of interest. An illustration for this optics is given in Fig. 2.3 above. The thickness of the light sheet is a compromise between the point that it should be thin enough that the particles do not obscure each other, yet thick enough that the particles do not leave the light sheet due to out of plane motion.

2.6.1.3 Recording Technique

For 2-dimensional – 2 velocity components (2D-2C) PIV, the camera is perpendicular to the light sheet and is focused on it. The method used to evaluate velocities in this thesis is called double frame single exposure recording. For this method, the camera takes two images on two different frames with a very short time delay. In this time the particles have moved a certain distance. Usually digital cameras are used today because they offer lots of advantages (e.g.,

recording results are directly available, pictures can be processed automatically, no errors due to photo chemical effects, etc.). For PIV recordings a sufficient sample size and image resolution is important to track the particles with the software. If the particles move too fast, they leave the interrogation area (area in which the algorithm calculates the velocity vectors) and their velocities cannot be computed. If the number of particles is too small, not enough vectors can be calculated to get a good resolution of the flow field; details cannot be seen.

2.6.1.4 PIV Evaluation

The pictures of the double frame single exposure recording are evaluated using the digital cross-correlation method. It statistically evaluates the pictures and determines the movements of the particles. The velocity vectors can be calculated by taking additionally the scale and the time delay Δt into account.

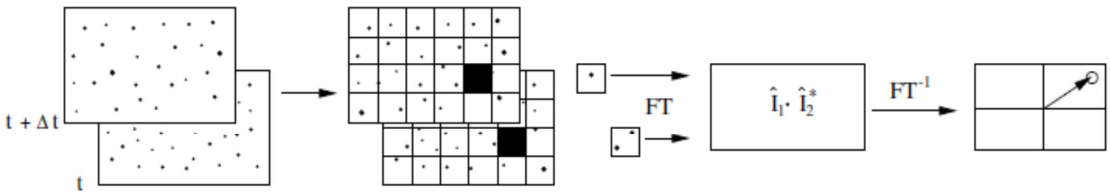

Fig. 2.4 Analysis of double frame/single exposure recordings by the digital cross-correlation method [59]

Firstly, the algorithm divides the pictures into smaller interrogation windows. The data in this thesis is processed with a final interrogation window size of 32x32 pixels. A smaller interrogation window size would increase the spatial resolution of the velocity vector field produced, but it also increases the uncertainty of the velocity vectors calculated. This is believed to be due to the greater probability of particle images being truncated at the edge of the smaller interrogation window[60]. The software calculates now the cross-correlation function of these small areas for the intensity matrices of the pictures. The resulting matrices show peak values at the positions to which the particles have moved.

2.6.1.5 Ensemble Average and RMS Velocity Calculation

Ensemble average velocity vector fields and ensemble RMS fields were visually compared side-by-side. Only the in-plane velocity components were considered for LES, because the PIV measurements provide only two velocity components. At every point in each plane the ensemble average and ensemble RMS were calculated, over all n cycles, as follows:

$$V_{avg} = \frac{1}{n}\sum_{i=1}^{n} V_i \left[\frac{m}{s}\right] \quad (20)$$

$$V_{rms} = \sqrt{\frac{1}{n-1}\sum_{i=1}^{n}\left(V_i - V_{avg}\right)^2} \left[\frac{\mathrm{m}}{\mathrm{s}}\right] \quad (21)$$

2.6.1.6 Flow Field Convergence and Statistical Error Estimates

The accuracy of the ensemble-averaged velocity and ensemble-RMS velocities are a function of the number of cycles used to compute the values, the location, and crank angle. To illustrate this, the ensemble average and RMS velocities for select locations at 100 and 300 CA aTDC exhaust are shown in Fig. 7. The velocity at 100 CA aTDC was chosen since the strong intake jet is present and 300 CA because the large intake structures have dissipated significantly. The sample locations were chosen based on points of interest to be discussed when the results are presented. The convergence of the velocities at each of these locations is shown in Fig. 7 for sample sizes of 10 to 3000 cycles. The samples were averaged over consecutive cycles (i.e., 1-10, 1-20, 1-40, …, as opposed to randomized sampling) analogous to LES with an increased number of continuous cycles.

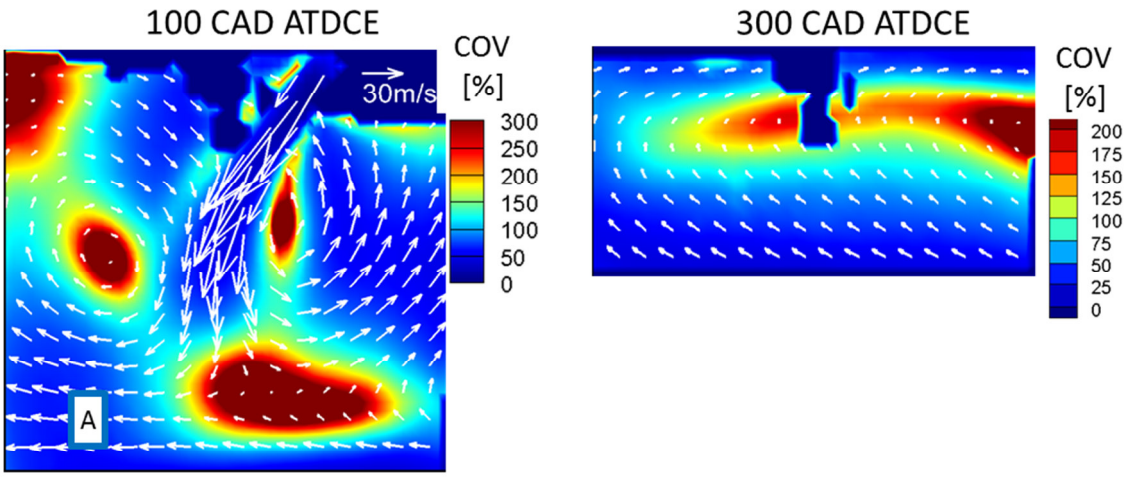

a) Color maps of coefficient of variance (COV) at 100 and 300 CAD ATDCE

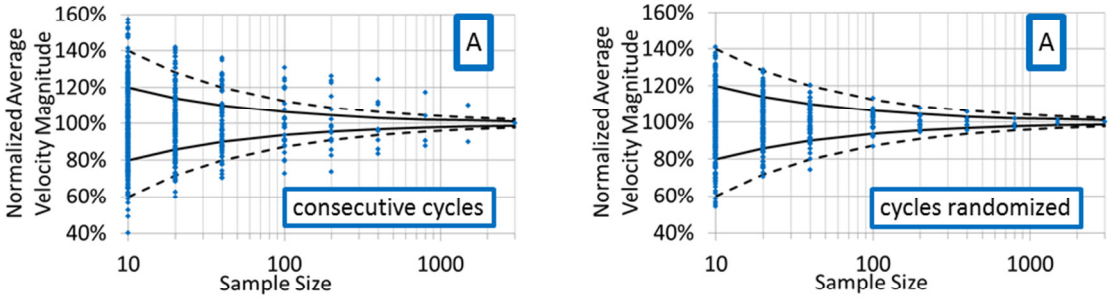

b) Distribution of sub-sample normalized average velocity magnitudes at points A and K as a function of sample size [cycles]

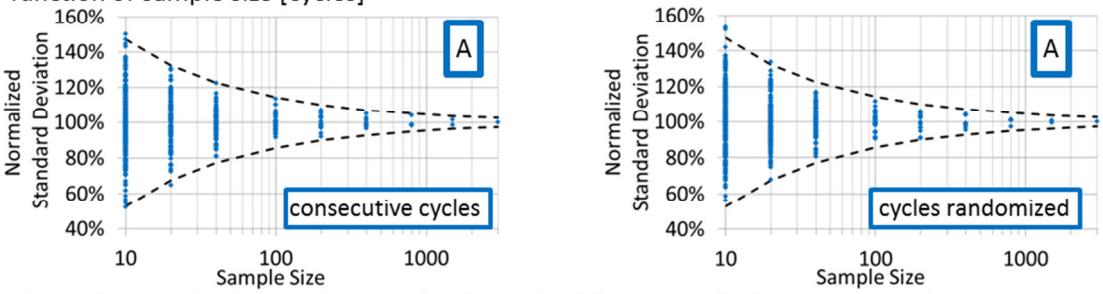

c) Distribution of sub-sample normalized standard deviation of velocity magnitudes at points A as a function of sample size [cycles]

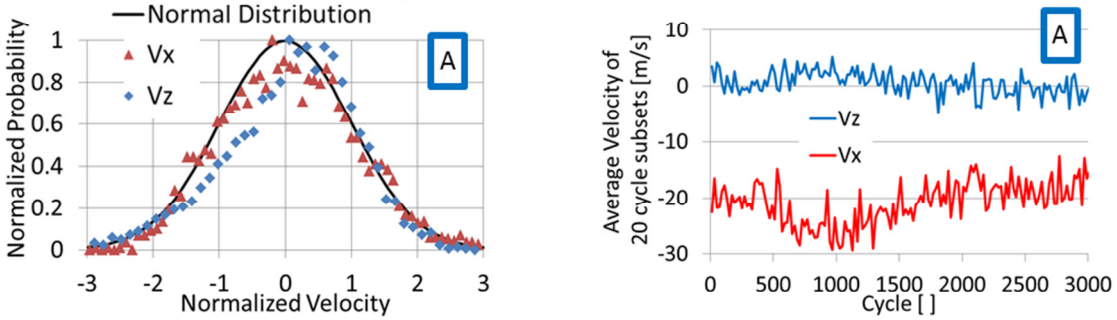

d) Probability distribution of velocity magnitude follows normal distribution (3035 Samples); Temporal evolution of 20 cycle sub-sample averages of both velocity components

Figure 2-14: Sample-size convergence of ensemble average velocity and of standard deviation in the y=0mm plane. All data are normalized to the average of a 3000-cycle motored run (S_2014_05_20_03).

To illustrate the statistical error of the measurements as a function of crank angle, Figure 2-15 plots both the coefficient of variation (COV = spatial average of ensemble RMS divided by spatial average of ensemble average) and the statistical error (COV divided by square root of sample size) at each crank angle. For most of the cycle the estimated average-velocity error is below 10%, with the exception of both top dead centers where an error of 18% can be expected. These errors are always less than 7% of the COV, which is a measure of cycle-to-cycle variability.

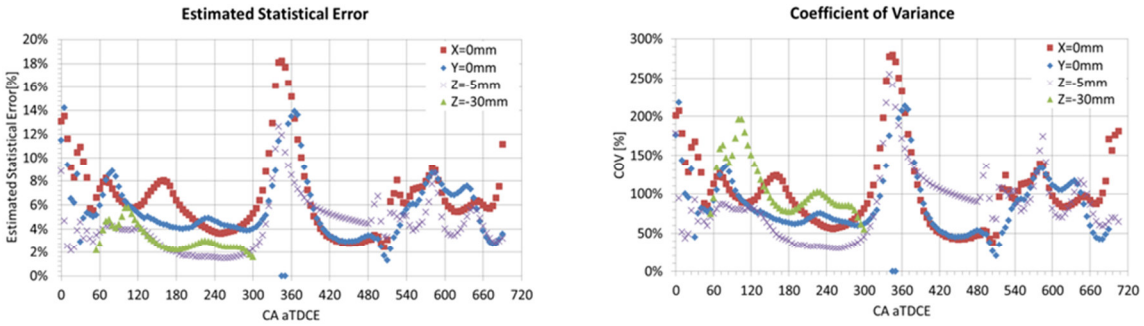

Figure 2-15 : Ensemble-averaged velocity (a) statistical error and (b) cov computed from spatial-average of ensemble average velocity and ensemble RMS (cyclic variability) in the respective measurement planes.

2.6.2 Test-to-Test Variability in Flow Field

For the assessment of test-to-test flow stability, the ensemble average velocity was sampled along the centerline of the cylinder (x = 0, y = 0) for the x-z and y-z planes as shown in Figure 2-16. The planes require different experimental setups, and the three tests were taken at early, middle, and late times during the six-month measurement campaign.

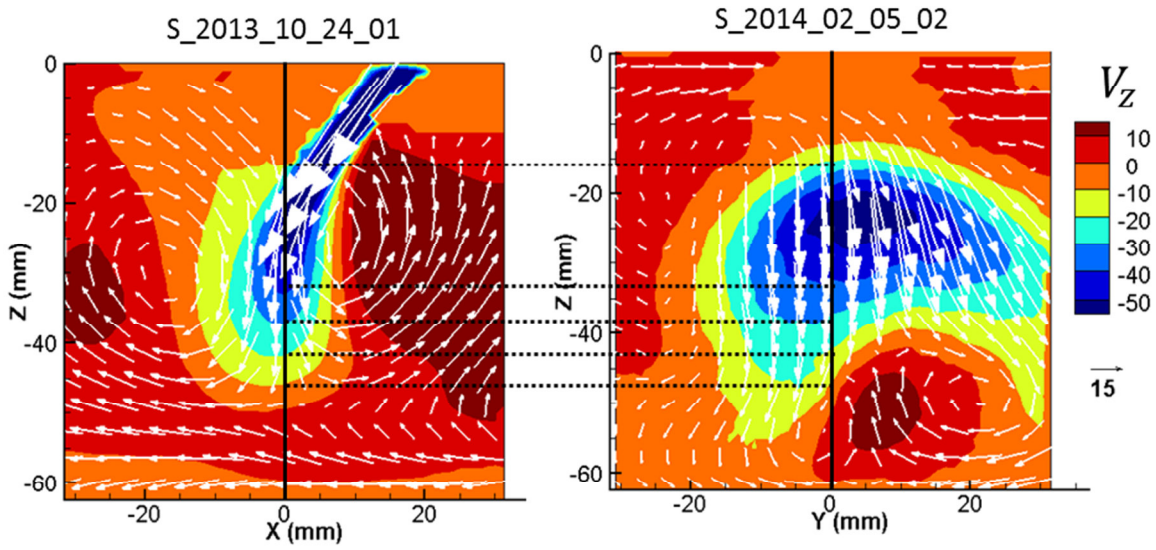

a) Comparison of ensemble averaged Vz contour plots between two different tests in two different planes

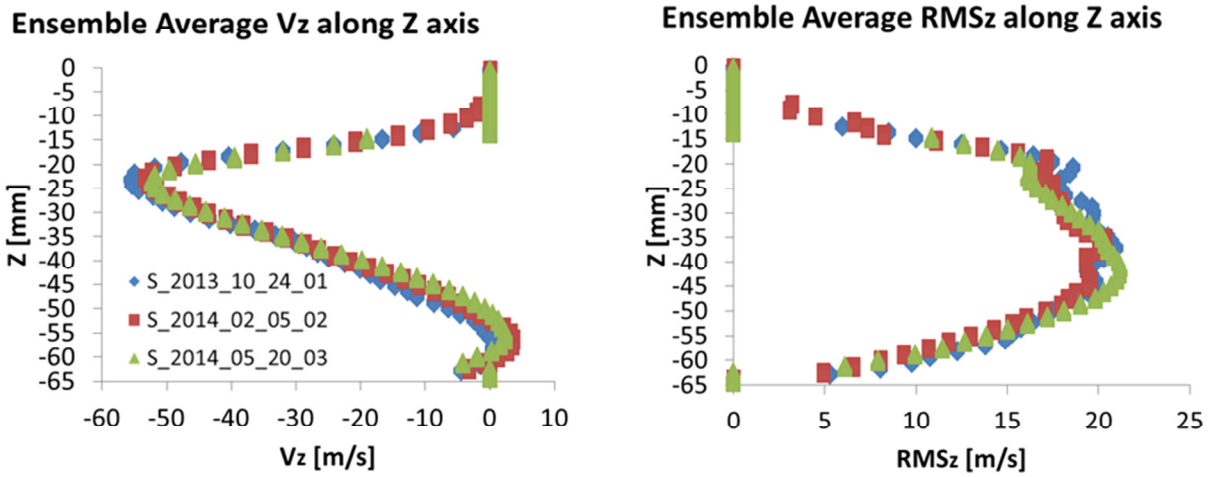

b) Comparison of ensemble averaged Vz (left) and RMSz (right) of three runs along Z axis

Figure 2-16: Ensemble-averaged V_z and RMS_z at 100CAD ATDCE from the series' first test (S_2013_10_24_01, y=0, 240 cycles), a mid series test at an orthogonal view (S_2014_02_05_02, x=0, 235 cycles), and the series' last test (S_2014_05_20_03, y=0, 3035 cycles).

In order to confirm that velocities in three dimensions are correct and the experiments in the different planes were setup correctly and capture the same mean and RMS velocities, the velocity components at point (0/0/-30) were compared. This point was chosen because the three planes intersect at this location. In theory all three velocity components were also acquired in the spark plug during the different experiments but vector processing there is not possible due to strong laser light reflections.

In Figure 2-17 the magnitudes of the velocity components of three different motored tests (two vector components per test) were plotted from 60 to 300CAD ATDCE. Different line plot styles indicate different data sets, whereas colors denote the velocity component. In general agreement in the mean velocity and RMS is within a few meters per second between different tests. Only during early intake stroke the velocity X-component in the swirl plane does not agree with measurements in the horizontal plane. This deviation exceeds resolution or statistic errors. The flow field at this CA shows very steep velocity gradients (see Figure 3-3 60CAD Z=-30mm point (0/0)) where a small mismatch in position causes big differences in velocity. Further the RMS value at this point are greater than the mean velocity values indicating high variability at this point from 60-90CAD.

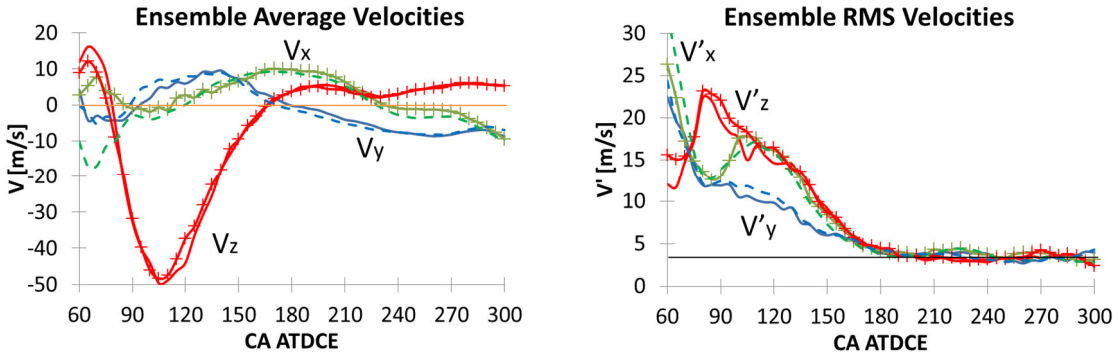

Figure 2-17 Agreement between motored ensemble average velocity components measured in different planes at point (0/0/-30); Solid lines: X=0mm, S_2014_02_05_02: Crossed lines: Y=0mm, S_2013_10_24_01; Dashed lines: Z=-30mm, S_2014_04_16_02

Interesting to note is that, during the compression stroke the RMS values collapse for all three components to about 4m/s. This indicates isotropic flow at this point after the intake jet disappeared. Unfortunately, no further points are currently available to check for this in other positions, but comparisons between the long lines of intersection of different experiments could be done.

In the fired cases, agreement between different tests at the same point is also within a few m/s throughout the entire range of CA investigated. Differences in the x-component are small compared to the motored tests.

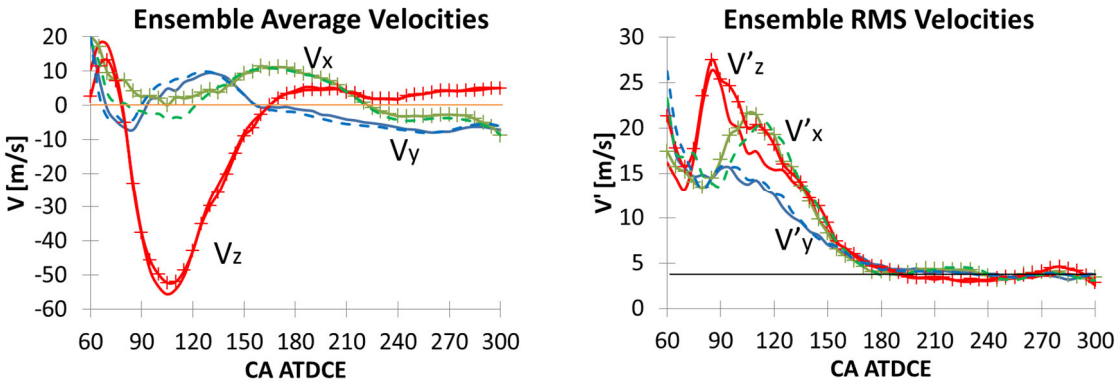

Figure 2-18 Agreement between fired ensemble average and RMS velocity components measured in different planes at point (0/0/-30); Solid lines: X=0mm, S_2014_02_13_02: Crossed lines: Y=0mm, S_2013_10_29_01; Dashed lines: Z=-30mm, S_2014_04_03_02

The RMS magnitude is similar as in the motored case at about 4m/s for all velocity components throughout the compression stroke. A more detailed comparison between motored and fired flow fields at this point can be found on page 106. To estimate the combined error of the ensemble average flow field, it will be tested for continuity at this point.

The compressible continuity equation ensures that mass is conserved:

$$\frac{\partial \rho}{\partial t} + \nabla \cdot u = 0 \qquad (22)$$

$$\frac{\partial \rho}{\partial t} + \nabla \cdot u = \frac{Velocity\ Error}{\Delta_{PIV}} \qquad (23)$$

Change in density plus the velocity gradients have to sum up to zero. The density ρ is given by the ideal gas law $\frac{p}{RT} = \frac{m}{V} = \rho$. R(=287J/kgK) is the specific gas constant for dry air, the in-cylinder pressure p is measured directly, but the in-cylinder air temperature needs to be estimated using a polytropic compression

$$\frac{T_1}{T_2} = \left(\frac{p_2}{p_1}\right)^{\frac{n-1}{n}} \qquad (24a)$$

The time increment is approximately $\Delta t = \frac{\Delta CA}{RPM * 6}\ [s]$ (24b)

The sum of the velocity gradients are calculated as follows for a volume of 2x2x2mm at point (X/Y/Z)=(0/0/-30):

$$\nabla \cdot u = \frac{u_i^{x-1} - u_i^{x+1}}{2\,\Delta_{PIV}} + \frac{u_j^{y-1} - u_j^{y+1}}{2\,\Delta_{PIV}} + \frac{u_k^{z-1} - u_k^{z+1}}{2\,\Delta_{PIV}} \qquad (25)$$

Because of the flow variability in the engine, the limited sample size and measurement error the continuity equation does not sum up to exactly zero, allowing the result to be defined as the error. By multiplication of the error with twice the PIV grid spacing Δ_{PIV}, gives the error in [m/s] for given crank angles. See the top figure in Figure 2-19. The velocity error is highest during intake stroke and approaches zero during compression. Considering that the PIV velocity resolution is limited and that the ensemble averages are not fully converged, the data holds to the continuity criterion well. The velocity resolution is adjusted throughout the cycle by varying the laser pulse separation dt. A detailed list of dts can be found in Appendix F.

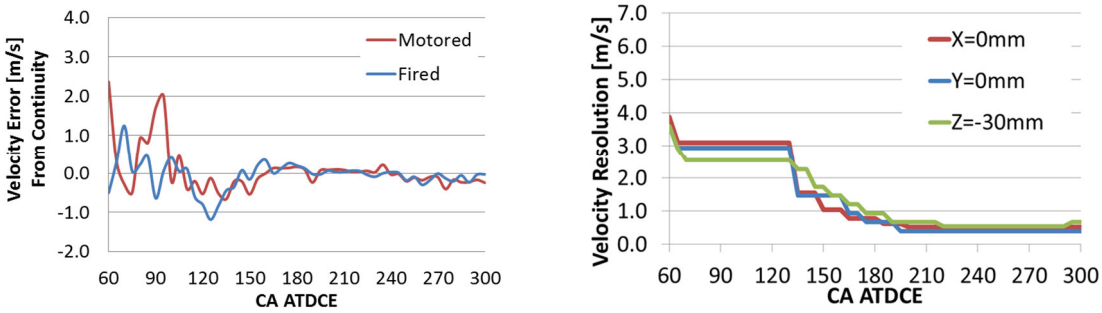

Figure 2-19 Top: Velocity Error calculated from Continuity Equation; Bottom: PIV velocity resolution in three different planes

2.6.3 PIV camera setup

In this thesis two PIV setup's on the engine were used to first image the bulk flow in various planes to quantify cycle-to-cycle flow variability in a motored engine under different engine speed and IMAP conditions, and a higher resolution setup to measure flow velocities and their impact on combustion in late compression stroke. For the full field-of-view (FOV) experiments, a VisionResearch Phantom v1610 CMOS camera was used in combination with a Nikon Nikkor 200mm macro imaging lens. Details on this experiment can be found on page 91. In the second experiment a VisionResearch Phantom v7.3 CMOS camera with constant dt=10µs was used to capture the flow velocities before ignition and in the unburned gas region. This camera gives the advantage of a more compact setup and a higher intensity dynamic range which helps to

improve image quality close to surfaces. 75mm of extension tubes and a 105mm Nikon AF-DC Nikkor at an aperture setting of f/2.8 gave a magnification of 0.032mm/pixel over a 22mm FOV. Distortions from the curved quartz liner are reduced, are especially prominent at high magnification settings. A long focal length cylindrical length in the optical path is used to correct for these distortions. At these high magnifications dirt on the cylinder liner can significantly reduce image quality and the run time. A low f/# setting and putting the camera lens as close to the cylinder as possible decreased the focus of dirt particles on the liner and as such greatly improved the image quality under dirty conditions. A 532nm laser line filter minimized flame luminosity and as such increased the contrast between burned and unburned gas areas, which is critical for burned gas contour recognition.

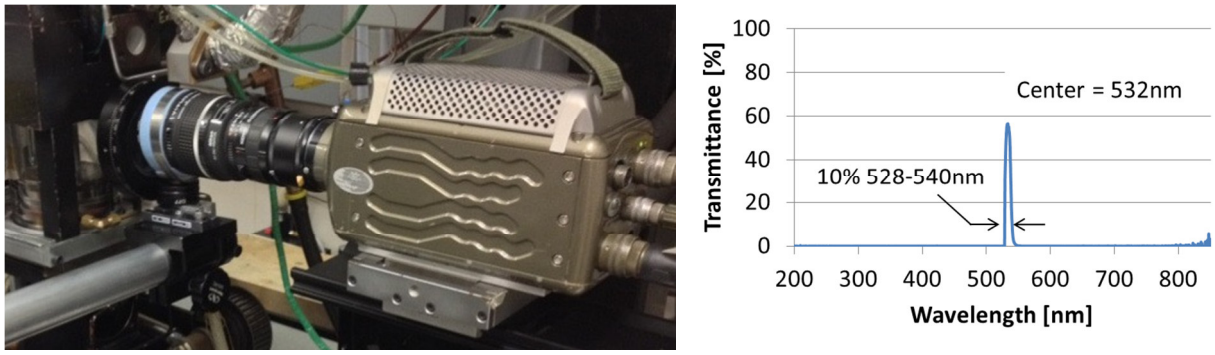

Figure 2-20 PIV camera setup and 532nm laser line spectral transmittance curve

2.6.4 Flow Field Decomposition Methods POD and ICA

One hypothesis that is to be tested in this thesis is that flow field structures have an effect on combustion. There are various ways on how to quantitatively isolate flow structure features from the flow of which two have been tested here, Proper Orthogonal Decomposition (POD) and Independent Component Analysis (ICA) .

The idea behind both methods is to decompose the individual flow fields into a set of modes/independent components, which represent certain flow features, and a matrix of coefficients that give a factor and direction of each mode (Figure 2-21). In order to synthesize the original flow field again, the modes are multiplied with their respective coefficient, and the as such weighted flow fields are added up. When all modes are included in this summation the original flow field is reconstructed, but if a lower number of modes are included in this

summation results in a filtered version of the original flow field. The idea behind performing POD and ICA is to isolate certain flow structures (e.g. vortices, jets,etc.) that can potentially affect engine combustion.

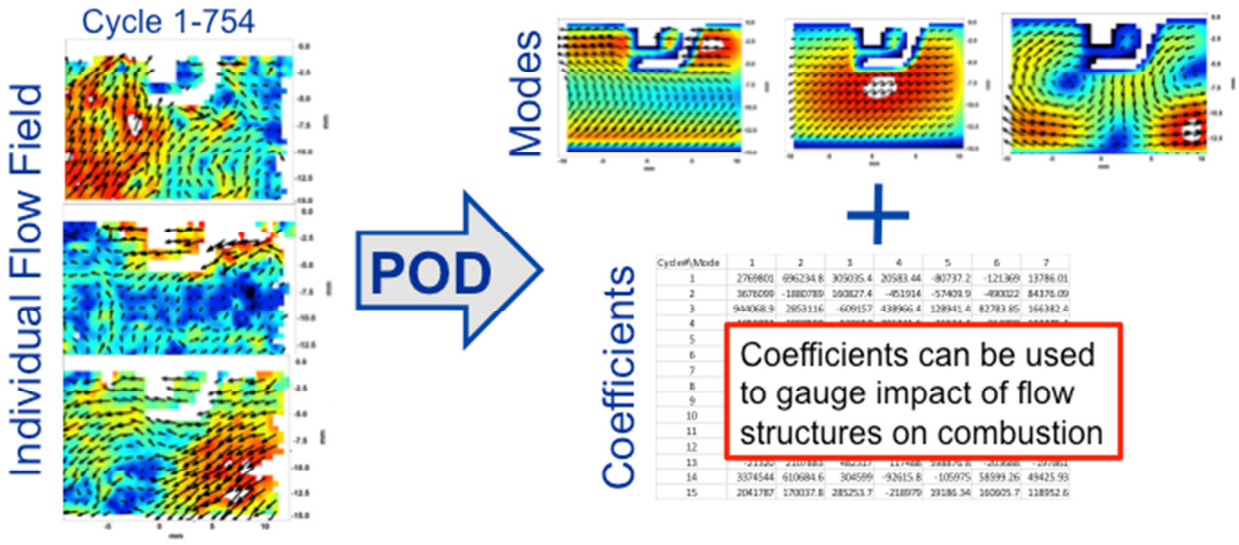

Figure 2-21 Flow chart of POD analysis

POD calculates the eigenvector of the flow fields and then decomposes the flow fields into different structures according to their energy content. An exact methodology and a lot of background on the POD analysis can be found in [61-63], where it has been employed for quantitatively comparing advanced large eddy model simulations and experimental flow field results. Here phase dependent POD was performed which is applied to each CAD individually, as opposed to phase invariant POD where all flow fields from all CAD are treated simultaneously.

Although the eigenvectors are determined individually for each CAD, the Mode results are similar (Figure 2-22) and seem to evolve with time as the piston motion compresses the flow. This is also true for higher order modes that are less energetic and less frequently occurring shows that POD provides repeatable results. The similarity with time is confirmed by a more traditional turbulent flow time scale analysis on page 117 which shows that around the time of ignition the integral time scale is about 20CAD in x and y direction and about 10CAD in z-direction.

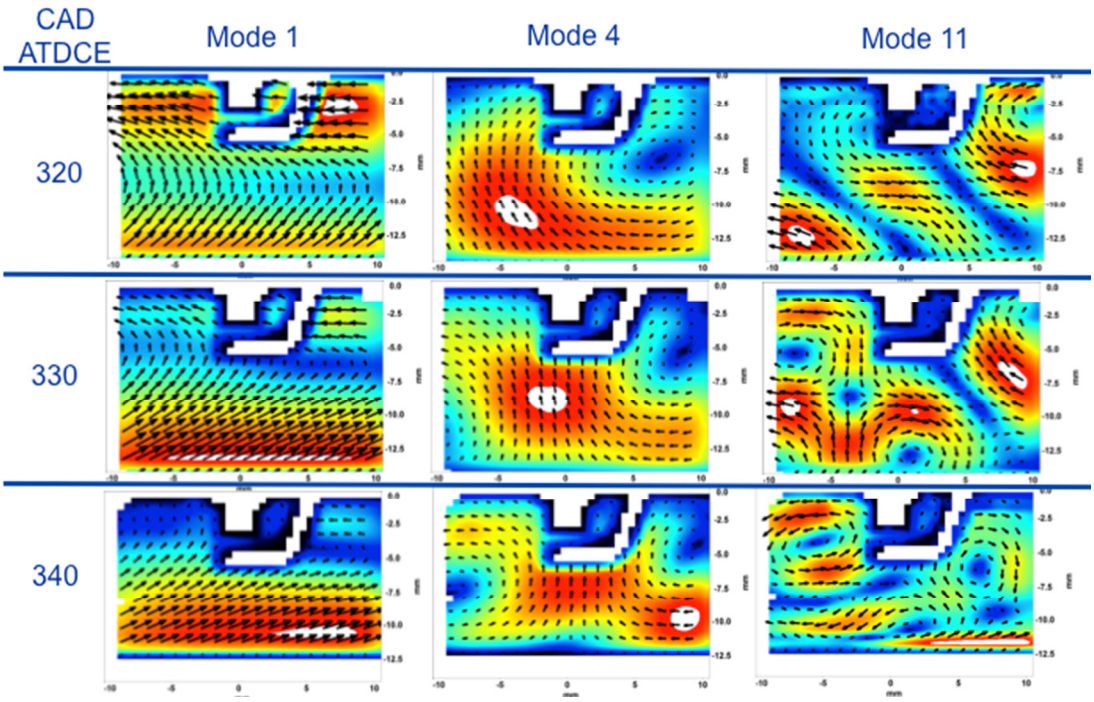

Figure 2-22 POD analysis mode results. Flow structures even in higher order modes are similar from CAD to CAD, indicating that POD provides repeatable results

ICA builds on POD results as an initial filtering step (needed to speed up the computationally expensive processing) but then decomposes the flow fields into statistically independent components as opposed to most energetic structures in POD. This method delivered impressive results in identifying different sound sources or in image processing [64, 65]. Patrick Kranz, who interned at the University of Michigan, pushed ICA to also be able to work on flow field results [53]. His Matlab ICA code is used to identify flow structures that might impact combustion.

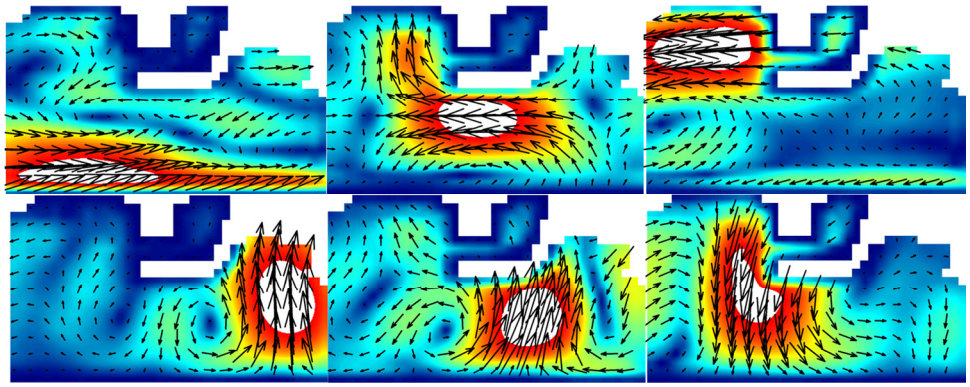

Figure 2-23 ICA analysis results show more locally isolated structures. These six example independent components are from a 10 dimensions & 10 independent components ICA at 342 CA ATDCE. (every 4th vector shown)

2.6.5 Stereo Particle Image Velocimetry

In the constant volume combustion vessel experiments in Orléans a stereo PIV (SPIV) setup (Figure 2-24) was chosen to measure three flow velocity components in a single plane in order to quantify the flow impact on the flame development. This configuration also helped to accommodate a path for the cumulated Schlieren beam to travel between both PIV cameras. For this flow measurement, two high-speed CMOS cameras were available; a VisionResearch Phantom v1210 and a Phantom v1610. Both have the same 1280x800pix^2 chip size and a 12bit ad-converter and differ just by their maximum imaging rates at full image resolution.

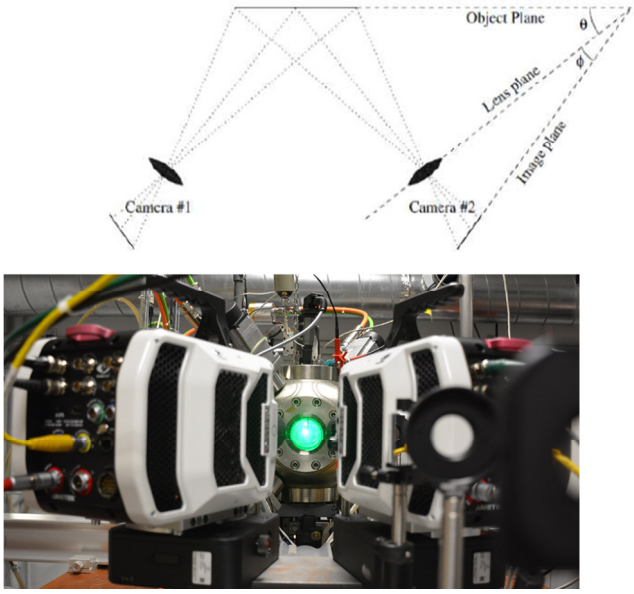

Figure 2-24 Scheimpflug condition [59] schematic and stereo PIV camera setup

In this SPIV configuration it is necessary to tilt the focal plane in order to image all particles in focus. This can be done by setting the camera and lens up under the so called Scheimpflug condition[66]. It describes that when object plane (laser sheet), lens plane and image plane (camera chip) intersect at one point the image is in focus as shown in Figure 2-26. Here the angle between left camera and light sheet is -30degrees and for right camera +6degrees. These angles were caused by the tilted laser sheet, geometrical constraints from the Schlieren setup, and the limited aperture (70mm) of the vessel window. This shallow angle between the cameras causes the out-of-plane velocity error to be about 3x bigger than the in-plane error according to [67].

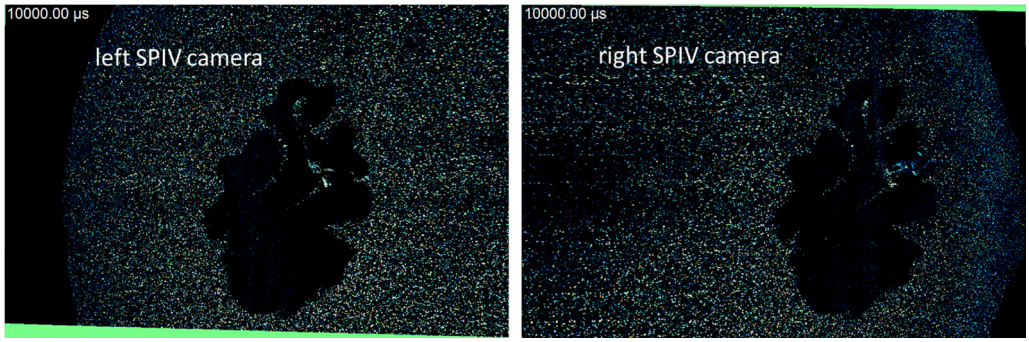

Figure 2-25 Mie scatter images from left and right SPIV cameras show differences of perspective

Figure 2-25 shows post-processed (for details see next chapter) Mie scatter images from the left and right SPIV cameras. The edge of the quartz windows acted as aperture and reduced the light collection on the close edges for each camera. In addition to the regular PIV pre-processing steps a white field correction has been performed to equalize the intensity and the image quality.

Also, the SPIV images were processed in DaVis 8.2 to extract velocity information. The cross-correlation procedure follows the same steps for each camera as in the regular PIV, plus one additional step in which the flow fields of each camera are mapped together using the stereo-calibration information. From the differences in the X velocity in each image, a corrected actual X velocity and the third velocity component V_z are computed. An example flow field is shown in Figure 2-26.

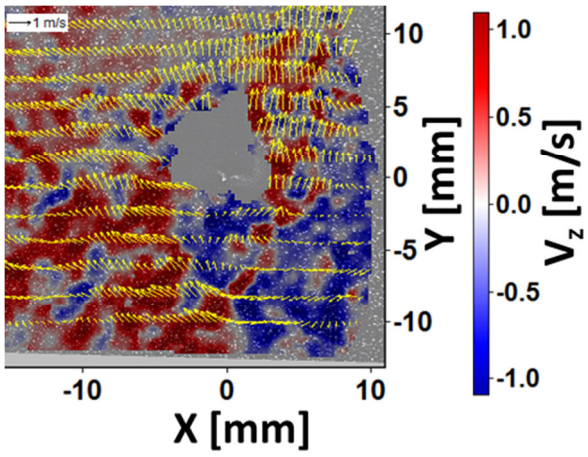

Figure 2-26 Example SPIV flow field in the unburned gas region. Every 4th vector shown in y-direction. Z velocity component is color coded

2.6.6 Mie Scatter planar contour recognition

From the Mie scattering images, information about the planar flow field (as shown in the previous chapter) and when there is a flame the planar burned gas region contour can be extracted. Generally in the “dirty” environments (combustion vessel and especially engine), the acquired images need to be pre-processed to extract accurate velocities and burned gas contours.

Figure 2-27 shows the various pre-processing steps that will be explained in this paragraph. The raw image shows high intensity reflections on the vessel window also the electrodes are clearly visible. Both structures influence cross-correlation and the intensity based contour recognition algorithm. A subtract time series minimum filter of 9 images total filter length (4 images before and after the image that is being processed) is applied. This filter determines the local minimum intensity in a certain pixel in the chosen interval around the image of interest and subtracts this minimum value from the current image. The idea behind the filter is that the oil droplets in the flow are in constant motion, whereas the reflections and geometric features are fixed in space. If a particle passes by these features the individual intensity values are added up. By gently removing all the stationary intensities the particles become visible (compare top pictures in Figure 2-27). This filter is recommended for PIV pre-processing, because it preserves most of the particle intensities that are needed for good cross-correlation results. This one typically also eliminates some weaker particle intensities and the PIV algorithm tends to produce more noisy results. Nine or eleven images filter length is a good compromise between allowing even slow particles to sufficiently move to preserve their intensities, but is short enough to be computationally fast and to account for slow shifts in intensities (from added dirt on surfaces). This filter when applied to engine data is generally applied to images at the same CA.

The result from this filter might still leave some residual low spatial frequency intensities that can influence further processing results. A subtract spatial moving minimum or average filter of 9-21 pixel length helps to remove these changes in intensity. The filter needs be at least twice as big as the particle image. Bigger filters can cause issues close to geometric borders. In Figure

2-27 a 9x9 pixel^2 sliding average filter was used to decrease the intensity in the burned gas region compared to the surrounding particles.

Vignetting is an imaging artifact that reduces the image intensity close to the borders. In Figure 2-27 this can be seen on the left side of the image, where the light ray path for a part of the imaging system was obstructed by the combustion vessel window edge. A white field correction can be performed to increase the intensity in these areas. First, a white field image was created from 1000 pre-combustion Mie scattering images to which a 9x9 pixel^2 average intensity filter is applied to smear the particle images. Those images are then averaged and divided by the spatial average intensity. All pixels that are below a certain threshold set to intensity values of 10^{10} (this disables these areas in the images to which the white field, is applied). When the image of interest is then divided by the white field the particles have a more uniform intensity (compare bottom row images Figure 2-27). This is especially important for the contour recognition algorithm to avoid areas with low intensity particles on the edges being recognized as burned gas.

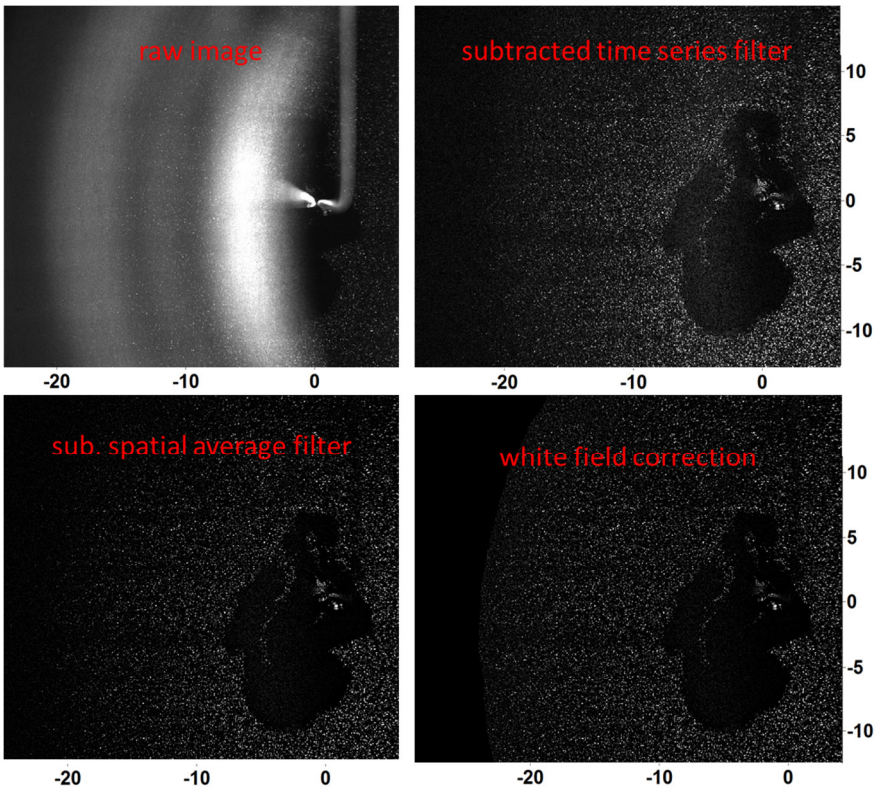

Figure 2-27 Mie scattering image processing steps

In the next step, the images are remapped to real world coordinates. This step is especially important for SPIV images due to the big distortions in the images. If there is little distortion as in the PIV images the error in the burned gas area is about 1%.

Finally the pre-processed corrected images are read into a contour recognition algorithm. A Matlab hysteresis filter from Luke Xie (mathworks file ID 44648) is modified by adding an iterative loop and a dilation function. The algorithm utilizes two user-defined thresholds: (i) high, over which is definitely unburned gas, and (ii) a low threshold, below is definitely burned gas. In between is a medium level of intensities that are between burned and unburned gas. The hysteresis algorithm sets then all pixels on the medium level that are in the neighborhood of a high level also to a high level. The added dilation function increases the range in which these medium levels pixels are then considered for the high threshold. This process is iterated in a loop to fill up all spaces between the particles. A spatial Gaussian filter is applied afterwards to smooth the contours of the recognized contours. Here a filter length of 9x9pixel^2 was used. The results of the contour recognition can be found in Figure 2-28. The hysteresis filter finds the contour of the burned gas region, but over estimates the unburned gas area. This can be improved by fine-tuning parameters and setting narrow thresholds, but comes at the cost of robustness. Here, hundreds of thousands of images had to be processed, so that a robust recognition is a necessity. Instead of fine-tuning parameters for each test condition, a robust set of parameters was tested for each dataset and used in the hysteresis algorithm. The exact contour was then determined by a standard Matlab active contour recognition algorithm. In order to maximize speed by reducing the number of iterations of this code, the result from the hysteresis filter was used as a starting point for the active contour, which expanded the contour within a maximum of five iterations to the actual burned gas contour determined by the individual particles. In case of the clean combustion vessel particle images, no more than 5 iterations are recommended to avoid a penetration of the contour between the particles which would artificially increase surface area.

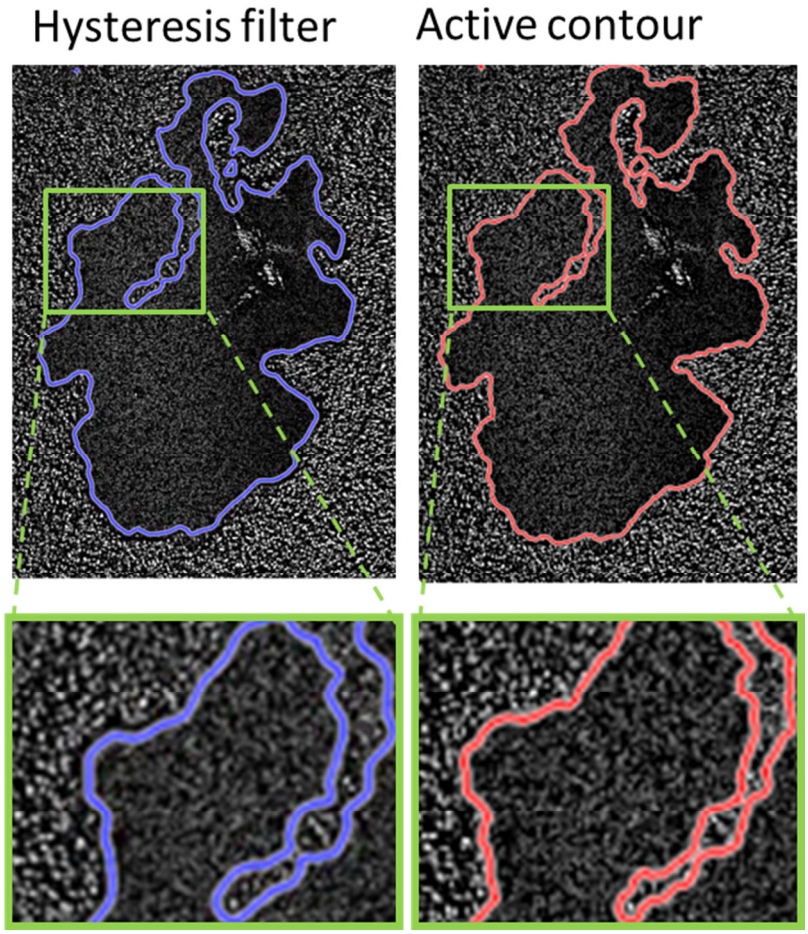

Figure 2-28 Contour recognition algorithm results. Left hysteresis filter contour. Right active contour recognition algorithm expands hysteresis contour to the edge of particles to give the accurate burned gas contour.

This algorithm setup runs reliably on the expanding combustion vessel data for which a time series result can be seen in Figure 2-29 where even fine structures of unburned particles in the unburned gas were identified. Contour recongnition was done for all images past 2-3ms after igntion until the flame touched the perifery of the image. At early times the gap of unburned gas and burned gas is small and could not be recognized reliably; also because of some sparks and material being ejected from the spark event.

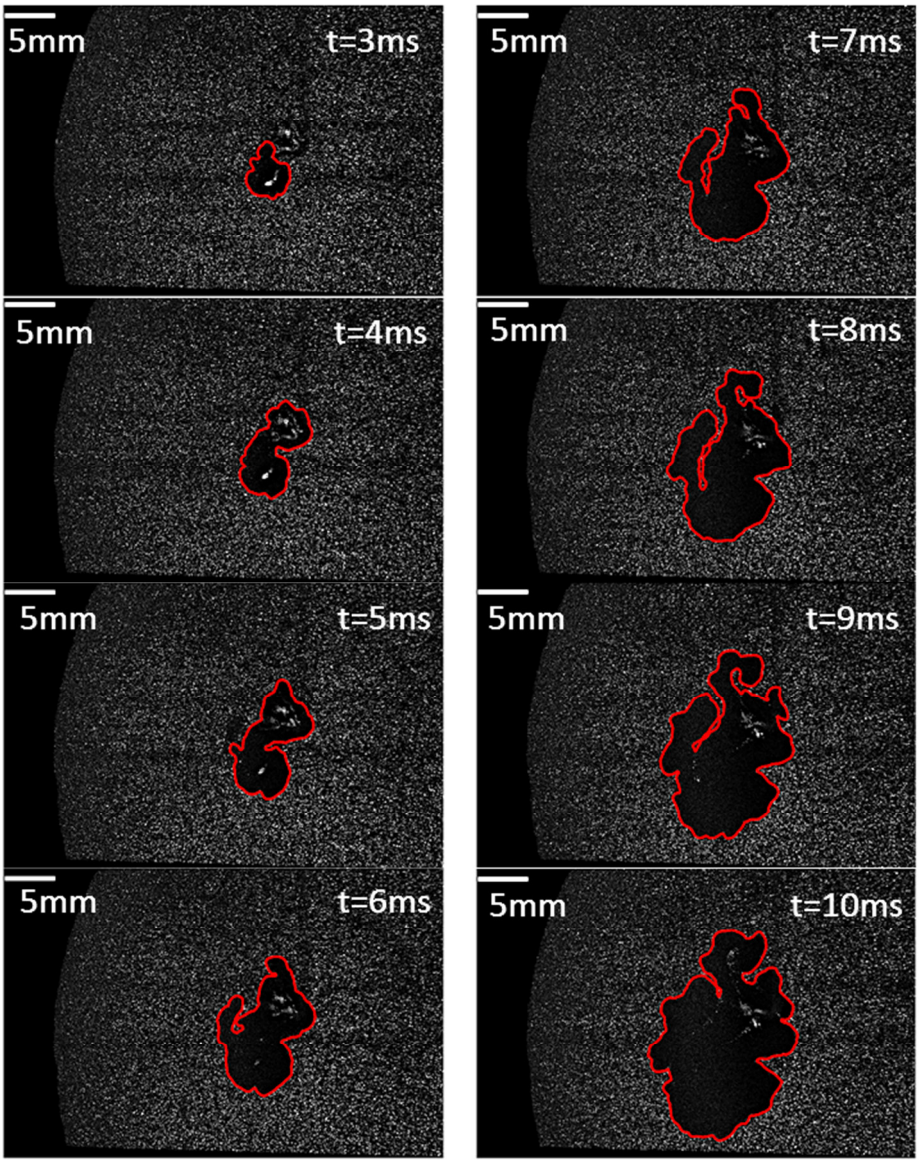

Figure 2-29 Contour series for Methane ϕ=0.69 (C11_20150903_195846)

The contours in the combustion vessel were of high quality and clean contours were detected. However, the engine the environment is dirtier and geometric features like the cylinder head and spark plug cause reflections in the images that could not be removed completely by the previously introduced pre-processing steps. One particular difficulty is also high intensities in the burned gas region especially towards later CA 356-360 CA ATDCE. In order to account for the intensity increase, the lower boundary of the hysteresis algorithm is increased in a linear or square fashion of the CAD (depending on background intensity in the respective dataset). In general, the contours recognized represent the burned gas areas in the engine, but some

imaging artifacts translated into the results for some images. Figure 2-30 shows a variety of recognized flame contours at different CA for different cycles to point out the strength and weaknesses of the procedure. Figure 2-30 (a) contains a narrow flame contour at early CA where the flame burned through the light sheet plane in two spots. The centroids of each burned gas island are indicated with a yellow cross. Part (b) illustrates a flame at 358CAD for a slow burning condition. Close to the cylinder head surface a streaky area can be seen that originates from laser light reflections off the surface. In this area, it cannot be determined with certainty if the gas is burned. Part (c) and (d) of Figure 2-30 show later CAD, at which some islands or peninsulas of unburned gas remained in the FOV. The algorithm recognized the main flame features but some details and smaller islands in (c) were not recognized as unburned gas. High intensities of burned gas in (f) cause the contour to be in the wrong position and not capture the correct flame contour for this cycle. Increasing the threshold to a higher level would push the boundary further out but at the risk that also parts or the entire unburned gas falls below the threshold.

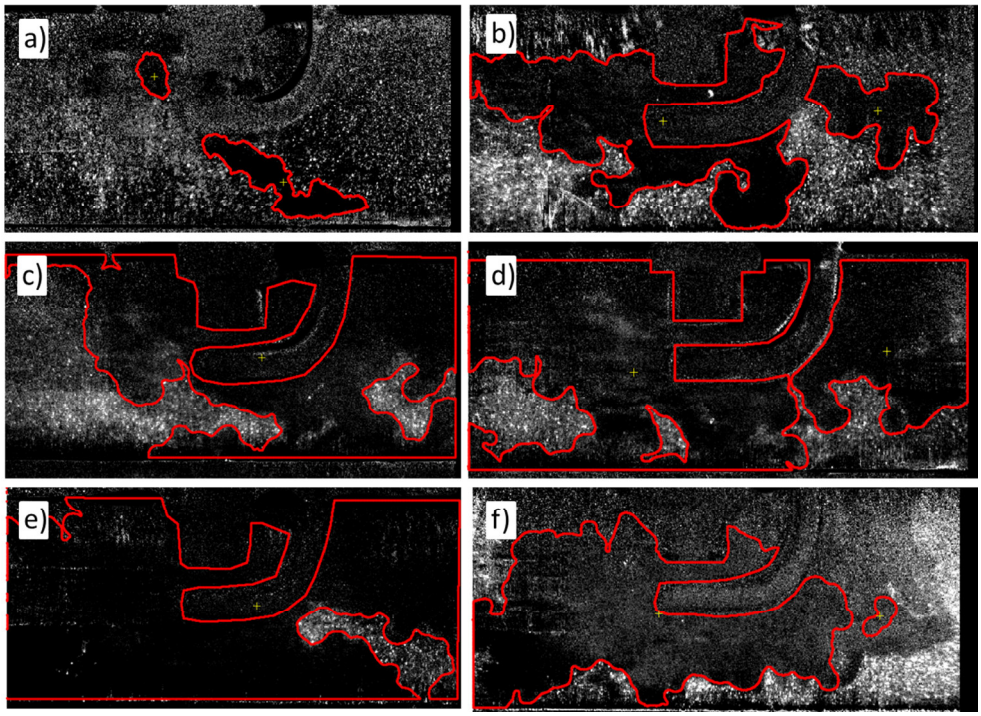

Figure 2-30 Contour recognition problems in TCCIII engine images

Although great care was taken in tuning the contour parameters and verifying the results in some cases overcompensation from reflections or low intensities at the edges of the images due to vignetting falsely caused the burned gas recognition algorithm to detect burned gas. Figure 2-31 shows the probability of burned gas to at different CA. Especially at early CA, effects from erroneous contours can be seen because the overall probability that flames burned through this plane is low.

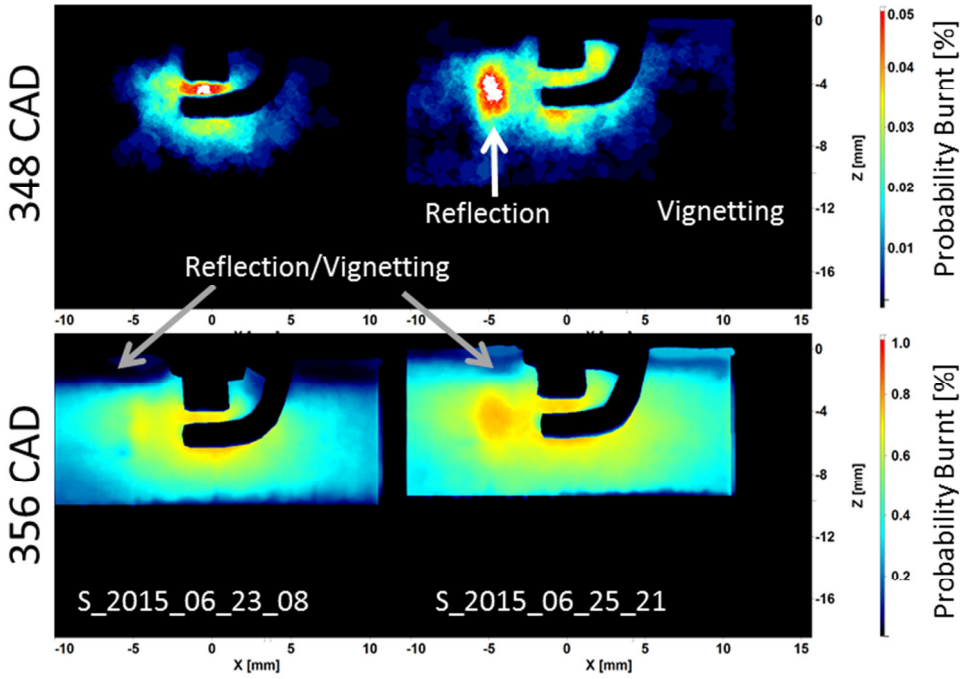

Figure 2-31 Probability plots of burned gas plots for two different CA

2.6.7 Line-of-sight Integrated OH* Chemiluminescence

In flames various species can be used to determine the flame front position (see Figure 1-23). The OH* radical is a tracer for the flame front, which emits chemiluminescence signal in the UV range at 306.4nm [68]. As opposed to other alternative techniques like planer laser-induce fluorescence (PLIF) of the OH molecule, this line-of-sight integrated technique does not require a laser, but directly images the line-of-sight integrated emission from the chemically excited OH* radicals.

The OH* signal was filtered by a combination of optical filters (UG11 and a 330nm short-pass filter) that centers on 307nm with a 25nm wide 10% cut-off to isolate the 306.4nm band from emissions of other major combustion products over 330nm [68].

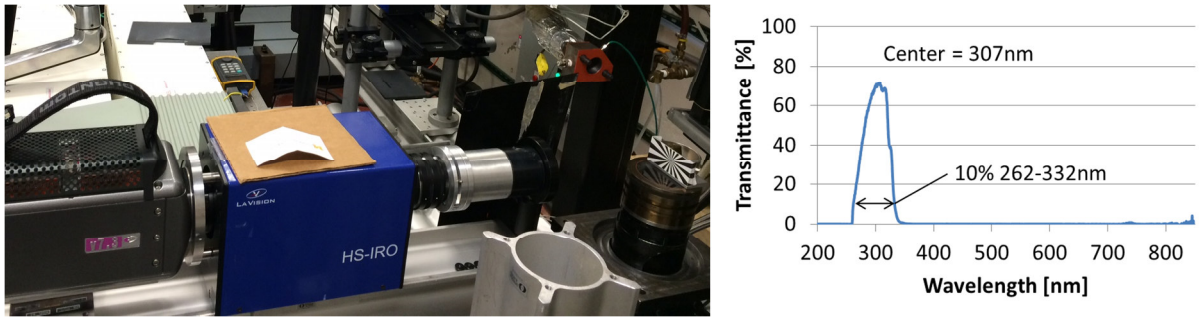

Figure 2-32 OH* Chemiluminescence setup and imaging filter transmittance spectrum

The spatial resolution of the imaging setup is strongly degraded by the high-speed image intensifier. The spatial resolution was quantified with a Siemens star to be about 0.5mm. This is sufficient to serve the purpose in this work of determining the burned gas area and the early flame kernel convection. The area at early CA is important because of the low pressure increase and the insufficient sensitivity of the pressure transducer. Figure 2-33 shows the cylinder derived mass fraction burned curve in orange and the OH* image derived flame kernel radius in [mm]. At 1% burned fraction the flame kernel already extended over the clearance height of 9.56mm. Laminar-to-turbulent flame transition occurs before the pressure is sensitive enough and was determined for cycle by finding the intersection point of the lines fit through the laminar and turbulent regimes in the log burned gas area versus time plot shown in Figure 2-33 [69]. The laminar region was defined from start of ignition to the point of maximum positive curvature. The turbulent regime line was fit from this point to the point of maximum negative curvature. Burned gas area is stagnating towards the end because the flame reaches the limits of the FOV.

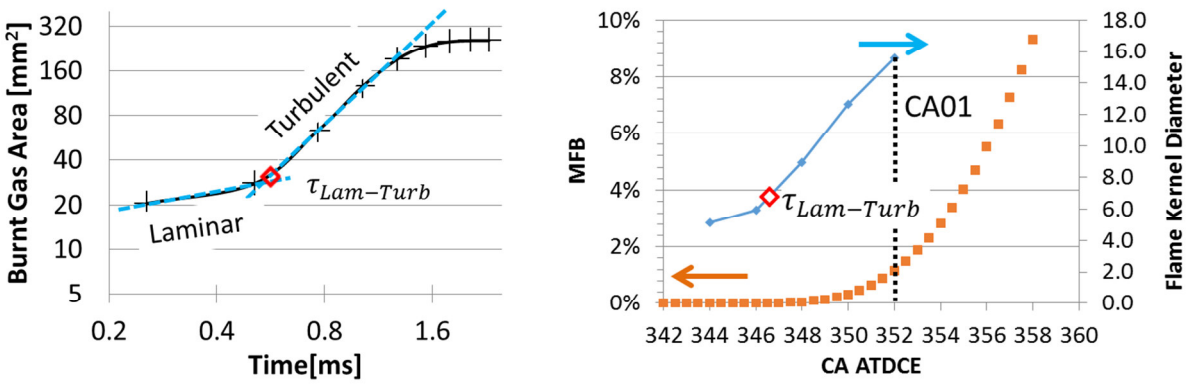

Figure 2-33 Comparison of MFB and OH* derived radius. Laminar to turbulent regime transition point in stoichiometric propane combustion (S_2015_06_18_03).

2.6.8 OH*- Post-Processing Procedure

To account for spatial differences in intensifier efficiencies, all acquired images are first white field corrected and a spatial calibration is applied. Then, a hysteresis threshold algorithm is used to determine the border of the burned gas area. A low threshold is determined by the average value of the maximum values in each cell. The parameterization of this threshold improves capturing the burned gas area region and allows a higher degree of automation.

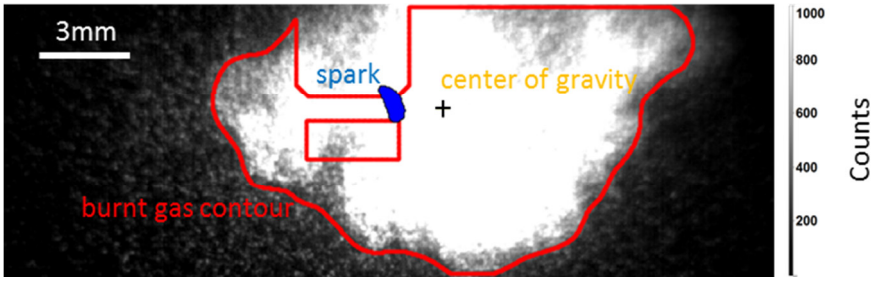

Figure 2-34 Example OH* recognized contour of burned gas (red), its center of gravity (black cross) and spark (blue), stoichiometric propane combustion

The spark area is recognized by setting a threshold at 16000 counts close to the saturation limit of the camera (2^{14} =16383 counts). Also, the center of gravity position, the area, and the eccentricity of the spark plasma channel were extracted.

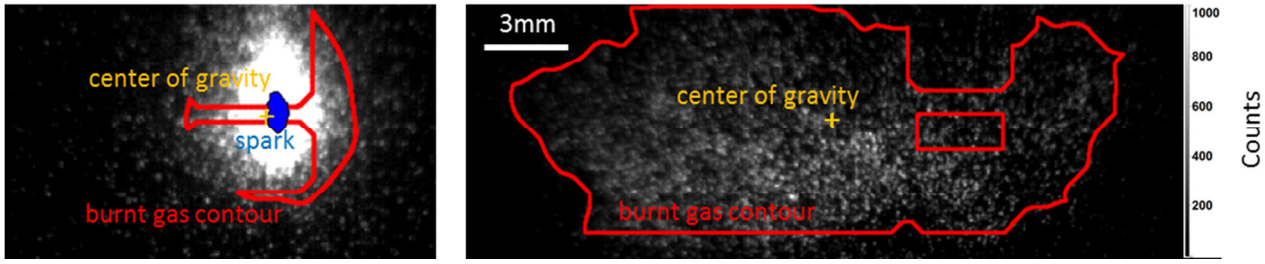

Figure 2-35 Example OH* contour at early spark times (344 CA ATDCE) and at TDC for weak intensity lean methane flames

2.6.9 Toluene Planar Laser Induced Fluorescence (PLIF)

Tracer based PLIF imaging can be used to measure heat transfer and mixing phenomena [68]. In the context of this thesis PLIF is used to determine the effects of temperature stratification on the combustion process.

The LIF technique is based on the principle of electronic excitation (by Laser light) of a particular wave length of the tracer molecule and a subsequent photon emission usually in a longer (red shifted) wave length, which is captured by a detector (camera) [68]. This captured signal is proportional to tracer number density, temperature, and the laser beam intensity.

In the excitation process a molecule is lifted from its ground state to an unstable higher energy state. The energy needed for this process is provided by a photon from the laser beam. Because of the unstable nature of this molecular energy state, the molecule returns to its ground state either by spontaneous emission (the desired fluorescent signal), thermal energy transfer or quenching [70]. The quenching effect depends on the tracer, the gas' density, and the temperature, which complicates achieving quantitative measurements in the cylinder [68, 70]. In this study, toluene and 3-pentanome as temperature sensitive tracers were tested for which a fluorescence signal can be modeled by knowing laser pulse energy and wavelength, number density of the tracer, tracer absorption cross-section, and the fluorescence quantum yield [71].

Due to a strong cross talk of 3-pentanome fluorescence with fluorescence of the silicone oil used as PIV seed particles, toluene had to be used as tracer. Toluene suffers from a strong oxygen quenching effect that reduces signal intensities by an order of magnitude if air is used as bath gas compared to pure N2.

Toluene was added to the heated intake air just after the mixing cross fitting after the air heater to maximize the mixing time and mixture homogeneity. A high-performance liquid chromatography (HPLC) pump was used to control the tracer flow to the engine to yield 0.012g/s, which in the lean cases add-up energy to the system that is equivalent to about 10% of the original lower heating value (LHV). In engine tests and ChemKin flame speed simulations it was verified that adding this amount of tracer does not change combustion behavior if the equivalence ratio was adjusted. The construction of the pump allows additional 7% tracer (for IMAP=40kPa) to be sucked into the intake system when running an IMAP below atmospheric. This extra tracer is already included in the quoted 0.012g/s and all equivalence ratio calculations were updated accordingly. For future tests, it is recommended to add a finer capillary tube than, the one currently in use to eliminate any pressure difference effect on the tracer flow rate.

Toluene molecules were excited with a quadrupled Nd:YAG 266nm pulsed UV laser (Spectra Physics Quanta-Ray INDI) with a shot energy of about 14mJ of energy available in the combustion chamber (as opposed to laser out 20mJ). Three cylindrical UV grade lenses were used to create an 18mm wide light sheet (details on page 154).

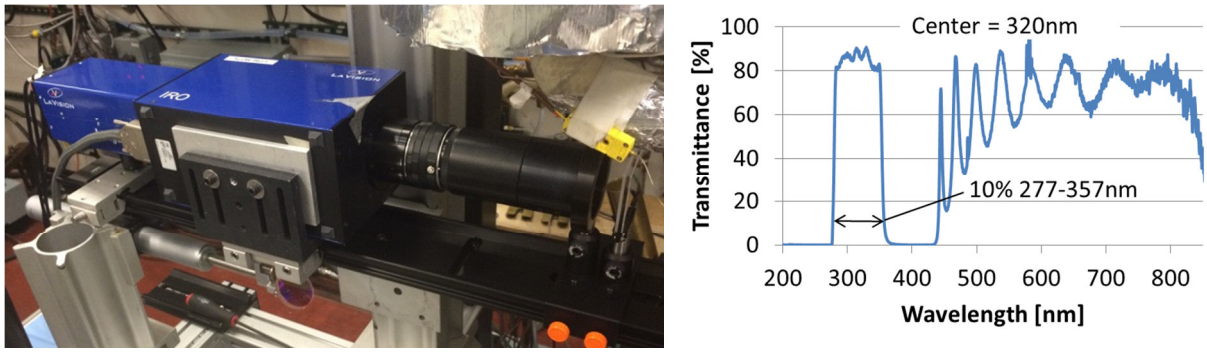

Figure 2-36 Toluene PLIF setup and transmittance profile of imaging filter combination

The fluorescence signal intensified by a LaVision IRO low speed intensifier (at 6.7 which is equals to about 5 [counts/photo electron]) was imaged with a LaVision "Imager Intense" CCD camera. A 100mm Halle UV lens (f/# = 2.0) in combination with 30mm extension tubes were used to achieve a magnification of 0.054mm/pix. In order to maximize the Toluene signal to background noise and avoid laser light reflections, two 275nm (Asahi Spectra ZUL0275) edge long pass and one 350nm (Asahi Spectra ZUS0350) short pass filters were used. A measured

transmittance spectrum of the filter combination can be found in Figure 2-36 (right). All tests on the TCC engine performed during June 2015 include PLIF images. A combination of low signal levels, caused by small tracer amount(to minimize impact on combustion) and oxygen quenching, and increased background, due to seed oil fluorescence, results in low signal to noise ratio (for details see [53]). Thus, further processing is not proceeded by the author and no further results on PLIF will be presented in this thesis.

2.6.10 Schlieren Imaging

Schlieren imaging relies on the principles of visualizing refractive index changes in a measurement volume. It is a very sensitive line-of-sight technique that was originally used to ensure the optical quality of imaging lenses [72]. Schlieren imaging is mostly used for qualitative imaging of mixing processes, thermal boundary layer phenomena, and shock waves [72]. In the context of this thesis, it is used to observe outwardly propagating flames in the University of Orléans combustion vessel in high temporal and spatial resolution. For this a combination of two Z-type 2-mirror Schlieren system was imaged to track the volumetric flame propagation and convection.

The Schlieren Z-type setup in general consists of a point light source, two parabolic mirrors, a knife edge, and an imaging device (see Figure 2-37). In this thesis in particular, a green high power LED (HARDsoft IL-106X, λ_{Center} =528nm 40nm FWHM) in continuous wave (CW) mode with a luminous flux of 2100lm in combination with a 1mm aperture was used as light source. A smaller aperture would have improved depth of focus, but also decreased the intensity of the images. Two identical parabolic 864mm focal length first surface aluminum mirrors (Edmund optics R5000193218-15105) were used to collimate and refocus the light. For this purpose, the point light source needs to be located in the focal point of the first parabolic mirror. The combustion vessel is located at the indicated test region of collimated light shown in Figure 2-37. A dot shaped filter matrix is located at the position where the knife edge would be located in a traditional Schlieren setup. A dot diameter of about 0.9mm gave here the highest image contrast between burned and unburned gas, while still allowing enough light to pass. In

microscopy, this kind of filter refers to dark-field imaging, which blocks out the DC component of the light and only passes the higher spatial frequency components[72]. The filter dot also has the advantage over the traditional knife edge of resolving gradients in both directions. The sensitivity of the system increases with the focal length of the mirrors and with an increase of blocked out light by the knife edge [72]. While in theory no imaging lens is needed to take the Schlieren image on a camera chip, in the used setup (Figure 5-2) two lenses for each Schlieren channel were used to project a sharp image with the desired magnification at the needed position on the camera chip.

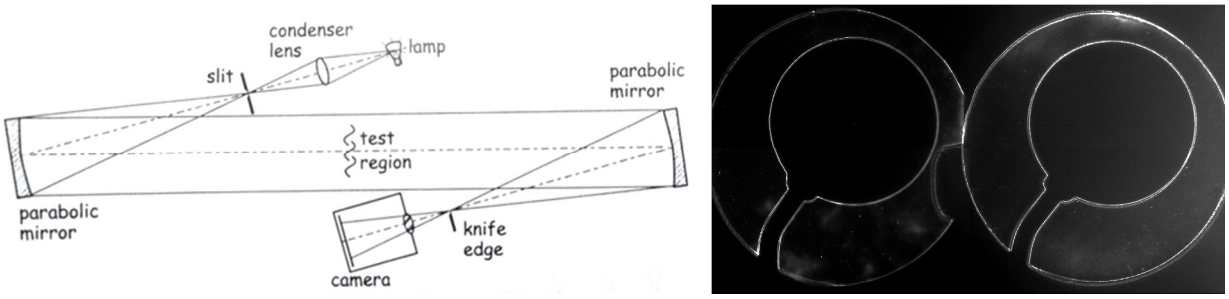

Figure 2-37 Schematic of Z-type Schlieren setup [72, 73]; Spatial calibration target for dual-pass Schlieren system.

As already afore mentioned the Schlieren technique is a line-of-sight integrated technique to image changes in the refractive index (n=speed of light in vacuum/speed of light in medium), where the refractive index n is proportional to the gas density ρ [74].

$$n - 1 \sim \rho$$

The angle with which the beam is deflected by a temperature change and causes a deviation at the Schlieren filter matrix. In this thesis the change in temperature of the outwardly propagating flame changed the refractive index as well the change of molecules on the inside of the flame. On the right side of Figure 2-37 the edge of the calibration marble (diameter 42.08mm) can be seen as bright high intensity line, because of the steep gradient in change of refractive index.

Figure 2-38 shows an example of both the front and side view Schlieren channels. From both images the approximate flame volume can be determined when an elliptical flame shape is assumed, according the procedure used by [17].

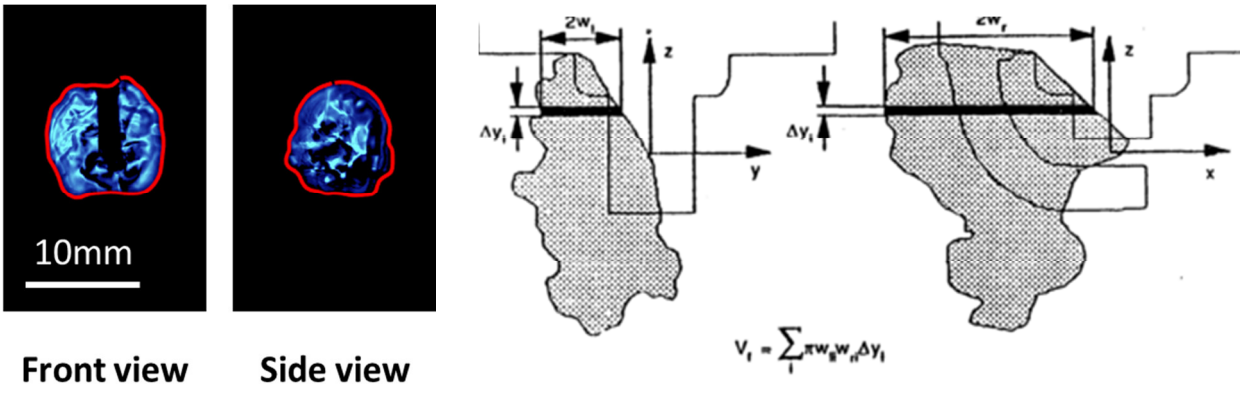

Figure 2-38 Recognized burned gas contours on Schlieren images, front view and side view of early flame Kernel (left); Volume reconstruction assuming elliptical flame shape (right; figure taken from [17])

From all Schlieren images, the contour information has been extracted to be able to quantify the flow field impact on the early flame kernel phase (for details see page 147 ff.). In order to recognize the contours reliably for hundreds of images of several hundred tests, this contour recognition also had to be automated and tested for accuracy and robustness. In contrast to PIV images, in the Schlieren image processing only backwards oriented time filters have been used to preserve the outer flame contour of the image of interest. In the raw image (Figure 2-39), a flame and the electrode are visible. A 21 image long backwards oriented subtract minimum filter was used to remove the spark electrodes or dirt spots from the images (see two left images in Figure 2-39). However, this step creates holes at the positions where the electrodes are "piercing" the projected flame surface. During most of combustion these holes can be filled by a regular dilation function. When the electrode shade covers an excessively big stretch of the flame contour, the subtract time filter step can create a big hole in the flame contour that cannot be filled with dilation functions (3rd image from left, later time than 2nd image). In order to still achieve meaningful contours in these images a backwards oriented maximum time filter can be applied to the images. Here, a 21 image long filter is chosen to thicken even slowly expanding flame fronts. This filter sets each pixel of the image of interest to

the highest intensity value of the previous 21 images. Here, it is appropriate to use this filter because the flame speeds are greater than flow convection velocities and as such are continuously expanding in all directions. These thick contours allow to fill the electrode gap again, and to find the flame contour in a robust fashion.

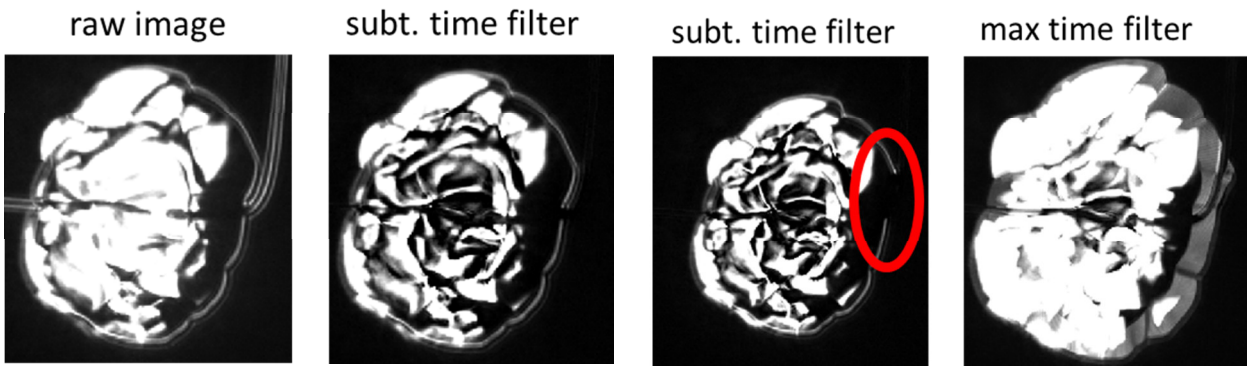

Figure 2-39 Processing steps of Schlieren images for robust contour recognition

For the contour recognition a code developed by Benedicte Galmiche from the University of Orléans has been largely rewritten and adapted to recognize electrode contours and accommodate the volumetric reconstruction from the simultaneously imaged front and side views. Figure 2-40 shows an image time series of an outwardly expanding lean Methane flame. On the left side, raw images are shown. 2ms after ignition, it is already visible that the flame kernel is distorted from the surrounding flow and it is not spherically expanding. On the right side, the red flame contours are overlaid on pre-processed images. The thickened edges from the time series filter and the removed low spatial frequency component in the center region of the flame are clearly visible especially at later times.

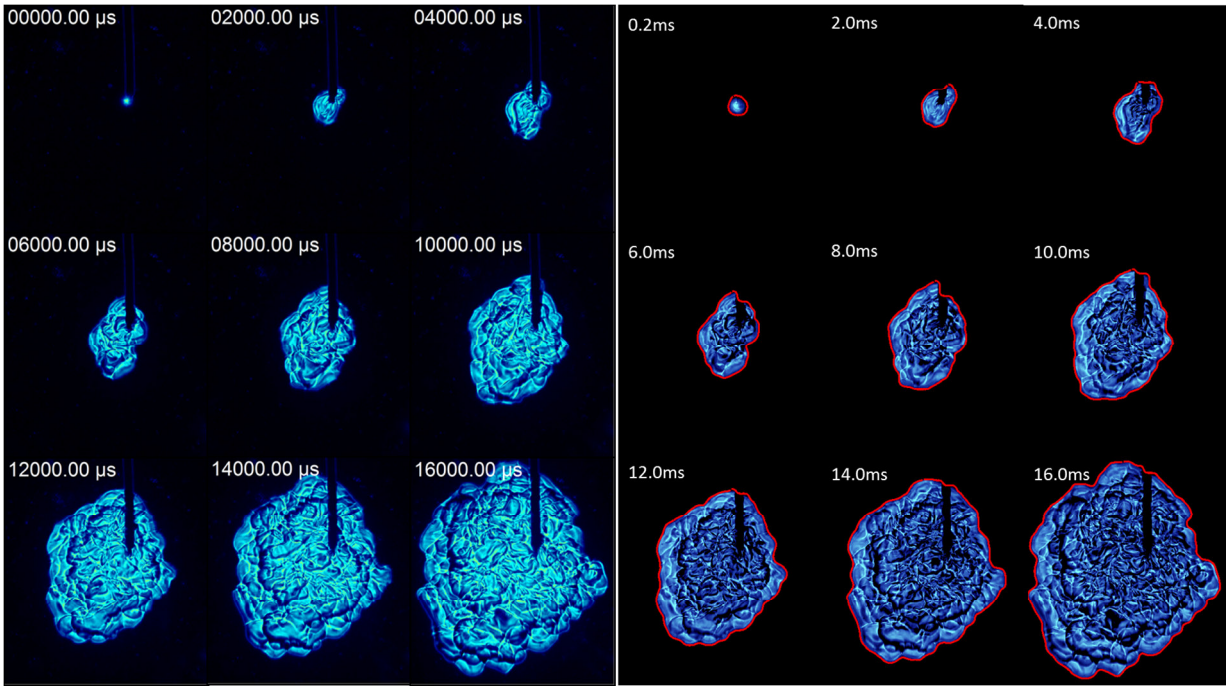

Figure 2-40 Time sequence of Schlieren front view combustion images. left raw images, right pre-processed images with recognized contour in red

Besides utilizing the flame contour and the burned gas volume information, it was also attempted to utilize the internal structure information. To segment the images, a watershed algorithm was used to identify the contours of each individual cellular structure (see Figure 2-41). The algorithm tends to create too many fine segments that are not visible by eye from images. An attempt to reduce the intensity dynamic range to match the user's eyes by binning intensities worked in some cases, but not in a reliable fashion. Additionally the interpretation of these structures is difficult due to the ambiguity of the line-of-sight integration through the flame volume. For this reason, only flame contour information is used in the following chapters.

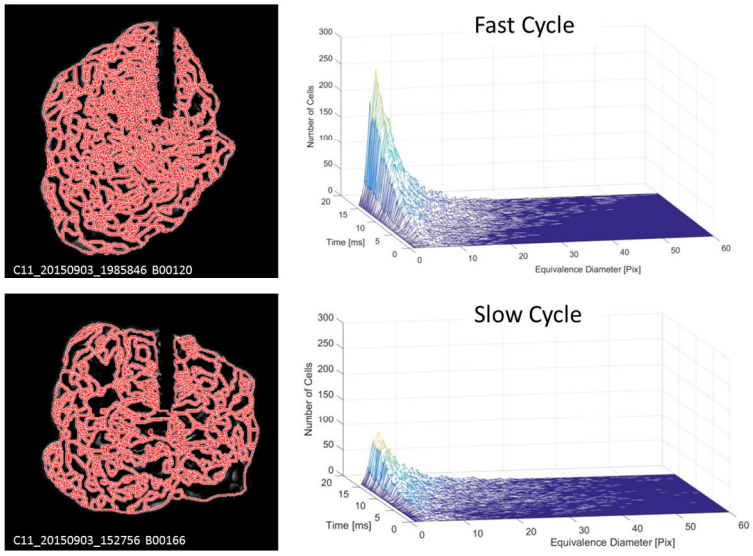

Figure 2-41 Extraction of Schlieren flame structure information

2.6.11 Burned Gas Volume Variability – A Comparison Pressure Based Parameters vs. Image Derived Volume

In the experiments covered in this thesis, certain parameters are measured by multiple diagnostic techniques simultaneously. In all combustion experiments, a pressure transducer and a form of optical imaging system are used to track flame growth. The optical technique is primarily important for the early kernel phase at which pressure transducers are not sensitive enough to resolve small pressure increases. Pressure information becomes important when the flame exceeds the field of view of the images. To verify the consistency and data quality between both techniques the combustion variability as indicated by COV of burned gas volume is compared in the overlap region in which both techniques are sensitive.

A two-zone model according to Heywood's textbook is used for the burnt gas volume estimation from the pressure traces. The unburned and burned gas temperatures are calculated from as function of polytropic compression by the pressure increase. This way of calculating the burned gas temperature was necessary, as the equation used in [4] led to unphysical temperatures in case of the combustion vessel, but will result in an overestimation of the burned gas temperature.

$$\overline{T_u} = T_0 \left(\frac{p}{p_0}\right)^{\frac{\gamma_u - 1}{\gamma_u}} \;\&\; T_b = T_{ad} \left(\frac{p}{p_0}\right)^{\frac{\gamma_b - 1}{\gamma_b}} \quad \text{(26a) and (26b)}$$

From this and the thermal properties from the Chemkin chemical kinetics software, the burned mass fraction could be calculated as follows:

$$\chi_b = \frac{V(p-p_0)+(\gamma_b-\gamma_u)\, m\, c_{v,u}(\overline{T_u}-T_0)}{m\left((\gamma_b-1)(h_{f,u}-h_{f,b})+(\gamma_b-\gamma_u)c_{p,u}\overline{T_u}\right)} \quad (27)$$

Mass burned fraction and volume burned fraction are related over following equation by the ratio of the burned and unburned gas densities.

$$y_b = \frac{1}{\frac{\rho_b}{\rho_u}\left(\frac{1}{\chi_b}-1\right)+1} = \frac{1}{\frac{R_u T_u}{R_b T_b}\left(\frac{1}{\chi_b}-1\right)+1} \quad (28)$$

Typical burned to unburned gas density ratios are $\frac{\rho_b}{\rho_u} \approx 4$ in the engine, but $\frac{\rho_b}{\rho_u} \approx 8$ in the combustion vessel due to the low initial gas temperature.

In Figure 2-42 the pressure and image variability are compared over the mean flame volume, as measure of combustion progress. There is good agreement between the different techniques which gives overall confidence that the measurements are of high quality, correctly processed and accurate. At low burn volumes (= early times) the pressure measurement is insensitive and the mean volume is small, resulting in an increased and noisy COV value. To calculate the volume from the line-of-sight projection of the OH* measurement a disc shaped flame was assumed with the disc height being the piston clearance at the respective CA.

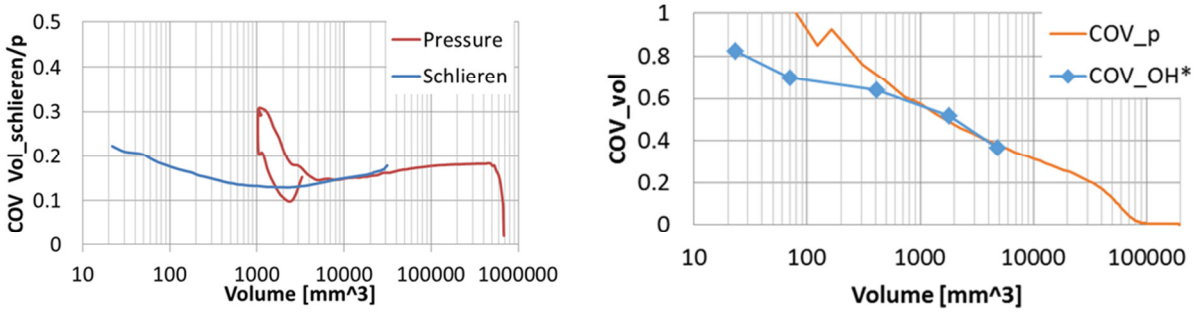

Figure 2-42 Comparison of Burned Gas Volume Variability as a function of mean flame volume. Left: Combustion COV in the combustion vessel of pressure and Schlieren image derived volume variability agree well in the overlap region from 5000-30000mm^3. Right: Combustion COV in the TCC-III engine of pressure derived heat release and OH* derived volume agree from 500-5000 mm^3.

CHAPTER 3 ENGINE FLOW VARIABILITY

Flow and turbulence conditions influence combustion in every engine. In this chapter the flow field evolution is shown throughout the cycle, and how the flow velocities scale with engine speed and load. The differences from motored to fired conditions are shown first in the pre-ignition cold flow and then quantitatively analyzed in a length and time-scale analysis.

3.1 Experimental Approach

In order to assess the properties of the bulk flow in the TCC engine the velocity in the cylinder was measured with time-resolved PIV with 5CAD resolution, in separate runs in four different cutting planes. The in-cylinder flow measurements, with and without combustion, were conducted throughout the engine cycle.

First, the vector fields at an engine speed of 1300RPM and 40kPa IMAP, here referred to as the motored baseline condition will be discussed. Then all three motored conditions will be compared to each other by normalizing the ensemble average flow and RMS data to mean piston speed, in order to show the sensitivity of the flow to changes in engine speed and load. Then, a stable Φ=1.0 fired case will be discussed and the flow field's similarities and differences to the motored flow will be shown.

3.1.1 Optical Setup

The PIV measurements were recorded successively in the four planes shown in Fig. 4, every 5 CAD, and for at least 235 consecutive cycles per test. The field of view (FOV) is restricted by the piston window to approximately the center 70mm for both vertical and horizontal cutting planes. In both z=-5mm and z=-30mm planes, the light sheet is brought into the cylinder from the positive x-direction. Thus, during intake stroke, a major part of the FOV is blocked by the intake valve and its shadow for the z=-5mm images. The vertical cutting planes have a FOV from piston to cylinder head with an approximate width of just below 70mm. Images are recorded using a monochrome high-speed camera (Vision Research, Phantom v1610) with a 1280x800

pixel sensor and 12-bit dynamic range. Silicone-oil droplets (1µm) are added to the intake air and illuminated by a high-repetition-rate dual-cavity frequency doubled Nd:YLF laser (Darwin Duo, Quantronix). The light sheet thickness is 2.0 – 2.4mm in the different cutting planes adjusted based on the in-plane resolution set by the 210mm Nikon Micro-Nikkor ED lens with an aperture of f/5.6 and the distance to the imaging plane.

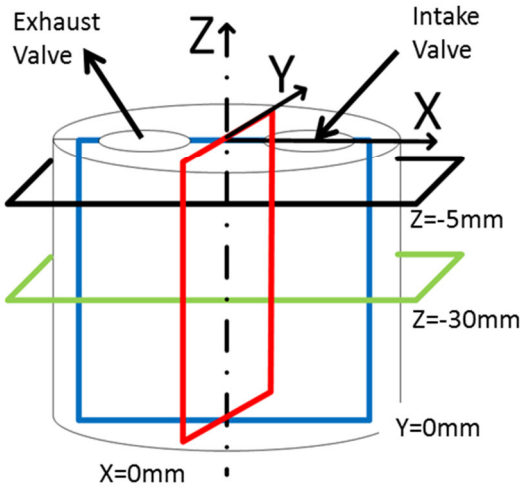

Figure 3-1: Laser-sheet locations and definition of coordinates. All laser sheets and fields-of-view are truncated by the 70mm diameter piston window.

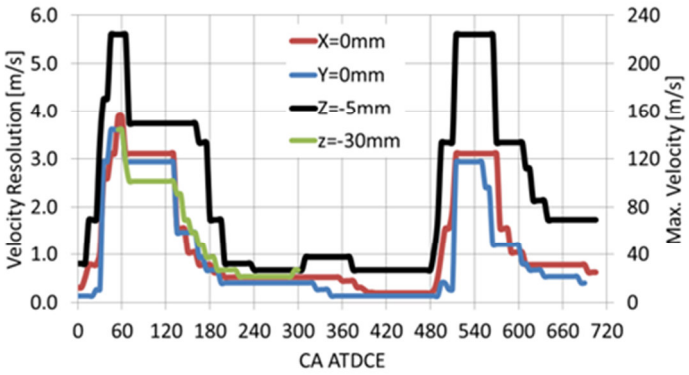

Figure 3-2: PIV velocity resolution based on 0.2 pixel velocity resolution and maximum velocity

Image processing begins by remapping the raw images to eliminate non-linear distortions caused by the cylinder and thick piston window. A 3rd-order polynomial fit is used for all data recorded in a vertical plane to account for the distortions caused by the quartz liner. A linear fit is sufficient to map the horizontal planes that are imaged through the flat piston window. Then a sliding minimum intensity subtraction is performed to reduce reflections from cylinder head, valve edges and spark plug. All vector fields are calculated using a commercial PIV code (DaVis 8.x, LaVision) employing a decreasing interrogation window size (1x 128x128pixel, 50% overlap then 2x 32x32 Pixel, 50% overlap). The final interrogation window spot size is 2.5 to 2.8mm with a vector separation of 1.25-1.4mm. The percentage of first-choice vectors of the

experimental data shown here is >98%, meaning that less than 2% of the vectors of the instantaneous flow fields have been of lower than 1st choice or have been interpolated.

The velocity dynamic range of PIV is limited to roughly 40:1. The upper limit is defined by a maximum particle image displacement of 8 pixels (one quarter of the interrogation window) [75] and lower limit of 0.2 pixels (sub-pixel displacement detection) is based on a previous analysis performed under optical engine conditions [76, 77]. To make best use of this velocity dynamic range, the laser-pulse separation, dt, is adjusted on a per CAD basis during the cycle [78]. Here, dt ranged from 3µs during the intake and exhaust strokes when velocities are high, to 80µs around TDC compression when velocities are lowest. For the Z= -5mm plane, out-of-plane velocities are very high and the laser pulse separation time dt needs to be shortened accordingly to avoid out-of-plane particle-pair losses. Figure 3-2 shows the velocity resolution and maximum velocity as a function of crank angle based on the 0.2 pixel detection limit and 8-pixel maximum, respectively. Figure 3-2 can then be used to estimate the experimental error, which is important when making quantitative comparisons with simulation data.

3.2 Motored Flow in Various Planes at 1300RPM 40kPa

In this comparison the flow fields at several discrete crank angles during intake and compression strokes are examined and discussed. Data is acquired every 5CAD throughout the entire engine cycle.

3.2.1 Evolution of Mean Flow Throughout Intake and Compression Strokes

As illustrated in Figure 3-3, at 60CAD ATDCE the intake valve is still in the process of opening and air is streaming at high velocities into the cylinder, while the piston is moving downward. In plane Y=0mm, the jet streaming through the valve gap is joining with the high velocity flow that is deflected by the piston just beneath the intake valve. This creates a vortex at the lower left side of the FOV. The air at the cylinder head is entrained by the jet and is flowing towards the intake valve. In the x=0mm plane, two counter rotating vortices are formed where in the center the flow is again deflected upwards from the piston and joins the intake jet. The air by the cylinder head is again entrained by the high jet velocities and is streaming towards the center of

the cylinder. The horizontal plane at Z=-30mm has just been cleared by the piston. Here, the effect of the flow coming down the cylinder wall and being redirected by the piston is the most visible. The flow velocity where the intake jet impinges on the piston in this plane is zero, and its magnitude increases as it streams along the piston top.

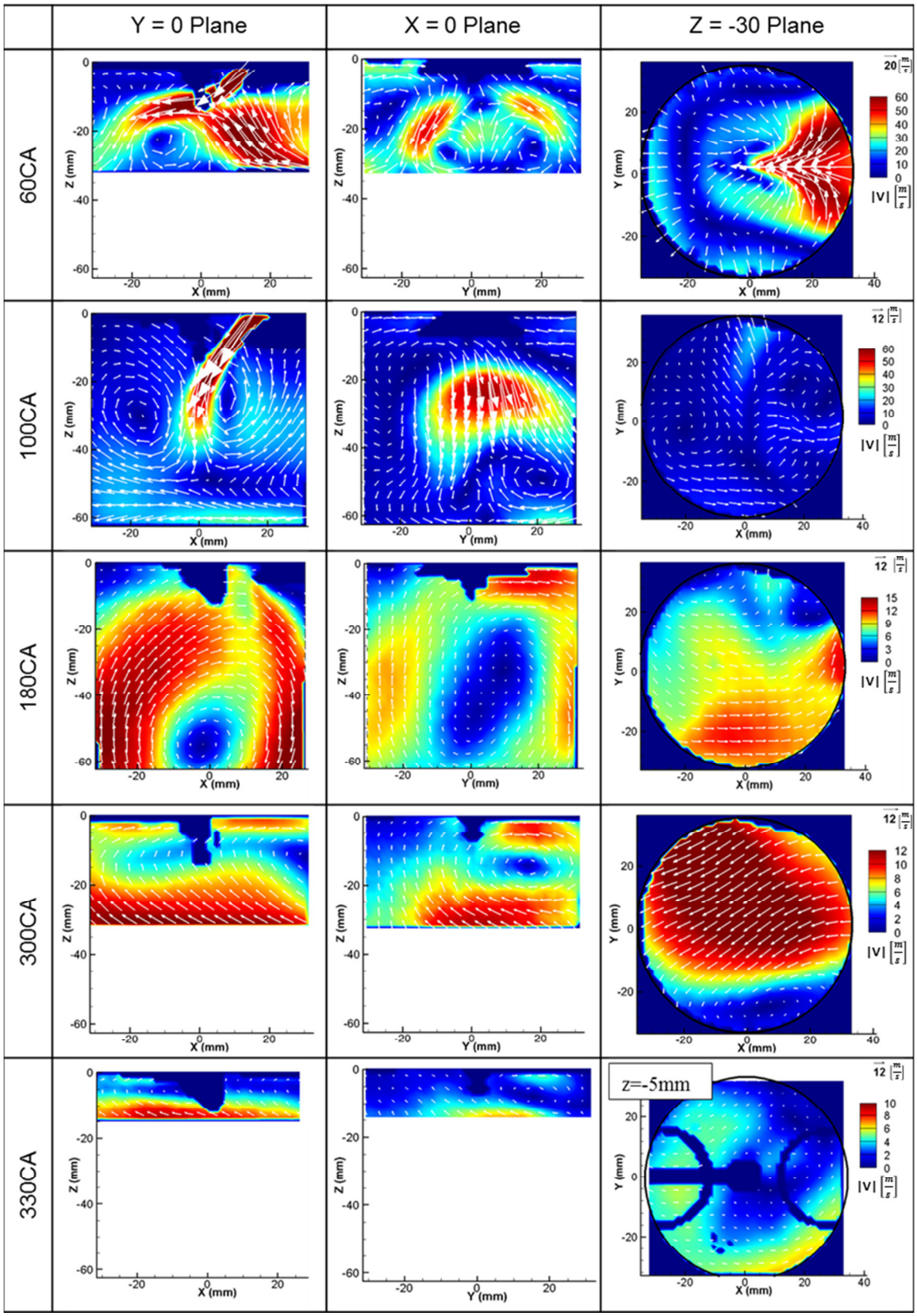

Figure 3-3 Ensemble average flow field evolution at 1300RPM 40kPa motored in three planes

At 100CAD, the piston is still moving downward but decelerating from its maximum velocity and the valve is about to approach its peak lift at 114CAD. The intake jet now has more space to develop and penetrates about 40mm in the cylinder. In the Y=0mm plane there are two entrainment vortices, one on either side of the jet. The flow by the cylinder head continues to flow towards the intake valve in both vertical planes. Below the height at which the jet penetrates the x=0mm plane, the two counter rotating vortices still exist. The jet shape is not perfectly symmetric because of the cylinder head flow box design. The flow magnitude in the horizontal plane is lower than in any of the vertical planes. The particular flow structures are finer than in the vertical planes and are consistent between different data sets at this condition. There is again a region of zero in-plane velocity where the edge of the jet that is facing the intake valve is cutting through the plane. Some indications on the clockwise swirl bulk motion can be seen on the perimeter of the FOV.

Both vertical velocity fields have been cropped at the bottom at 180CAD ATDCE in order to fit more flow fields at different CA on one sheet. At bottom dead center (BDC), in both vertical planes a clockwise bulk tumble motion has established, which implies that the tumble core in the 3D flow field is under some angle. Flow velocities in the Y=0mm plane are higher and the tumble core is better defined compared to X=0mm. The counter clockwise swirl is now more prominent, but no clear swirl center is visible in this plane at this CA.

During the compression stroke, the flow is compressed by the upwards moving piston. Dissipation reduces the flow velocities, while close to the piston top, the z-velocity component is increased by the upwards moving piston. The tumble centers are moving in both vertical planes to the top right corners. Velocities close to the cylinder head are lower compared to the piston. The influence of the piston on the flow field in the horizontal plane at this CA is prominent.

Towards TDC compression, the flow field structures in both vertical planes essentially do not change, except that their magnitudes keep decreasing. The swirl plane shown at this CAD, cuts through the spark plug gap at about a 5mm distance from the cylinder head. A counter

clockwise rotation persists until the end of the compression stroke, creating an average velocity of less than 3m/s.

3.2.2 Evolution of RMS Throughout Intake and Compression Stroke

Similar to the mean velocity fields, the magnitude of the RMS (see Figure 3-4) is highest during the early intake period and it decreases as the flow becomes more organized, but then close to TDC when the flow is being compressed the RMS levels increase again.

RMS levels at 60CAD in the Y=0mm plane are at 30m/s almost throughout the FOV, except in the center of the jet and the region to the right where the air was deflected from the cylinder. Highest RMS magnitudes in X=0mm are in the centers of the vortices, which indicates that the flow is changing there the most from cycle-to-cycle. At the piston center, RMS levels are the highest in the horizontal plane.

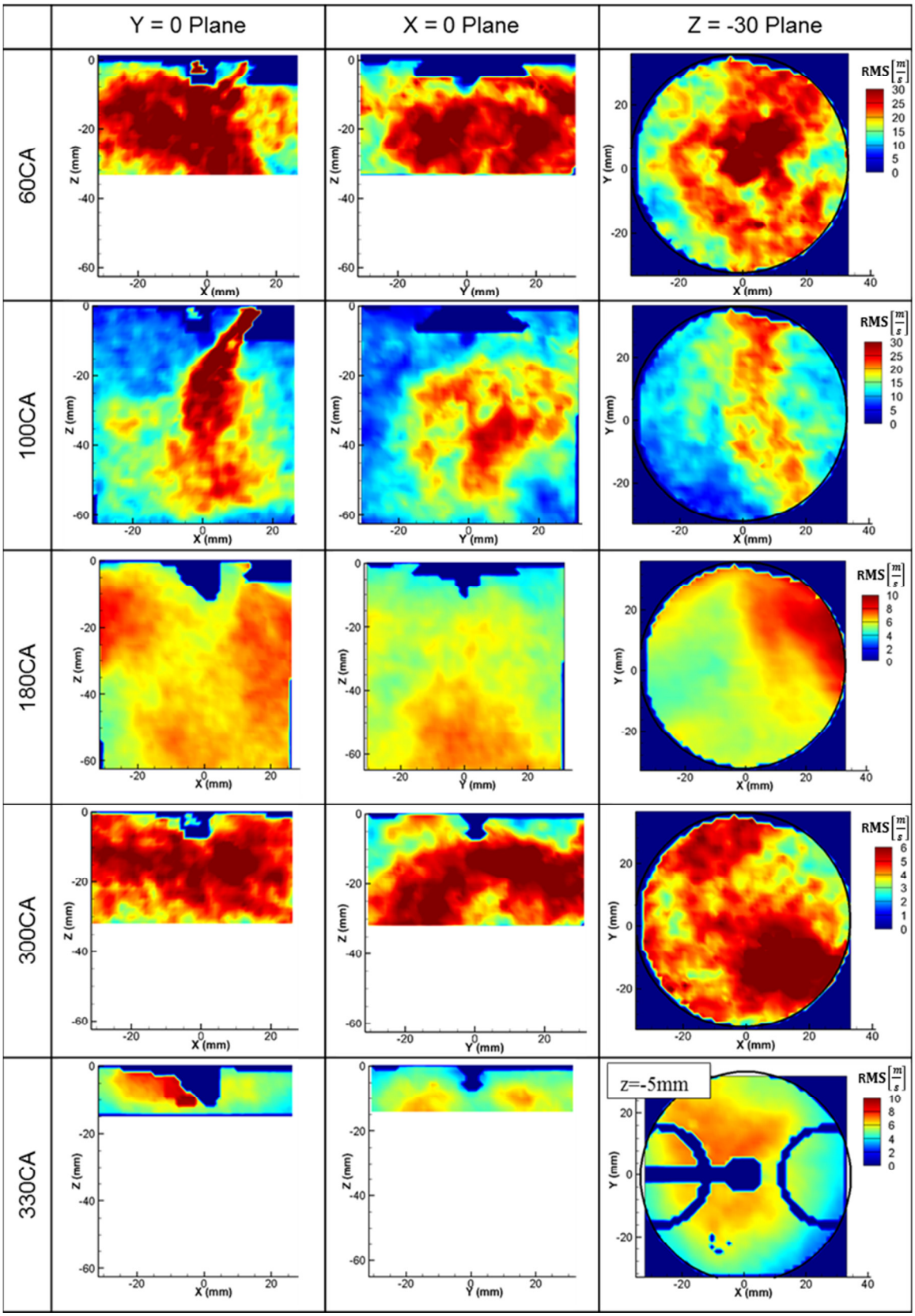

Figure 3-4 Ensemble RMS field evolution at 1300RPM 40kPa motored in three planes

During mid-intake stroke, variability is highest in the jet regions. In the Y=0mm plane, the variability in the jet center is again lower than on its edges, which are regions of high shear. Note that the jet is unstable so that these edges experience higher fluctuations. Below, the jet RMS magnitude is increased because the flow changes direction. In the other vertical plane (X=0mm plane) the jet shows again the highest variability together with the higher velocity region between both counter rotating vortices. In the horizontal plane, variability is increased in areas where the jet is crossing the Z=-30mm plane, creating a band of increased RMS values of about 20 to 25m/s.

At BDC, RMS magnitudes decreased, and high variability regions can mostly be found in tumble centers and low velocity regions in the horizontal cut plane. During compression at 300CAD, RMS levels stay about constant while low mean flow velocity regions continue to show higher RMS levels.

At 330CAD, RMS values increased in the Y=0mm plane to about 6-8m/s in vicinity of the spark plug indicating that in this region the flow is different from cycle-to-cycle, considering that there are only low mean flow velocities. Variability in X=0 stays at the same level of 5m/s in the spark plug region, and increases in the tumble center. In the swirl plane RMS values are on the order of 7m/s by the spark plug, confirming that the flow field around the spark plug is likely to deviate from the mean from cycle-to-cycle at the point of ignition.

3.2.3 Scaling of the Flow at Different Engine Speeds and I MAP

In order to see the influence of engine speed and load transients on the ensemble average flow field and the RMS, PIV measurements at engine speeds of 800 and 1300RPM, and 40 and 95kPa IMAP are performed (Figure 3-5, Figure 3-6). In-cylinder turbulence is expected to scale with engine speed [79], while no big changes in the flow field are expected from throttling the engine. The intake jet has lower momentum, but also penetrates a less dense environment in throttled cases. In order to compare results better and confirm the scaling of turbulence with engine speed, the flow and the RMS fields have been normalized by mean piston speed (MPS).

At 100CAD ATDCE (Figure 3-5) flow fields at all three operating conditions look similar and mean flow magnitudes are comparable. The unthrottled cases show 20% increased magnitudes

in the bottom left corner in the Y=0mm plane as well as in the high velocity regions in the horizontal plane. RMS levels in the 40kPa case in the Y=0mm plane are increased in the jet but lower in the region below it. RMS levels in the horizontal plane are lower for the 40kPa case but the RMS distribution is the same compared to the 95kPa cases. During the intake stroke mean and RMS magnitudes scale well with the engine speed while lower IMAP reduces both in the entrainment regions, but not in the jet penetration in the Y=0 plane.

In the compression stroke at 260CAD (Figure 3-6, Figure 3-7) flow differences in the flow fields become bigger between different operating conditions. Both 1300RPM 40kPa and 800RPM 95kPa cases show similar structures in mean and RMS fields, with some features slightly shifted, but the magnitudes at lower engine speed are smaller in all planes, both for RMS and mean velocities. At this crank angle, velocity magnitudes are comparable for the 1300RPM cases, but the flow fields seem to be shifted by approximately 45deg in counter-clockwise direction from 40 to 95kPa, as indicated by the rotation of the low velocity regions in both horizontal planes (Z=-5mm, Z=-30mm). Interesting to note here is the wake in the tumble flow caused by the spark plug in the Z=-5mm plane. In this area, mean velocity is reduced by about a factor of two while RMS is about doubled compared to the unperturbed flow (Figure 3-7).

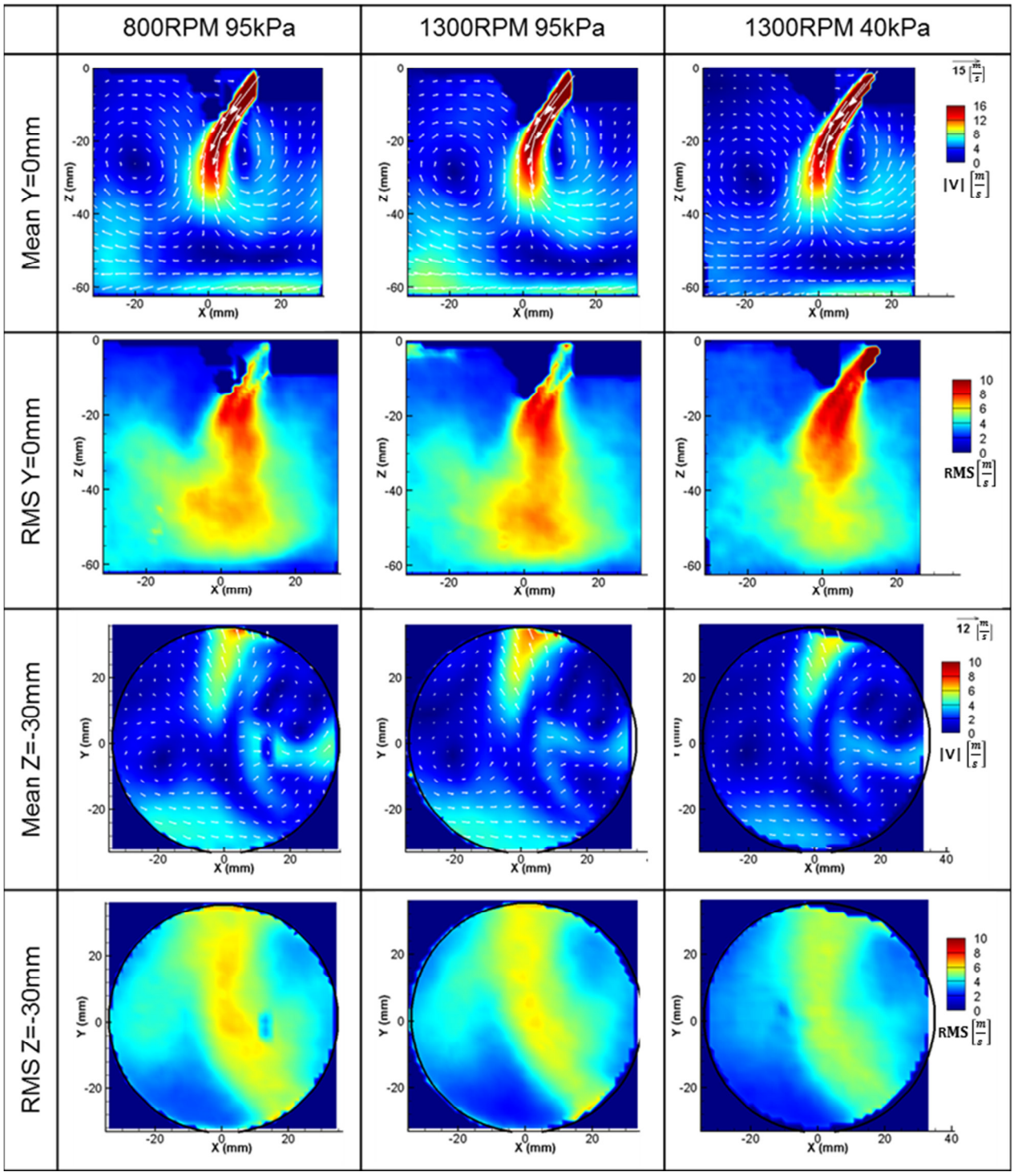

Figure 3-5 Mean and RMS velocities normalized by piston speed for three operation conditions at 100CAD ATDCE

At 300CAD ATDCE (Figure 3-7) 1300RPM 40kPa has the highest mean flow velocities. In the Z=-5mm plane the 1300RPM 95kPa flow field shows different velocity magnitude distributions and

shows increased RMS values. The wake regions in the horizontal plane continue to be at the same angle as at 260CAD ATDCE.

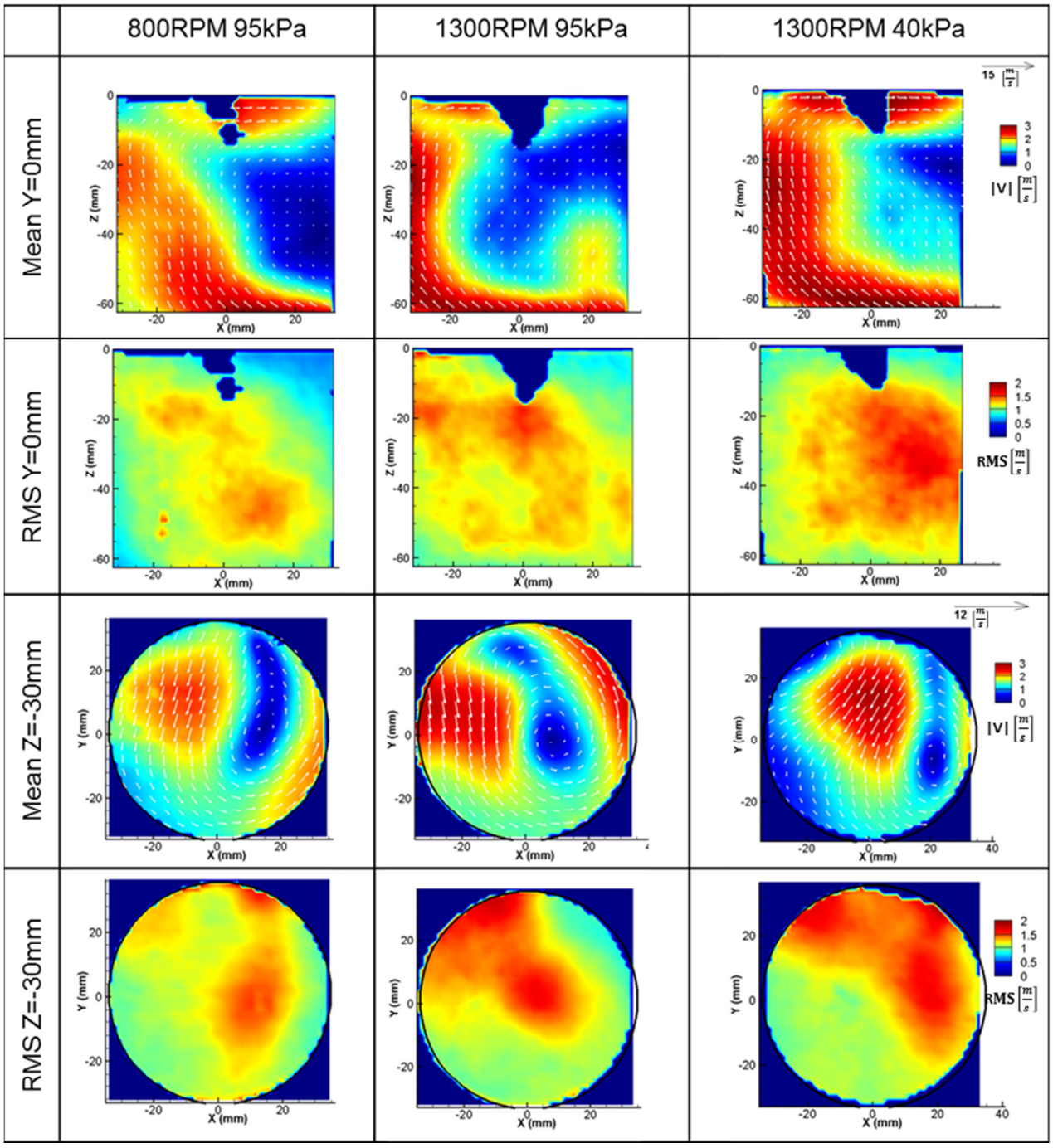

Figure 3-6 Mean and RMS velocities normalized by piston speed for three operation conditions at 260CAD ATDCE

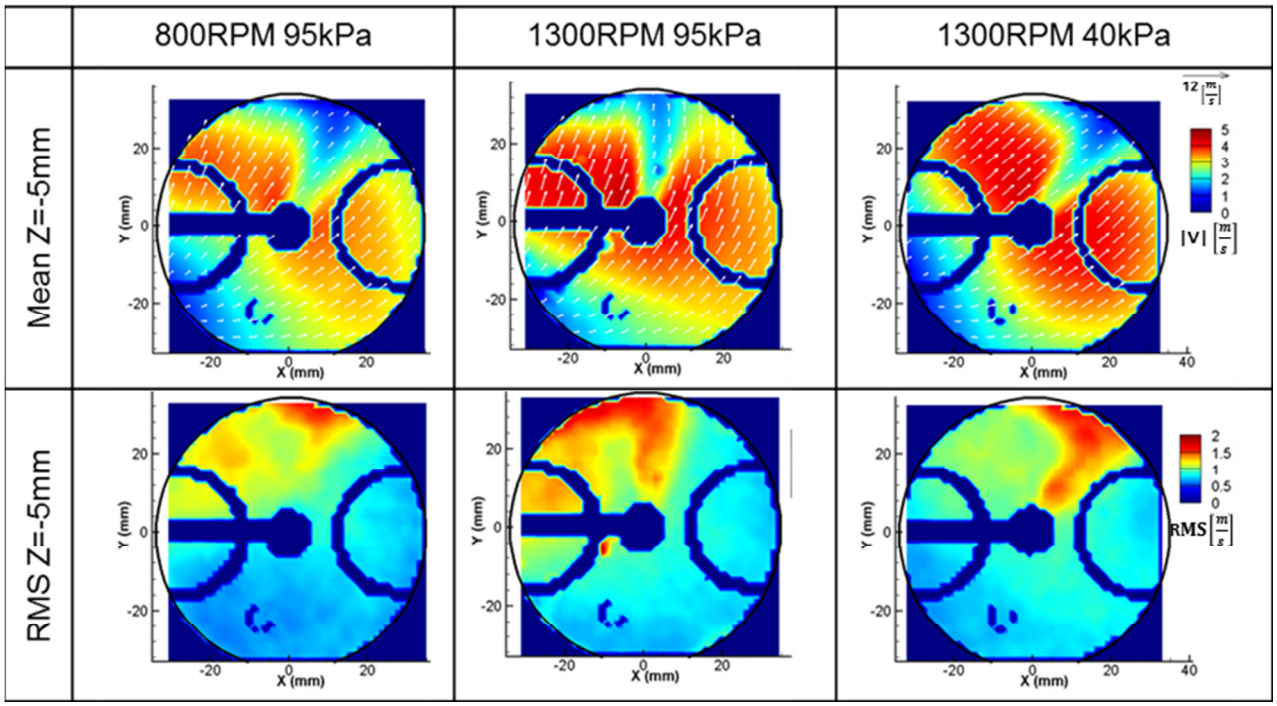

Figure 3-7 Mean and RMS velocities normalized by piston speed for three operation conditions at 260CAD ATDCE

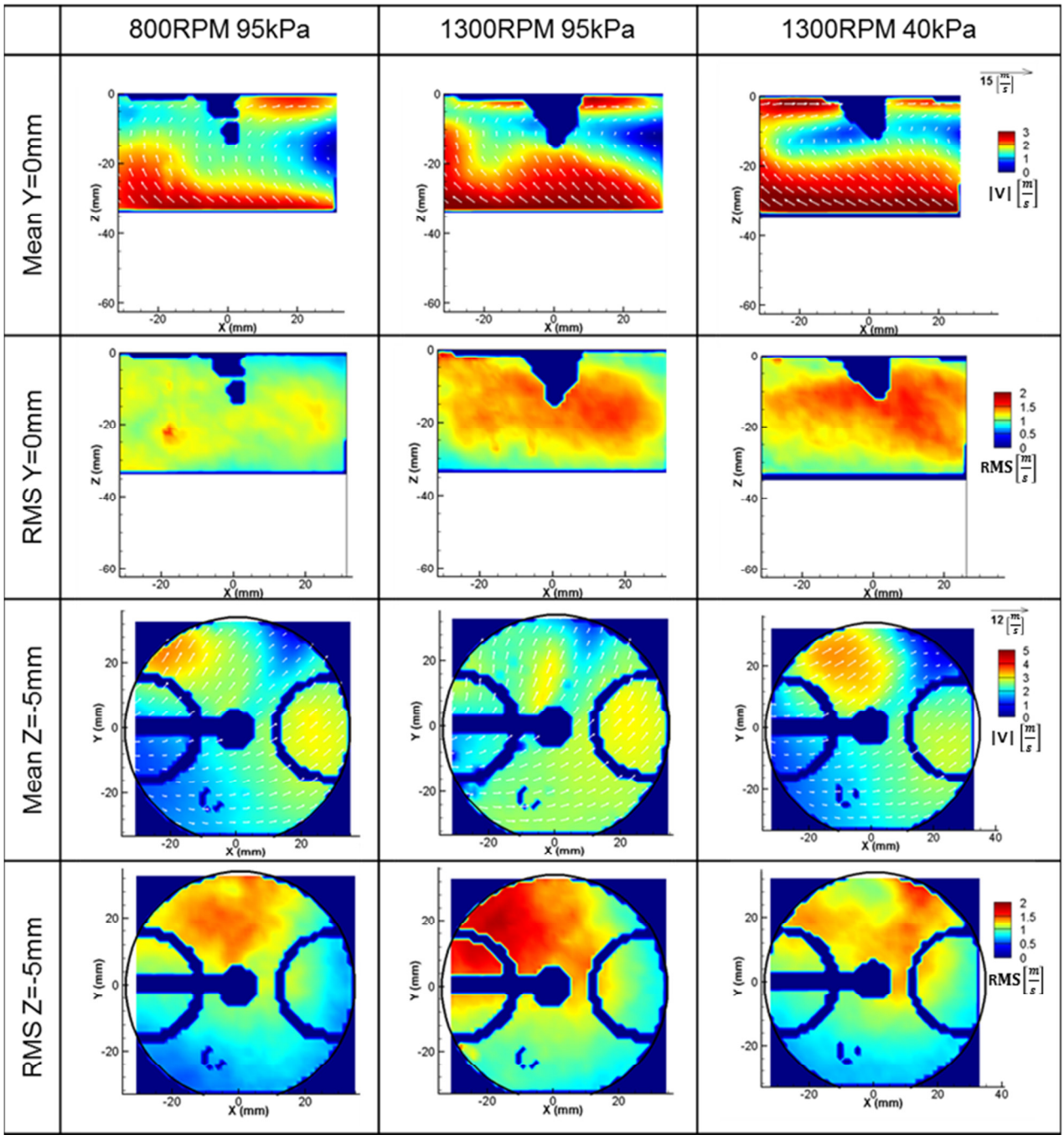

Figure 3-8 By mean piston speed normalized mean and RMS velocities for three operation conditions at 300CAD ATDCE

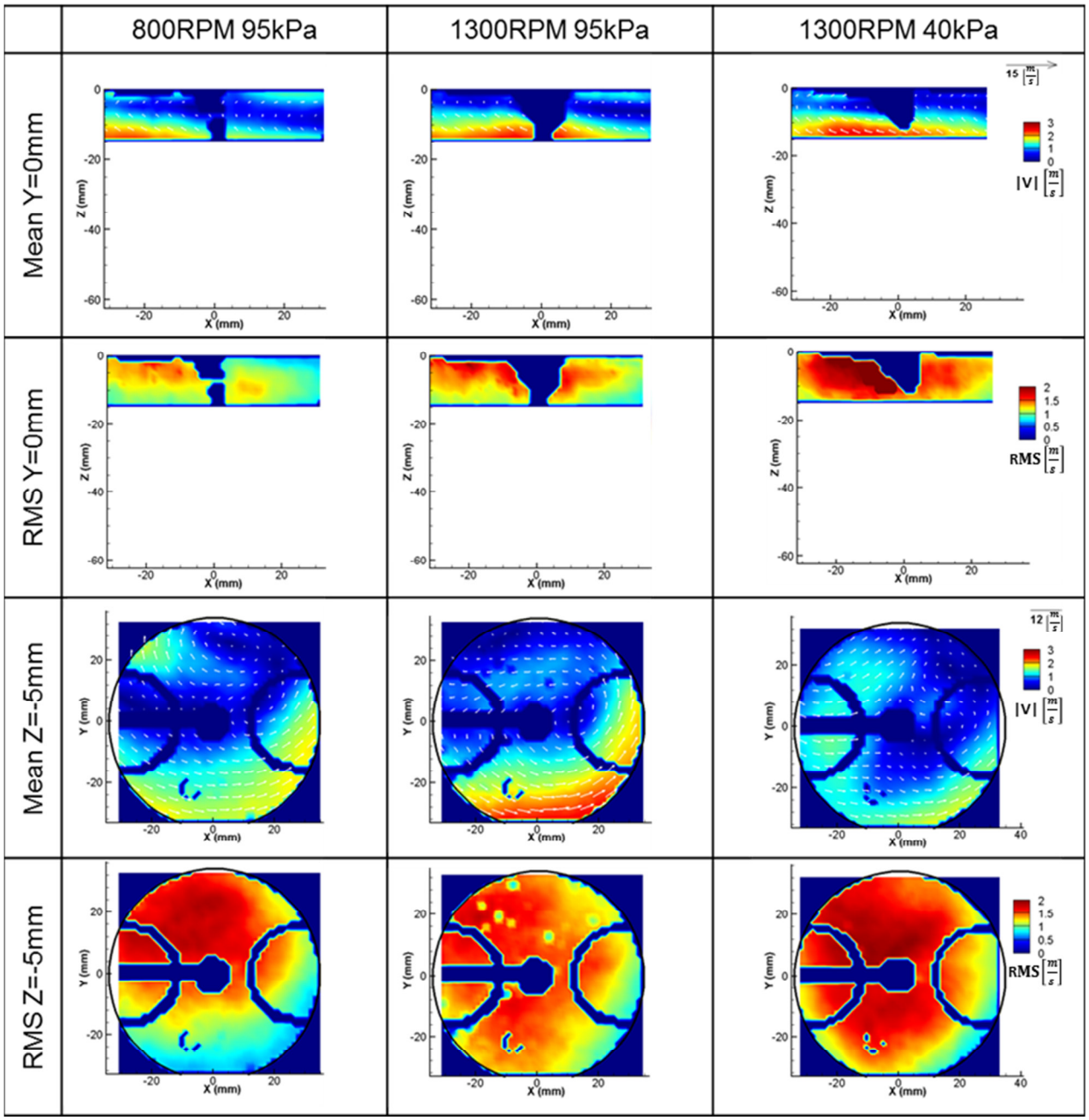

Figure 3-9 Mean and RMS velocities normalized by mean piston speed for three operation conditions at 330CAD ATDCE

At 330CAD ATDCE (Figure 3-9), flow fields in the swirl plane are vastly different between operating conditions. The 1300RPM 95kPa condition sustains a defined swirl motion up to this crank angle while at the other two conditions the swirl breaks up and the flow field becomes more chaotic. This is also reflected in the higher RMS values.

All three operating conditions have similar flow fields during the intake phase and the scalability of turbulence with RPM holds, true while throttling the engine causes only minor reductions in the magnitudes. During compression stroke, differences in mean and RMS flow fields for different RPM and IMAP increase. Similarities in the flow structures are highest between 800RPM 95kPa and the 1300RPM 40kPa condition, whereas the tumble axis seems to be rotated in the 1300RPM 95kPa case. Magnitudes of both ensemble average and RMS are higher for the 1300RPM cases. There are major differences in the mean flow fields at 330CAD. The 1300RPM 95kPa case continues to have a stable swirl component, whereas this bulk flow motion was already broken up by the compression of the turbulence structures by the piston. This might indicate that flow induced CCV in combustion increases with lower engine speeds and loads, for this particular engine configuration.

3.3 Motored vs. Fired Operation

It is important to quantify the impact of fired operation on the flow fields, in order to understand its sensitivity to increased wall temperatures, fuel, and residual burned gas on the cylinder charge motion. During the intake stroke (Figure 3-10) flow fields between fired and motored operation at 1300RPM 40kPa do not show any obvious differences in the flow fields, besides the smoother appearance of the fired data. This is an effect of the increased sample size at fired operation. The data can only be taken up to the early expansion/power stroke because at this point the flame consumed all the seed particles in the FOV, which saves memory to record more cycles.

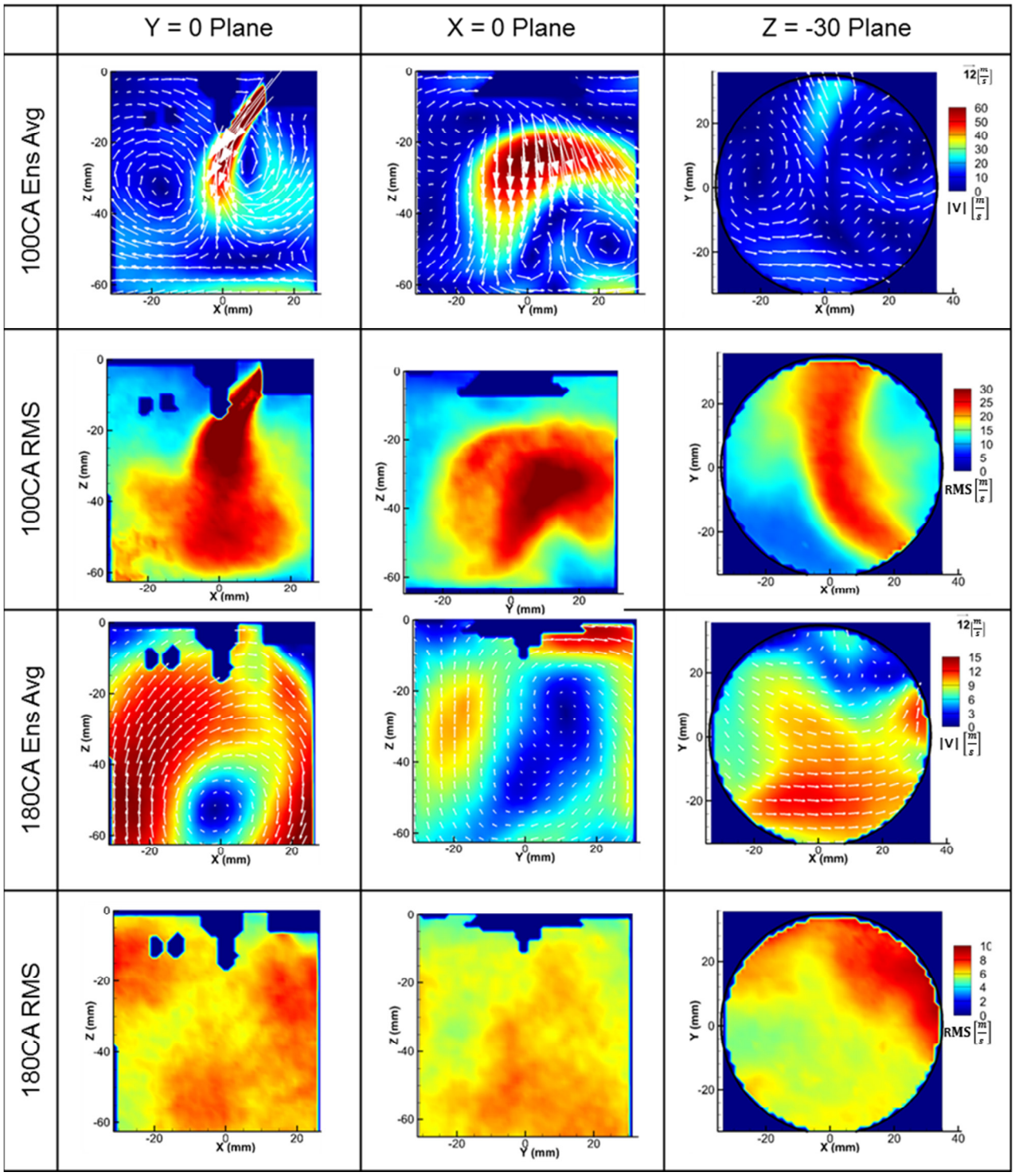

Figure 3-10 Fired ensemble average and RMS velocities at 100 and 180CAD ATDCE

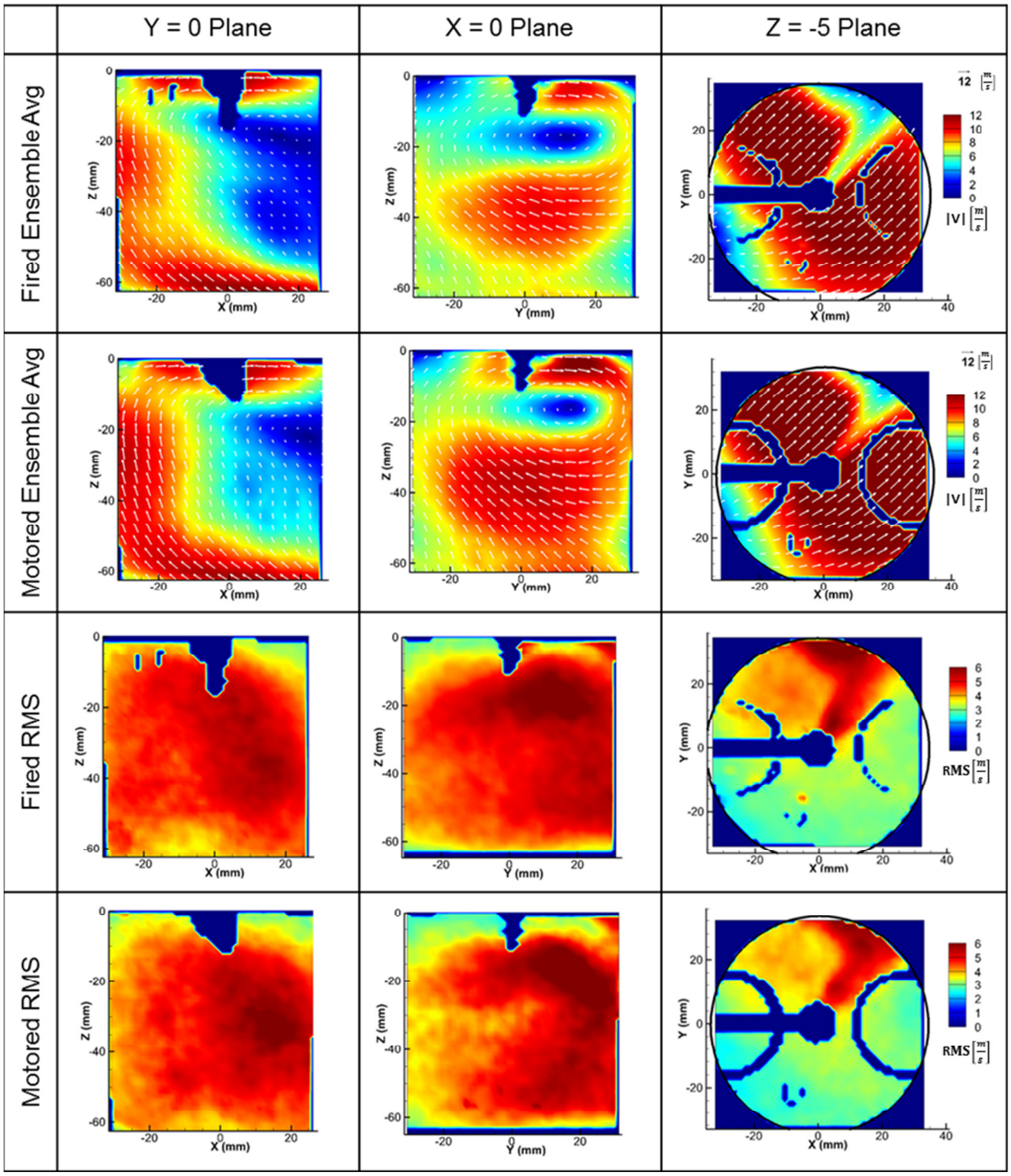

Figure 3-11 Comparison of motored and fired ensemble average and RMS velocities during compression stroke at 260CAD ATDCE

At mid compression stroke (Figure 3-11), the fired operation shows approximately 5-10% decreased magnitude in the mean flow compared to the motored operation. Further

differences in the flow pattern are not obvious. This trend continues on to 300CAD (Figure 3-12). Mean velocity magnitudes increase by 10-20% in the fired engine compared to the motored engine. This might be an effect of the increased compressibility of the gas due to an increased fraction of three and more-atomic gas molecules added, by the fuel and the residual burned gas from the previous cycle.

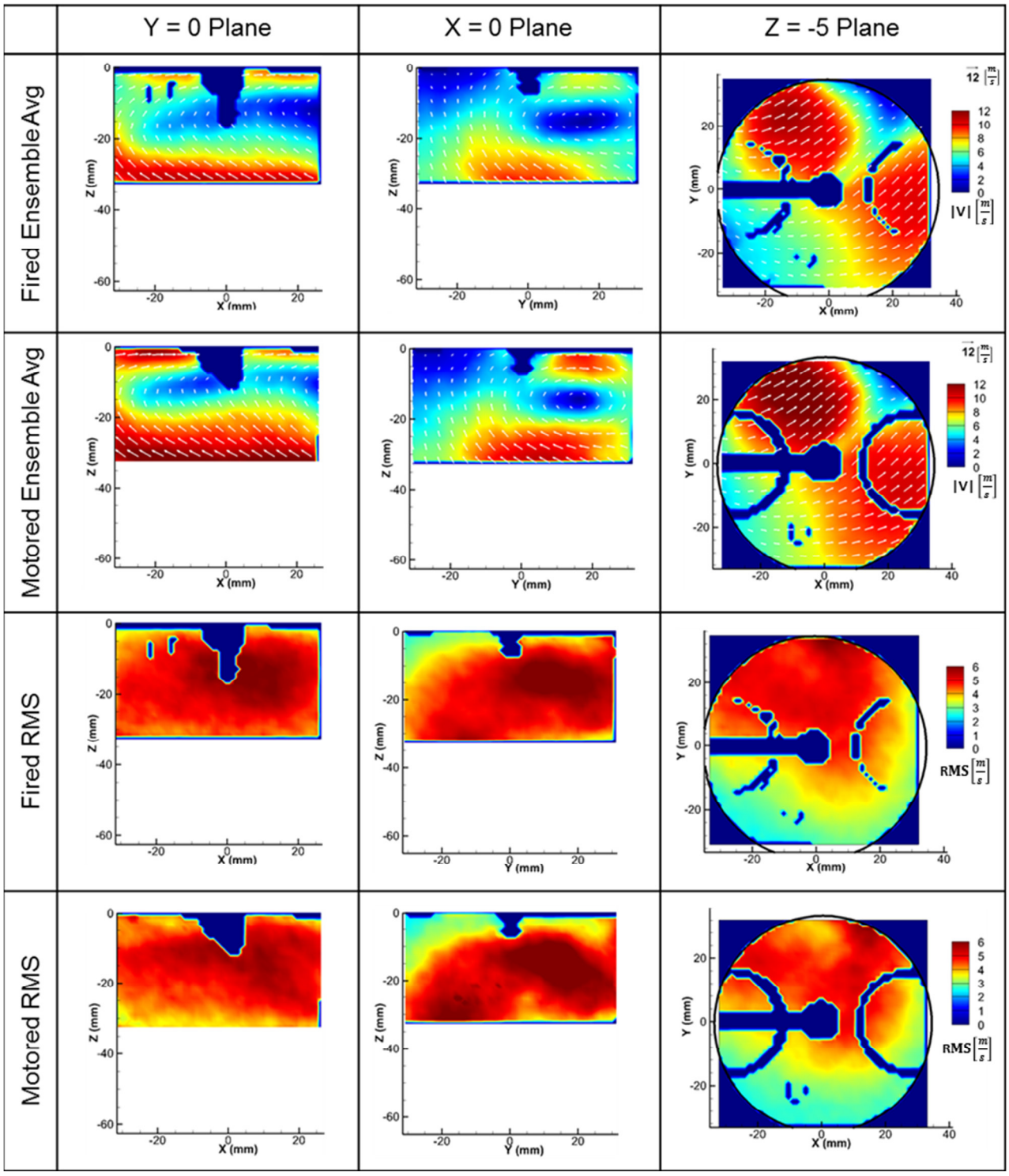

Figure 3-12 Comparison of motored and fired ensemble average and RMS velocities during compression stroke at 300CAD ATDCE

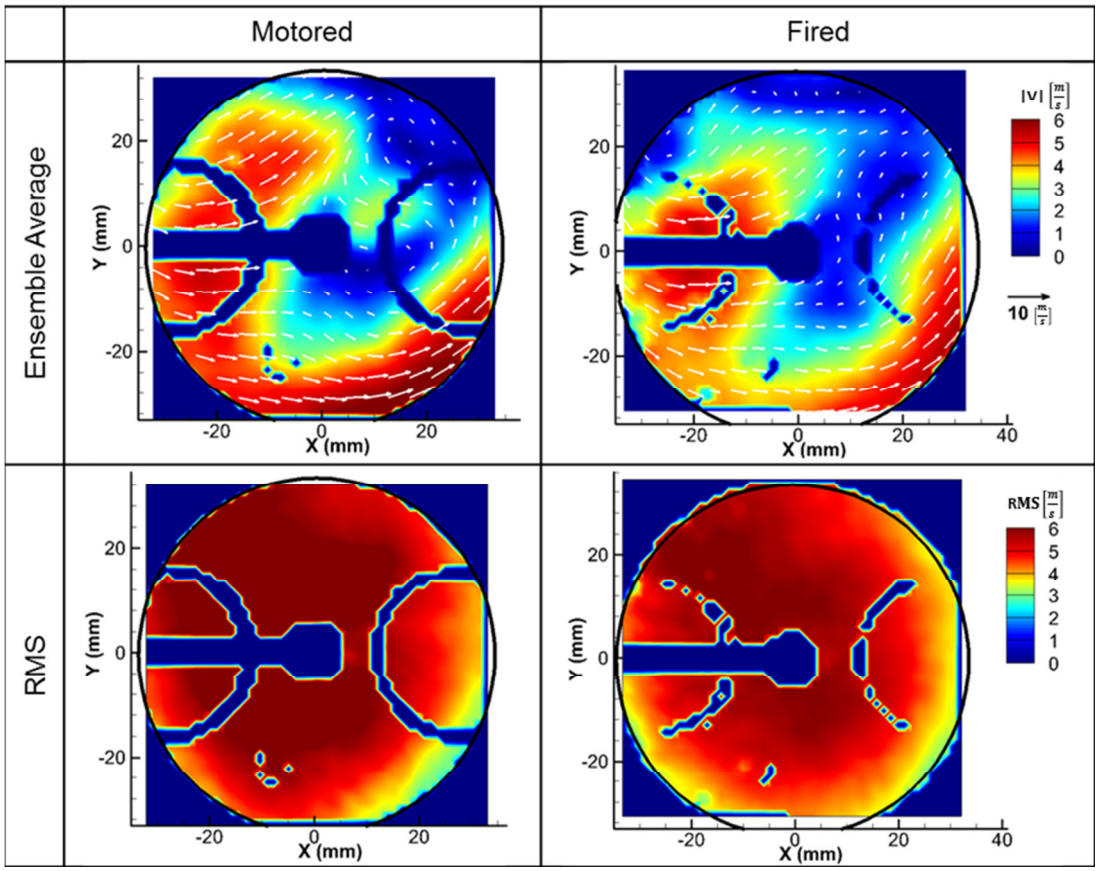

Figure 3-13 Comparison of motored and fired ensemble average and RMS velocities during compression stroke at 330CAD ATDCE in Z=-5mm plane

Differences between motored and fired are again increasing during late compression stroke (330CAD ATDCE, Figure 3-13). Mean and RMS velocity magnitudes are up to 10% lower in the fired case. The fired flow field by the spark plug is missing a higher velocity region that is flowing from the intake valve towards the spark plug. This difference becomes bigger 10CAD later (34CAD ATDCE, Figure 3-14). The flow velocity in this region increases in the motored flow, but is still missing in the fired case.

340CAD (Figure 3-14) is two CAD before ignition and the flow field at this point affects the combustion behavior and the ignition delay. A flow that predominately pushes the flame kernel towards the ground strap, which increases heat loss of the kernel to the electrodes, reduces flame kernel growth rate, and retards combustion.

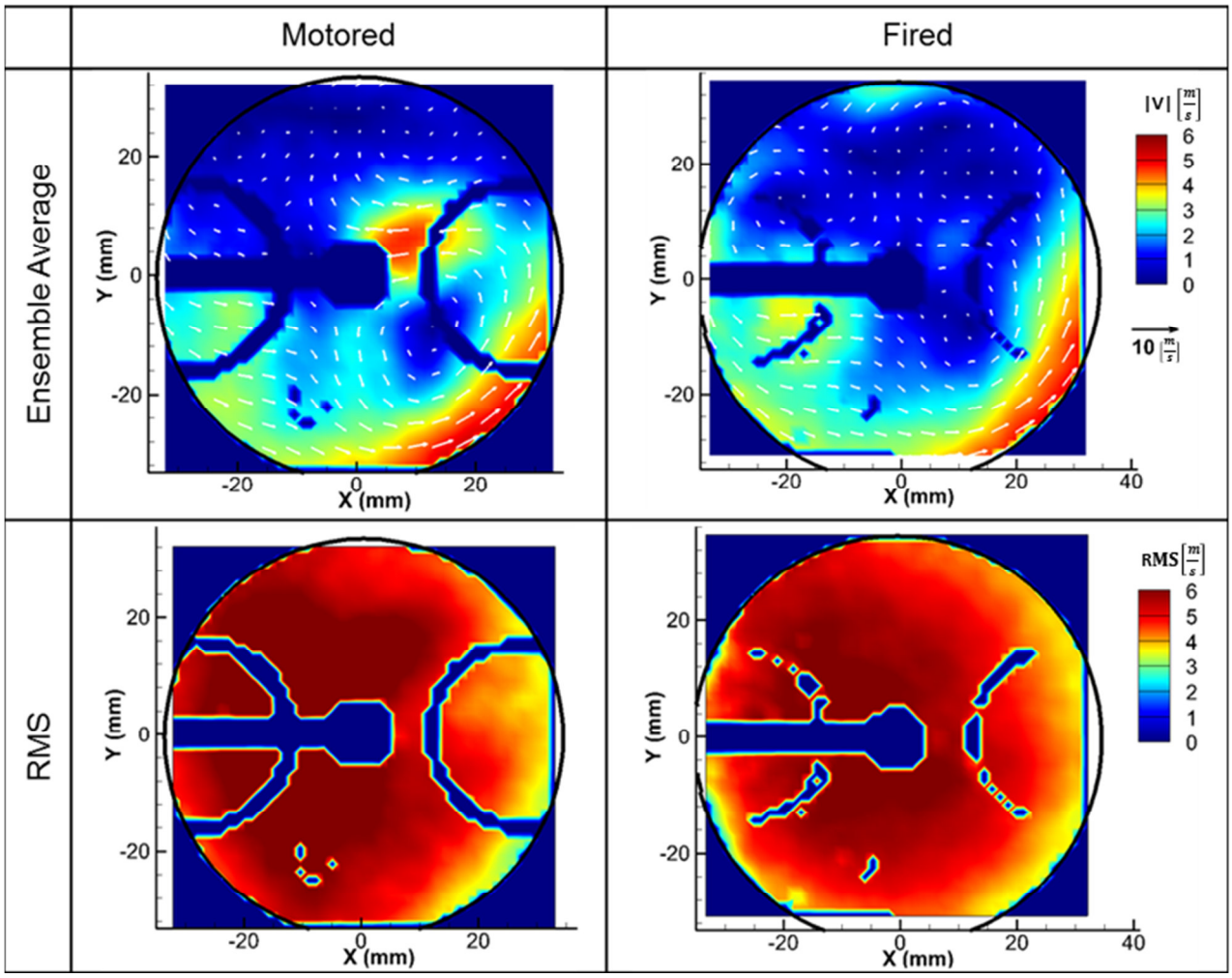

Figure 3-14 Comparison of motored and fired ensemble average and RMS velocities during compression stroke at 340CAD ATDCE in Z=-5mm plane

Although ensemble averages and RMS fields give a good sense of how similar or different two conditions are, ideally one wants to do a quantitative comparison of the flow fields of the different test conditions. One way to compare the flow direction is to calculate the so called structure index [80] (also known as relevance index). The structure index can be applied to any flow fields, but in the context here it makes only sense to compare the ensemble average flow fields at various CA until the point of ignition, because of the big variations in the flow from cycle to cycle. The structure index (SI) is calculated as

$$SI = \frac{u_{ref}u_{sample}+v_{ref}v_{sample}}{|U_{ref}|+|U_{sample}|} \qquad (29)$$

where u and v are respectively the x and y-velocity components of either the reference or the sample flow field, with the flow velocity magnitude |U| for reference and sample flow field being:

$$|U| = \sqrt{u^2 + v^2} \quad (30)$$

For a comparison as shown in Figure 3-15, an ensemble average of all three motored tests (+1200 cycles sample size) in the Z=-5mm plane is computed as the reference flow field to which all ensemble flow fields are compared. One requirement for this is to have all flow fields on the same vector grid. The structure index is color-coded such that very similar flow directions are red (exactly the same vector direction SI=1) and less similar flow regions are blue (exact opposite vector direction SI=-1), where the threshold shown as white color is set to SI=0.9. In Figure 3-15, the reference flow field is compared to the ensemble average of the fired stoichiometric propane test S_2014_05_06_01. Just after 300CAD, the flow field in the wake of the spark plug starts to deviate from the reference field. This trend continues as the tumble dominated bulk flow motion breaks down as the mixture is compressed by the upward moving piston. The restriction in z-direction causes the destruction of the tumble motion such that an off-center swirl motion dominates close to TDC. The spark timing of 18CAD BTDCC falls in the chaotic transition period. The flow direction of fired flows is mostly different in low velocity regions, while the more energetic flow features remain similar between motored and fired tests.

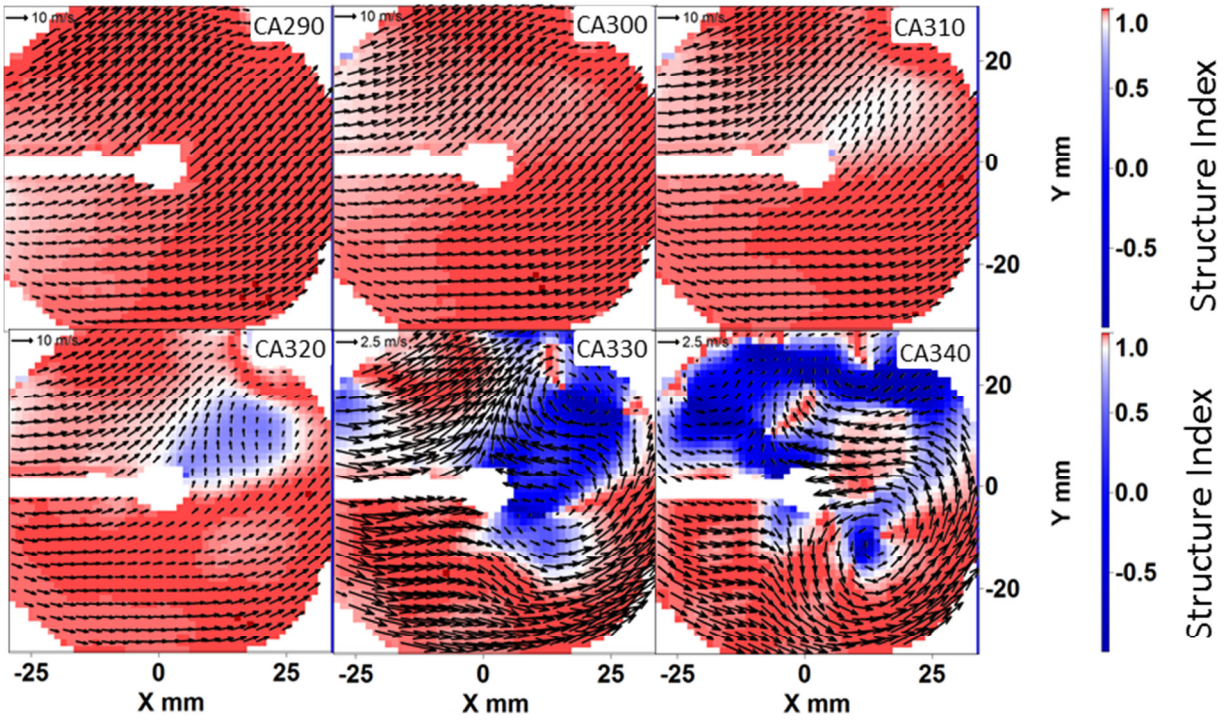

Figure 3-15 Spatial distribution of structure index comparing a ensemble average flow field of a fired test to the reference ensemble average flow field with overlaid motored ensemble average reference flow field (every 4th vector shown).

To further compress the quantitative comparison, the structure information is spatially averaged and plotted as a function of CAD as shown in Figure 3-16. The top left figure shows the ensemble and spatial average velocity magnitude of the combined more than 1200 motored cycles from which the reference flow fields in the z=-5mm plane are calculated. At early CA, the velocities in the plane are high (black solid line) with a high spatial velocity standard deviation, because of the intake jet crossing through this plane. The velocity decreases then steeply due to the intake valve blocking the light sheet in the center of the field of view. Around BDC, the valve allows the light to pass again and the user defined masks that are created to disable vector calculation in the shade of the valve are removed. The deletion of these masks is not exactly the same for all experiments, leading in the comparison to spikes around BDC. At around 300CAD, a sharp decrease in velocity can be noticed due to the breakdown of the tumble flow. In the same interval, an increase in flow RMS magnitude can be noticed, potentially increasing the combustion variability. On the top right the ensemble average and spatially averaged flow field magnitudes are compared to the one of the reference

(baseline) flow field. The fired tests seem to show a stronger flow during the intake period just until BDC. After intake valve closing (240CAD ATDCE), the flow magnitudes in the fired cases show consistently 10% lower mean flow velocities than the motored flow cases. On the bottom left, the spatial average of the ensemble SI for motored and fired cases are compared. From motored to motored tests, small variations in the flow direction can be observed during early intake and during the tumble breakdown phase. Compared to the motored test, the fired tests show a higher deviation from the reference flow field until BDC. During most of the compression stroke, the flow field structures are close to identical between motored and fired flows until about 310CAD ATDCE. Then the tumble seems to breakdown differently in the fired cases. One reason for this could be the different scavenging behavior or different flow viscosities and charge compressibility, due to increased mixture temperature and different mixture species. The differences can be mostly seen in the low velocity regions where a small change can reverse the local flow direction resulting in negative SI values. On the bottom left, motored reference normalized spatial mean of the ensemble RMS fields are compared. While the motored RMS values for most of the cycles are within less than 5% difference, the fired tests show a higher variability behavior until about 300CAD. The tumble breakdown in the fired tests might be more consistent from cycle-to-cycle than in the motored tests.

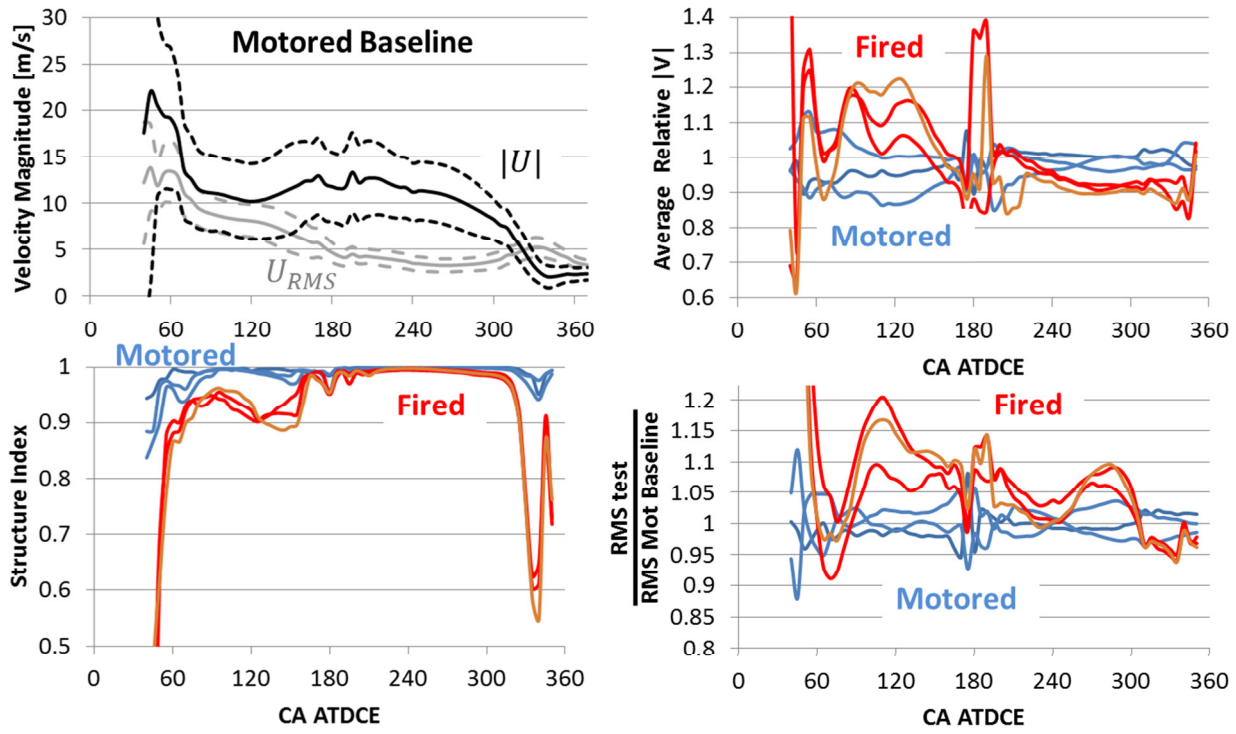

Figure 3-16 Quantitative comparison of motored to fired mean flow (black) and RMS (grey) magnitude. Top left: spatial mean velocity magnitude and RMS are printed in solid lines, while the dashed lines represent one spatial standard deviation of the respective quantity. Top right: ensemble and spatially averaged velocity magnitudes relative to the baseline flow field. Bottom left: spatially averaged structure index compared to reference flow field. Bottom right: ensemble and spatially averaged RMS values relative to the reference RMS field.

In Figure 3-17 ensemble average and RMS flow components for motored and fired tests are compared at point (0/0/-30). Fired tests (black lines) show higher X and Y velocities at 60 and 65CAD ATDCE, and higher jet velocity magnitudes between 90 and 120CAD ATDCE. RMS magnitudes during mid-intake stroke are higher in all three dimensions in the fired cases. In the compression stroke, motored and fired, mean and RMS values are the same. Variability in the Z direction reduces as the piston approaches the measurement point just before 300CAD ATDCE.

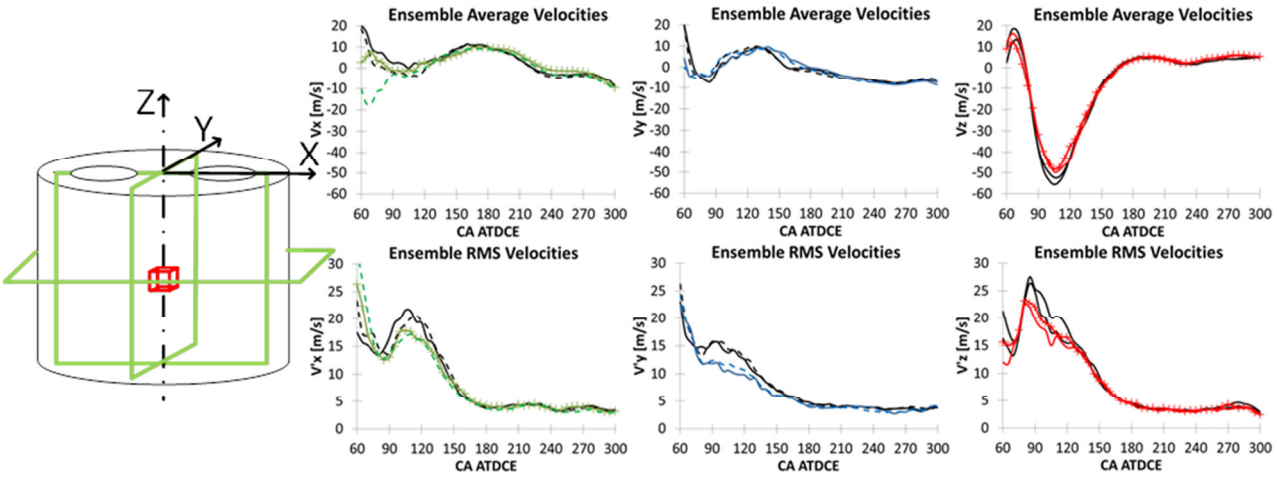

Figure 3-17 Comparison between motored and fired ensemble average and RMS velocity components in different planes at point (0/0/-30); Motored tests lines are colorful, Fired tests lines are black.

3.4 TCC III Length and Time Scales

Varying geometric boundaries and non-isentropic flow features like intake jet and exhaust blow down cause the turbulent length and time scales to change spatially and temporally throughout the cylinder volume and cycle. Here, the length scales were calculated from the spatial correlation function derived from a point 5mm below the intake valve of individual flow fields from which the ensemble average was subtracted. Many of the correlations and methods used in this chapter originate from isentropic high turbulence cases, but were used for the lack of more applicable alternatives. The flow in the engine is not directionality homogeneous due to targeted jets and physical boundaries and is in the laminar-to-turbulent transition regime.

Here the largest turbulent eddies are characterized by the integral length scale. In order to determine the integral length scale the space correlation for each velocity component were integrated along their respective longitudinal and transversal axes. The integration was performed from the point of interest in positive x direction until the space-correlation function dropped below 0.02. In many cases the longitudinal correlation had to be extrapolated with an exponential function to calculate the integral length scale.

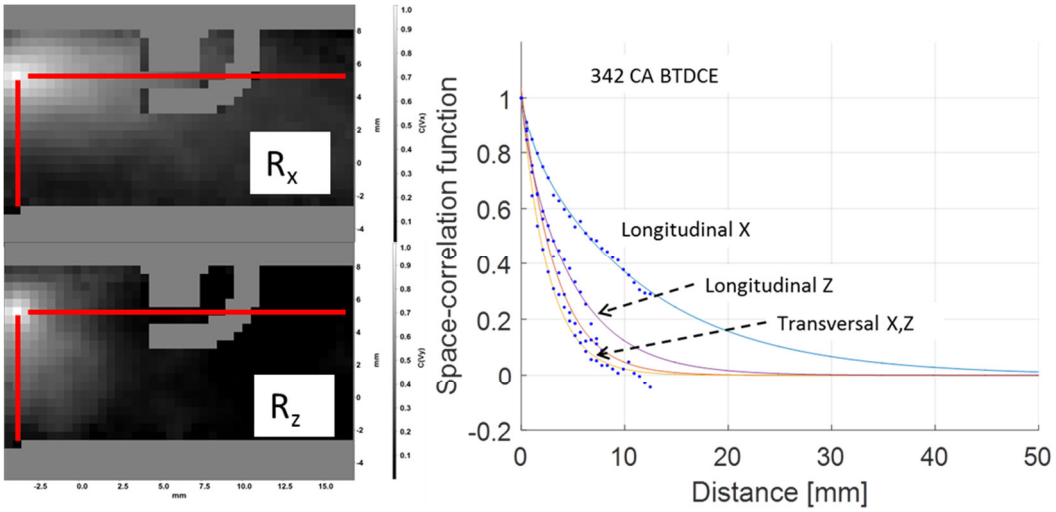

Figure 3-18 Spatial correlation function in y=-5mm plane; Integral length scale determination from extrapolated space-correlation data. Top left shows x-velocity spatial correlation map. Bottom left shows z-velocity spatial correlation map. Right shows correlation values extracted along red lines as distance from reference point. Longitudinal means in direction of the velocity component, transversal perpendicular to the direction of the respective velocity component.

In the energy cascade of turbulent flows, the Taylor microscale determines the point where the large kinetics dominated eddies break into smaller eddies dominated by viscosity. Here, the Taylor microscale is again determined by fitting parabola through the space correlation function f_s at the reference point of the space correlation function. When following the analysis of [81] for isentropic highly turbulent flows, the Taylor micro scale λ_{Taylor} is calculated to be

$$\lambda_{Taylor} = \sqrt{\frac{2}{-f_s''}}$$

where f_s" is the second derivative of the parabola. Assuming isotropy and high Reynolds number flow are not applicable in this in-cylinder flow, but there is no better way known to the author on how to estimate the Taylor micro scale. Here, it is found that, the Taylor micro scale calculation is dependent on the resolution of the PIV experiment. From three different experiments with spatial resolutions ranging from 2.4 to 0.25mm, the actual micro scale is extrapolated to be about 0.8mm in this engine at the time of ignition (Figure 3-19).

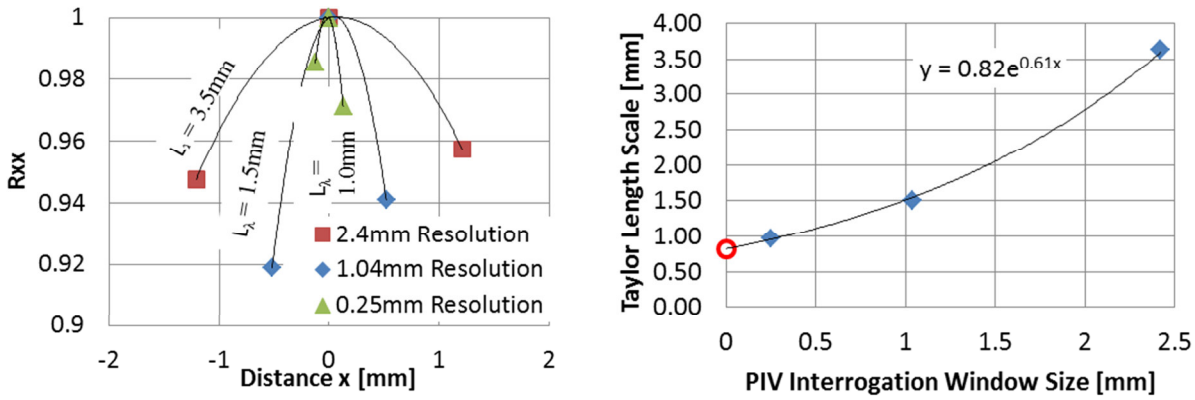

Figure 3-19 Convergence of Taylor scale with PIV grid size at 340CAD ATDCE; Left: Spatial correlation function for different grid sizes for illustrating the effect on curvature at x=0mm. Right: The curvature related Taylor scale is an exponential function of the grid size. For an infinitesimally small interrogation window under these conditions the Taylor length is about 0.8mm.

In contrary to the Taylor microscale, the integral length scale is not affected by PIV resolution for the tested interrogation windows. The average of longitudinal and transversal integral length scale changes throughout the cycle, as shown in Figure 3-20. In the vertical plane, the integral length is slowly increasing after mid-intake stroke until the piston is restricting the flow in z-direction and the integral length scale drops to about 1/3 of the clearance distance. In the expansion stroke, the largest flow structures grow continuously with CA until the exhaust valve opens and the blow down jet introduces new small scale flow features. Although all three tests are taken in different years in different field of views and under motored and fired conditions, the integral length scales are similar until shortly after start of ignition at 342CAD ATDCE. From mid-compression stroke to exhaust valve opening at 480CA ATDCE, the average integral length scale is about 1/5th of the clearance height.

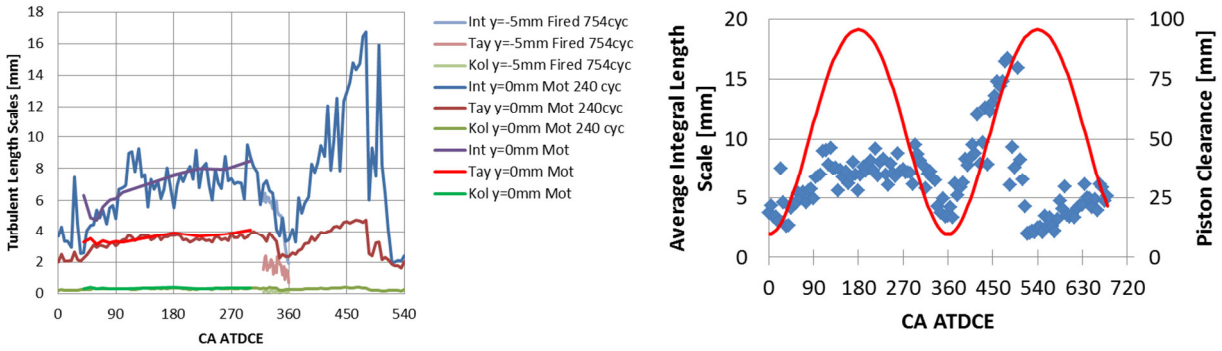

Figure 3-20 Average of integral length scales, Taylor micro scale and from this derived Kolmogorov scale as function of CA for various tests of 240, 754 and 3000+ cycles.

Although the flow in the expansion and exhaust stroke are of academic interest, from here on the analysis will focus on the intake and compression stroke for the sake of clarity and brevity. In Figure 3-21, longitudinal in X and Z-direction as well as their transversal counterparts are shown for motored and fired tests in y=0mm, y=-5mm and z=-5mm planes. In the first graph, the longitudinal length scale in X-direction is similar for motored tests (S_2013_10_24_01) and fired tests (S_2013_11_07_03, S_2014_05_13_01 and S_2015_06_25_21) at around 15mm until the point of ignition. The longitudinal integral length scale in z direction is about 8mm from mid intake to late compression stroke. In transversal direction the integral length scales are about 5mm and similar for x and z direction for all tests. In isentropic turbulent conditions the transversal integral length scale is about a factor $\sqrt{2}$ shorter than the longitudinal length scales. This is here approximately the case in z-direction, but in x-direction eventually effects from the tumble flow and wall increase to about a factor of 2-3.

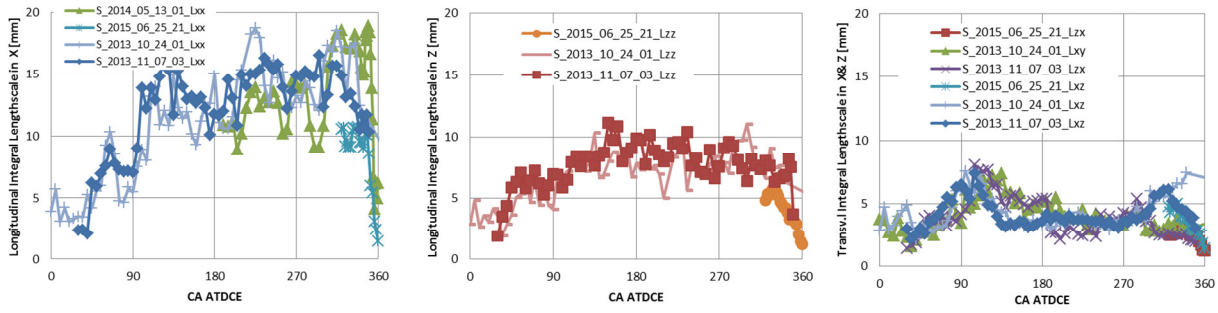

Figure 3-21 Longitudinal and transversal integral length scales

From integral length and Taylor microscale, a Reynolds number can be calculated. The equation used here is derived from high Reynolds number flows and an order of magnitude estimate of the turbulence conditions at the point of ignition [82].

$$Re_L = 15\left(\frac{L}{\lambda}\right)^2 \approx 500 - 5000 \qquad (30)$$

The Kolmogorov scale can be determined from the Reynolds number and the integral length scale and is according to [81]:

$$\eta = {Re_L}^{-0.75} * L \approx 0.02 - 0.04\, mm \quad (31)$$

The turbulence intensity based on these length scale parameters ranges from 1.5-5m/s where the kinematic viscosity is $\nu = 1.158 * 10^{-5}\frac{m^2}{s}$ at start of ignition. It is calculated using:

$$u' = \frac{Re_L}{L}\,\nu \qquad (32)$$

When comparing these length scales and Reynolds number determined in the engine to a turbulent jet with a charcteristic length of the engine's bore of about 90mm and an approximate Re_L=2500, then the Taylor micro scale is about an order of magnitude larger (≈7mm) compared to the measured one (0.8mm). This confirms again that the scaling laws derived from high turbulence experiments, don't yield accurate results at this unsteady low turbulence flow.

The standard deviation of the velocity at the same location including the cycle-to-cycle flow variablity is around U_{RMS}= 5m/s (see Figure 3-14). These results are comparable to results by Heywood who measured standard-deviation and turbulence intensity also in a disk shaped engine at 300RPM to be U_{RMS} =1m/s and u'=0.6m/s ([4], page 411), which are similar to the values obtained here when scaled by mean piston speed (factor of 4.3, U_{RMS}≈4.3m/s, u'≈2.5 m/s).

Like the turbulent length scales, also the turbulent time scales in the engine are varying throughout the cycle. As during processing the spatial scales, also here the ensemble flow fields are subtracted and the velocities by the intake valve from an area of one interrogation window

(average of 4 vectors, 1x1mm^2 area) are extracted and the time correlation with subsequent CA is calculated. The difference in results of subtracting vs. not subtracting the mean flow at each CA is shown in Figure 3-22. The strong mean flow component causes a long lasting correlation from the intake closing to the end of compression stroke. However, these large scale flow structures affect heat transfer and convection of the flame kernel. In order to quantify the "turbulent" flow in the cylinder the time correlation is performed only on the variable component of the flow fields. These time correlations for a fired case are shown on the right in Figure 3-22. During the fast intake jet period, correlations are short and are at 5CAD steps temporally under resolved in these experiments. The time correlations increase until the time of ignition at 342CAD when the extending flame affects the flow measurements.

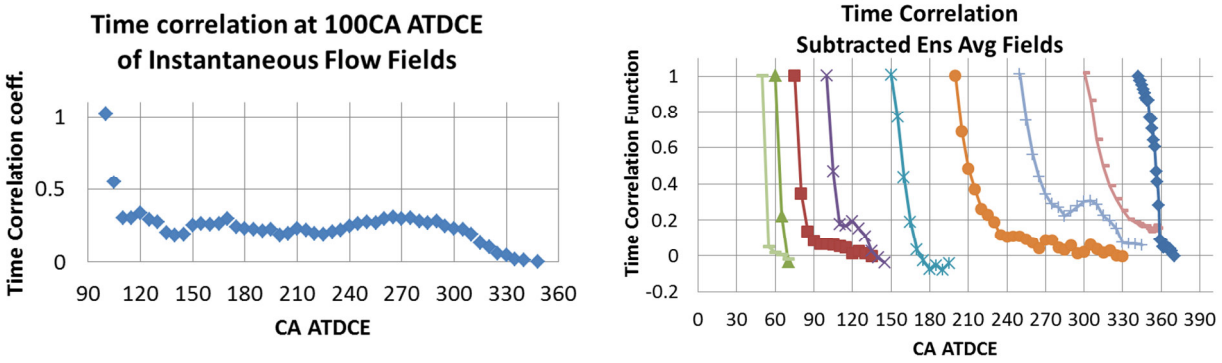

Figure 3-22 Time correlation without the ensemble average flow field subtracted (left); Time correlations for various CA of only the varying components of the flow field (right).

This analysis has been carried out for motored and fired tests (fired test time scales drop to 0 before TDC due to flame interference with the measurement) in vertical and horizontal planes at a distance of 5mm from the cylinder head. In Figure 3-23, arguably the influence of the wall can be seen when comparing differences in integral time scale in x (turquoise) and y (black) with z (orange) velocity components. The integral time scale increases at a rate of about 30CAD per revolution as indicated by the dashed lines. The integral length scales increase in the x direction from mid-stroke intake to exhaust valve opening and in Z-direction from mid-stroke compression to EVO. In the fired cases, the integral time scale begins dropping off to zero about one integral time scale before ignition (indicated by vertical dashed line).

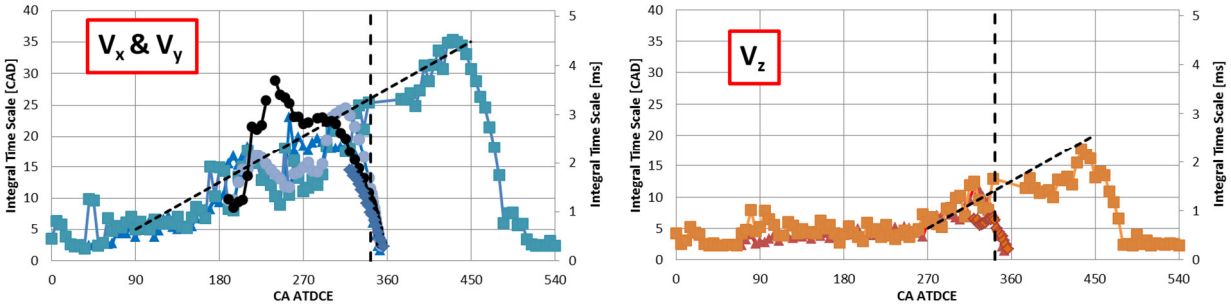

Figure 3-23 Integral time scales for motored and fired engine tests. Symbols indicate from time correlation derived integral time scale.

3.5 Summary and Conclusion In-Cylinder Flow Variability

In this chapter, bulk flow motion in two swirl and two tumble planes is measured throughout the engine cycle at 800 and 1300RPM, and 40 and 95kPa IMAP. It is demonstrated that mean flow magnitude and RMS magnitude scale with engine speed, as reported in literature, while the flow field pattern remains similar. Motored and fired pre-combustion flow fields are compared qualitatively and quantitatively. Fired flow fields mainly differ from the motored test cases during intake phase and during the last 60CAD before TDC compression. During the end of the compression stroke, the bulk tumble-structure is broken down by the approaching piston and transitions into a swirl motion. Especially the increased RMS velocities during the late phase have the potential to impact combustion. Although differences in flow pattern and flow velocity magnitudes between motored and fired cases are observed, turbulent integral length scales and timescales are the same for both conditions throughout the cycle.

CHAPTER 4 DEFINITION OF TEST MATRIX AND PRELIMINARY STUDY OF FLOW EFFECTS

In this chapter, the engine combustion performance is mapped out and a test matrix to isolate laminar flame speed, thermo-diffusive and change of deficient component effects is established. In some preliminary results from pressure analysis, spark discharge characteristics, and flow field results are presented for two extreme cases. It is shown that combustion parameters, like IMEP and CA10, correlate with the energy output of each cycle. Proper orthogonal composition is used to isolate flow structures, which may have an effect on the combustion process.

4.1 Definition of Test Conditions

As already discussed in the introduction, one goal of this thesis is to show how much the change of thermo-diffusive effects, deficient species and laminar flame speed affect cycle-to-cycle variations. For this reason, a test matrix is set up to vary the inlet mixture to isolate these effects by having a minimum of test conditions but gaining new learnings about how the variables affect combustion in a turbulent environment. In this study, only data points at stoichiometry (being the most stable condition, industry standard, and simple exhaust after-treatment with a three way catalyst) and practical lean, rich and dilute combustion limits (as defined by the variability limits at COV_{IMEP}=5%) are considered.

Laminar unstretched flame speed is reduced by adding nitrogen (Figure 4-1 left), while having a minimal impact on Markstein number. To isolate Markstein number effects the laminar flame speed of methane is matched by adding nitrogen to the propane-air mixture (Figure 4-1 middle). Then the combustion variability behavior between both fuels is compared. The effect of deficient species is investigated by measuring at fuel lean and rich conditions (Figure 4-1 right).

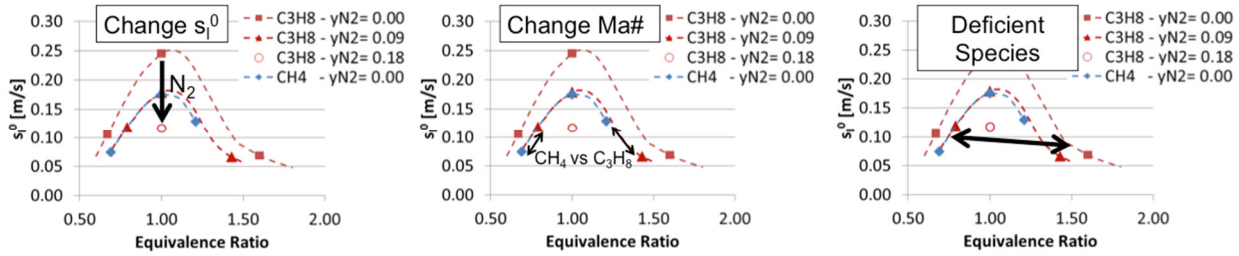

Figure 4-1 Schematic of defining test matrix for 323K and 6bar. Left: Add nitrogen dilution to propane-air mixture to reduce laminar flame speed. Middle: Change fuels to change Markstein number. Right: Change lean to rich to change deficient reaction species from fuel to oxygen.

These considerations are important to isolate effects and to populate a test matrix efficiently. To define the exact test conditions the engine is supposed to be tested at, equivalence ratio sweeps are conducted for undiluted propane, undiluted methane, and dilute propane with the same laminar flame speed as methane. All these tests (Figure 4-2) are run at a nominal engine speed of 1300RPM, a total intake mass of 2.14g/s (resulting in an IMAP of about 40kPa) under cold conditions with constant spark timing of 18CAD BTDCC. It is important to do the engine mapping under the same conditions as the tests with optical diagnostics to achieve the same variability behavior. Here especially the engine temperature plays an important role, as warmer conditions run more stably due to the increase in laminar flame speed ($s_l \, \alpha \, T^2$). The spark timing is kept constant to the MBT timing of stoichiometric propane to expose the flame kernel to the same thermodynamic and flow conditions for each mixture. It is understood that the variability limits could be extended by advancing the spark timing, but this changes flow, temperature and pressure conditions throughout the flame development process.

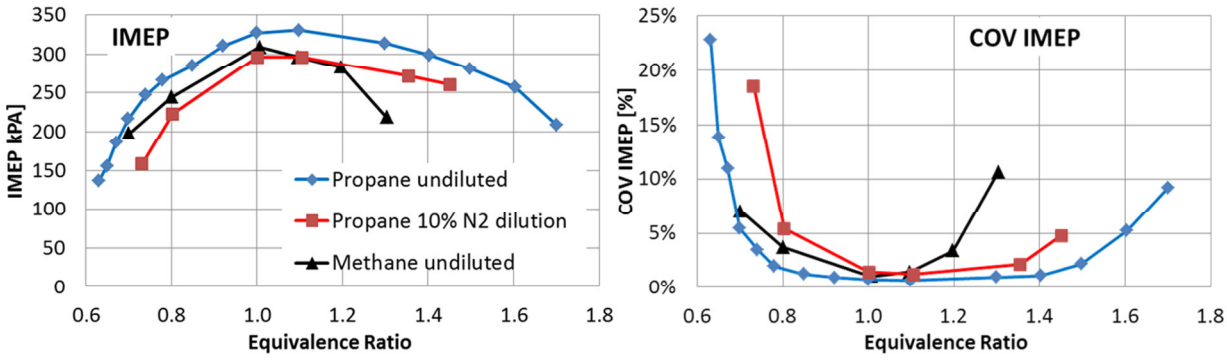

Figure 4-2 Mapping combustion variability in the TCC-III engine at 1300RPM for different fuels, dilution and equivalence ratios

The tested engine conditions are listed in Table 4-1 together with other important mixture properties. y_{N_2} denotes the added pure nitrogen mass fraction of the total air fuel mixture such that $\mathrm{y_{Air}} + \mathrm{y_{Fuel}} + \mathrm{y_{N_2}} = 1$. The laminar flame speeds were calculated using a Lawrence Livermore n-alkane mechanism [83, 84] in the chemical kinetics software package CHEMKIN PRO.

Thermo-diffusive properties describe if a flame's reaction is stable or unstable to a perturbation. Stable flames counteract the perturbation and tend to smoothen the flame surface, while an unstable flame reinforces the perturbation and creates more wrinkles. Both Lewis and Markstein numbers are used to describe flame stability behavior. Mixtures with Lewis numbers below 1 and negative Markstein numbers tend to develop unstable flames, while greater values tend to be stable. The effective Lewis number is calculated from the ratio of thermal diffusivity of the mixture and the molar diffusivity of the deficient species (fuel in lean environment; oxygen in fuel rich flames). From this, the effective Lewis number is calculated according to the methodology of Bechtold and Matalon [37]. Thermal and mass diffusivities are calculated using CHEMKIN chemical kinetics package [85]. Opposed to the theoretically derived Lewis number, the Markstein number is usually an empirically derived quantity. According to [35], Le and Ma numbers are related as follows

$$Ma = 0.5Ze\left(\frac{1}{Le} - 1\right) \qquad (30)$$

where the Zel'dovich number Ze is a non-dimensional number describing the temperature sensitivity of the reactions [35]. The Markstein number is typically determined from the Markstein length L, observed in experiments by the change of laminar flame speed with geometrical stretch rate κ. by [34]

$$S = S^0 - L\kappa \qquad (7)$$

The non-dimensionalized Markstein number is the Markstein length L divided by the laminar flame thickness. Here, Markstein number correlations for propane and methane are extracted from Driscoll's review paper on turbulent premixed combustion [39].

Fuel	Equivalence Ratio		Y N_2	Eff Lewis #	Ma	Sl_0 [m/s]	Markstein Length [mm]	Flame Thickness [mm]
Propane	Lean	0.67	0.00	1.62	6.2	0.74	0.125	0.020
	Lean	0.79	0.09	1.56	5.2	0.77	0.101	0.019
	Stoich	1.00	0.00	1.36	3.4	1.22	0.040	0.012
	Stoich	1.00	0.09	1.37	3.4	0.98	0.050	0.015
	Stoich	1.00	0.19	1.38	3.4	0.68	0.074	0.022
	Rich	1.43	0.09	1.12	-0.3	0.59	-0.007	0.024
	Rich	1.56	0.00	1.08	-1.4	0.57	-0.033	0.024
Methane	Lean	0.69	0.00	1.01	-0.5	0.60	-0.013	0.027
	Stoich	1.00	0.00	1.06	2.7	0.96	0.045	0.017
	Rich	1.21	0.00	1.09	4.8	0.86	0.090	0.019

Table 4-1 Tested TCC-III engine mixtures including their properties at start of ignition p= 6bar T=700K

The same table is calculated for the combustion vessel cases at lower temperatures (Table 4-2).

Fuel	Equivalence Ratio		Y N_2	Eff Lewis #	Ma	Sl_0 [m/s]	Markstein Length [mm]	Flame Thickness [mm]
Propane	Lean	0.67	0.00	1.77	6.2	0.11	0.183	0.030
	Lean	0.79	0.09	1.70	5.2	0.12	0.136	0.026
	Stoich	1.00	0.00	1.45	3.4	0.24	0.056	0.016
	Stoich	1.00	0.09	1.46	3.4	0.18	0.040	0.012
	Stoich	1.00	0.19	1.47	3.4	0.12	0.079	0.023
	Rich	1.43	0.09	1.17	-0.3	0.07	-0.013	0.043
	Rich	1.56	0.00	1.13	-1.4	0.08	-0.051	0.037
Methane	Lean	0.69	0.00	1.01	-0.5	0.07	-0.026	0.051
	Stoich	1.00	0.00	1.06	2.7	0.17	0.058	0.021
	Rich	1.21	0.00	1.10	4.8	0.13	0.143	0.030

Table 4-2 Tested combustion vessel mixtures including their properties at start of ignition p= 6bar T= 323K

Figure 4-3 shows the flame speed correlations for combustion vessel and TCC-III engine conditions. The mixtures used in the experiments are indicated by the symbols. The shapes of the flame speeds are similar for both temperatures. The magnitudes for each mixture scale approximately with the square of the temperature.

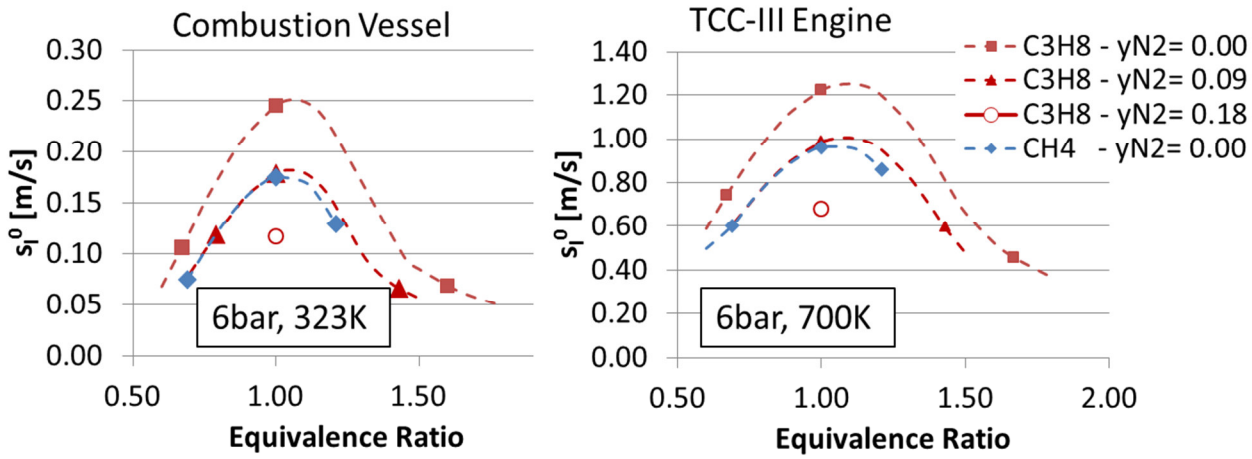

Figure 4-3 Laminar unstretched flame speeds for combustion vessel and TCC-III engine tests

Effective Lewis number and Markstein numbers are similar for both temperatures and as such only one set of figures is shown in Figure 4-4.

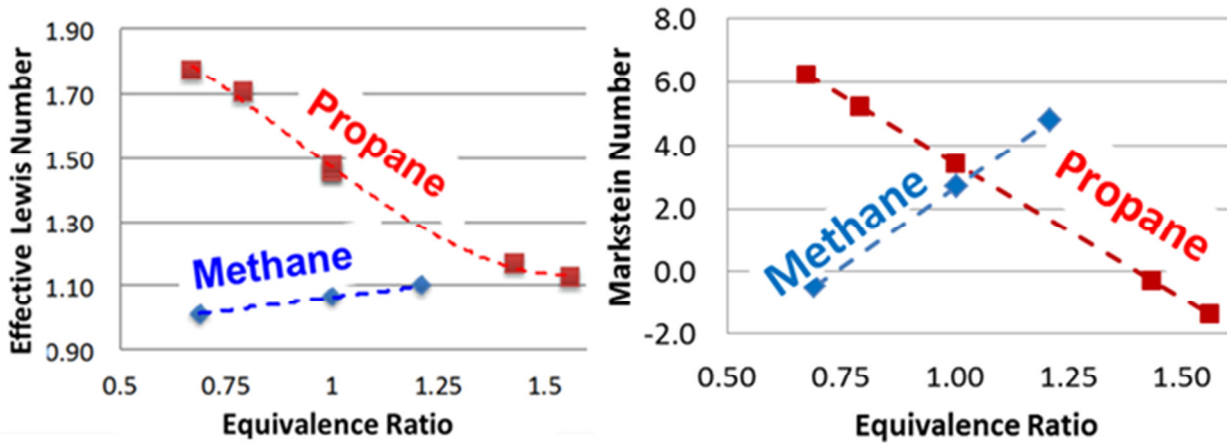

Figure 4-4 Lewis number and Markstein numbers for methane and propane as function of equivalence ratio

4.2 Experimental Assessment of Important Factors for CCV

Until now, the engine operation and the flow fields are characterized for different motored and fired operation conditions, and it is demonstrated that the tests are repeatable and data acquisition is accurate (Chapter 2.4). In this chapter, the previously introduced flow field and pressure data is used to identify factors contributing to cycle-to-cycle combustion variations. Data of fired tests are mined for correlations between CA10 and flow, spark, and pressure characteristics to identify which parameters influence combustion the most at different conditions. For this purpose, two tests at two extreme conditions, stable stoichiometric and at the lean misfire limit, are conducted. In the lean test (ϕ=0.61) the start of ignition is advanced to 318CAD ATDCE to match CA50 combustion phasing. At this early CAD, the flame kernel experiences a different flow field and different thermodynamic environment, with lower pressures and temperatures. This adds uncertainty to the comparability of the results and is avoided in later tests in this study by maintaining constant spark timing.

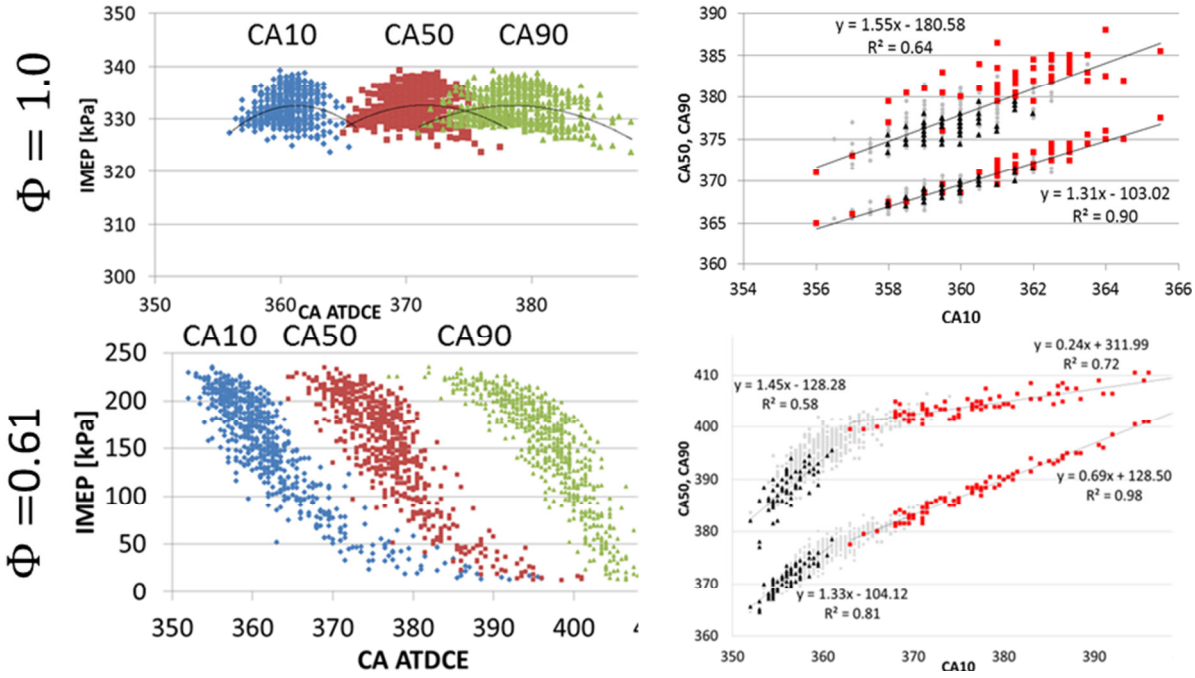

Figure 4-5 Engine pressure derived IMEP and MFB curves for stoichiometric propane mixture (top) and lean propane mixture ϕ=0.61 (bottom). On the right the 10% fastest and slowest burning cycles are marked in black and red, respectively.

In the top part of Figure 4-5, IMEP of stoichiometric propane is plotted as a function of 10,50 and 90% MFB timings. IMEP values are distributed around the apex of the indicated curves confirming MBT timing. IMEP varies between 325 to 340kPa, with phasing variability of 10CAD for CA10 increasing to about 20CAD at CA90. On the right hand side of the same figure, the dependence of CA50 and CA90 on the ignition delay, denoted by CA10. Cycles that show early ignition delays continue to burn fast, while late cycles continue to burn slowly, as the increase in slopes indicates. The black triangles indicate the 10% highest IMEP cycles distributed around 359CAD, while the 10% low IMEP cycles span across the entire range, but show higher concentrations to the extreme early and late phased cycles.

The same comparison is done for the 40% COV_{IMEP} lean mixture case at ϕ=0.61 (bottom of Figure 4-5). Here, the spark is retarded compared to MBT leading to increased levels of late burns and high variability in combustion phasing and IMEP. Although not relevant for practical applications, this condition illustrates high variability behavior, thus might reveal more sources of variability than in the stoichiometric test case. Advanced cycles show the highest energy

output, while more retarded cycles show lower IMEP values. On the right hand side of the same figure black triangles indicate the 64 highest IMEP cycles, which are now clustered towards small ignition delays, while poor burning cycles (indicated by red squares) are retarded. Cycles that show CA10 values below 365CAD have similar correlations of their CA50 and CA90 values like in the stoichiometric case. If CA10 is after 365CAD ATDCE, the CA10-90 burn duration shortens, indicating partial burns in the late cycles.

Some engines are sensitive to the combustion event of previous cycles [86, 87], caused by feedback of residual-gas composition. In order to see if this is the case in the TCC engine, IMEP of cycle n+1 is plotted as a function of the IMEP of the previous cycle n (Figure 4-6). There is no obvious correlation between cycles in the established steady state condition not for IMEP or CA10 phasing.

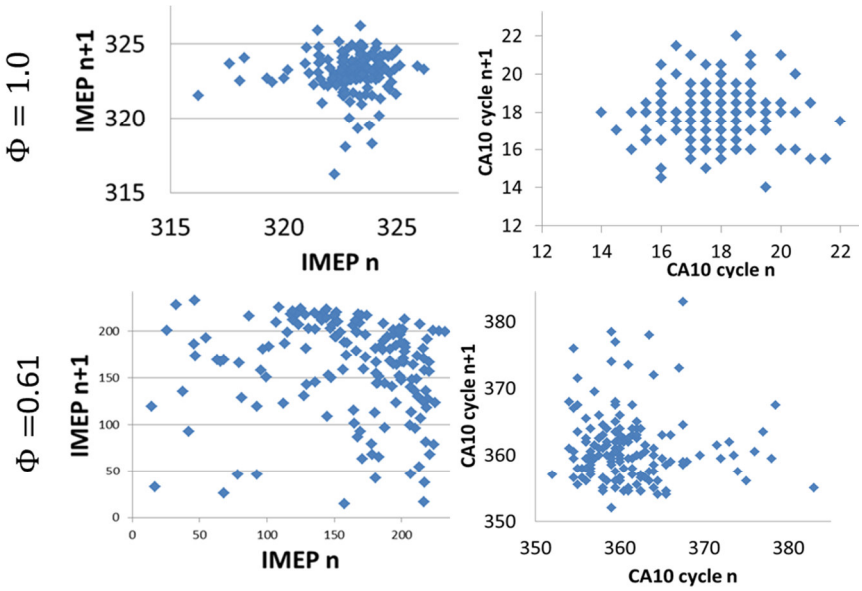

Figure 4-6 Dependence of IMEP and CA10 on previous cycle.

Under the lean condition with partial burns, a stronger dependence of cycle n+1 on the previous cycle can be expected, due to partial burns and misfires resulting in residual-gas composition changes in the preceding cycles. However, as in the stoichiometric case, no correlation in combustion phasing and IMEP could be established, indicating a small effect of RBG on the cyclic variability behavior in this engine under the tested operating conditions.

The correlation between IMEP and CA10, and other performance parameters are computed using the coefficient of determination R^2 of their respective linear correlation shown in Figure 4-7. At an equivalence ratio of ϕ=1.0 linear flame speed is high, minimizing time for perturbations during the early flame kernel phase, showing only small CCV. Some weak correlations between IMEP and pressure derived quantities, intake and exhaust pressures, and shear strain by the spark plug are observed (see top Figure 4-7).The combustion phasing parameter CA10 shows stronger correlations with other measured quantities. Ignition delay parameter CA10 shows higher correlations with peak pressure location and magnitude and other combustion phasing parameters. This is because earlier phased cycles show higher peak pressures at earlier crank angles. CA10 is not sensitive to spark energy under this condition, but the shear strength in a 10x10mm field around the spark plug seems to be of increased importance.

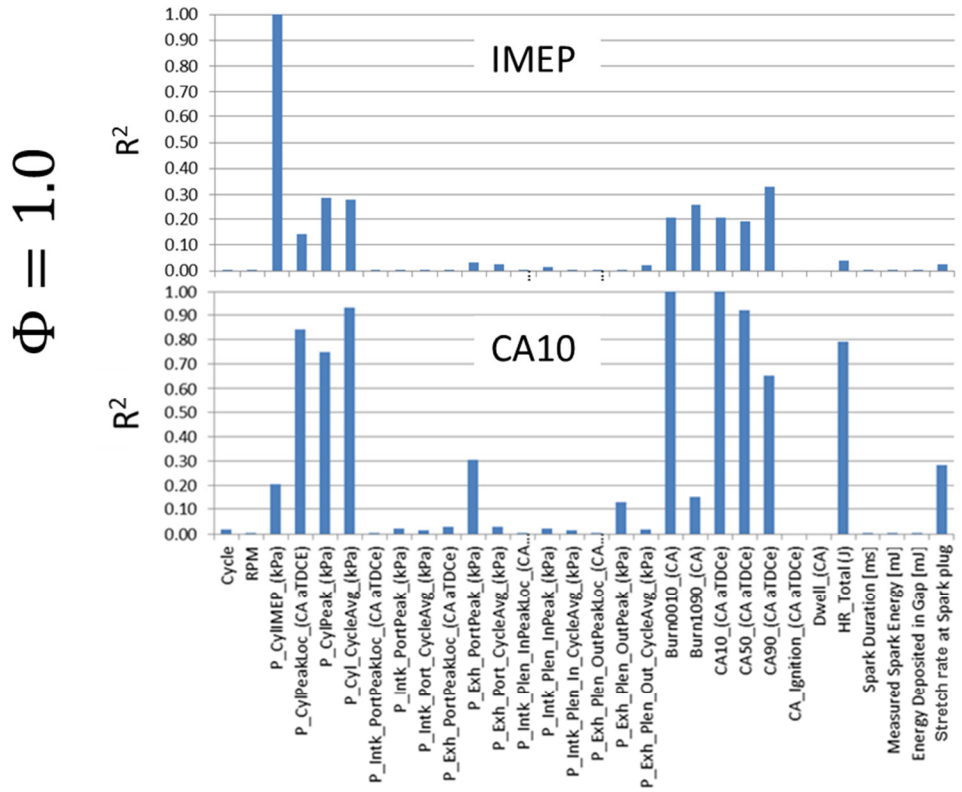

Figure 4-7 Linear correlation coefficient between IMEP and engine parameters (S_2014_05_13_01)

Correlations between phasing parameters such as location of cylinder peak pressure, CA10, CA50, CA90, Burn 00-10 , and Burn 10-90 are shows again that the combustion phasing is determined during the early combustion phase. Correlating IMEP with these phasing parameters in this condition does not yield high correlations, as at MBT the correlation curve is a parabola with the mean IMEP centered around the maximum. The correlations between CA10 and exhaust pressure dynamic metrics are not helpful in determining the contributing factors to CCV as those are phenomena after the combustion event.

In order to show the relation between ignition delay and shear strength, they are plotted for two different stoichiometric tests (see Figure 4-8). Low spatial average shear strength at the spark plug at the start of ignition increases the CA10 variability and can delay CA10, whereas high shear strain advances the 10% MFB time.

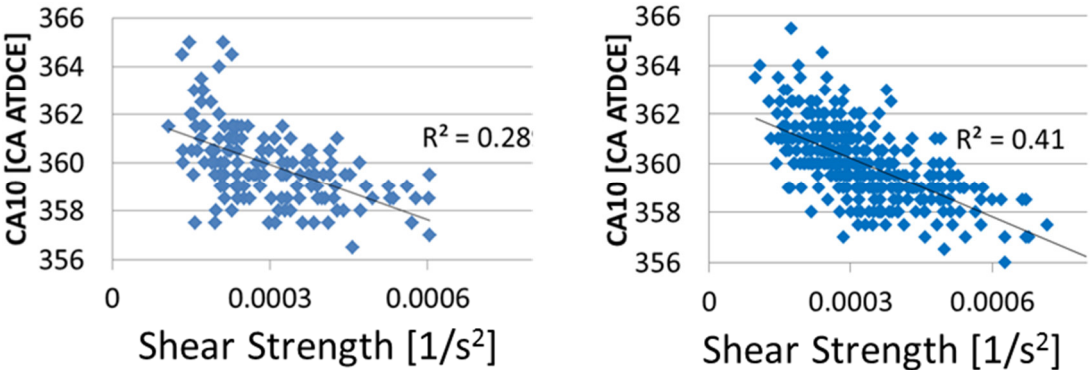

Figure 4-8 Dependence of CA10 on shear strength by the spark plug (left: S_2014_05_13_01; right: S_2014_05_08_01)

In the lean case, laminar flame speed is lower, which allows more time for perturbations to interact with the flame kernel, causing higher levels of fluctuations in ignition delay and as such also in IMEP (see Figure 4-9). This higher sensitivity towards fluctuations should reflect in higher correlations with different pressure, spark, and flow parameters. In Figure 4-9, linear correlation coefficients of IMEP with different pressure derived parameters and spark parameters are shown. In this case, a linear correlation between ignition delay and IMEP can be achieved because the spark timing is retarded compared to MBT timing and the IMEP is

continuously dropping with increasing ignition delay. Here, also the spark energy delivered to the spark plug electrodes seems to have an effect on IMEP. The ignition delay has a greater importance to the IMEP than the 10-90%MFB duration.

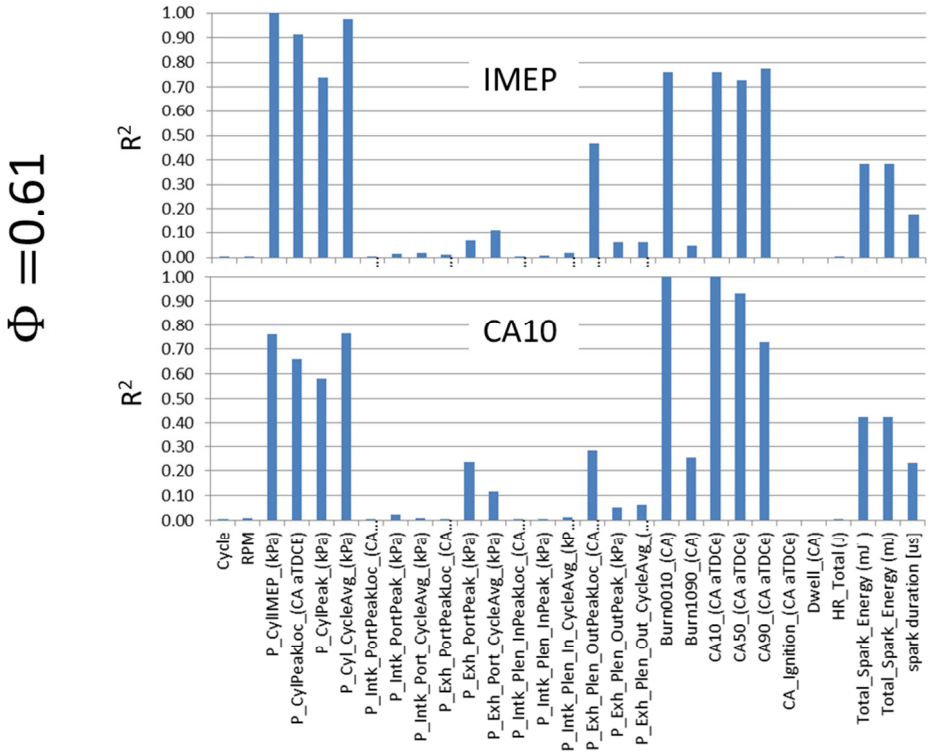

Figure 4-9 Correlation coefficient between IMEP and CA10, and engine, and spark parameters.

The spark energy seems to have a more direct effect on the ignition delay (Figure 4-10), and also on the energy output of the engine. The spark energy seems to be of higher importance at this lean limit condition, whereas at the stoichiometric condition, sufficient energy is always available to spark a self-sustaining flame propagation [16]. When more than 36mJ of energy is delivered to the spark plug electrodes, misfires and partial burns are not observed and CA10 times occurred earlier than 370CAD ATDCE. This suggests that this condition is close to the minimum ignition energy threshold (61mJ at 6bar and ambient temperature [16]). Higher energies allow the flame kernel to initially grow faster. Cycles with low ignition energy show higher levels of variability in ignition delay and the following IMEP output.

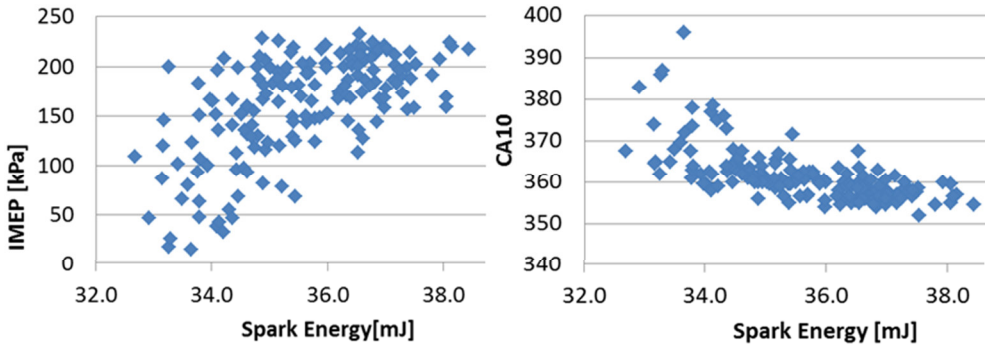

Figure 4-10 IMEP and CA10 as function of Spark Energy for lean high COV case

4.3 Impact of Flow Structures on Combustion

In order to evaluate the influence of the flow field on IMEP, POD mode coefficients of the flow fields at time of ignition are correlated with IMEP. Figure 4-11 shows weak correlations between IMEP and POD mode coefficients at the point of ignition.

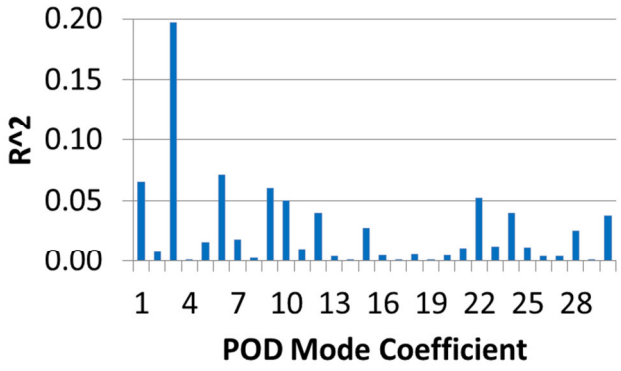

Figure 4-11 Correlation coefficient between CA10 and POD mode coefficients at SOI (S_2014_05_13_01). Full FOV in z=-5mm plane.

Compared to the IMEP results, higher linear correlations between CA10 and POD mode coefficients can be found. Especially, Mode 3 shows a high correlation coefficient ($R^2 \approx 0.2$), but also Modes 1 and 6 seem to have some influence on the ignition delay. Also, some higher modes show some correlations with the ignition delay, but their energy content, and as such the relative importance, is lower. The three modes that show the highest linear correlations with the ignition delay are shown in Figure 4-12.

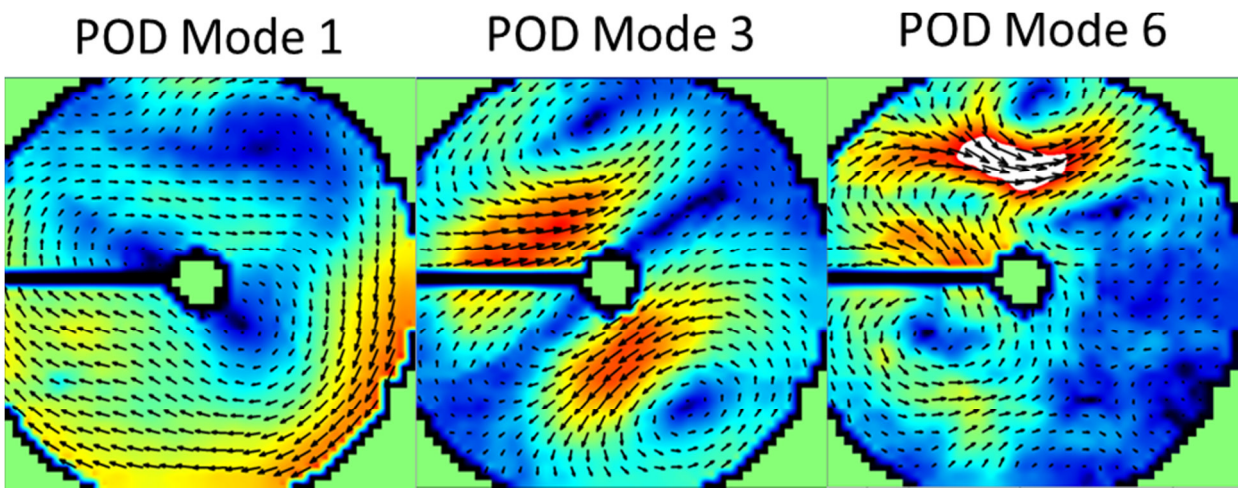

Figure 4-12 POD modes at start of ignition (S_2014_05_13_01)

Mode 1 is the inverted ensemble average flow field. Mode 3 shows two vortices rotating in counter-clockwise direction with a high shear region crossing the spark plug, this observation backs the observation of the influence of shear strength influencing CA10. Mode 6 contains smaller flow features with some velocity vectors in the cross flow of the spark plug.

For the lean case the influence of the flow on combustion is assessed in the same manner (Figure 4-13), using a linear correlation between POD mode coefficients at the point of ignition (318CAD ATDCE). One important observation is that the correlation values increase with a reduction of the FOV to about 10mm (Figure 4-13).

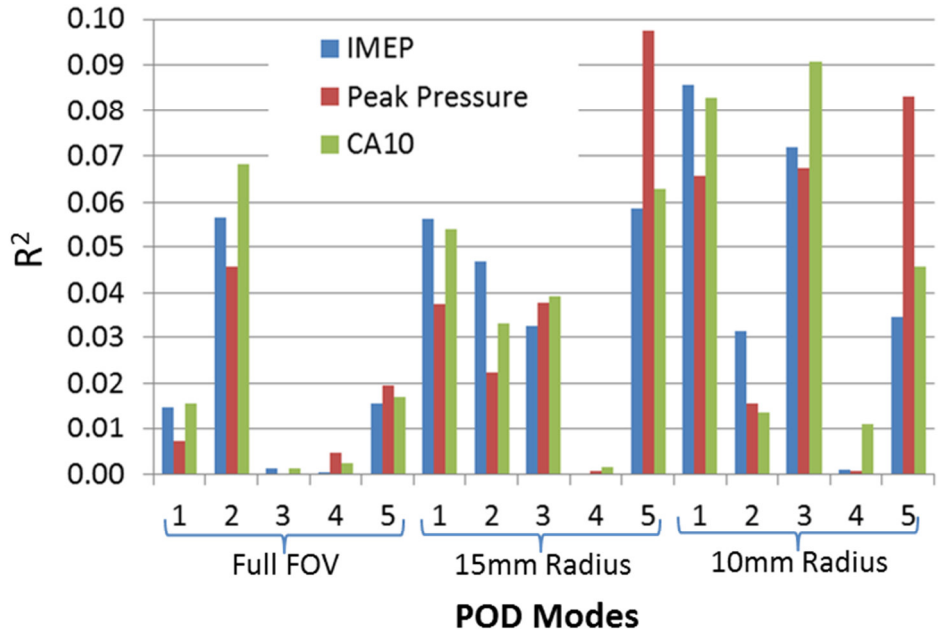

Figure 4-13 Correlation of IMEP and CA10 with POD mode coefficients of different fields of view

All correlations are below R^2 values of 0.1 and no correlation with shear strain at the location of the spark plug is observed (not shown here). Correlations here might be weak due to long ignition delays and the flow changes during the ignition period so that more factors influence the initial kernel growth.

Figure 4-14 First five POD modes for only ten mm radius around spark plug

In the future it would be of value to perform POD in a limited window around the spark plug to measure the significance of different flow structures. Also higher resolution of the flow in close proximity to the spark plug is desirable since the correlations improve when focusing on the flow by the spark plug.

4.4 Summary of Strategy for Next Tests in This Study

This chapter is dedicated to design an experiment and test condition that is intended to find the root causes of cycle-to-cycle variations in engine combustion. A test matrix is designed to isolate, laminar flame speed, Markstein number, and change of deficient species effect on combustion variability. As such, the engine will be solely run at 1300RPM with a total intake mass flow of 2.14g/s (leads to nominally 40kPa intake manifold pressure) with a constant spark timing of 342CA ATDCE, while changing the equivalence ratio, fuel and dilution. In preliminary tests the variability limits of the engine are determined and documented in Table 4-1, including some fundamental mixture properties.

In further preliminary experiments, the experimental needs are investigated to improve future experiments. One important finding is that flow features close to the spark plug at time of ignition matter more to the subsequent combustion development than features that are further away. As a consequence future experiments (covered in Chapters 5 and 6) will focus on acquiring flow data in high resolution in close proximity to the spark plug. Further, it is shown that POD has the potential to identify some sources of variability but is not able to fully capture all sources of variability. Low R^2 numbers between individual parameters and CA10 also identified the need for a deeper understanding of flow-flame interactions. One key here is to identify leading flow parameters that affect flame growth. Thus a clean combustion experiment is needed to isolate flame-turbulence interactions (by removing any convection, heat loss to walls and mixture in-homogeneities) and to identify critical flow parameters. The next chapter is dedicated to simplify the problem and measure the flow velocity while igniting the same mixtures and at the same pressure as at the time of ignition in the engine but in a field of homogeneous isentropic turbulence, without flame-walls, or mixture stratification effects.

CHAPTER 5 ISOLATED VARIABILITY OF FLOW-FLAME INTERACTION

In SI engines various parameters influence combustion variability simultaneously in a non-linearly coupled manner. This coupling makes it difficult to isolate cause-effect relationship and uniquely identify a particular source for advanced or retarded phasing during one particular cycle. To reduce the parameter space and increase optical access to the electrode gap a multi diagnostic experiment at the University of Orléans combustion vessel [54, 88, 89] was setup to isolate variability effects of spark discharge and flow-flame interaction under engine like conditions (Figure 5-1).

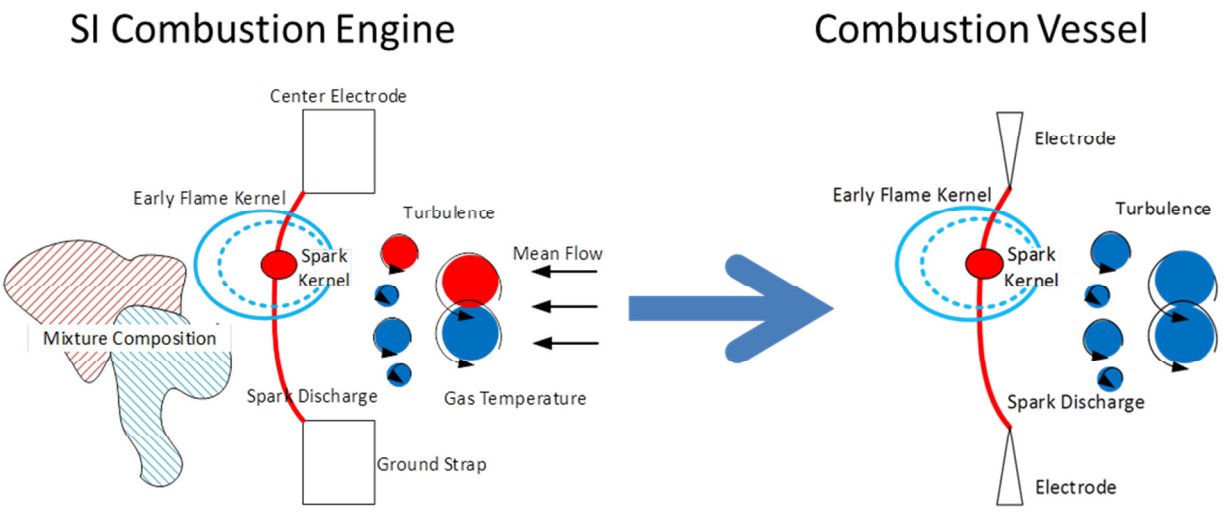

Figure 5-1 Schematic of sources for combustion variability in the engine and combustion vessel

Besides taking stratification effects and flame-surface interactions out of the equation, the combustion vessel has the advantage of increased optical access to image flame growth and to measure flow parameters in the electrode gap.

Flame kernel growth measurements over several orders of magnitude were achieved with a combination of dual-pass Schlieren volumetric imaging and pressure based metrics. Turbulent flow effects are imaged with stereo particle image velocimetry (SPIV) and their influence on the

combustion is analyzed in detail for a variety of conditions. Laminar flame speed, Markstein number and the effect of the deficient species were evaluated by strategically choosing fuel-air mixtures at the practical combustion limit, as determined in previously conducted engine experiments.

In the past, researchers investigated the stretch effect of flames and how the flame speed changes for different mixtures. Average flame speeds and Markstein numbers in laminar combustion vessels [40, 43, 90] are determined for various fuels, equivalence ratios, dilution fractions, pressures and temperatures. The impact of thermo-diffusive properties on the cellularity and combustion regimes in turbulent combustion was characterized [46, 91, 92]. Markstein number effects measured in combustion vessels, even at lower pressures, were shown to translate into engine results and affect the average combustion behavior as shown by [93]. These previous studies were targeted on understanding the mean combustion behavior whereas in the present study the focus is on understanding the effects of flame speed, change of deficient species, and thermo-diffusive properties on combustion variability. Two studies were found that investigated cyclic variations of premixed propane-air combustion in constant volume chambers. One with velocity point measurements at low temporal (<1kHz) resolution and for only one mixture [94]. The other was performed without in-test velocity measurements, but used a jet to perturb the flame [95].There is no fundamental understanding of how turbulent flow structures affect cycle-to-cycle variations and how this sensitivity changes with mixture composition. The wide range of experimental conditions that are investigated here seek to add insights into this aspect.

5.1 Experimental Setup

In the isentropic turbulence of the 200mm inner diameter combustion vessel [54], the spark ignited flames were recorded at 10kHz from two orthogonal views with a single camera two pass Schlieren setup shown in Figure 5-2. Both views were imaged side-by-side on the rectangular CMOS chip of a VisionResearch v1210 monochrome camera (Figure 5-3 right). A 0.1mm spatial resolution allowed to measure the early kernel growth, its transition from a laminar to turbulent flame, and its three dimensional position with high precision. Additionally,

the volume of the flame kernel could be estimated from the two orthogonal images as demonstrated by [17]. In their approach, the flame kernel is sliced in y-direction and each slice is assumed to have an ellipsoidal shape. The integral in y-direction of the ellipsoidal area equals the estimated flame volume.

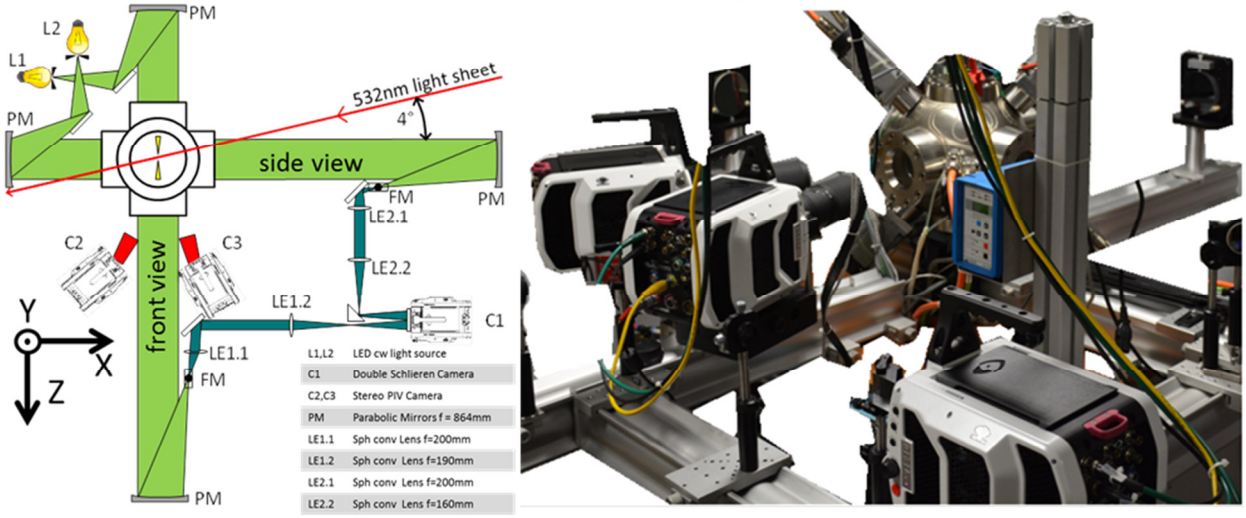

Figure 5-2 Schmatic of the light pathways and photo of the experimental setup.

To link the variability of the flame growth to the flow conditions at a particular test, high-speed SPIV was used to measure all three velocity components with 1.2mm spatial resolution in a plane cutting through the spark electrode gap. A commercial cross-correlation algorithm (LaVision DaVis 8.2) was used with decreasing interrogation window size (first pass 128x128 pixel^2 to a final interrogation window size of 32x32pixel^2 with 50% overlap). Image n is correlated with image n+3 to achieve a maximum pixel displacement of 8pixels in instantaneous flow fields, to optimize the velocity dynamic range to about 0.02 to 1m/s. Although a recording frequency of 10kHz oversamples the velocity field, it allows to study the development of flame wrinkling and Schlieren based burned gas volume in detail. The burned gas area is identified using an iterative hysteresis filter with added dilation function and subsequently masked out to avoid the calculation of erroneous vectors in this region. This contour information is also used to determine the flame wrinkling factor ($W = \frac{P}{C} = \frac{P}{\sqrt{4\pi A}}$) calculated from the ratio of perimeter P of flame and circumference C of a circle with equal

area A. The higher the W, the bigger the surface area of the flame becomes. PIV flow features are extracted just before time of ignition as a spatial average of a 5x5mm^2 area around the spark plug electrodes.

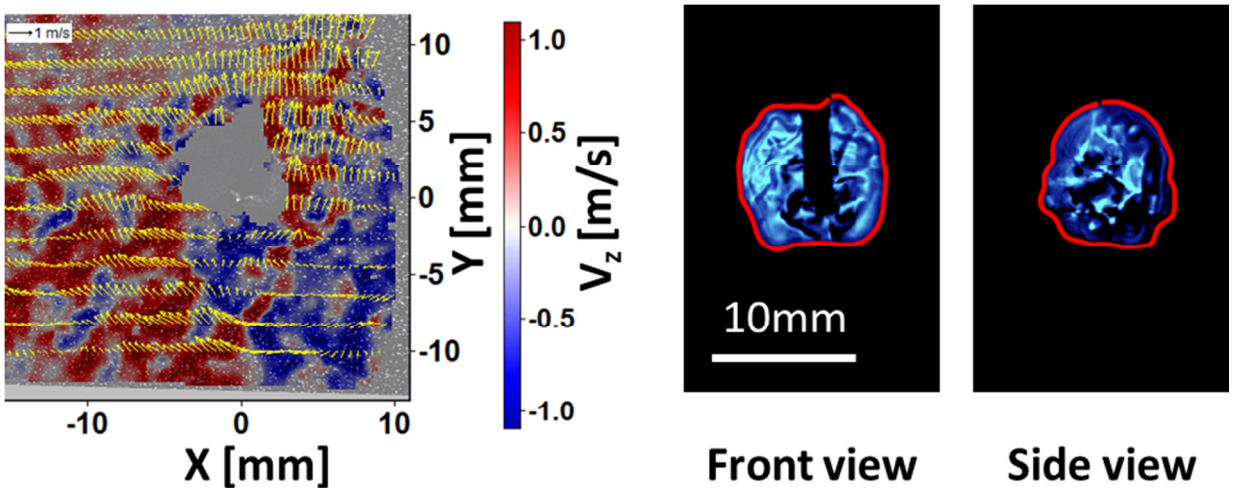

Figure 5-3 Example experimental results. Left: Flow field results overlay on Mie scattering signal (every 4th vector shown in Y-direction). Right: Front and side view of flame kernel Schlieren image.

Additionally, ignition system secondary voltage and current are measured during each spark discharge at 500 kHz to monitor the performance of the ignition system and evaluate its influence on combustion variability. Once the flame exceeded the field of view of the imaging techniques, the burned gas volume is estimated from the recorded pressure using a two-zone model.

The estimated digitization error in the Schlieren volume calculation is ±0.5 pixel. This error is especially critical during the early kernel part of the development, while lens and mirror imperfections will mainly influence the analysis during later burn phases when the flame front is further off axis. Assuming a spherical burned gas volume for the error estimation yields

$$V = \frac{4}{3}\pi\left(r \pm \frac{1}{2}Pixel\right)^3 \qquad (31)$$

Performing a factorial expansion and simplification by assuming that r >>Pixel size yields

$$\Delta V = 4\pi r^2 Pixel \qquad (32)$$

Substituting volume for r and plugging in the pixel magnification value (here 0.1mm/Pixel) one obtains the binarization error estimate as a function of burned gas volume size.

$$\Delta V = 0.484\, V^{2/3}\ [mm^3] \text{ or as relative error } \frac{\Delta V}{V} = \frac{0.484}{\sqrt[3]{V}}\ [\%] \qquad \text{(33a) and (33b)}$$

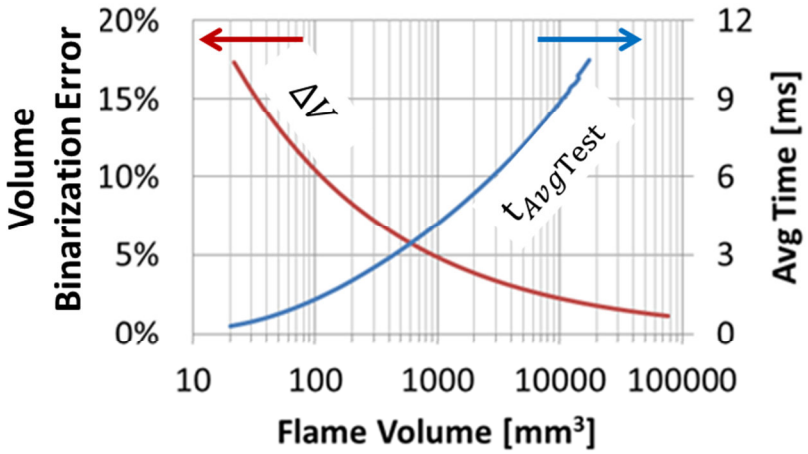

Figure 5-4 Relative volumetric binarization error as function of volume for a representative range used in this study; On second axis average time needed for all mixtures in this study to reach the specified burned gas volume

Also the influence on the 0.5mm pointed tungsten electrodes on the flame growth rates in radial and axial direction of the electrodes. Figure 5-5 illustrates that up to 4ms after start of ignition, the radial growth rate is higher than the axial growth rate, causing the flame to be flatter in axial direction. Despite the use of small electrodes, the heat and radical losses to the metal affect the flame growth.

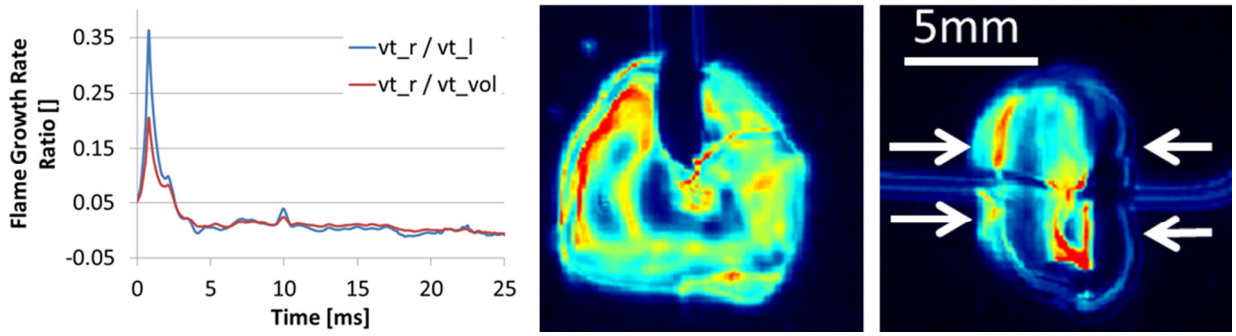

Figure 5-5 Influence of 0.5mm pointed tungsten electrodes on flame growth. In blue the front view growth rate is compared to the side view growth rate. Right: Images illustrating the deformation of the flame kernel due to the spark electrodes.

5.2 Characterization of Combustion Vessel Turbulence

The characterization of the turbulence in the combustion vessel is important to transfer the results obtained to other combustion devices (e.g. combustion engines). Results from previous studies of a detailed characterization of the turbulence in the vessel were reported earlier [54], and here these results are confirmed for the present operation conditions of 6bar and 323K.

The integral time scale τ_L in the combustion vessel determined from the integral of the time correlation function R_i.

$$\tau_L = \int_0^\infty R_i(t)dt \approx 80ms \quad \text{with} \quad R_i(t) = \frac{\overline{u_i(t_0)u_i(t_{0+\tau})}}{u_i'^2} \qquad (34a) \text{ and } (34b)$$

This result is confirmed by scaling the integral time scale results obtained by Benedicte Galmiche for rotor speeds of 5000 and 10000RPM. The scaling was performed as suggested by Abdel-Gayed et al. $L = \overline{s}\,\tau_L$ where the integral length scale L is a function of the geometry and as such constant. The pseudo convective velocity $\overline{s} = \sqrt{\frac{8}{\pi}}u'$ scales with the turbulence intensity u' in this kind of stagnant flow [Abdel Gayed et al.] while Galmiche and others showed that u' is proportional to RPM [54, 96]. This leads to

$$\tau_L \propto \frac{1}{u'} \propto \frac{1}{RPM} \text{ and confirms the integral time scale } \tau_L \approx 80ms.$$

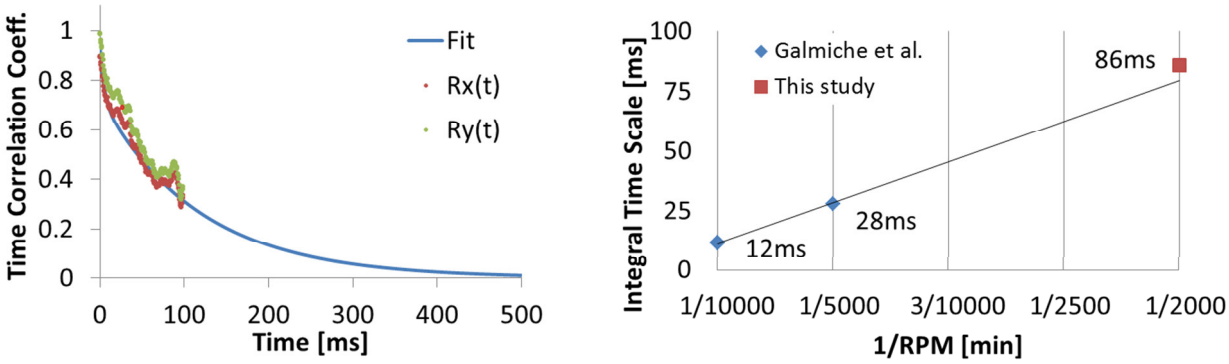

Figure 5-6 Integral time scale calculation from time correlation (left) and scaling of literature values (right)

The turbulent time scales are much longer than the time needed for the flame to grow to scales, which is important to link flow structures before the time of ignition to combustion behavior of fully developed flames.

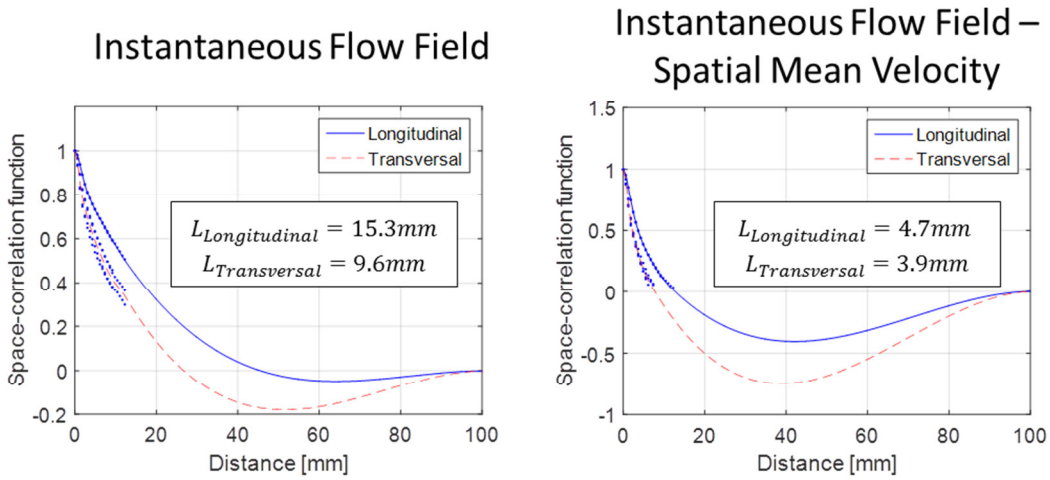

Figure 5-7 Velocity space correlation for determination of integral length scale calculation of instantaneous flow field (left) and instantaneous flow fields of which the spatial mean velocity is subtracted (right). Subtraction of the mean velocity reduces the integral length scale by about a factor of 3

To cover both combustion regimes prevailing in the engine at start of ignition, the thickened wrinkled flame and wrinkled flame with pocket flame regimes, the ratio of turbulence intensity and laminar flame speed was kept constant (Figure 5-8). As the temperature had to be limited in these experiments, to be able to clean the windows, a reduction in laminar flame speed had to be compensated with the reduction in turbulence intensity. The mean flow in the center of

the vessel is close to 0m/s on average with a turbulence intensity u'≈0.5m/s ($u'_x = u'_y = u'_z = 0.28\mathrm{m/s}$). The integral length scales as determined by the spatial correlation functions in the combustion vessel (Figure 5-7) are about 4mm and are comparable with length scales in the engine along the cylinder axis (normal to axis length scales are about 4x bigger) at the start of ignition (Chapter 3.4).

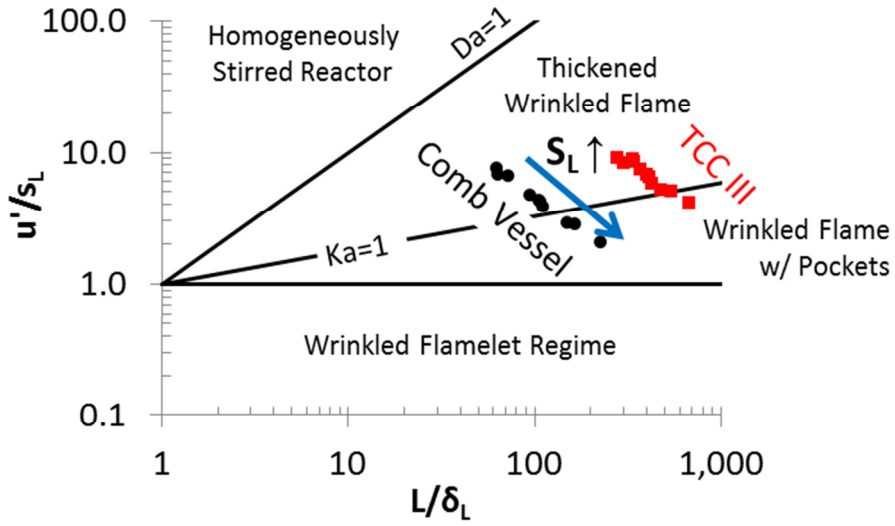

Figure 5-8 Borghi diagram showing the combustion regimes of combustion vessel experiments in comparison to TCC engine experiments

The reduction in turbulence intensity compared to the engine, $u'_{Engine} \approx 3$ m/s vs. $u'_{Vessel} \approx 0.28$ m/s, increases the integral time scale from $\tau_{\mathrm{L\,Engine}} = 1-2\mathrm{ms}$ to $\tau_{\mathrm{L\,Vessel}} \approx 80\mathrm{ms}$ in the combustion vessel as described above.

To link the test specific variability to fluid mechanic parameters, the combustion behavior is correlated with flow magnitude $|\mathrm{V}|$, individual velocity components Vx, Vy, Vz and various flow gradient parameters like flow acceleration $(= \frac{\mathrm{d}|\mathrm{V}|}{\mathrm{dt}})$, swirl and shear strength. These parameters are calculated in a 5x5mm^2 area around the spark plug (Figure 5-9) just before the time of ignition.

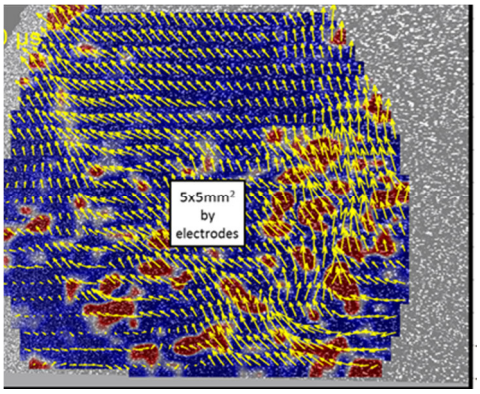

Figure 5-9 Illustration of spatial averaging area around the spark electrodes.

5.3 Results and Discussion

Two aspects of cycle-to-cycle combustion variability are treated in the following section. First, the overall level of combustion variability for different fuel-air mixtures was related to their Markstein number and their related sensitivity to shear strength. Second, the rich undiluted propane-air mixture, that exhibits the strongest sensitivity to shear strength, was examined in detail for the cause and effect mechanism(s) responsible for the high levels of variability.

All mixtures show an exponential burned gas volume increase with time, with a slight increase in slope when transitioning from the laminar to turbulent combustion regime. In Figure 5-10, the y_{N_2}=0.091 dilute propane mixture burned gas volume growth is plotted for the average stoichiometric, lean and rich mixtures, together with the respective fastest and slowest burning test. While the stoichiometric mixture burns fastest as expected, fuel rich and lean mixtures burn on average at the same rate, but the rich mixture shows a much bigger spread in burn curves indicating higher combustion variability. This means that the mean turbulent flame speed is the same for both mixtures, although the laminar unstretched flame speed at the rich condition is slower than in the lean case (see Table 4-2). There are two mechanisms that equilibrate the difference in flame speed, the first one being the Markstein number, which defines how the flame speed changes with stretch, and secondly surface area increase due to wrinkling. The sensitivity to surface stretch is especially important at small flame size and as such high stretch rates at that time are critical. Lean propane mixtures have a high Markstein number, which causes a reduction in laminar flame speed, whereas rich propane mixtures have

a small negative Markstein number and experiences a small increase in laminar flame speed, due to stretch.

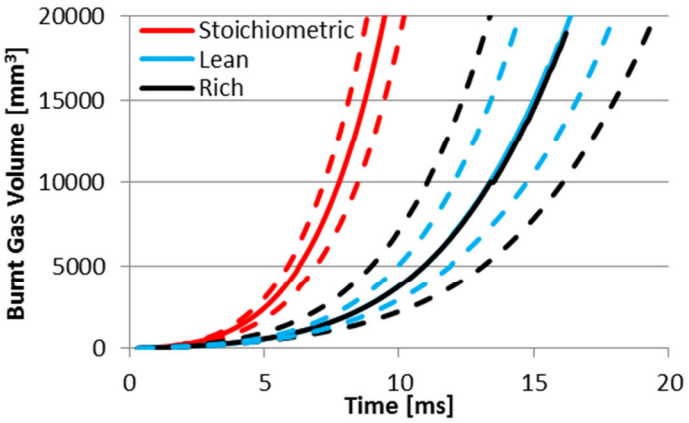

Figure 5-10 Average burned gas volume as function of time for propane with y_{N_2}=0.091 dilution. Dashed lines show the fastest and slowest burning test for each condition.

The variability behavior, quantified by the $COV(=\frac{Standard\ Deviation}{Average})$ of both flame volume and vessel pressure, is determined for all conditions and the variability is summarized in Figure 5-11. Fuel/air mixtures are separated by their variability behavior observed in the engine into low ($\mathrm{COV_{IMEP}} \approx 1\%$) and high ($\mathrm{COV_{IMEP}} \approx 5\%$) variability, in the left and right part of Figure 5-11 respectively. Despite similar operating conditions, the variability behavior in the combustion vessel does not follow the engine trends, but instead shows a wide spread in the high COV results. The maximum statistical error ($=\sqrt{\frac{2}{n-1}}$) in the COV for the sample size of 20-60 tests per mixture was determined to be 30-20% of the actual value, respectively. Based on this estimate, the observed differences in COVs for the different mixtures are statistically significant. Flame kernel volume is determined from the Schlieren images at early times when the pressure increase in the vessel is too small to be measured reliably. At later times, when the flame exceeds the field of view, the pressure signals are used for burned gas volume estimation. Both methods agree in the overlap region in which both techniques are sensitive as Figure 5-11 illustrates.

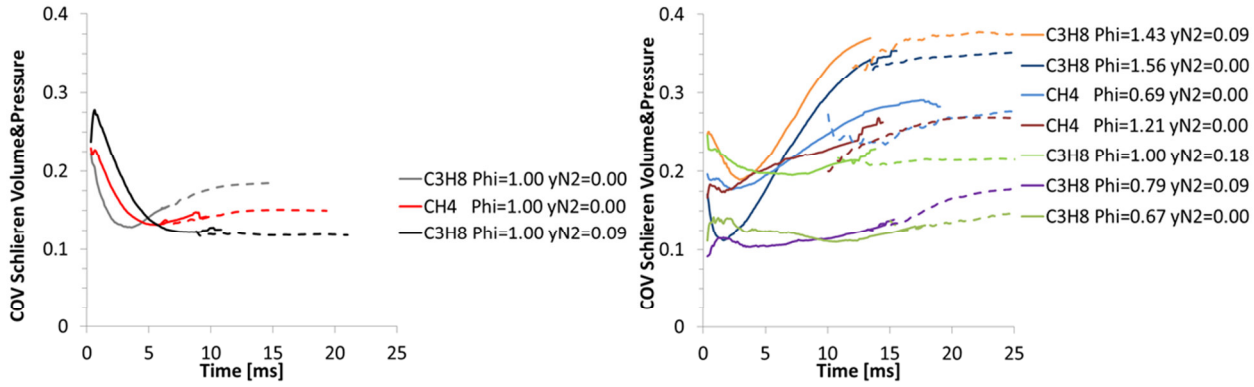

Figure 5-11 Coefficient of variance (COV) for various fuel air mixtures. Solid lines show volume data derived from Schlieren images, dashed lines show pressure based data that is used once the flame size exceeded the field of view of the Schlieren experiments. Left: Mixtures that have COV_{IMEP} ≈ 1% in engine tests. Right: Fuel-air mixtures with COV_{IMEP} ≈ 5% in engine tests.

The multi-diagnostics study presented here now allows further investigation into the causes for the observed variations in COV of flame growth; in particular the role of flow-related quantities is of interest here. Various flow parameters were examined for their influence on combustion events, including instantaneous velocity fields, shear and swirling strength, as well as their spatial and temporal evolution.

In the following section, the propane phi=1.56 case is investigated in detail for its high sensitivity to shear strength behavior as representative of the low Markstein number cases. Fig. 8 and 9 show the relation between shear strength in the flow, the subsequent wrinkling of the flame and its effect leading to faster flame growth due to increased surface area.

Experimental results are conditionally sampled by combustion rate, as measured from the development of the flame volume and it is found that tests with higher levels of flow acceleration and higher shear strength in the vicinity of the spark plug (see Figure 5-10) had faster combustion. Similar correlations are observed with other spatial and velocity gradient parameters in the flow field, but the effect is most pronounced in shear strength.

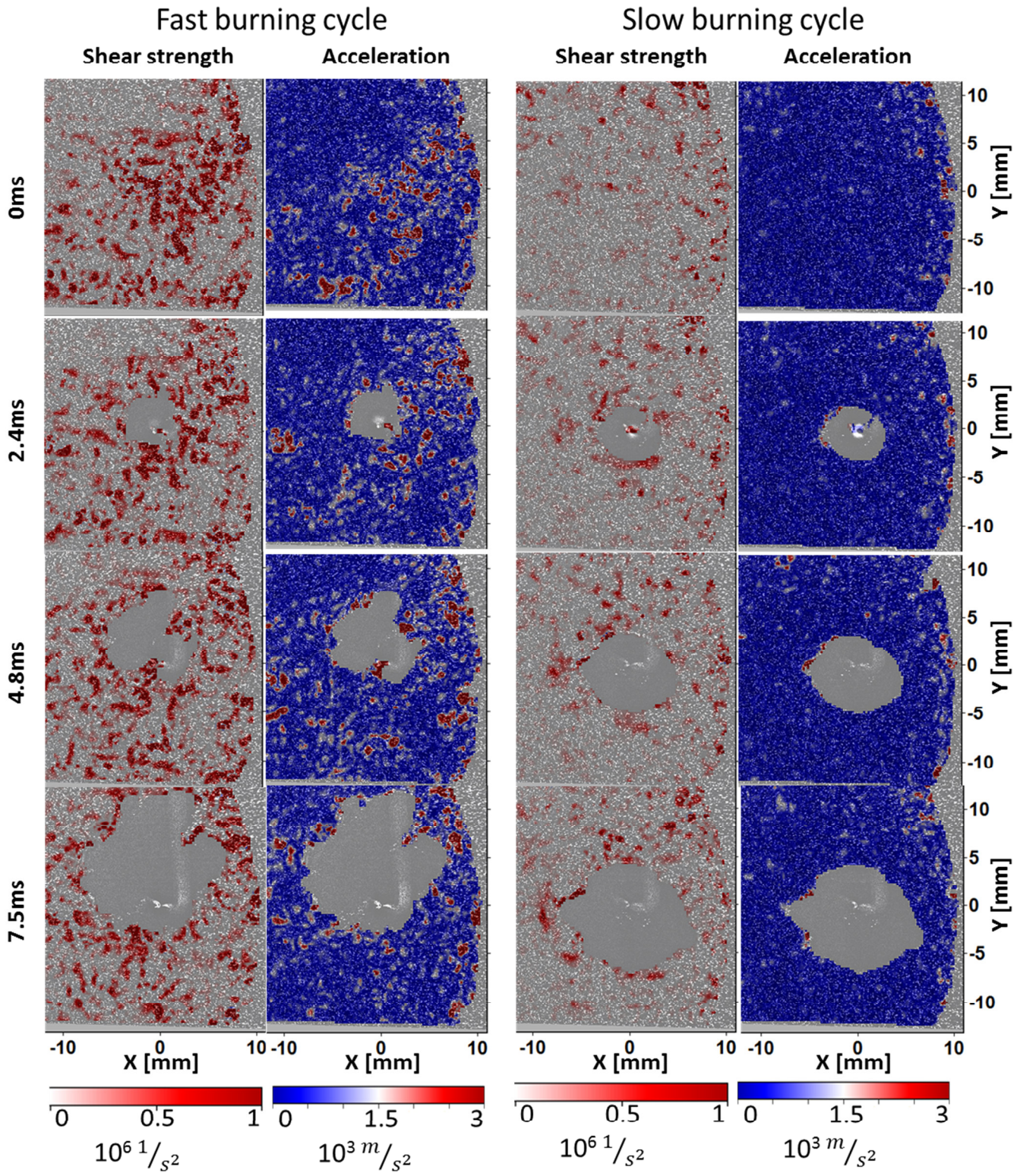

Figure 5-12 Magnitude of shear strength and flow acceleration are higher for fast burning cycle (left) compared to slow burning cycle (right) for different times at and after start of ignition.

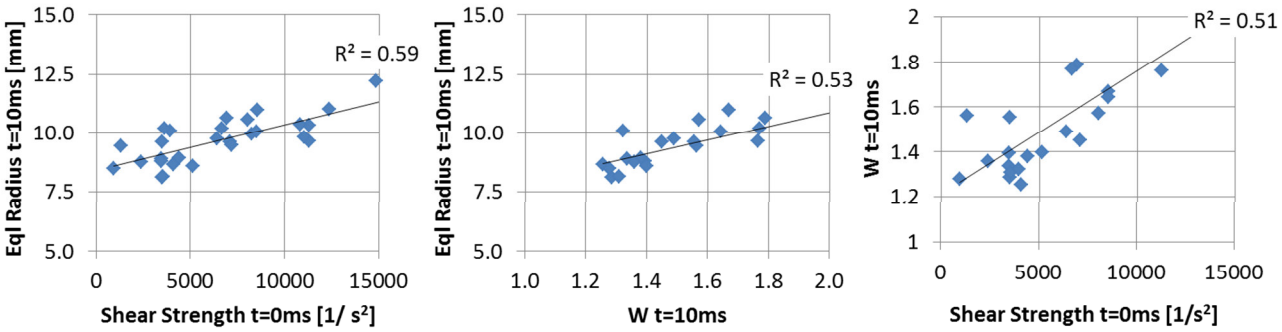

Figure 5-13 Higher shear strength at the time of ignition leads to faster flame growth (left). Bigger flames after 10ms have higher degrees of wrinkling W (middle). Higher degree of flame wrinkling correlates with higher levels of shear strength (right).

The effect of high levels of acceleration and shear strength on the flame wrinkling can be seen when comparing the wrinkling of the burned gas area edges for fast and slow burning cycles in Figure 5-12 and Figure 5-13. This behavior is more prominent for flames with lower Lewis number and small laminar flame speed as it is the case for both rich propane flames (shown in Figure 5-11). Low Lewis number flames tend to be more unstable, meaning that perturbations in the flame are self-enhancing (small cusps develop into big cusps). Thus even small perturbations have a significant effect on the later flame development. These findings are in agreement with LDV results for lean methane-air mixtures in an optical engine[24] that show the accelerating effect of increased turbulence intensity on flame growth up to u' values of 2.5m/s, the primary mechanism for generation of small scale turbulence is shear, which correlated with the flame development.

The level of combustion variability for different mixtures was found to be a function of the thermo-diffusive properties for the tested mixtures as shown in Figure 5-14 (right). Markstein numbers of a mixture of less than zero indicate that the flame is unstable; meaning that cusps, caused by perturbations (e.g. caused by flow), persist and grow bigger with time. This trend is confirmed when comparing the sensitivity of the flame to shear strength, as expressed by the correlation coefficient between the flame radii determined 10ms after ignition and the shear strength in the vicinity of the spark plug.

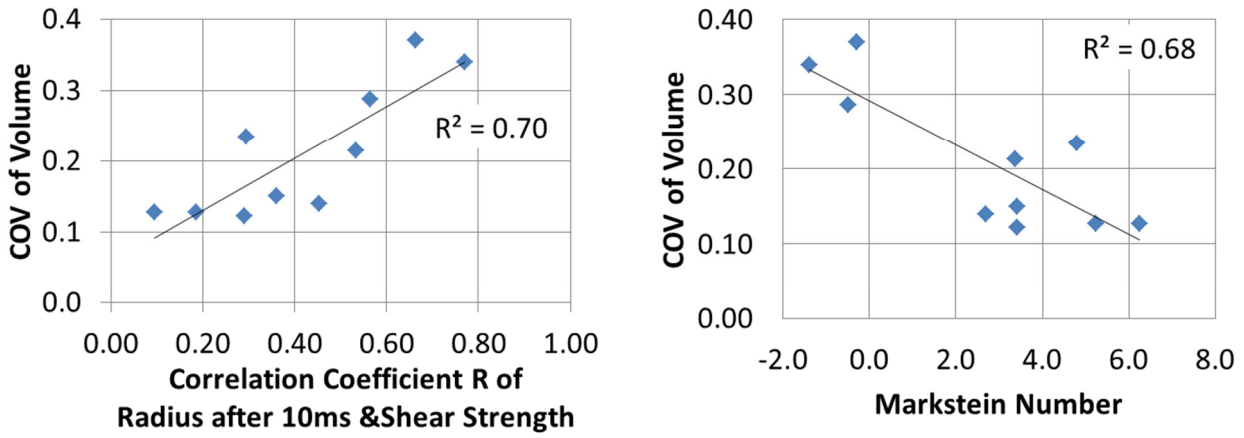

Figure 5-14 Left: Dependence of combustion variability on the mixtures' sensitivity to strength as determined by the correlation coefficient R between flame radius after 10ms and shear strength; Right: COV of burned gas volume dependence on Markstein number; linear fit quality to data points is given by coefficient of determination R^2.

This observed sensitivity of flame growth to flow properties scales linearly with equivalence ratio of the two fuels (Figure 5-15 left). When compared to the respective mixture's Markstein number the correlations for both fuels show that the smaller the Markstein number the more of the combustion variability can be linked to the shear strength at start of ignition (Figure 5-15 right). This indicates that cyclic variability behavior of flames is not only a function of laminar flame speed and turbulence [19], but also of the thermo-diffusive properties of the fuel air mixture. This is an important finding that needs to be included in advanced models to be able to predict cycle-to-cycle burn behavior for a variety of fuels and equivalent ratios.

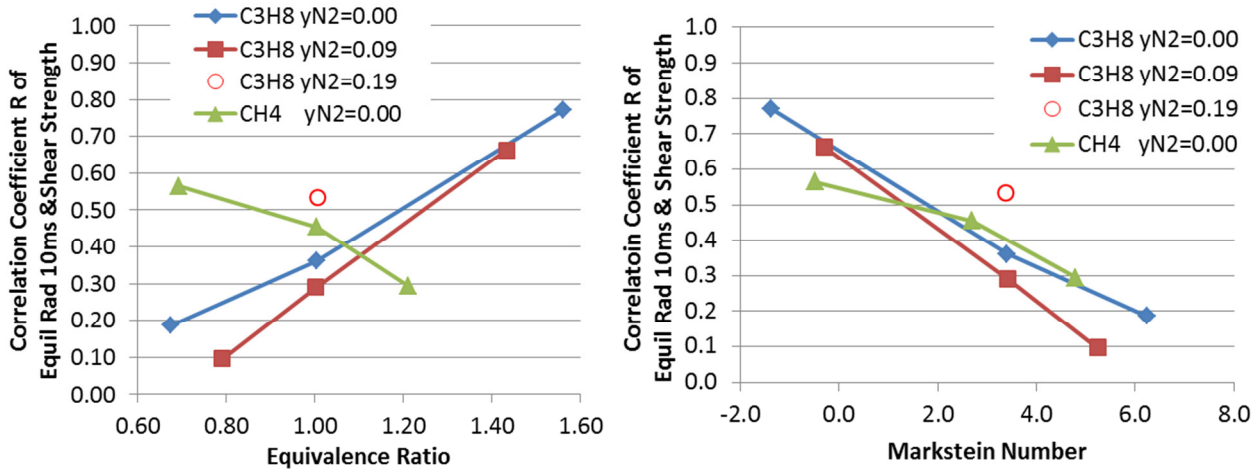

Figure 5-15 Sensitivity of combustion to shear strength for different fuel-air-nitrogen mixtures as function of stoichiometry and Markstein number

For the first time, this study showed the importance of the fuel's Markstein number and its impact on combustion variability. This is an important finding for practical applications especially when considering highly mass diffusive fuels like methane that are prone to these instabilities in lean mixtures. In these cases the combustion limit is influenced by the variability in shear strength in the vicinity of the spark plug by the point of ignition.

5.4 Conclusions

The combination of two-pass Schlieren, SPIV, high-speed pressure measurements, and spark voltage and current measurements was necessary for the in-depth analysis of combustion variability of methane and propane mixtures in a pressurized fan-stirred vessel. The optical measurements are used to track the three-dimensional motion of the flame, its 2-dimensional wrinkling structure, and to simultaneously measure quantitatively all three velocity components with high temporal resolution in a plane. The observed relationship between spatial and temporal gradient parameters, namely shear strength and acceleration, can be used to guide future engine experiments and systematically look for their influence on combustion with the goal to advance turbulent combustion models. It is demonstrated that the thermo-diffusive properties of the mixture are one factor that determines the level of combustion variability. For low Markstein numbers, the importance of the wrinkling due to shear and acceleration was shown in the combustion vessel under engine-like conditions. For rich propane flames with Φ=1.56, representative of low Markstein number mixtures, it is illustrated that gradients in the turbulent flow have a significant impact on the flame development. This knowledge can guide future in-engine tests that target cycle-to-cycle stability of combustion. CCV could be improved by designing combustion chambers that provide constant levels of shear strength and flow acceleration, allowing to push lean and highly dilute advanced engine concepts closer to the maximum efficiency limits. To capture the CCV behavior, mass diffusive effects should be modeled in engine CFD simulations for negative Markstein number mixtures when the flow time scales are long enough so that the instabilities have time to develop.

CHAPTER 6 ENGINE COMBUSTION VARIABILTY

All previous learnings are combined in this chapter to design multi-diagnostics engine experiments to improve the fundamental understanding of the causes to cycle-to-cycle combustion variations. Besides measuring pressures and spark energy at high temporal resolution, the flow field and temperature field by the spark plug and the early flame kernel growth are measured optically. The non-linear coupling requires that all these influencing variables are measured at the same time. In the previous chapters, it was shown that combustion variability is determined during the early part of combustion and that the closer parameters are measured to the spark plug, the more important they become for combustion. Pressure, spark, and image data was subsequently processed and characteristic metrics (velocities, flame kernel location, wrinkling, spark duration etc.) extracted to quantify the individual impact on combustion during each cycle for various combustion mixtures.

6.1 Experimental Approach

A three camera multi-diagnostic experiment is setup around the engine cylinder. All images are taken in vertical planes focusing on a 25x15mm^2 window around the spark plug. Figure 6-1 shows the combined system setup arranged around the optical engine as illustrated by the cylinder. A more detailed description of the individual techniques is provided in Chapter 2.

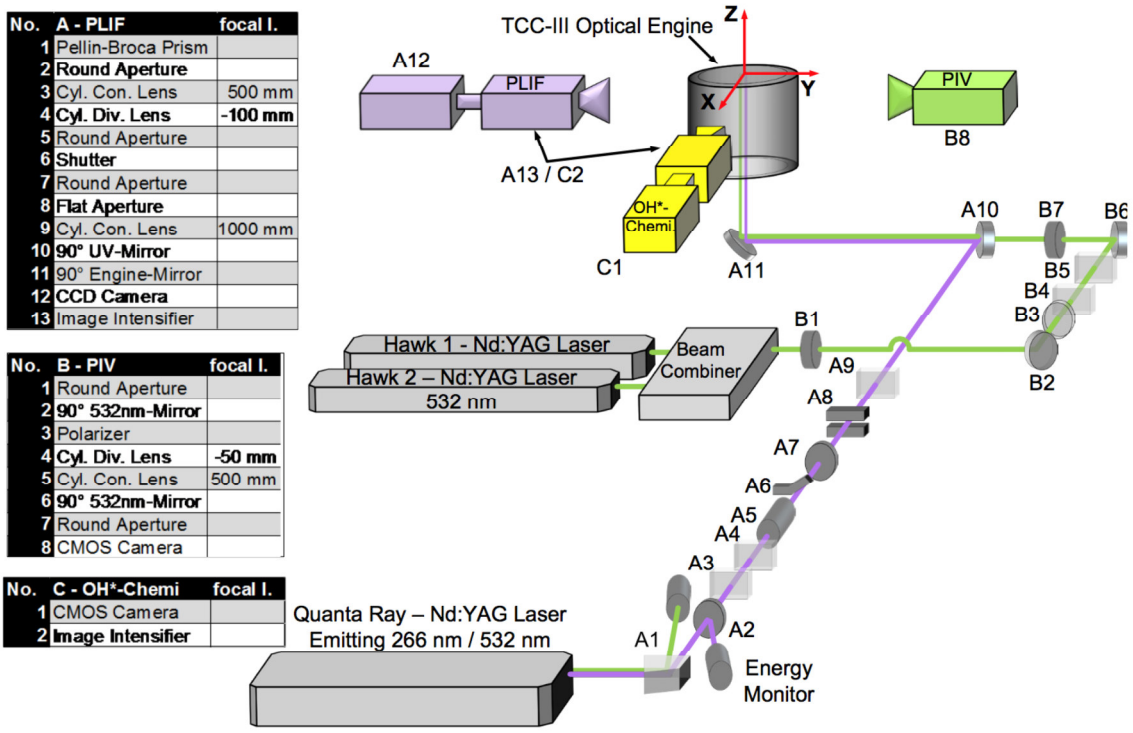

Figure 6-1 Multi-diagnostic optical setup at TCCIII engine; Figure extracted from [53]

Both planar light sheet based PIV and PLIF camera are on opposing sides of the engine facing each other, while the OH* chemiluminescence line-of-sight integrating camera tracks the flame motion perpendicular to the light sheets. Figure 6-2 shows a detail on the camera and light sheet positions as viewed from the bottom through the Bowditch port. Both light sheets are on the opposite side of the spark plug relative to their respective camera and in about 5mm distance to the cylinder center line. Although this is not the most desirable configuration to measure flow and gas temperature properties in the spark plug gap, it was the best compromise between image over exposure due to reflections of solid surfaces and proximity to the spark plug.

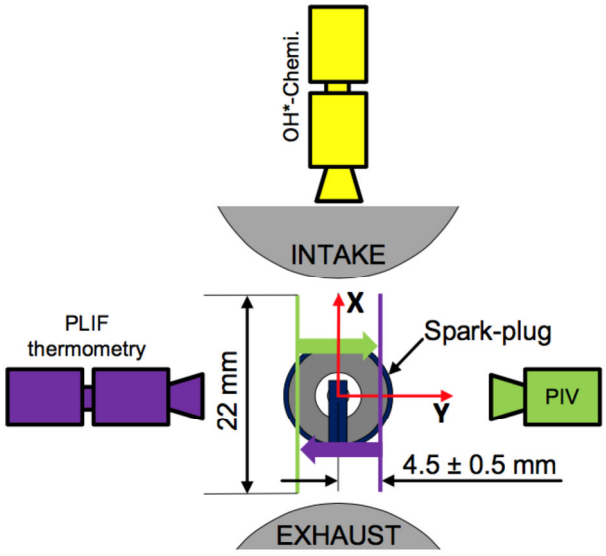

Figure 6-2 Bottom view of camera setup, with detailed laser sheet positions relative to spark plug; Figure extracted from [53]

The different imaging techniques were separated by wavelength using optical filters as well as temporally by offsetting laser pulses, camera exposure and image intensifier gate times. Both PIV double-frame and OH* images were taken every other CA, while PLIF temperature fields are acquired only once per cycle. Figure 6-3 shows a high-level trigger timeline illustrating when which system acquires data and how long the spark duration lasts. 12CAD before TDC, all three optical tools are used. Both PIV frames are acquired with a 10µs inter frame delay. During this dt period, first a PLIF temperature field is recorded, before imaging the OH*-Chemiluminescence of the growing flame kernel.

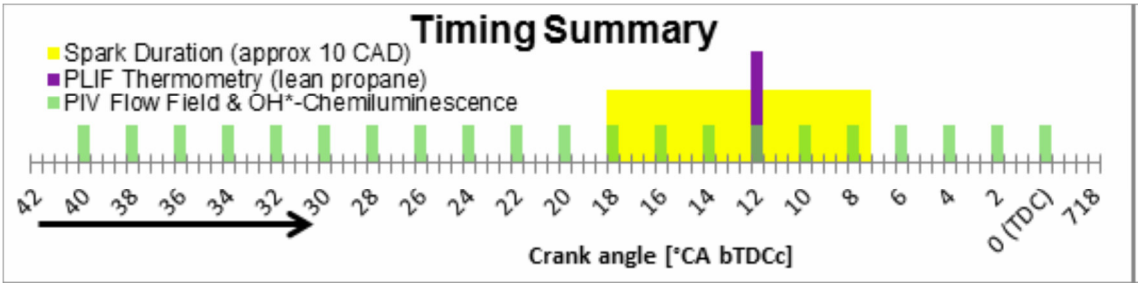

Figure 6-3 Multi-diagnostic timing; Figure extracted from [53]

6.2 Image Evaluation

For a cycle-to-cycle comparison, only cycle or spatial averaged quantities were considered as a robust metric to represent the in-cylinder conditions. Flow parameters of flow velocity

magnitude, x and z velocities, swirl and shear strength and vonMises Strain were extracted in a 12x6mm^2 area ((-4mm/-2mm) to (8mm/-8mm)) around the spark plug. In-order to retain more flow field information also POD coefficients 1 through 30 are taken into consideration. From Mie scattering and OH* imaging, the burned gas area information has been extracted and was also taken into account. For Mie scatter images the burned gas area, number of burned gas pockets and the wrinkling factor W as defined on Chapter 5.1, are extracted. In all OH* images, only one continuous flame source is identified and its area, centroid position, spark area at a threshold of 16000 counts, centroid of spark, and the ratio of minor vs major axis are extracted.

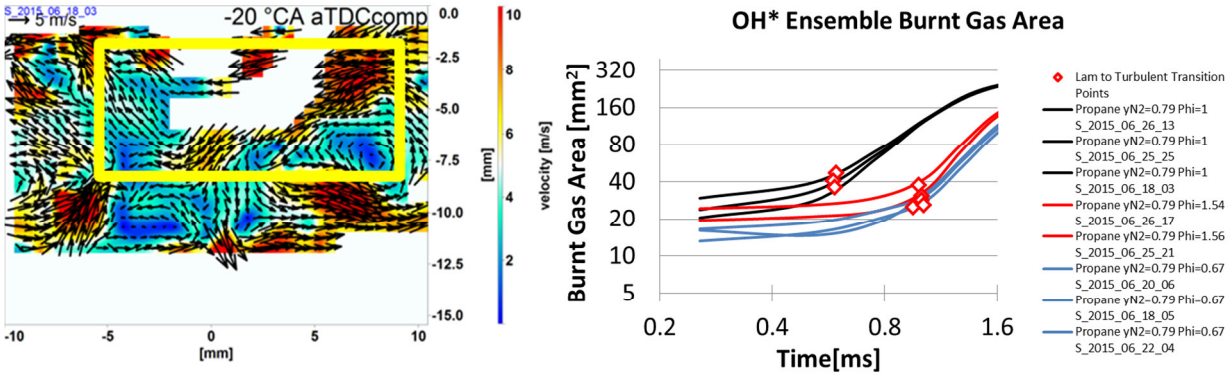

Figure 6-4 Left: Example flow field; Yellow box shows spatial averaging area; Right: Ensemble average OH* Chemiluminescence burned gas area shown in a log(A)-log(t) diagram; Squares show average mixture specific laminar to turbulent flame transition point.

A further processing of the OH* image data also the laminar to turbulent transition time was extracted according to the procedure explained on page 81.

6.3 Results

Combustion variability research is typically divided into two topics. Firstly, understanding the mean variability behavior of different conditions (Why does this condition on average show high or low variability?), and secondly, cycle-to-cycle combustion variability during steady state at one condition (Why did this cycle in particular burn fast or slowly?). Both CCV aspects are studied in this chapter in order to evaluate the effects of

- thermo-diffusive mixture properties
- flow patterns

on combustion and how the importance of different variability sources changes with different conditions.

6.3.1 Mixture Specific Mean Combustion Variability

The mean combustion variability behavior is well studied. Heywood and Ayala state that they observed COV_{IMEP} is proportional to the laminar flame speed divided by the eddy turn overtime [19]. In the TCC III engine a similar behavior is expected, because in the conducted experiments the engine speed is kept constant also the turbulence statistics and as such the eddy turn-over time remain constant and the COV_{IMEP} is a function of mixture properties only.

In the next chapter, it is shown that the laminar to turbulent transition time $\tau_{Lam-Turb}$ is important to determine the cycle-to-cycle combustion variations. It is desirable to know the average behavior of this factor macroscopically, for each test condition. The mean combustion variability is strongly correlated with CA10 combustion phasing as seen in Figure 6-5.

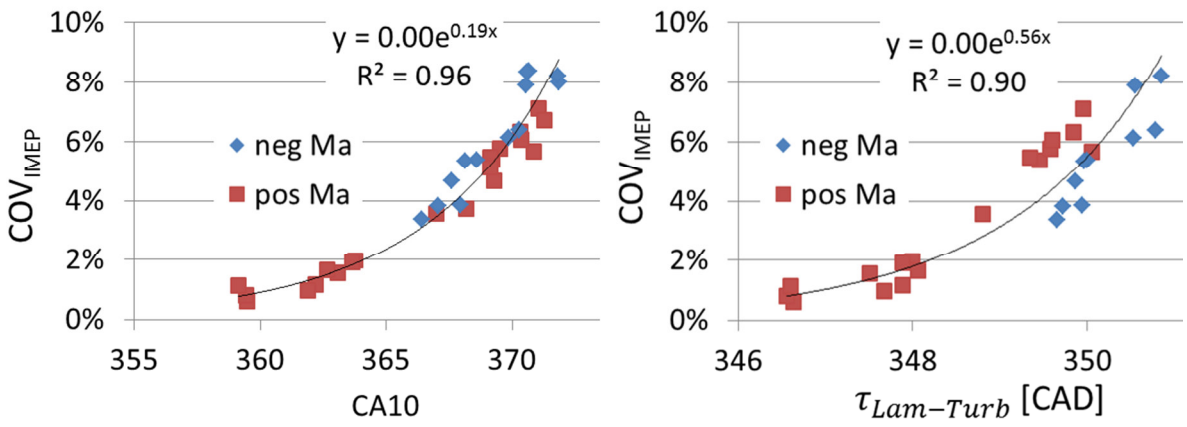

Figure 6-5 COV_{IMEP} scales exponentially with both phasing parameters CA10 (left) and laminar-to-turbulent time (right)

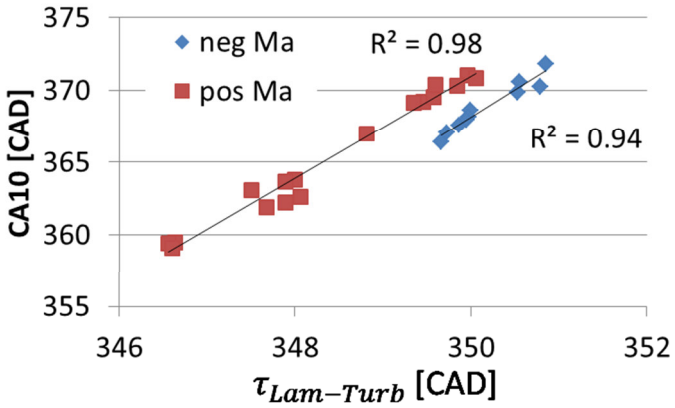

Figure 6-6 CA10 correlates linearly with laminar-to-turbulent time. Unstable negative Markstein mixtures advance faster to CA10 than positive stable flames.

The increase in $\tau_{Lam-Turb}$ with decreasing flame speed also increases the CA10 time (Figure 6-6). The transition time is solely dependent on the laminar unstretched flame speed (Figure 6-7) under constant turbulence conditions. The size at which the transition occurs is approximately constant with flame speed and is typically smaller than half the clearance distance (≈ 10mm) at these CAD.

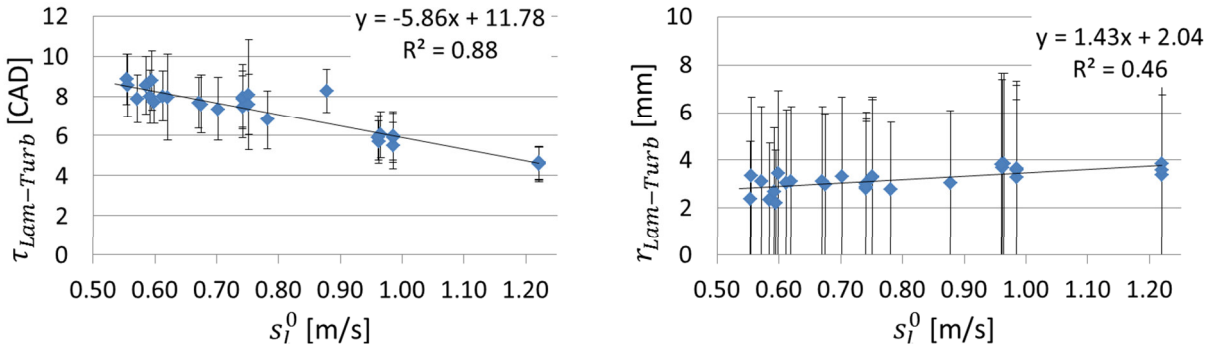

Figure 6-7 The laminar to turbulent transition time is uniquely a function of laminar flame speed. Symbols indicate mean values for each test. Error bars show +/- 1StDev. The radius at which the transition occurs is approximately constant and is typically smaller than half the clearance distance.

Laminar unstretched flame speed does determine for the most part combustion variability at constant engine speed. Here the flame speed is determined using a ChemKin model (for details see page 124).

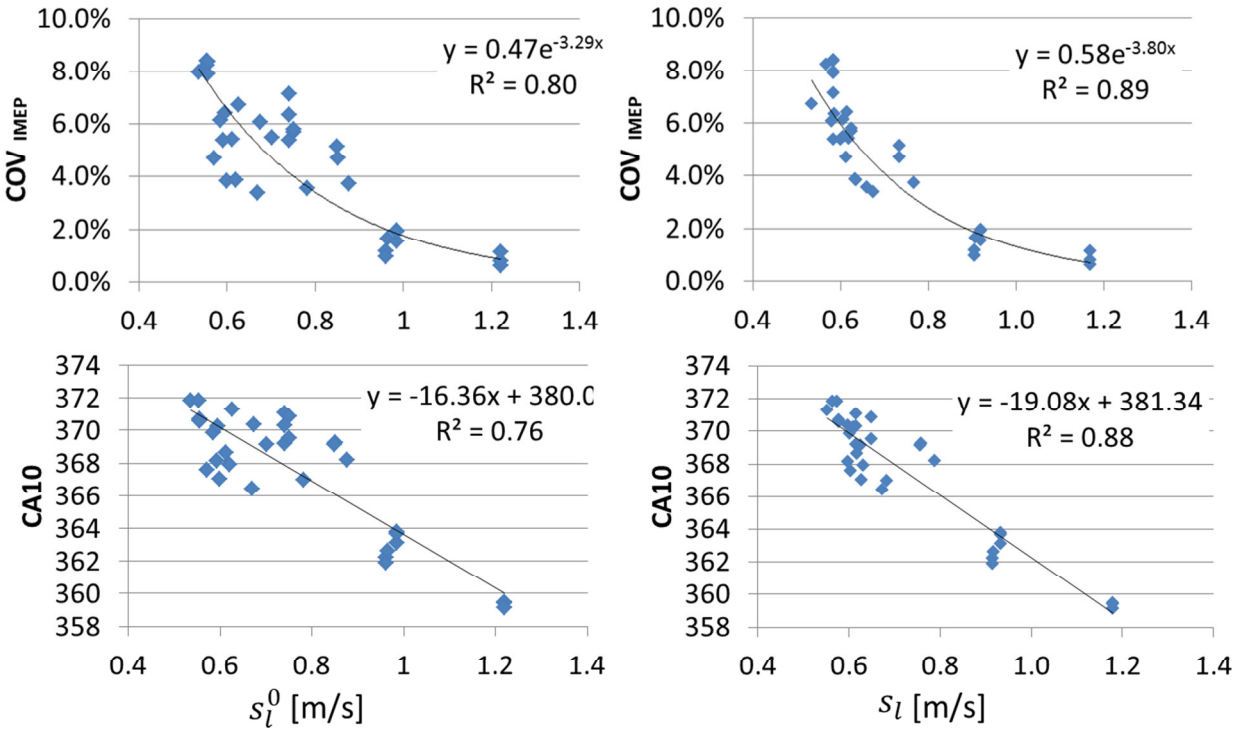

Figure 6-8 Correlation of combustion variability as measured by COV_{IMEP} (top) and combustion phasing (bottom) to unstretched laminar flame speed (left) and stretched laminar flame speed (right).

Based on the unstretched laminar flame speed, the stretched laminar flame speed is calculated by following the methodology of Law [35].

$$s_l = {s_l}^0 - L\kappa \quad (7)$$

L designates the Markstein length which is calculated from the fuel specific Markstein number correlation according to [39] and the flame thickness calculated in CHEMKIN. κ is the global flame stretch rate due to the propagation of an here assumed spherical flame.

$$\kappa = \frac{2}{r} * \frac{dr}{dt} \quad (6)$$

At early times when the flame is small, the stretch rate is calculated from the ensemble average line-of-sight integrated OH* area for each condition. It can be assumed that the flame is circular shaped, so that the flame radius can be calculated (Figure 6-9). With increasing flame size, the in-cylinder pressure measurement is more accurate and the flame volume can be calculated from the mass fraction burned as described in detail in Chapter 2.6.11. The volume is again estimated to be of spherical shape. With increasing flame size this assumption is less appropriate as the flame is restricted by piston and cylinder head and this leads to an underestimation of the stretch rate on the flame fronts.

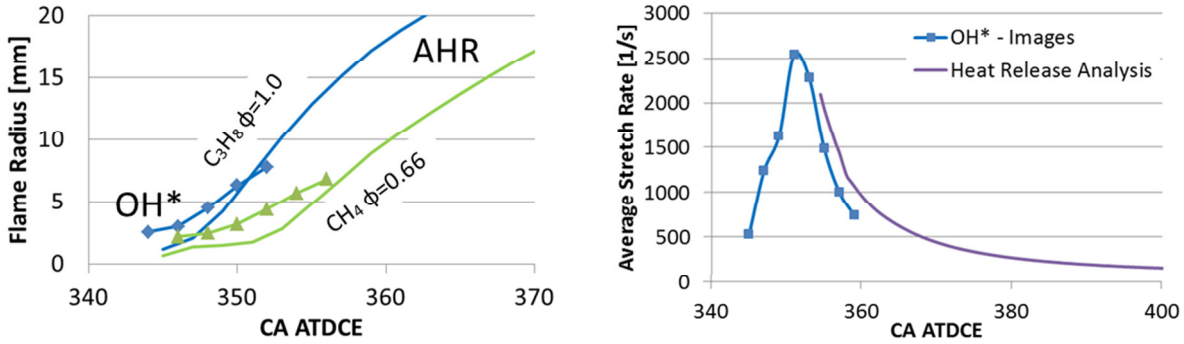

Figure 6-9 Flame radius and stretch rate for mean flame growth as determined by OH*-images and in-cylinder pressure measurements.

The agreement between images and pressure derived stretch rate is generally satisfying. The pressure over predicts especially at early CAD the stretch rates due to the small flame radii. From the stretch rate curve an average stretch rate needs to be determined to calculate the

stretched laminar flame speed. However Figure 6-10 shows that the exact stretch rate is not crucial and that the coefficient of determination R^2 is improved in almost the entire range of measured stretch rates over.

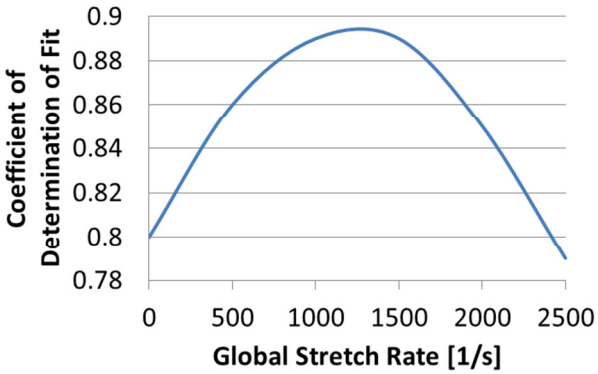

Figure 6-10 Sensitivity of R^2 in stretched combustion variability correlation in Figure 6-8 (right) to global geometric stretch rate.

6.3.2 Cycle-to-Cycle Combustion Variations

After understanding the mean variability behavior of each condition, the focus shifts to understanding why a particular cycle burns faster or slower. The flame is affected by various parameters at the same time, each contributing to the combustion progress. A multi-variant model approach is chosen to determine which parameters are the most important ones to combustion. In the previous chapter, it is demonstrated that the mean variability can be determined from the laminar-to-turbulent transition time. On a cycle-to-cycle basis this is not the case as Figure 6-11 illustrates. At stoichiometric conditions at MBT timing, the power output is not sensitive to phasing. For all other test mixtures, the combustion phasing is important as these conditions show higher variablity and the spark timing is kept constant. In these test cases the work output for a specific cycle is mostly determined in the period up to CA10. Although the laminar-to-turbulent timescale correlates linearly with CA10 on a test average basis, from cycle-to-cycle this correlation is not very strong (up to R^2 of about 0.2 is observed).

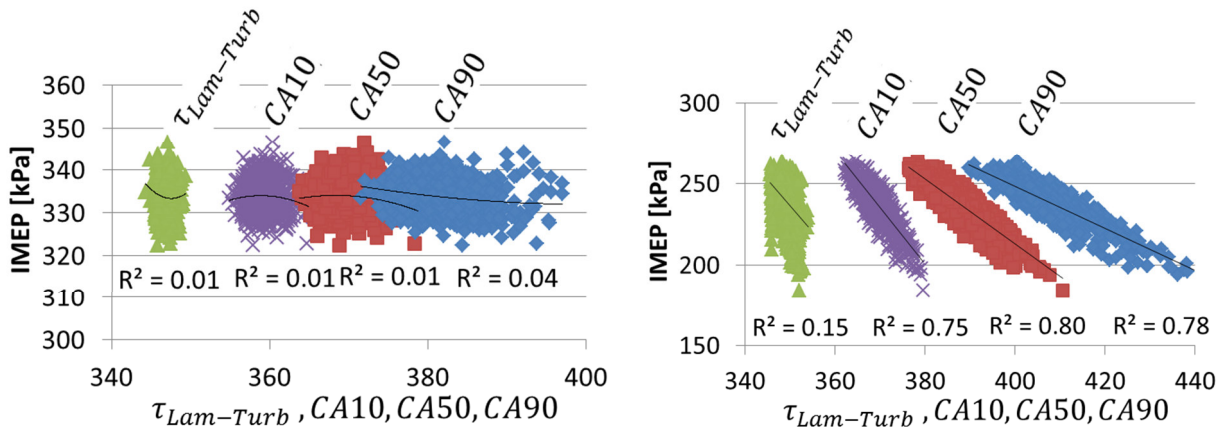

Figure 6-11 Cycle specific correlation between combustion phasing parameters and IMEP for an undilute stoichiometric propane (left) and a lean un-dilute propane condition (right).

Besides laminar-to-turbulent timescale, more than 400 variables have been calculated from all diagnostic techniques combined that can potentially affect combustion. Building a model on so many variables is not useful and a pre-screening to identify statistically relevant parameters is needed. A p-value analysis is used to quantify the statistical significance of each variable individually on the CA10 combustion phasing. It is not able to show any causality between the two respective parameters. In this study first a null hypothesis for in this case CA10 assuming there is no correlation between CA10 and null hypothesis. The p-value between the variable and the null hypothesis indicates if the variable is likely to be similar to the null hypothesis or if it shows rather an extreme phenomenon [97]. If it is an extreme phenomenon the null hypothesis is rejected and the variable investigated is correlated with CA10. This is essentially a double negative test. In Figure 6-12, an example of p-value distribution is shown for various flow quantities compared to the CA10 value. The gradient parameters shear, swirl, and von Mises, velocity magnitude and x-velocity component show for several CAD a statistical significance on CA10, whereas the z-velocity component is constantly below the set threshold having probably no statistical significance on CA10. More of these plots can be found in the appendix on page number 188. Low p-values indicate a high statistical significance to CA10, while p-Values of 1 indicate no correlation of the particular variable and CA10. As threshold of statistical significance, a p-value of 0.05 is typically used in literature [97]. It means that there is a 5% likely hood that the two variables are not correlated. In discussions with the University of

Michigan's CSCAR advisors it was recommended to use a p=0.05/400 threshold due to the large number of variables [personal conversation with Alex Cao, CSCAR advisor]. The variables identified as statistical significant are further reduced, by removing correlated values and only picking the most relevant ones (e.g. when Vx at 342CAD and Vx at 338CAD are identified as statistically significant only the most relevant is selected, because both are related as identified by the integral time scale of about 20CAD during this part of the cycle (see page 117)). All statistically significant parameters are cycle number, intake port pressure, exhaust port pressure of the previous cycle, spark duration, laminar-to-turbulent time, velocity magnitudes and x-velocity component at 320 and 342CA ATDCE, shear strength, swirl strength, and von Mises Strain at 342CAD.

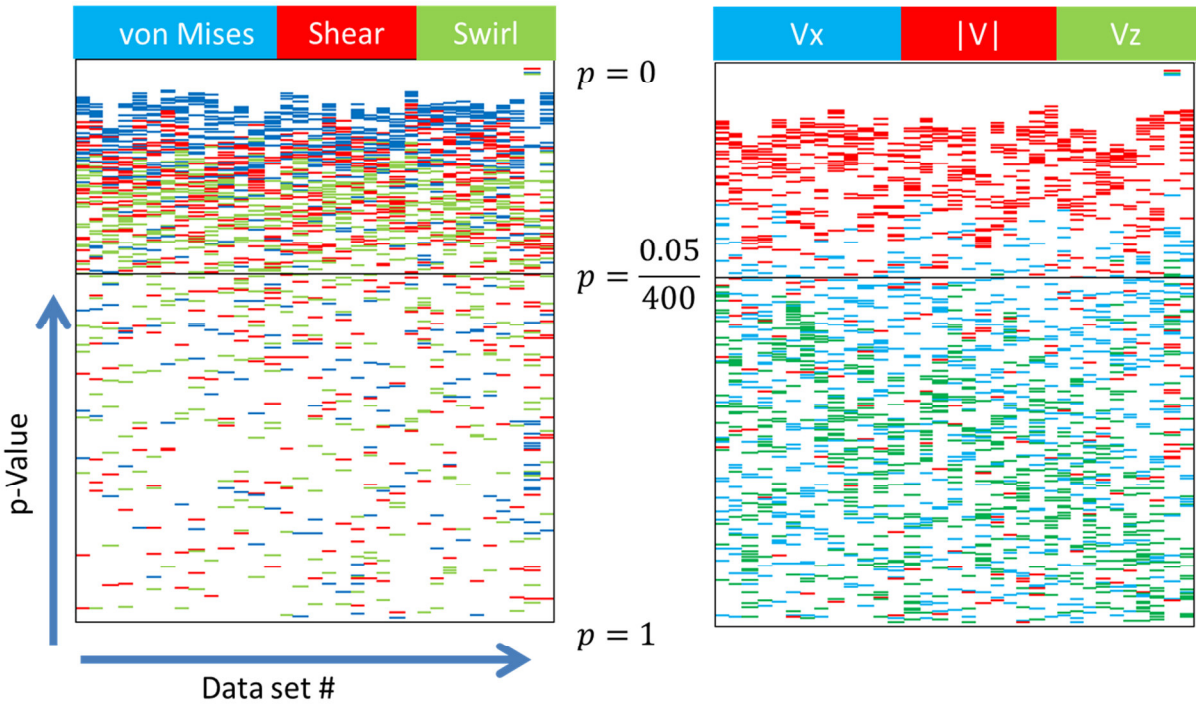

Figure 6-12 p-Value diagram to determine the statistical significance of each variable on CA10

Based on these variables, five linear models are generated to gauge which flow parameters are the most suitable to describe flow-flame interactions that impact combustion. Pressure and spark based parameters were used in all the models, but flow parameters were selected either from the ICA analysis, different POD mode combinations or physical flow parameters. Two ICA

cases were computed assuming three and ten independent sources for the flow field. More background on this analysis can be found on page 68. Here, it should just be noted that the lower number of independent components or sources show a spatially more homogenous flow velocity magnitudes than for the 10 source case which shows locally high velocities. The two models that contain POD mode coefficients contain either the five lowest (most energetic or most often occurring) mode coefficients at 320CAD and 342CAD ATDCE or the lowest 15 modes at the time of ignition at 342CAD ATDCE. The fifth model contains velocity magnitude and x-velocity component at 320 and 342CAD together with shear and swirl strength at 342CAD and von Mises strain also at 342CAD.

The models can consist of terms that are linear, square and interactions between the individual components. Individual terms are added and removed from the model, to check their relevance. For this, the build-in MATLAB algorithm (stepwiselm) tunes the coefficient after each iteration of adding and removing variables. Besides the model, coefficients, individual contributions of each independent variable, also the adjusted R^2 value are output as a result. The R^2 value determines the overall quality of the model.

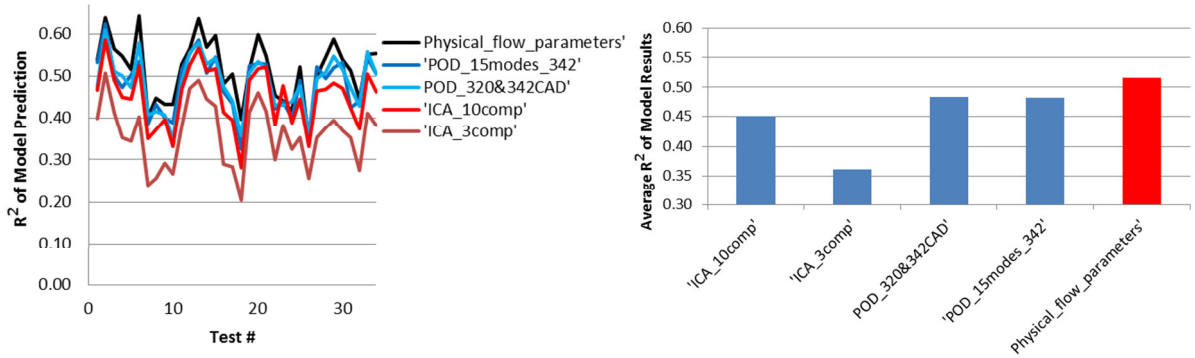

Figure 6-13 Comparison of model quality. High R^2 values indicate that the model containing physical flow parameters is better able to capture cycle-to-cycle variability effects.

For all tests but two, the model using physical flow parameters as inputs is able to better capture variability effects than the ones using POD or ICA coefficients. Although R^2 values of about 0.6 seem low, one needs to keep in mind that only data from a 2D cutting plane is available but the flame is influenced by a three dimensional flow. Due to its slightly higher capability of capturing variability and the easier interpretation of results on the actual flame

physics, only physical flow parameters are considered further in the model. Also in the case of the POD modes the correlations and as such the eventual effects causing CCV can be spread over a larger number of modes, which makes it difficult to point to a specific reason for a fast or slow burning cycle. The POD analysis here is performed on all 25000+ cycles, for which 80% of the energy is contained in the 35 lowest modes at the time of ignition (see Figure 6-14). The first mode represents the ensemble average flow field and contains about a third of the total flow energy. In this unsteady flow in this particular y=-5mm plane the POD modes don't show a pronounced shear flow by the spark plug as test in the z=-5mm plane showed (see Figure 4-12).

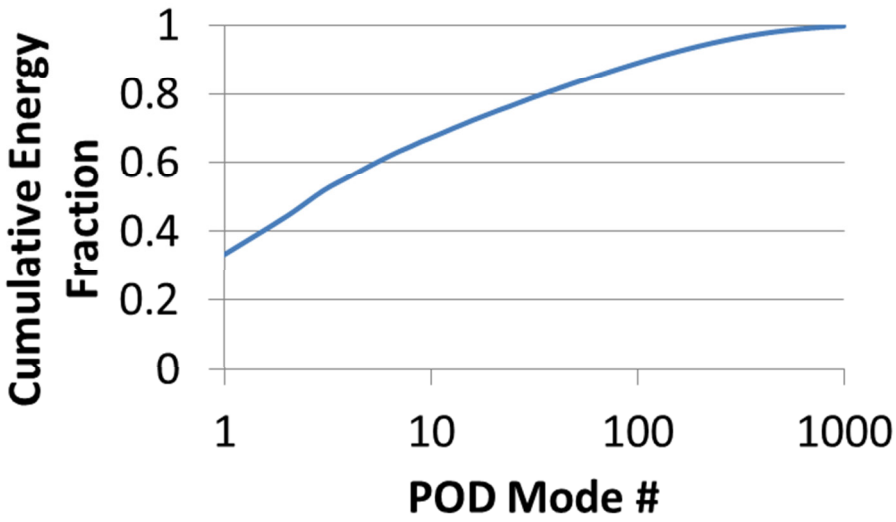

Figure 6-14 Cumulative energy fraction for POD modes at 342CA ATDCE. First 1000 modes contain 99.8% of the total energy.

The model is performing worse at low Markstein number cases, as shown by the lower R^2 values in Figure 6-15. This is a surprising outcome considering that especially those mixtures, showed a high sensitivity to shear strength in the combustion vessel experiments (Chapter 5) and their combustion progress. One reason for this difference might be that due to the low turbulence levels in the vessel flame wrinkling due to thermo-diffusive effects is a leading factor in creating surface area and accelerating combustion, whereas in the engine environment high velocities and higher turbulence level dominate the creation of wrinkles. This strengthens the

point already brought up in the previous chapter that thermo-diffusive effects are of secondary importance, compared to laminar flame speed and turbulence effects.

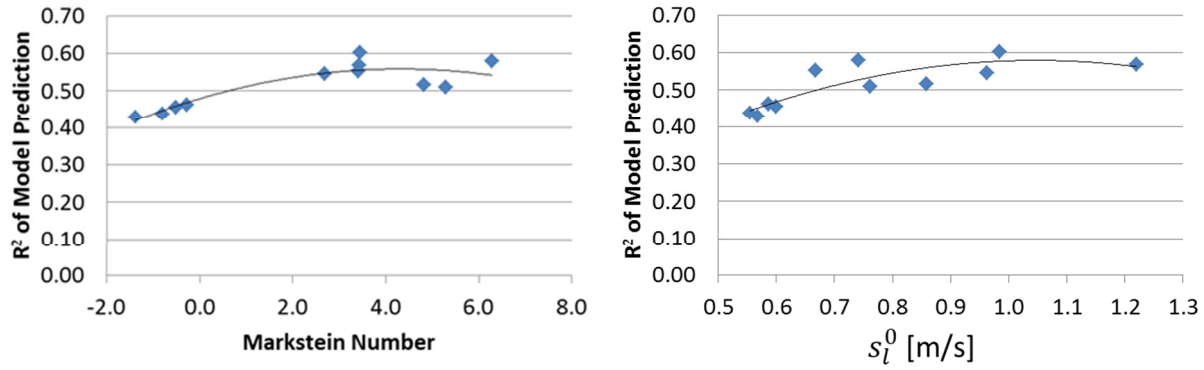

Figure 6-15 Performance of model using physical engine flow input parameters at different mixture properties.

The purpose of the model is primarily to learn about what factors are important to combustion and how they change with mixture properties and not to use the model in a predictive manner in an engine simulation. To learn about the importance of each variable the t-Statistic value is used rather than the model coefficients because the units and magnitudes of the input variables are not the same/comparable. The t-Statistic value is a measure of the importance of the individual variable to the model. It is calculated as [97]

$$t = \frac{\overline{y_1} - \overline{y_2}}{S_p \sqrt{\frac{1}{n_1} - \frac{1}{n_2}}} \qquad (35)$$

with $\overline{y_1} - \overline{y_2}$ being the difference in the means, S_p a estimate of the common variance, and n the sample sizes. S_p is computed from

$$S_p^2 = \frac{(n_1 - 1)S_1^2 + (n_2 - 1)S_2^2}{n_1 + n_2 - 2} \qquad (36)$$

with S_1^2 and S_2^2 being the variances from the individual samples. The variance is the square of the unbiased standard deviation and is calculated according to

$$S^2 = \frac{\sum_{i=1}^{n} (y_i - \bar{y})^2}{n - 1} \qquad (37)$$

If the magnitude of the t-Statistic is under 2 there is only a weak influence of the parameter on the result. If the magnitude is over 5 there is a strong influence of the output variable on the result [personal conversation with Kirby Shedden, CSCAR advisor] [97].

All significant effects are illustrated in Figure 6-16. Here the sign of the variables indicates in this particular case if with an increase of the variable CA10 increases (+) or decreases (-). The main contributors to cycle-to-cycle variations are cycle number, velocity magnitude and the laminar to turbulent transition time. During all tests the engine is still in a thermal transient such that with increasing cycle number, or runtime, the engine is heating up. This increases the mixture temperature and the laminar flame speed, causing the CA10 phasing to advance in the progress of a test. Also better ring performance and higher sparkplug temperatures could increase the gas temperature and as such the laminar flame speed. To reduce the effect only the last 400 cycles of each test were used for the model building. Higher flow velocities at the time of ignition also advance combustion. At this point in time at the measurement location the velocity direction seems to play a smaller role than the magnitude. A negative value for the x-velocity component implies that a flow directed away from the ground strap is favorable for the early flame growth. The longer the flame kernel needs to transition from laminar to turbulent, the later CA10 tends to be. Here, it is important to note that the laminar to turbulent time scale was identified to be directly correlated to the laminar flame speed, which in itself is a strong function of temperature. A higher x-velocity at 320CA degrees decreases the CA10 time. If referring to the full field of view flow fields in the z=-5mm plane (Figure 3-13) one can see that a high negative x-velocity at 320CA indicates a higher tumble and swirl motion, which advances combustion. Compared to the flow, the spark duration has a smaller effect on CA10 phasing (Figure 6-16). Longer duration sparks, tend to provide less electrical energy and cause a delayed combustion. The spark ignition event is also strongly influenced by the flow, as high cross flows increase the length of plasma arc jet, increasing the resistance (=more heat generation) and higher efficiency of transferring the heat to the gas as it is further away from the metal electrode surfaces. As such also the effect of the spark under these conditions might be attributed to the variability in the flow. At 342CA ATDCE the overall magnitude is more important than the sign of the x-velocity component. The z-velocity component is not

separately included in the model as it did not shown to be statistically significant on CA10 in the previously performed p-value analysis. As already observed in the combustion vessel experiment in the engine as well the gradient parameter shear is important for the flame development, but is not the leading cause in the engine. Higher levels of shear strength by the spark plug at the time of ignition foster the flame development and advance combustion. The opposing trend between CA10 and IMEP is due to the retarded timing of most of the operating conditions for which early CA10 cycles (lower CA10 value) have a higher IMEP. For the variable cycle number, this is different because this is a temperature transient effect because of which a decrease in work output is related to a reduction in in-cylinder trapped mass due to a lower density of the hotter charge mixture.

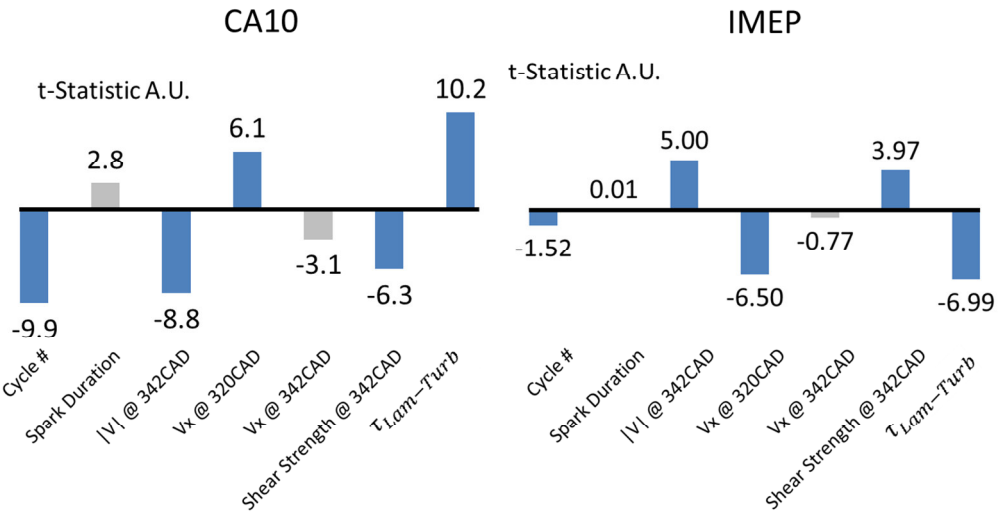

Figure 6-16 Importance of critical variables to CA10 combustion phasing (left) and IMEP (right) for all test cases.

Although the importance of the variables to the CA10 combustion phasing is presented in a concise manner in Figure 6-16, the results might be difficult to interpret. For illustration purposes, the data is subsampled to about the 10% slowest burning cycles. The distribution of these slowest burning cycles is compared to the entire dataset. The bar histogram shows the measured data, whereas the curves are fitted normal distributions for all cycles and fitted generalized extreme value distributions for the latest burning cycles (Figure 6-17 and Figure 6-18). These distributions are overlaid to improve the visualization, and also to better illustrate the skewedness in the distribution of the late burning cycles.

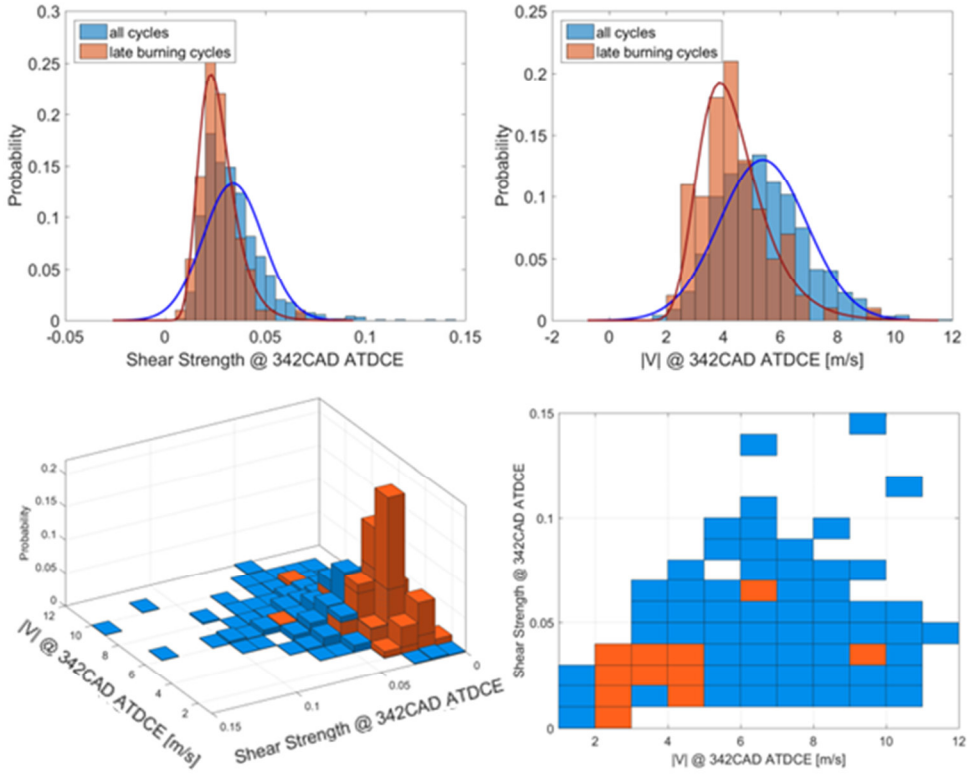

Figure 6-17 Probability distribution of 10% slowest burning cycles compared to the entire tests for propane ϕ=1.56. Examples shown here are shear strength and velocity magnitude.

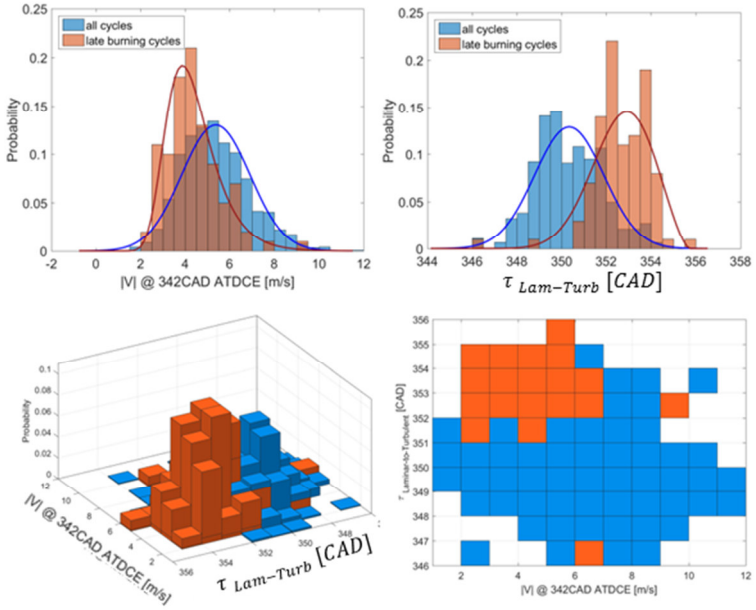

Figure 6-18 Probability distribution of 10% slowest burning cycles compared to the entire tests for propane ϕ=1.56. Examples shown here are velocity magnitude and laminar-to-turbulent time.

The coefficients in Figure 6-16 can be understood as the shift in probability in Figure 6-17 and Figure 6-18 of the slowest burning cycles compared to the entire dataset. For example, lower shear strength value to increase (delay) CA10, so the t-Statistic coefficient is negative (compare Figure 6-17 top left and the coefficient for shear strength in Figure 6-16 left). Lower velocity magnitudes at 342CA ATDCE delay (increase) CA10 combustion phasing, so this coefficient is also negative (compare Figure 6-17 top right and the coefficient for |V| at 342CA ATDCE in Figure 6-16 left). The skewedness of the distribution of the subsampled latest burning 10% cycles can be understood as the magnitude. When combining these two parameters in a 3-D plot (Figure 6-17 bottom) one can see that the late burning cycles are cornered. The coefficients in Figure 6-16 can be now understood as a multi-dimensional representation of these, showing what increases the probability of an earlier or later burning cycle.

After the evaluation of the average importance of flow, spark, and pressure variables, the change of importance of the individual variable on CA10 is discussed for different conditions (see Figure 6-19). In general, the variability behavior is similar between conditions, but some trends of change in importance are observed. Figure 6-20 illustrates how these trends can be understood and the t-Statistic values interpreted on the example of shear strength. Mixtures with lower shear strength tend to show lower combustion acceleration with increased shear. The t-Statistic value of about -4 indicates here that there is a weaker correlation between shear strength and CA10 which is illustrated in Figure 6-20 left. The undiluted propane case with high flame speeds shows a higher impact of shear at the time of ignition on the later combustion event Figure 6-20 right. Especially the lower sensitivity to shear is an unexpected result to find, as those were the mixtures that showed the highest dependence on shear in the combustion vessel experiments. Slower flames should also be more susceptible to perturbation, but in the dilute case also more time elapses between start of ignition and CA10, such that the correlation is weakened as more flow structures interact with the flame. The results on unstable low Markstein number flames showing a lower sensitivity to |V|, shear, and cycle number can be interpreted in a similar manner.

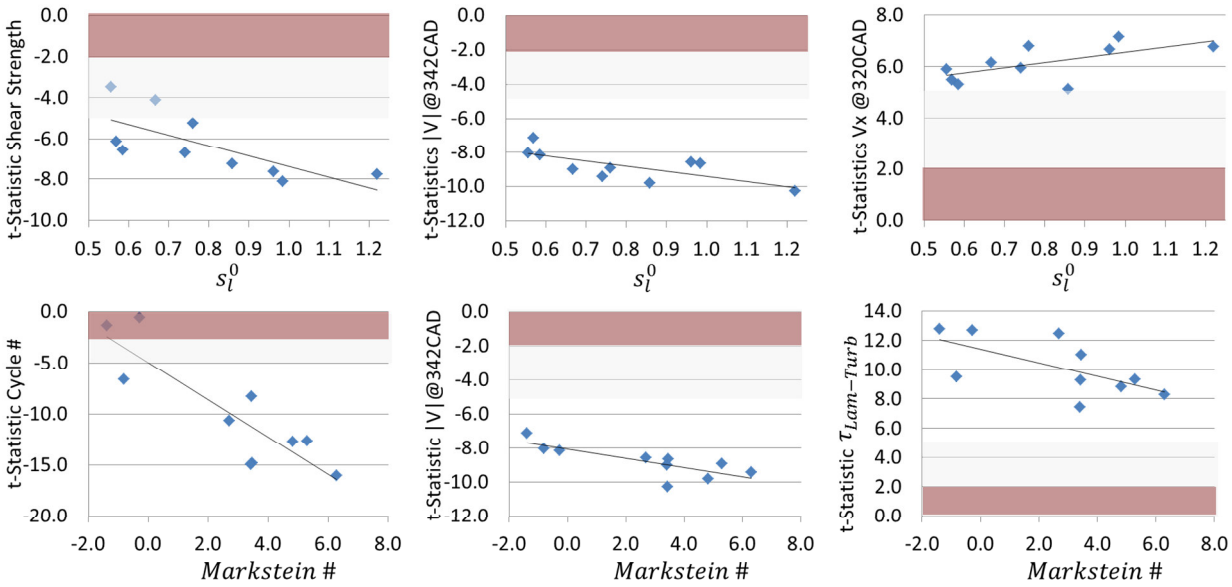

Figure 6-19 Change of importance of various variables on cycle-to-cycle CA10 variations with different mixture properties. Range of weak and medium importance to model are colored in red and grey, respectively. Black lines indicate linear fits. Flame speed in meter per second.

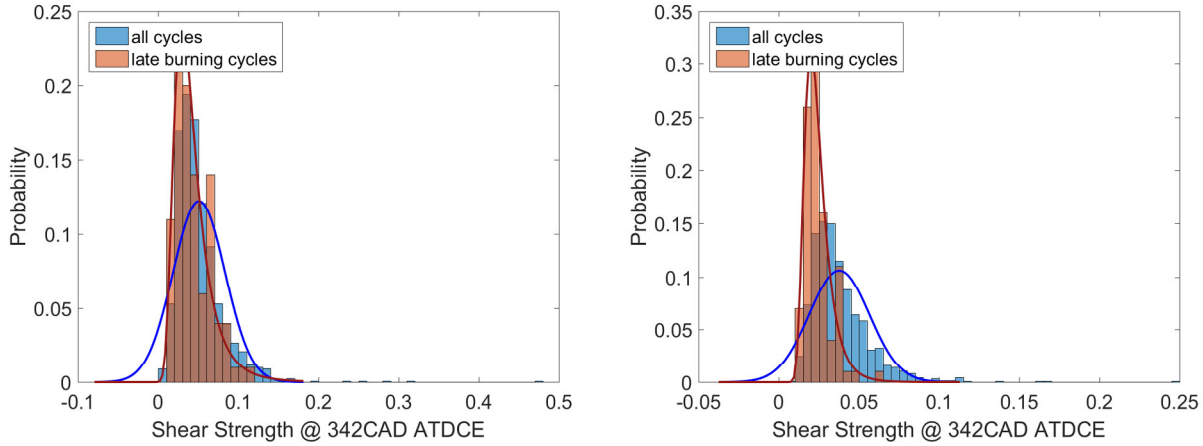

Figure 6-20 Probability distribution of 10% slowest burning cycles compared to all cycles for N2 dilute stoichiometric propane (left) and undiluted stoichiometric propane air mixture (right). A t-Statistic value of about -4 the distributions between late burn and all cycles is more similar for the dilute case (left) than for the t-Statistic value of -8 for the stoichiometric mixture (right).

6.4 Conclusion

A multi-diagnostic experiment is set up to explore the root causes of cycle-to-cycle variations in a spark-ignited optical engine. Strategically chosen premixed methane and propane-air

mixtures are used to determine the effects of laminar flame speed, thermo-diffusive effects, and changing the deficient species on the engine's variability behavior. Pressures, spark energies, flame contours, and velocity fields are measured simultaneously at kHz to MHz sampling rates to evaluate their respective contribution to the acceleration of the combustion event during a particular cycle.

The level of COV_{IMEP} for a specific condition is correlated to the laminar-to-turbulent flame transition time, which was determined optically from OH* images, and typically occurs before pressure diagnostics are sensitive enough to capture the growing flame. CA10 is linearly correlated with $\tau_{Lam-Turb}$ for positive and negative Markstein number mixtures. The difference in the thermos-diffusive properties between the mixtures results in an offset, such that unstable negative Markstein number mixtures show a higher growth rate from $\tau_{Lam-Turb}$ to CA10. The average laminar-to-turbulent transition time is dependent on the laminar unstretched flame speed only for a given turbulence condition, and the transition seems to occur for flames smaller than the piston-to-cylinder-head clearance distance. That the laminar flame speed is the determining factor for the COV_{IMEP} level as documented in literature, is confirmed in this study. A new finding here is that when stretch effects on the laminar flame speed are taken into account, the COV_{IMEP} can be captured approximately 10% more accurately. Taking the mass diffusive properties into considerations, could improve CFD modeling results especially for extremely lean and rich mixtures.

At each operating condition, the main contributors to cycle-to-cycle variations are identified and their relative impacts on combustion are quantified. From over 400 variables the statistically significant ones on the combustion event were filtered out using a p-value analysis. Of the important variables, different multi-variant models are created to assess the respective predictive capabilities of physical flow parameters, POD coefficients or ICA coefficients on combustion. It is shown that despite having fewer variables, the model containing physical flow parameters showed the best results and that the flow structures as identified by ICA or POD are not of special significance to the flame. The model identified that the transient state of the engine, velocity magnitude and shear strength at the time of ignition, the x-velocity component

as potential measure of swirl strength 22CAD before ignition, and $\tau_{Lam-Turb}$ are important factors for combustion phasing and work output of a particular cycle. In the practical variability limits tested here, the significance of the different variables did not change significantly for different operating conditions.

CHAPTER 7 SUMMARY, CONCLUSION AND FUTURE WORK

Stricter governmental emission regulations, the threat of a permanent climate change, and consumer demands for high fuel efficiency push the development of advanced cleaner and more efficient combustion strategies. All techniques that rely on spark ignition are limited in the efficiencies they can achieve by excessive cycle-to-cycle combustion variations. In order to push the efficiency envelop, a fundamental understanding of the root causes of these cycle-to-cycle combustion variations is instrumental.

A constant-volume combustion chamber and an optical spark-ignited 4-stroke 2-valve engine (TCC engine) are used to identify sources of combustion variability in homogenously pre-mixed propane and methane flames. Various passive and laser-based optical techniques are used in three test series to measure various factors that impact flame growth. 10 different fuel-air mixtures are strategically chosen to isolate the effects of laminar flame speed, thermo-diffusive mixture properties, and variation of stoichiometrically deficient species on the mechanisms that are responsible for cycle-to-cycle variations. The critical research questions that are answered in this thesis are first listed in a short list and then explained in a verbose manner:

1) How do the in-cylinder flow field average and flow variations change from motored to fired conditions?
   - In fired tests, the flow mean and RMS velocities are higher during gas exchange process, but lower at the time of ignition, due to higher charge viscosities, caused by higher temperatures.
   - The flow structures between fired and motored tests are similar during early compression stroke, but deviate especially in areas where the bulk flow motion is broken down into smaller structures.
   - Integral length and time scales in the pre-ignition flow are the same motored to fired.
2) What is the impact of the charge mixtures thermo-diffusive properties on cycle-to-cycle variations?

- In low isentropic turbulence conditions in a constant volume combustion vessel the sensitivity of flame growth to flow perturbation could be related to the mixtures' Markstein number.
- It is demonstrated that low Markstein number mixtures show advanced combustion phasing when exposed to high shear strength during the early flame kernel period in a low turbulence (u'=0.5m/s) constant volume combustion vessel.
- However in the engine experiments thermo-diffusive properties play a secondary role in determining CCV levels, after unstretched laminar flame speed.

3) Which flow properties impact cycle-to-cycle variations? Are decomposition methods like proper orthogonal decomposition (POD) and independent component analysis (ICA) suitable to isolate these quantities?
   - POD and ICA are not effective methods to isolate flow structures that impact CCV.
   - Parameters such as, spark duration, flow velocity magnitude and direction, shear strength, and laminar-to-turbulent time scale are identified to affect CCV in spark ignited engines. Their relative impact is quantified for different charge mixtures.

During the first set of experiments, the large scale flow field, as one of the major factors to CCV, is characterized in the TCC engine under motored and fired conditions. Crank-angle-resolved particle image velocimetry measurements are taken over several hundred consecutive cycles in two horizontal and two vertical cutting planes (only one plane at a time). Motored and fired flow fields are measured at engine speeds of 1300RPM with an intake manifold average pressure (IMAP) of 40kPa. Additionally, motored tests at 800 and 1300RPM with IMAP of 95kPa were conducted to show the scaling of flow field and mean and root-mean-square velocities with engine speed and intake pressure. Statistical error analysis and test-to-test repeatability show variations in boundary pressures of typically less than 2.5% and in-cylinder velocities of less than 2m/s for the respective condition. Turbulence length and time scales are found to be similar for motored and fired flows. Starting from mid-intake stroke, the integral time scale is increasing throughout the cycle until exhaust valve opening. The average integral length scale

as determined from the spatial correlation map, is from the intake stroke on increasing until the spatial flow structure size is being restricted by the piston motion in the late compression stroke. Next, the entire flow fields are compared and it is shown that differences between motored and fired flow fields occur especially during the early intake and late compression phase. In the fired cases, the intake jet shows initially higher velocities which are dissipated faster than in the motored case. Potentially lower kinetic energies or different gas viscosities increase the dissimilarities between motored and fired flow after 300CAD ATDCE when the well-structured tumble motion breaks down into a swirl dominated flow pattern due to the spatial restriction by the approaching piston.

In preliminary tests the rich, lean and nitrogen dilute variability limits, as defined by the coefficient of variance of the indicated mean effective pressure (COV_{IMEP}), are tested in engine experiments. The laminar flame-speed-effect on combustion is isolated by adding nitrogen dilution to stoichiometric propane-air mixture. To isolate thermo-diffusive effects, the laminar flame speed of propane is matched to the one of methane by adding nitrogen dilution. Both fuel rich and lean limits are investigated to explore the impact of deficient species. Besides the definition of a test matrix, PIV results are evaluated for a very lean propane case to gauge flow effects on combustion. It is shown that at the time of ignition flow structures close to the spark plug are of higher significance than bulk-flow-parameters further away. The next experiments focused on resolving the flow in the vicinity of the spark plug in greater detail. Also the need is identified to determine the most important flow parameters that affect the flame growth in a clean experiment, which isolates flow-flame interactions from temperature and mixture in-homogeneity effects and flame-wall-interactions.

In the University of Orléans fan-stirred combustion vessel, these variability effects of flame-flow interactions are investigated. To match the experimental conditions to the engine at time of ignition the same mixtures are ignited at the same pressure (6bar) as in-cylinder at the time of ignition. Due to the need to run the vessel at lower temperatures (323K) to be able to safely clean the windows, the turbulence intensity (u'=0.5m/s) is decreased such that the vessel experiments are in the thickened wrinkled flame and wrinkled flame with pocket combustion

regimes as in the engine. In terms of the mean combustion behavior it is shown that under these conditions thermo-diffusive effects are the leading factor contributing to the mixtures combustion variability. Unstable negative Markstein number mixtures tend to exhibit higher combustion variability than stable positive Markstein number mixtures. It is also demonstrated that steeper gradients in the flow field (e.g. flow acceleration, shear strength, etc.) at the time of ignition can enhance combustion especially for low Markstein number mixtures, such as rich propane or lean methane. High shear strength at the point of ignition fosters wrinkling of the flame, increasing the surface area, leading finally to faster combustion during this cycle. Thermo-diffusive properties of the mixture determine how sensitive the flames are to these perturbations and play as such an important role on the combustion variability behavior under these conditions. To capture the CCV behavior, mass diffusive effects should be modeled in engine CFD simulations for negative Markstein number mixtures when the flow time scales are long enough so that the instabilities have time to develop.

In order to verify if these findings hold true for cycle-to-cycle combustion variations in an actual engine, in-cylinder flow velocity, spark-discharge energy and duration, OH* chemiluminescence, and pressure are measured simultaneously. The mean combustion variability in the engine is mostly (≈80%) determined by the unstretched laminar flame speed of the mixture. When taking stretch effects into account the COV_{IMEP} can be predicted about 10% better than when using solely the unstretched flame speed. IMEP correlates well with CA10 (R^2 =0.94) and the laminar-to-turbulent transition time (R^2=0.9) when looking at test averages. Both CA10 and laminar-to-turbulence transition time are linearly correlated to the unstretched laminar flame speed. On a cycle-to-cycle basis, most of the variability (≈ 80%) for IMEP is determined during the CA10 period in the critical high-variability cases. Only a fraction of IMEP (≈ 15%) could be correlated to earlier laminar-to-turbulent transition times. Flow structures as identified by POD or ICA are not efficient in identifying structures that can be correlated to combustion variability. Physical flow parameters that could be identified to affect combustion are the velocity magnitude and shear strength at the time of ignition and the horizontal x-velocity component as potential indicator of swirl during a particular cycle. All tests had to be conducted at a semi-steady-state such that also the cycle number as a potential indicator of the

in-cylinder temperature affected combustion. The relative impact of these parameters to IMEP and CA10 is quantified for all mixtures and shows some weak dependence on Markstein number and laminar flame speed. The difference in variability behavior between combustion vessel and engine might be due to the differences in turbulence intensities and flow velocities. The creation of surface area in low turbulence environment is more dependent on flame instabilities, whereas in a high-turbulence environment the thermo-diffusive effects merely play a secondary role and the primary mechanism for creation of flame area is flow turbulence.

7.1 Future Work

During the course of this work more scientific questions opened up that would be worth investigating. Since turbulence is a three dimensional phenomenon it would greatly improve the understanding of cycle-to-cycle variation if a volumetric flow field around the spark plug is measured in high resolution even if only as a once per-cycle diagnostic. If only 2D diagnostics are available, the next best experiment is measuring the velocity in a horizontal plane, with a high dynamic range and high spatial resolution camera to resolve detailed structures around the spark plug. The z-velocity component did not seem to exhibit an effect on combustion variability, but this might be due to the approximately equal distance between sparkplug gap, cylinder head, and piston close to top dead center.

Future experiments of cycle-to-cycle variations should be performed under better steady-state conditions. Longer run times do not seem feasible with a full quartz liner. As such, it is recommended to use a metal liner and a quartz ring. Skip-fired operation is also a way of reducing the thermal load on the components but cleanliness might become an issue.

The laminar-to-turbulent time has an important effect on the variability. In contrast to the flow measurements, the flame time scales are much faster and a rate of at least 1 image/CAD is desirable. Because of the high luminosity of the spark, it is recommended to switch the ignition system from a slow glow discharge to a high power break down ignition system. If the change of the ignition system is not an option, imaging techniques such as Schlieren or shadowgraph techniques that are not sensitive to spark luminosity but have the drawbacks of being more sensitive to dirt on optical components and require a more complex optical setup than a direct

imaging of the flame. If done in 3D this technique could also allow a better understanding of flame wall interactions and as such IMEP variations that cannot be attributed to combustion phasing as determined during the early part of the cycle.

As shown in this work, many of the phasing parameters are strongly dependent on laminar flame speed. It is recommended to do a thorough analysis of temperature stratification by the spark plug to quantify cycle-to-cycle temperature fluctuations. For combined temperature and PIV measurements, different tracers or seeding particles should be used that do show less spectral overlap. A combination of toluene as temperature tracer and solid PIV seed particle would remove this cross-talk and allow some imaging of velocity information in the flame.

Thermal-diffusive instabilities and turbulence are both shown to affect flame surface area creation. An extension of the test matrix to lower turbulence conditions is advised (by changing either engine speed, spark plug location, or intake geometry) in order to find the primary factor of flame wrinkling under the different turbulent combustion regimes. Also, different ignition sources could be tested to change the initial flame kernel size to investigate the impact of different stretch rates during ignition.

In the preliminary tests the analysis of multi-variant data presented in this thesis with neural networks seemed to be promising, but had to be abandoned due to the lack of sufficiently large sample sizes. It could be worthwhile to do more research on deep learning techniques that require less training data to pick-up more of the variability aspects in spark-ignited engines.

APPENDIX A RECOMMENDED ENGINE DATASETS

The list of recommended tests should serve as reference of the most stable, cleanest data sets. In general for all 1300RPM 40kPa IMAP conditions three repeated tests were recorded and fully processed.

Data Set ID	RPM	MAP	Fired/Motored	Imaging Plane
S_2014_05_20_02	800	95	Motored	Y=0mm
S_2014_04_17_02	800	95	Motored	Z=-30mm
S_2014_05_13_03	800	95	Motored	Z=-5mm
S_2014_05_20_01	1300	95	Motored	Y=0mm
S_2014_04_17_01	1300	95	Motored	Z=-30mm
S_2014_05_13_02	1300	95	Motored	Z=-5mm

Wide open throttle recommended motored tests

Data Set ID	RPM	MAP	Fired/Motored	Imaging Plane
S_2013_10_24_01	1300	40	Motored	Y=0mm
S_2014_02_05_02	1300	40	Motored	X=0mm
S_2014_04_16_02	1300	40	Motored	Z=-30mm
S_2014_05_05_01	1300	40	Motored	Z=-5mm
S_2013_10_29_01	1300	40	Fired	Y=0mm
S_2014_02_13_02	1300	40	Fired	X=0mm
S_2014_04_03_02	1300	40	Fired	Z=-30mm
S_2014_05_08_01	1300	40	Fired	Z=-5mm

Motored and fired recommended datasets for full field of view PIV measurements

Test ID	Equival	Fuel	Dilutio	IMEP	COV IM
S_2015_06_22_04	0.67	Propane	0.79	230	7.1%
S_2015_06_18_03	1.00	Propane	0.79	334	1.1%
S_2015_06_26_17	1.54	Propane	0.79	293	3.8%
S_2015_06_22_08	0.78	Propane	0.81	244	5.7%
S_2015_06_25_23	1.00	Propane	0.81	313	1.5%
S_2015_06_23_03	1.43	Propane	0.81	270	5.4%
S_2015_06_26_15	1.00	Propane	0.83	264	5.5%
S_2015_06_26_23	0.66	Methane	0.79	211	7.9%
S_2015_06_23_10	0.69	Methane	0.79	229	6.4%
S_2015_06_26_03	1.00	Methane	0.79	330	1.0%
S_2015_06_19_07	1.20	Methane	0.79	296	3.7%

Recommended datasets for early kernel focused experiments

APPENDIX B TEST-TO-TEST PRESSURE REPEATABILITY

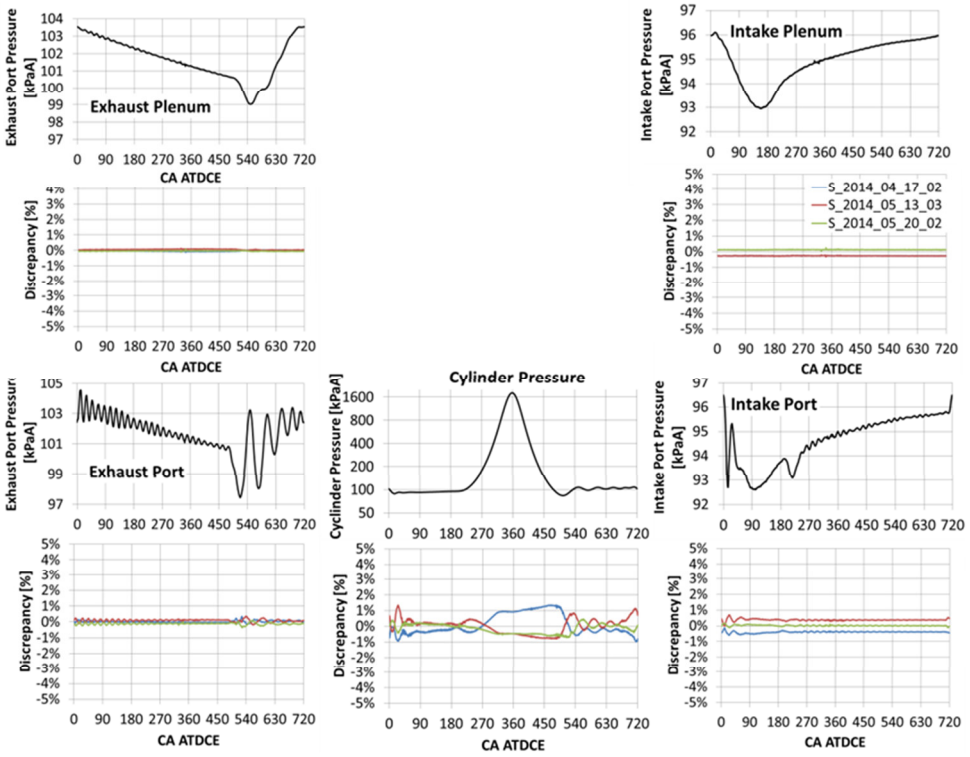

Pressure traces and test-to-test pressure discrepancy 800RPM 95kPa motored condition

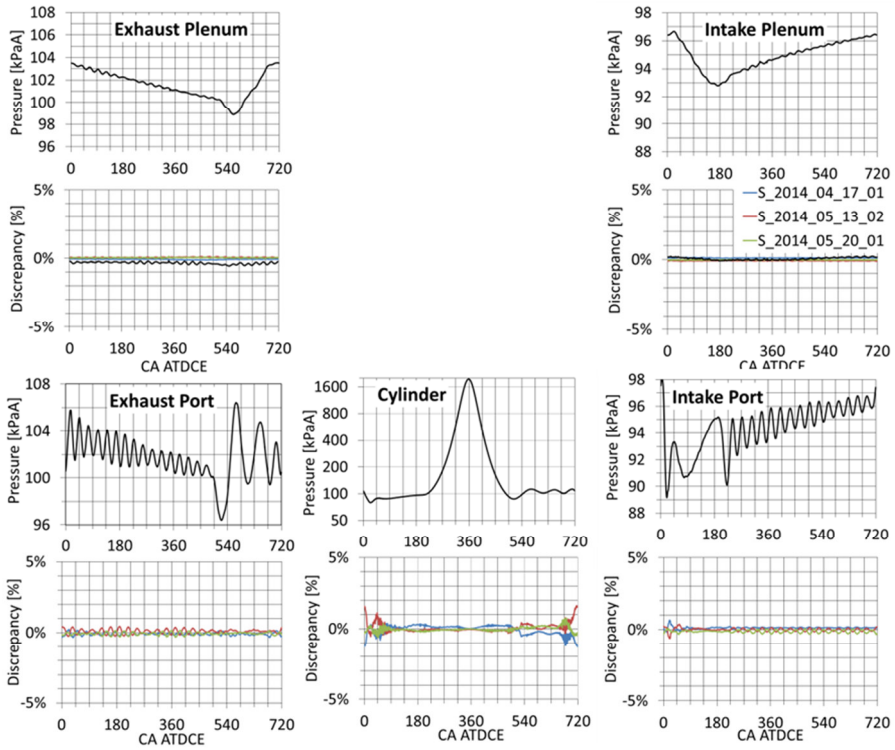

Pressure traces and test-to-test pressure discrepancy 1300RPM 95kPa motored condition

APPENDIX C QUANTITATIVE COMPARISON MOTORED VS. FIRED

Comparison of fired and motored flow field structure, mean and RMS velocity magnitude in different planes.

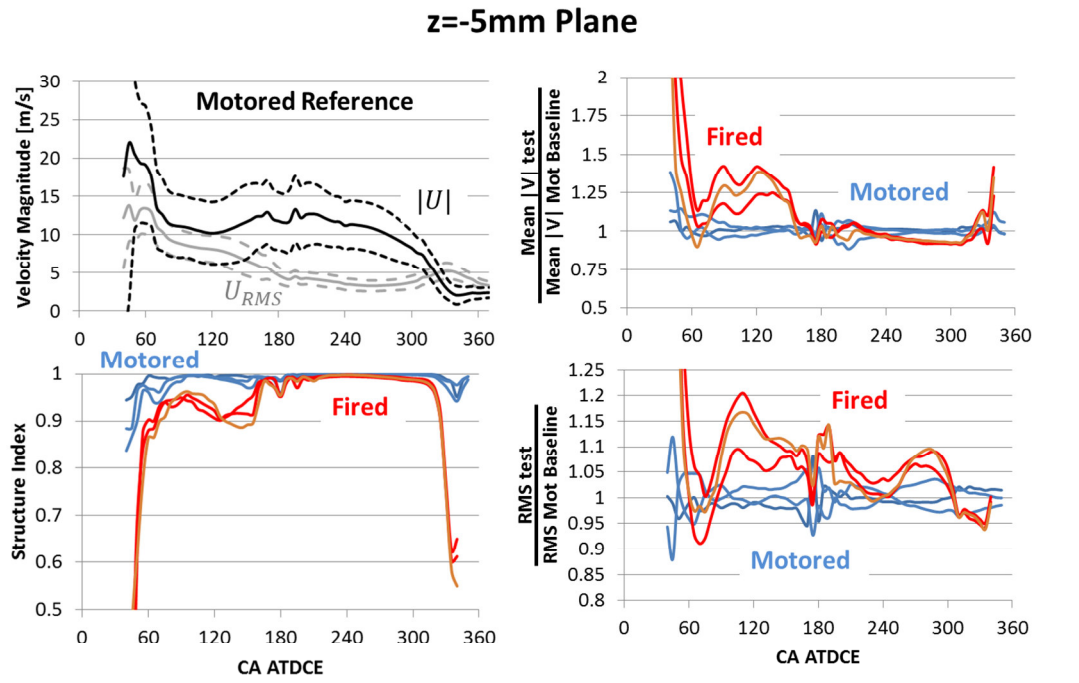

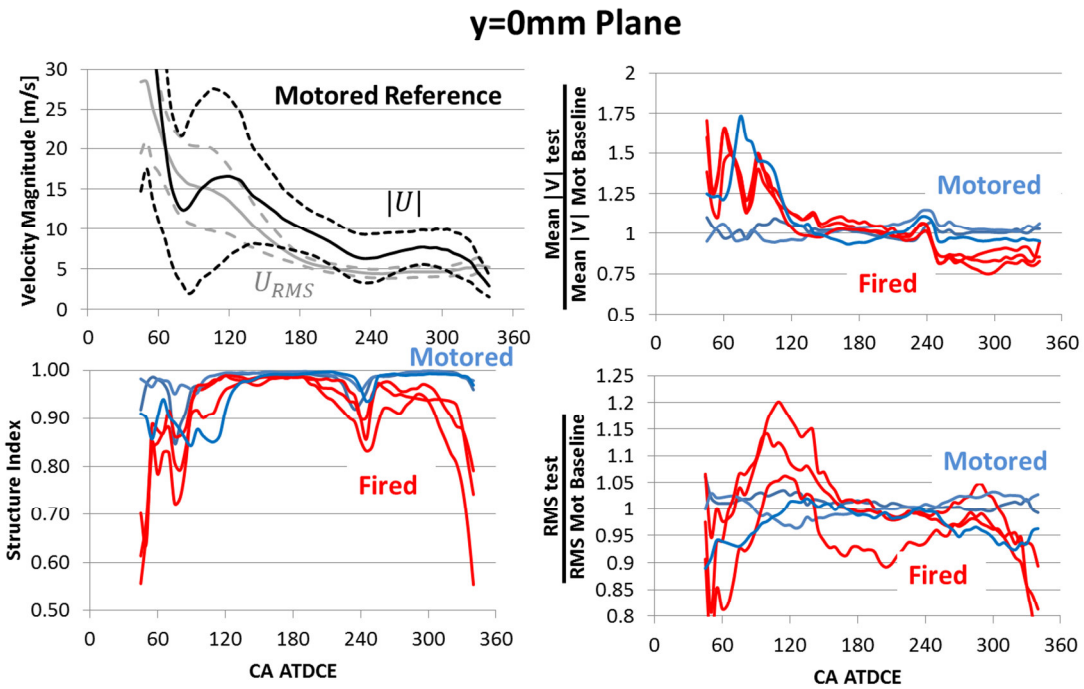

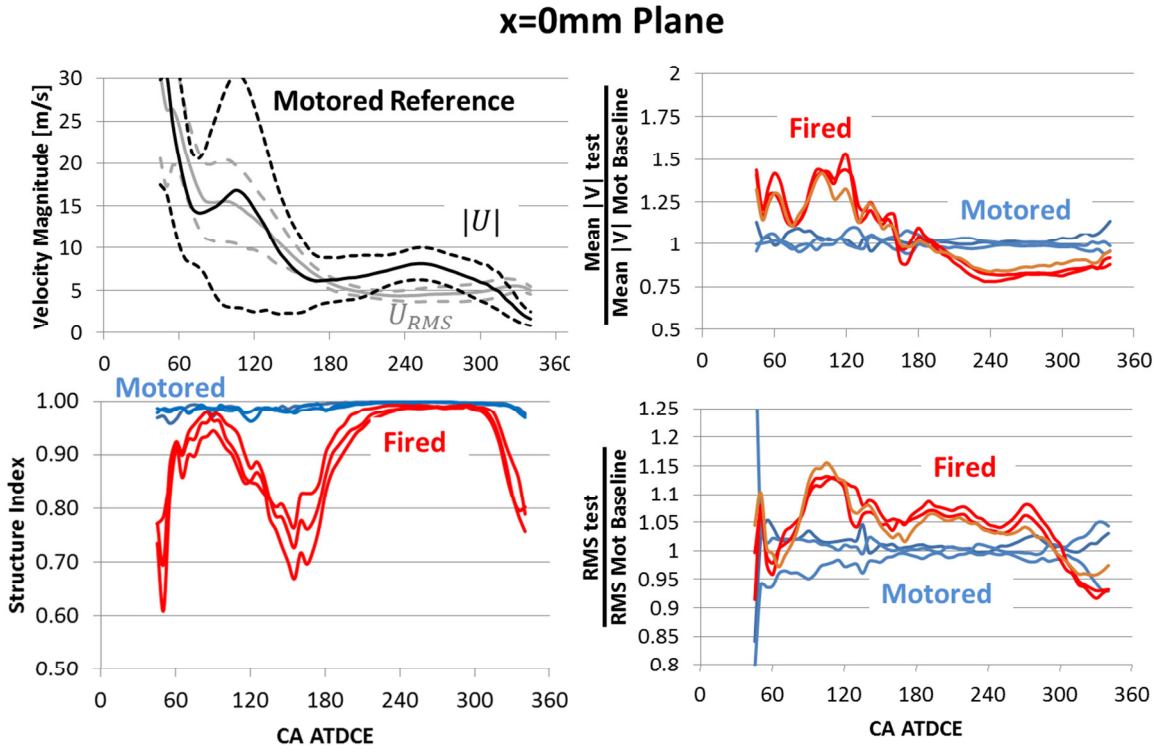
x=0mm Plane
Motored Reference
$|U|$
U_{RMS}
Velocity Magnitude [m/s]
Fired
Motored
Mean |V| test
Mean |V| Mot Baseline
Motored
Fired
Structure Index
Fired
Motored
RMS test
RMS Mot Baseline
CA ATDCE
CA ATDCE

APPENDIX D OH* CONTOUR RECOGNITION EXAMPLES

Here some example results of OH* contour recognition algorithm are shown here. The same algorithm was used without parameter tuning to process about a quarter million images under various operating conditions. This is possible due to a dynamic threshold based on image intensity. The suitable definition of this threshold is average of maximum intensity of each pixel column minus standard deviation of image intensity. This enabled to use the same algorithm for very bright stoichiometric propane flames and low intensity very dilute flames.

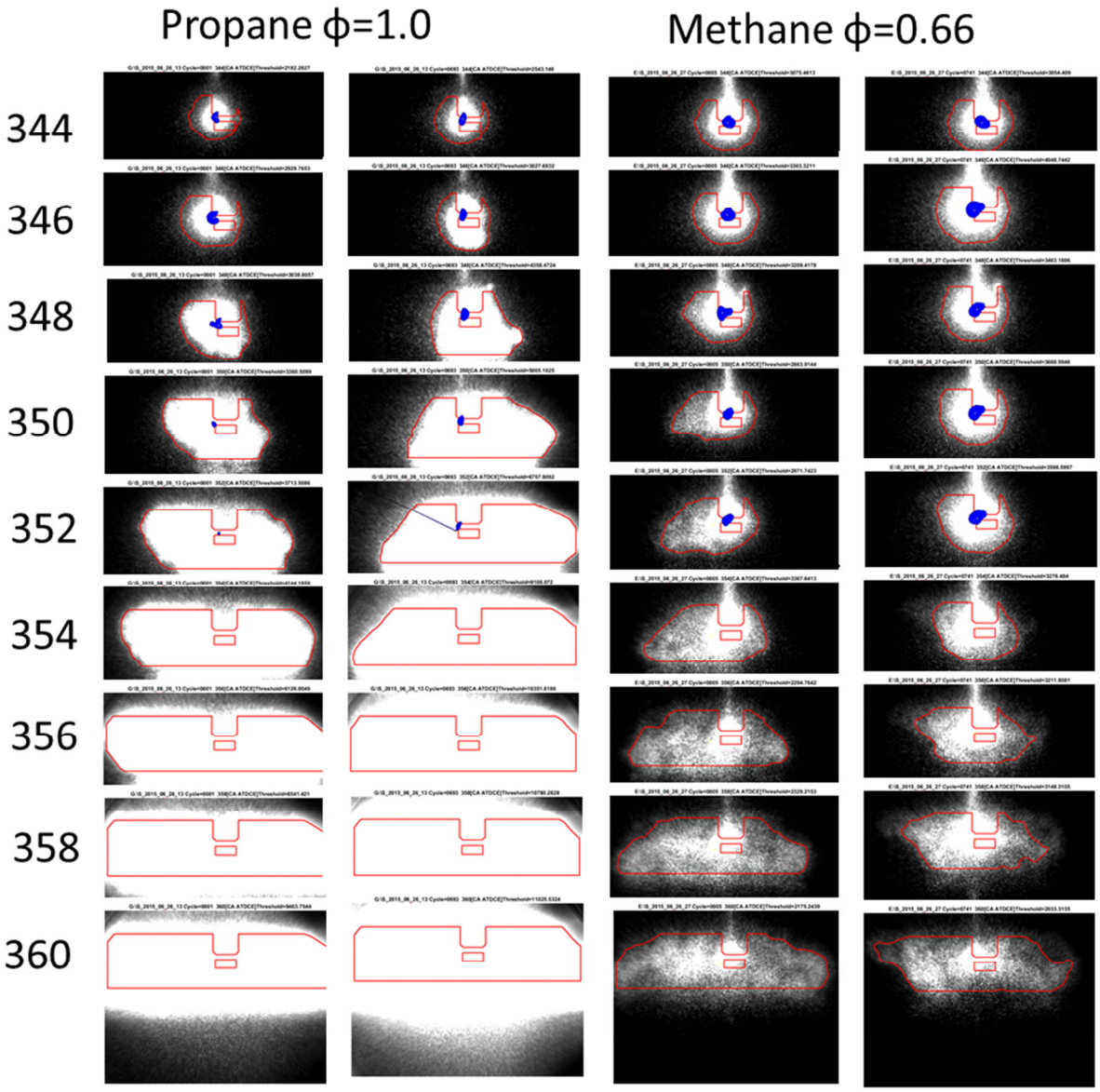

Examples of OH* contour recognition results

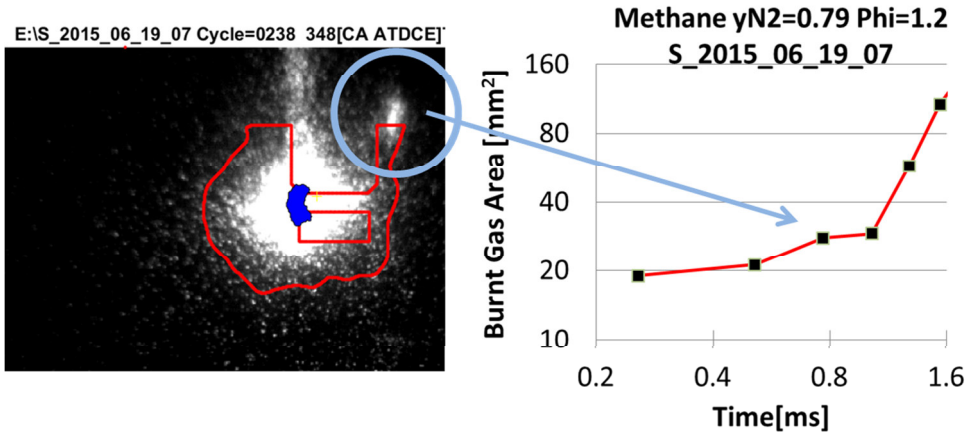

Interference of cylinder head paint excited by PLIF 266nm laser, causing measurement error in OH* area.

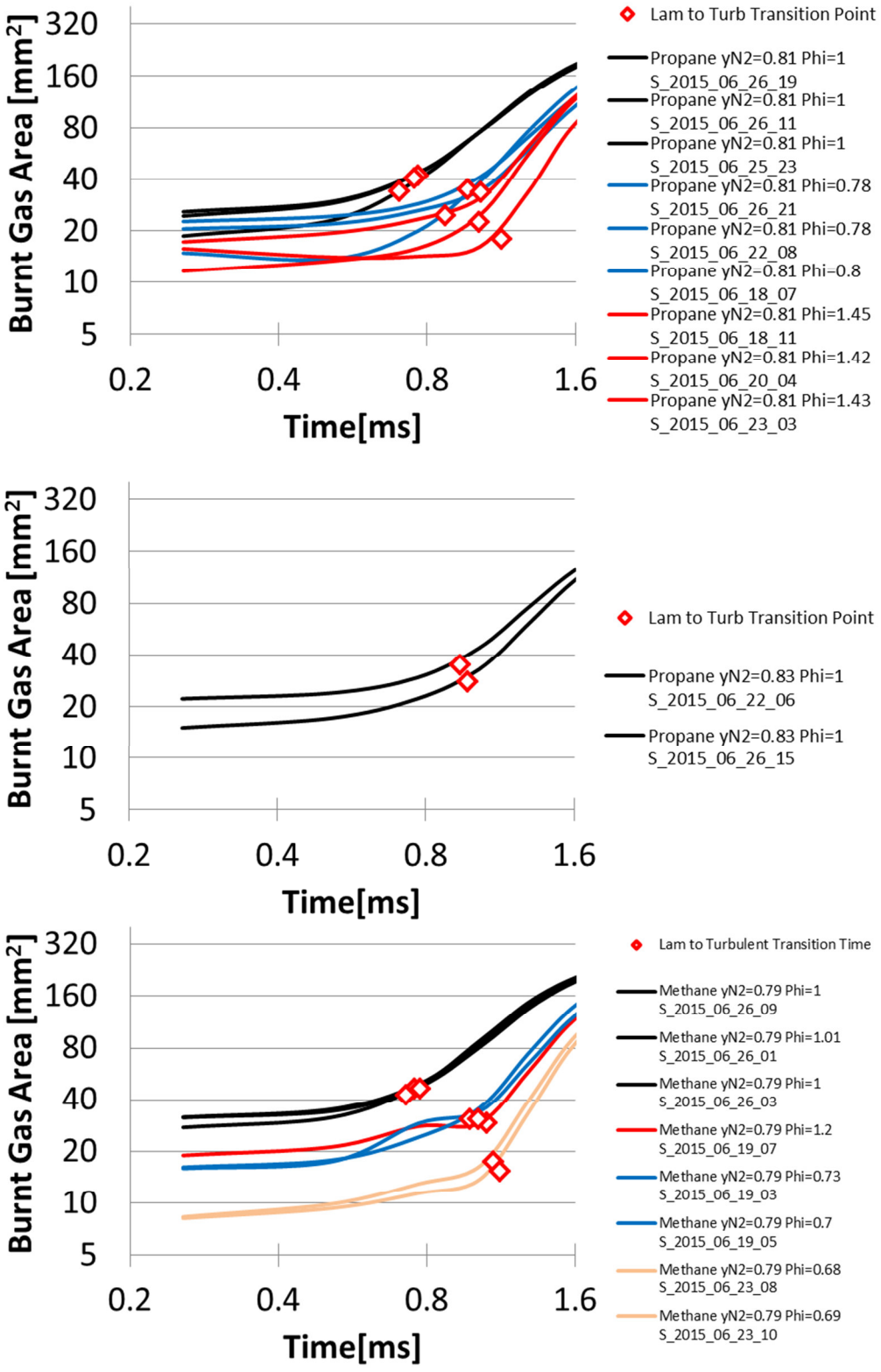

Average laminar to turbulent transition points for various mixtures and tests. Top: Dilute propane for stoichiometric, lean and rich conditions. Mid: Very dilute propane at 5% COV IMEP limit; Bottom: Methane tests at stoichiometric, lean and rich conditions

APPENDIX E P-VALUE ANALYSIS TO IDENTIFY STATISTICALLY IMPORTANT PARAMETERS TO COMBUSTION

p-Value plots for the identification of important variables to combustion.

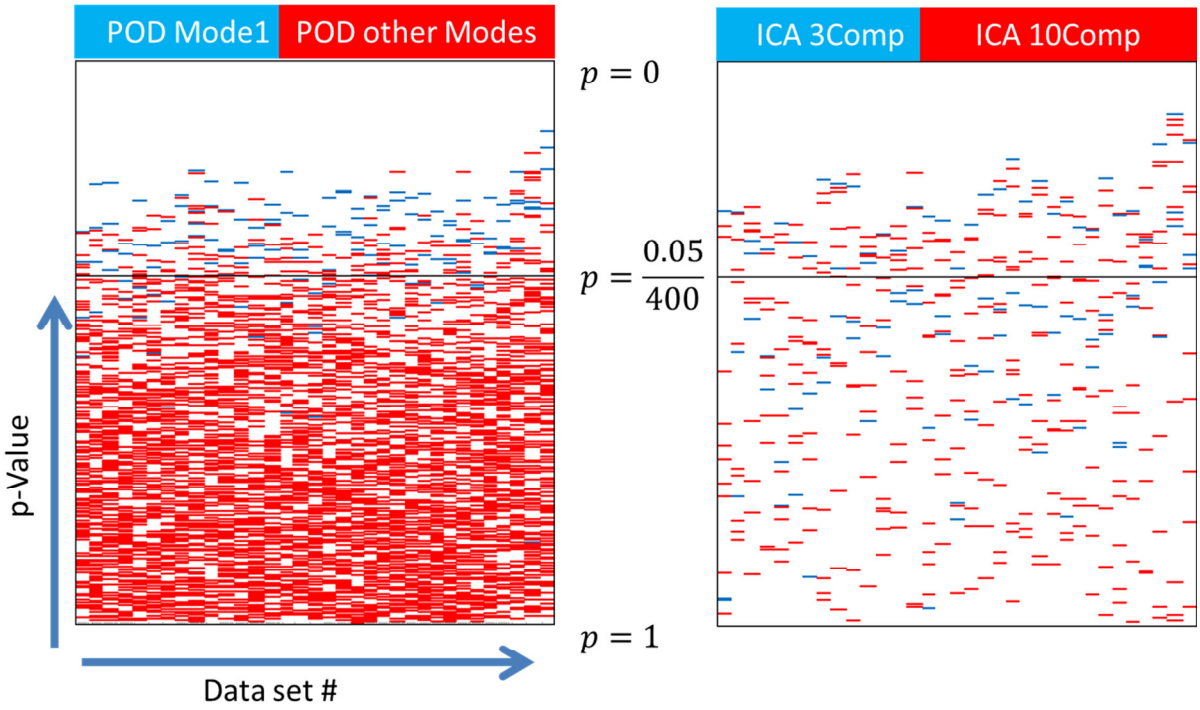

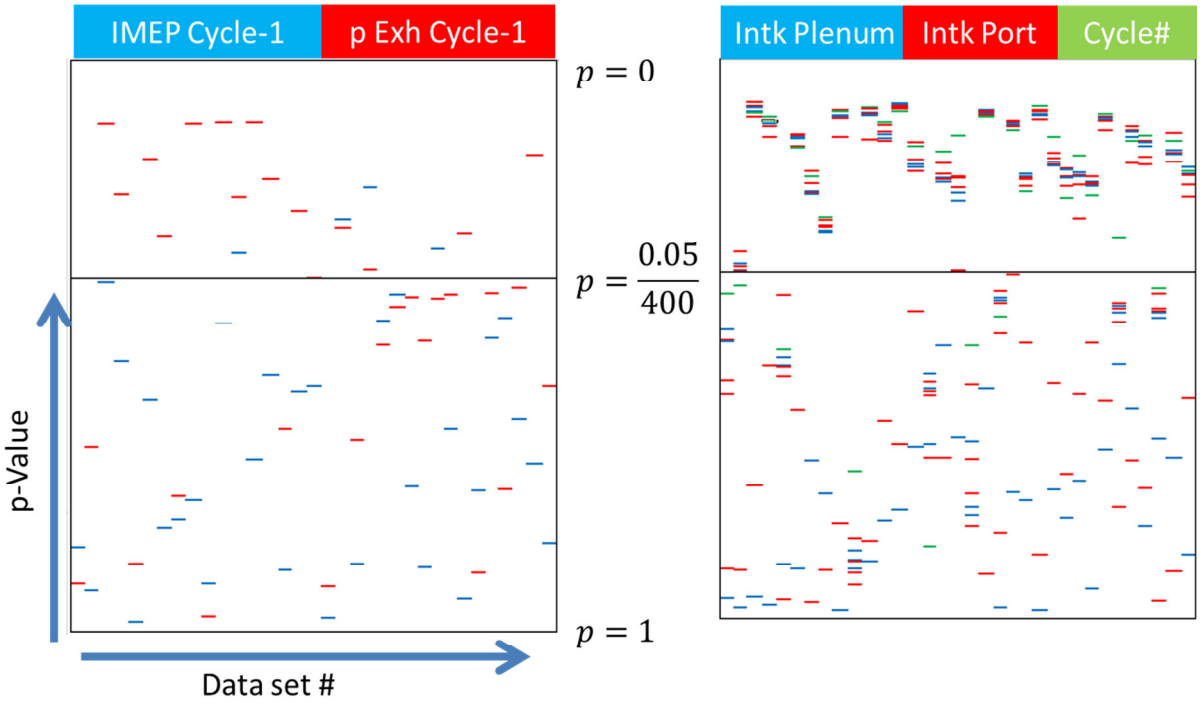

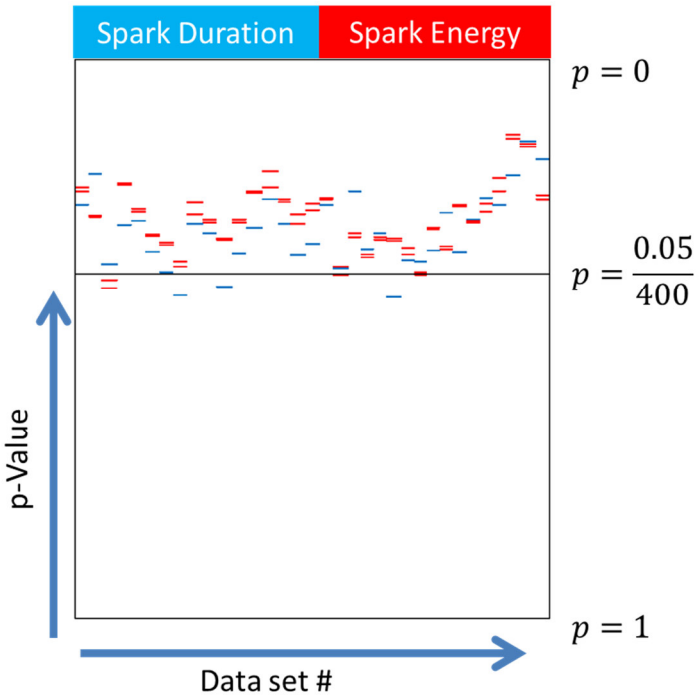
Spark Duration
Spark Energy
$p = 0$
$p = \frac{0.05}{400}$
$p = 1$
p-Value
Data set #

APPENDIX F PIV DT SETTINGS

1300RPM40kPa fired Dt z=-5mm		
CA Range (° ATDCc)		dt (µs)
-360	-350	20
-345	-335	10
-330	-330	5
-325	-325	4
-320	-295	3
-290	-190	4.5
-185	-180	7
-175	-165	10
-160	-125	20
-120	-55	25
-50	-20	20
-18	-2	25
-1	0	10
1	10	5

1300RPM40kPa fired Dt y=0mm		
CA Range (° ATDCc)		dt (µs)
-360	-350	100
-345	-335	60
-330	-330	40
-325	-325	10
-320	-260	5
-255	-225	10
-220	-200	15
-195	-180	20
-175	-165	25
-160	-30	30
-25	-20	40
-19	-2	25
-1	0	10
1	5	6

1300RPM40kPa fired Dt x=0mm		
CA Range (° ATDCc)		dt (µs)
-335	-335	20
-330	-330	15
-325	-320	6
-315	-310	5
-305	-300	4
-295	-240	5
-235	-230	8
-225	-215	10
-210	-205	15
-200	-195	20
-190	-180	25
-175	-135	30
-130	-65	35
-60	-17	40
-16	-11	25
-10	-5	20
-4	-2	15
-1	0	8
1	5	5

Fired Dt range for horizontal and vertical cutting planes

1300RPM40kPa motored Dt z=-5mm		
CA Range (° ATDCc)		dt (µs)
-360	-350	20
-345	-335	10
-330	-330	5
-325	-325	4
-320	-295	3
-290	-190	4.5
-185	-180	7
-175	-165	10
-160	-125	20
-120	-55	25
-50	-5	20
0	5	25
10	10	30
15	100	40
105	120	30
125	125	18
130	130	10
135	150	5
155	210	3
215	245	5
250	255	6
260	275	8
280	310	10
315	345	15

1300RPM40kPa motored Dt y=0mm		
CA Range (° ATDCc)		dt (µs)
-360	-350	100
-349	-335	60
-334	-330	40
-329	-320	10
-319	-310	5
-309	-300	4
-299	-225	5
-224	-200	15
-199	-180	20
-179	-165	25
-164	-30	30
-29	-20	40
-19	-5	50
-4	130	80
131	135	30
136	145	20
146	155	12
156	195	6
196	200	8
201	215	10
216	225	15
226	250	20
251	330	25
331	350	40
351	357	60

1300RPM40kPa motored Dt x=0mm		
CA Range (° ATDCc)		dt (µs)
-360	-355	50
-350	-350	30
-345	-335	20
-330	-330	15
-325	-320	6
-315	-310	5
-305	-300	4
-295	-230	5
-225	-215	10
-210	-200	15
-195	-180	20
-175	-165	25
-160	-5	30
0	15	35
20	25	50
30	30	60
35	40	75
45	120	80
125	125	60
130	130	30
135	135	15
140	145	10
150	150	8
155	210	5
215	225	10
230	245	15
250	330	20
335	345	25

Motored dt for horizontal and vertical cutting planes

BIBLIOGRAPHY

1. Council, N.R., *America's Climate Choices*. 2011, Washington, DC: The National Academies Press. 144.
2. Pera, C., V. Knop, and J. Reveillon, *Influence of flow and ignition fluctuations on cycle-to-cycle variations in early flame kernel growth.* Proceedings of the Combustion Institute, 2014.
3. Schiffmann, P., et al., *TCC-III Engine Benchmark for Large-Eddy Simulation of IC Engine Flows.* Oil & Gas Science and Technology–Revue d'IFP Energies nouvelles, 2015.
4. Heywood, J.B., *Internal combustion engine fundamentals*. Vol. 930. 1988: McGraw-Hill New York.
5. Merker, G.P. and C. Schwarz, *Grundlagen Verbrennungsmotoren*. 2009: Springer.
6. Arcoumanis, C. and T. Kamimoto, *Flow and combustion in reciprocating engines*. 2009: Springer.
7. Ozdor, N., M. Dulger, and E. Sher, *Cyclic variability in spark ignition engines a literature survey*. 1994, SAE Technical Paper 940987.
8. Teets, R.E. and J.A. Sell, *Calorimetry of Ignition Sparks*. 1988, SAE International 880204.
9. Maly, R. and M. Vogel, *Initiation and propagation of flame fronts in lean CH4-air mixtures by the three modes of the ignition spark.* Symposium (International) on Combustion, 1979. **17**(1): p. 821-831.
10. Maly, R., *Ignition model for spark discharges and the early phase of flame front growth.* Symposium (International) on Combustion, 1981. **18**(1): p. 1747-1754.
11. Dale, J.D., M.D. Checkel, and P.R. Smy, *Application of high energy ignition systems to engines.* Progress in Energy and Combustion Science, 1997. **23**(5–6): p. 379-398.
12. Santavicca, D.A., *Spark Ignited Turbulent Flame Kernel Growth*, in *Other Information: PBD: 1 Jun 1995*. 1995. p. Medium: P; Size: 14 pages.
13. Tagalian, J. and J.B. Heywood, *Flame initiation in a spark-ignition engine.* Combustion and flame, 1986. **64**(2): p. 243-246.
14. Gatowski, J.A., J.B. Heywood, and C. Deleplace, *Flame photographs in a spark-ignition engine.* Combustion and Flame, 1984. **56**(1): p. 71-81.
15. Ho, C. and D. Santavicca, *Turbulence effects on early flame kernel growth*. 1987, SAE Technical Paper 872100.
16. Ko, Y., R. Anderson, and V.S. Arpaci, *Spark ignition of propane-air mixtures near the minimum ignition energy: Part I. An experimental study.* Combustion and flame, 1991. **83**(1): p. 75-87.

17. Pischinger, S. and J.B. Heywood, *How Heat Losses to the Spark Plug Electrodes Affect Flame Kernel Development in an SI-Engine*. 1990, SAE Paper 900021.
18. Enaux, B., et al., *LES study of cycle-to-cycle variations in a spark ignition engine.* Proceedings of the Combustion Institute, 2011. **33**(2): p. 3115-3122.
19. Ayala, F.A. and J.B. Heywood, *Lean SI Engines: The role of combustion variability in defining lean limits*. 2007, Consiglio Nazionale delle Ricerche.
20. Keck, J.C., J.B. Heywood, and G. Noske, *Early flame development and burning rates in spark ignition engines and their cyclic variability*. 1987: Society of Automotive Engineers Warrendale, PA.
21. Chen, H., M. Xu, and D.L. Hung, *Analyzing In-Cylinder Flow Evolution and Variations in a Spark-Ignition Direct-Injection Engine Using Phase-Invariant Proper Orthogonal Decomposition Technique*. 2014, SAE Technical Paper.
22. Chen, H., et al., *Cycle-to-cycle variation analysis of early flame propagation in engine cylinder using proper orthogonal decomposition.* Experimental Thermal and Fluid Science, 2014. **58**: p. 48-55.
23. Chen, H., D.L. Reuss, and V. Sick, *Analysis of misfires in a direct injection engine using proper orthogonal decomposition.* Experiments in fluids, 2011. **51**(4): p. 1139-1151.
24. Johansson, B., *Cycle to cycle variations in SI engines-The effects of fluid flow and gas composition in the vicinity of the spark plug on early combustion*. 1996, SAE Technical Paper 962084.
25. Vermorel, O., et al., *Towards the understanding of cyclic variability in a spark ignited engine using multi-cycle LES.* Combustion and Flame, 2009. **156**(8): p. 1525-1541.
26. Bates, S.C., *Flame Imaging Studies of Cycle-by-Cycle Combustion Variation in a SI Four-Stroke Engine*. 1989, SAE Paper 892086.
27. Keck, J.C., J.B. Heywood, and G. Noske, *Early flame development and burning rates in spark ignition engines and their cyclic variability*. 1987, SAE Technical Paper 870164.
28. Ting, D.S., M.D. Checkel, and B. Johansson, *The Importance of High-Frequency, Small-Eddy Turbulence in Spark Ignited, Premixed Engine Combustion*. 1995, SAE Technical Paper 952409.
29. Hill, P.G. and A. Kapil, *The relationship between cyclic variations in spark-ignition engines and the small structure of turbulence.* Combustion and Flame, 1989. **78**(2): p. 237-247.
30. Aleiferis, P., et al., *Flame chemiluminescence studies of cyclic combustion variations and air-to-fuel ratio of the reacting mixture in a lean-burn stratified-charge spark-ignition engine.* Combustion and flame, 2004. **136**(1): p. 72-90.

31. Pera, C., S. Chevillard, and J. Reveillon, *Effects of residual burnt gas heterogeneity on early flame propagation and on cyclic variability in spark-ignited engines.* Combustion and Flame, 2013. **160**(6): p. 1020-1032.
32. Burluka, A.A., et al., *Effects of large-scale turbulence on cyclic variability in spark-ignition engine.* Experimental Thermal and Fluid Science, 2012. **43**: p. 13-22.
33. Aleiferis, P.G., et al., *The nature of early flame development in a lean-burn stratified-charge spark-ignition engine.* Combustion and Flame, 2004. **136**(3): p. 283-302.
34. Kuo, K.K., *Principles of combustion.* 1986.
35. Law, C.K., *Combustion physics*. 2006: Cambridge University Press.
36. Bell, J.B., et al., *Numerical simulation of Lewis number effects on lean premixed turbulent flames.* Proceedings of the Combustion Institute, 2007. **31**(1): p. 1309-1317.
37. Bechtold, J.K. and M. Matalon, *The dependence of the Markstein length on stoichiometry.* Combustion and Flame, 2001. **127**(1–2): p. 1906-1913.
38. Bradley, D., et al., *Turbulent burning velocity, burned gas distribution, and associated flame surface definition.* Combustion and Flame, 2003. **133**(4): p. 415-430.
39. Driscoll, J.F., *Turbulent premixed combustion: Flamelet structure and its effect on turbulent burning velocities.* Progress in Energy and Combustion Science, 2008. **34**(1): p. 91-134.
40. Tseng, L.-K., M. Ismail, and G.M. Faeth, *Laminar burning velocities and Markstein numbers of hydrocarbonair flames.* Combustion and Flame, 1993. **95**(4): p. 410-426.
41. Poinsot, T., T. Echekki, and M. Mungal, *A study of the laminar flame tip and implications for premixed turbulent combustion.* Combustion science and technology, 1992. **81**(1-3): p. 45-73.
42. Taylor, S. and D. Smith, *Comment on "laminar burning velocities and Markstein numbers of hydrocarbon/air flames" by L.-K. Tseng, MA Ismail, and GM Faeth.* Combustion and flame, 1995. **102**(4): p. 523-525.
43. Bradley, D., P.H. Gaskell, and X.J. Gu, *Burning velocities, markstein lengths, and flame quenching for spherical methane-air flames: A computational study.* Combustion and Flame, 1996. **104**(1–2): p. 176-198.
44. Echekki, T. and M. Mungal. *Flame speed measurements at the tip of a slot burner: Effects of flame curvature and hydrodynamic stretch*. in *Symposium (International) on Combustion*. 1991. Elsevier.
45. Durox, D., S. Ducruix, and S. Candel, *Experiments on collapsing cylindrical flames.* Combustion and Flame, 2001. **125**(1): p. 982-1000.

46. Palm-Leis, A. and R.A. Strehlow, *On the propagation of turbulent flames.* Combustion and Flame, 1969. **13**(2): p. 111-129.
47. Ibarreta, A.F., J.F. Driscoll, and D.A. Feikema, *Markstein numbers of negatively stretched premixed flames: microgravity measurements and computations.* Proceedings of the Combustion Institute, 2002. **29**(2): p. 1435-1443.
48. Sun, C.J., et al., *Dynamics of weakly stretched flames: quantitative description and extraction of global flame parameters.* Combustion and Flame, 1999. **118**(1–2): p. 108-128.
49. Wu, M., et al., *Turbulent premixed hydrogen/air flames at high Reynolds numbers.* Combustion science and technology, 1990. **73**(1-3): p. 327-350.
50. Matekunas, F.A., *Modes and measures of cyclic combustion variability*. 1983, SAE Technical Paper 830337.
51. Soltau, J., *Cylinder pressure variations in petrol engines.* Proceedings of the Institution of Mechanical Engineers: Automobile Division, 1960. **14**(1): p. 99-117.
52. Reuss, D.L., *Cyclic Variability of Large-Scale Turbulent Structures in Directed and Undirected IC Engine Flows.* SAE Paper 2000-01-0246, 2000.
53. Kranz, P., *Cycle-to-cycle variability in a gaseous-fuel spark-ignited engine characterized by optical diagnostics*, in *Institute of Combustion and Gas Dynamics*. 2015, University of Duisburg and Essen. p. 110.
54. Galmiche, B., et al., *Turbulence characterization of a high-pressure high-temperature fan-stirred combustion vessel using LDV, PIV and TR-PIV measurements.* Experiments in fluids, 2014. **55**(1): p. 1-20.
55. Galmiche, B., F. Halter, and F. Foucher, *Experimental Investigations for Turbulent Premixed Flame Analysis*. 2013, SAE Paper 2013-24-0043.
56. Raffel, M., C. Willert, and J. Kompenhans, *Particle Image Velocimetry: a practical guide,(1998)*. Springer.
57. Adrian, R.J. and J. Westerweel, *Particle image velocimetry*. 2011: Cambridge University Press.
58. A/S, D.D. *http://www.dantecdynamics.com/Default.aspx?ID=820*. http://www.dantecdynamics.com/.
59. Raffel, M., et al., *Particle Image Velocimetry - A Practical Guide*. 2007, Goettingen: Springer-Verlag Berlin Heidelberg.
60. al., W.e., *Digital particle image velocimetry.* Experiments in Fluids, 1991. **10**: p. 181-193.

61. Chen, H., D.L. Reuss, and V. Sick, *On the use and interpretation of proper orthogonal decomposition of in-cylinder engine flows.* Measurement Science and Technology, 2012. **23**(8): p. 085302.
62. Chen, H., et al., *A practical guide for using proper orthogonal decomposition in engine research.* International Journal of Engine Research, 2013. **14**(4): p. 307-319.
63. Fogleman, M., et al., *Application of the proper orthogonal decomposition to datasets of internal combustion engine flows.* Journal of Turbulence, 2004. **5**(23): p. 1-3.
64. Hyvärinen, A., J. Karhunen, and E. Oja, *Independent component analysis*. Vol. 46. 2004: John Wiley & Sons.
65. Bizon, K., et al., *Analysis of Diesel engine combustion using imaging and independent component analysis.* Proceedings of the Combustion Institute, 2013. **34**(2): p. 2921-2931.
66. Scheimpflug, T., *-scheimpflug*. 1904, Google Patents.
67. Prasad, A.K., *Stereoscopic particle image velocimetry.* Experiments in fluids, 2000. **29**(2): p. 103-116.
68. Zhao, H. and N. Ladommatos, *Engine combustion instrumentation and diagnostics.* Warrendale, PA: Society of Automotive Engineers, 2001. 842, 2001.
69. Arpacı, V.S., et al., *Spark kernel development in constant volume combustion.* Combustion and Flame, 2003. **135**(3): p. 315-322.
70. Schulz, C. and V. Sick, *Tracer-LIF diagnostics: quantitative measurement of fuel concentration, temperature and fuel/air ratio in practical combustion systems.* Progress in Energy and Combustion Science, 2005. **31**(1): p. 75-121.
71. Miller, V.A., et al., *Single-and dual-band collection toluene PLIF thermometry in supersonic flows.* Experiments in fluids, 2013. **54**(6): p. 1-13.
72. Settles, G.S., *Schlieren and shadowgraph techniques: visualizing phenomena in transparent media*. 2012: Springer Science & Business Media.
73. Schardin, H., *Das Toeplersche schlierenverfahren: grundlagen für seine anwendung und quantitative auswertung*. Vol. 367. 1934: VDI-verlag gmh.
74. Feldmann, O. and F. Mayinger, *Optical measurements: techniques and applications*. 2012: Springer Science & Business Media.
75. Adrian, R., *Dynamic ranges of velocity and spatial resolution of particle image velocimetry.* Measurement Science and Technology, 1997. **8**: p. 1393-1398.

76. Reuss, D.L., M. Megerle, and V. Sick, *Particle-image velocimetry Measurement Errors when Imaging through a Transparent Engine Cylinder.* Measurement Science and Technology, 2002. **13**: p. 1029 - 1035.

77. Megerle, M., V. Sick, and D.L. Reuss, *Measurement of Digital PIV Precision using Electrooptically-Created Particle-Image Displacements.* Measurement Science and Technology, 2002. **13**: p. 997 - 1005.

78. Abraham, P.S., D.L. Reuss, and V. Sick. *High-speed particle image velocimetry study of in-cylinder flows with improved dynamic range*. in *SAE Paper 2013-01-0542*. 2013.

79. Bopp, S., C. Vafidis, and J.H. Whitelaw, *The Effect of Engine Speed on the TDC Flowfield in a Motored Reciprocating Engine*. 1986, SAE Paper 860023.

80. Liu, K. and D.C. Haworth, *Development and Assessment of POD for Analysis of Turbulent Flow in Piston Engines*. 2011, SAE Paper 2011-01-0830.

81. Pope, S.B., *Turbulent flows*. 2000: Cambridge university press.

82. Hinze, J., *Turbulence McGraw-Hill.* New York, 1975. **218**.

83. Sarathy, S., et al., *An experimental and kinetic modeling study of n-octane and 2-methylheptane in an opposed-flow diffusion flame.* Combustion and Flame, 2011. **158**(7): p. 1277-1287.

84. Sarathy, S.M., et al., *Comprehensive chemical kinetic modeling of the oxidation of 2-methylalkanes from C 7 to C 20.* Combustion and flame, 2011. **158**(12): p. 2338-2357.

85. Kee, R.J., et al., *A FORTRAN chemical kinetics package for the analysis of gas phase chemical and plasma kinetics.* Sandia National Laboratories, 1996.

86. Vaughan, A., *Adaptive Machine Learning for Modeling and Control of Non-Stationary, Near Chaotic Combustion in Real-Time*. 2015.

87. Vaughan, A. and S.V. Bohac, *An Extreme Learning Machine Approach to Predicting Near Chaotic HCCI Combustion Phasing in Real-Time.* arXiv preprint arXiv:1310.3567, 2013.

88. Endouard, C., F. Halter, and F. Foucher. *Effects of CO2, H2O and EGR dilution on laminar burning velocities and Markstein lengths of iso-octane/air mixtures*. in *Ninth Mediterranean Combustion Symposium*. 2015.

89. Endouard, C., et al. *A Simultaneous Schlieren and Tomography Diagnostic for the Study of Premixed Turbulent Expanding Flames*. in *24th «Journées d'Etude» of the Belgian Section of the Combustion Institute*. 2016.

90. Galmiche, B., F. Halter, and F. Foucher, *Effects of high pressure, high temperature and dilution on laminar burning velocities and Markstein lengths of iso-octane/air mixtures.* Combustion and Flame, 2012. **159**(11): p. 3286-3299.
91. Abdel-Gayed, R.G., D. Bradley, and F.K.K. Lung, *Combustion regimes and the straining of turbulent premixed flames.* Combustion and Flame, 1989. **76**(2): p. 213-218.
92. Brequigny, P., F. Halter, and C. Mounaïm-Rousselle, *Lewis number and Markstein length effects on turbulent expanding flames in a spherical vessel.* Experimental Thermal and Fluid Science, 2016. **73**: p. 33-41.
93. Brequigny, P., et al., *Fuel performances in Spark-Ignition (SI) engines: Impact of flame stretch.* Combustion and Flame, 2016. **166**: p. 98-112.
94. Ghorbali, A., *Cyclic variation in combustion in a constant volume combustion chamber*. 1993: University of Ottawa (Canada).
95. Cole, D.E. and W. Mirsky, *Mixture Motion - Its Effect on Pressure Rise in a Combustion Bomb: A New Look at Cyclic Variation*. 1968, SAE International.
96. Sick, V., et al., *Turbulent scales in a fan-stirred combustion bomb.* Combustion and flame, 2001. **127**(3): p. 2119-2123.
97. Montgomery, D.C., *Design and analysis of experiments*. 2008: John Wiley & Sons.